# Converter Control for Wind Turbines when Operating in Weak Grids Containing Resonances

Von der Fakultät für Elektrotechnik und Informatik
der Gottfried Wilhelm Leibniz Universität Hannover
zur Erlangung des akademischen Grades

## Doktor-Ingenieur

(abgekürzt: Dr.-Ing.)

genehmigte Dissertation

von

## Dipl.-Ing. Felix Sebastian Fuchs

geboren am 20.06.1983 in Aachen

2017

1. Referent    Prof. Dr.-Ing. Axel Mertens
2. Referent    Prof. Frede Blaabjerg, Ph.D.

Tag der Promotion:    19.05.2017

mail@felix-fuchs.de

# Acknowledgements / Danksagung

# Abstract

This thesis is a contribution with respect to grid integration of wind turbines in weak grids containing resonances (grid resonances). Grid resonances can be evoked by capacitive elements in the grid (for example cable or power factor correction capacitances). The influence of grid resonances on a standard wind turbine converter control system is analysed. Stability critical grid resonances are identified, and methods to stabilise the control are developed.

According to harmonic grid codes a completely new 2 MW grid converter system is designed (being close to commercial wind turbine systems). The standard system, low voltage two-level paralleled converters, is analysed. Two different grid filter systems are common in wind turbine converters: LCL or trap filters. Both are designed and analysed in this thesis. In this way, there is a comparison which system is more sensitive to grid resonances. Both filter types contain resonances which can be excited and which could lead to control instability. Therefore two solutions are pursued: passive damping circuits or active damping by control. In this thesis, both methods are analysed. In particular, different passive damping approaches are compared. It is found, that completely different filter designs are necessary for stiff and weak grids (as a result of the grid codes). Due to this fact two different LCL/trap filters are designed, one for the stiff grid with a short circuit power ratio (SCR) of grid to turbine of higher than 50, and another one for an SCR of 10-50.

Working towards the design of a standard turbine grid converter system, a complete dq current control is set up for all filter topologies. As every measurement installed increases the costs, and due to the fact that a converter current measurement is always implemented for safety reasons, the converter current (and not grid current) is controlled in this work. An explanation that the symmetrical optimum and not the technical optimum is the right choice for a start design of the current controller is presented. Another focus is on measurement filters. It is found that a low pass filtering of the grid voltage prevents aliasing and increases the current control bandwidth. A model for the (medium voltage) grid, containing a resonance, is developed. This leads to the definition of a variable LCL-type grid resonance.

Then, for all designed converter controls, a transfer function stability analysis varying the grid resonance is performed. It is found that specific grid resonances, with resonance frequency near the -180° crossing frequency of the open current control loop, can be stability critical. It is shown that the control can be stabilised only with a new PI design. For the redesigned controls, the necessary current control bandwidth originating from the grid codes is still met.

The filter design, control design and stability analysis results are validated with a p.u. transformed laboratory setup. This is performed for all four designed filter topologies. Compared to the 2 MW system, significant lower X/R ratios are found for the passive elements. This leads to a higher system damping and therefore different stability results. As solution, the root locus analysis is applied. Using the critical PI gain (lowest gain leading to instability), the stability influence of several grid resonances is demonstrated.

In this thesis, all data is provided enabling reproduce of the results. The author is looking forward to discussion and/or comments (mail@felix-fuchs.de).

# Kurzfassung

Diese Arbeit ist ein Beitrag im Bereich der Netzintegration von Windenergieanlagen in schwache Netze mit Resonanzen (Netzresonanzen). Netzresonanzen können durch kapazitive Elemente im Netz hervorgerufen werden (beispielsweise Kabel- oder Leistungsfaktorkorrektur-Kapazitäten). Es wird der Einfluss solcher Netzresonanzen auf ein Standard-Windenergieanlagensystem analysiert. Dabei werden stabilitätskritische Netzresonanzen identifiziert und Methoden zur Stabilisierung der Regelung entwickelt.

Den Netzanschlussbedingungen für hochfrequente Ströme entsprechend wird ein komplett neues 2 MW Netzumrichter-System ausgelegt, wobei darauf geachtet wird, dass es sich um industrieübliche Designs handelt. Betrachtet werden parallel geschaltete Niederspannungs-2-Level-Umrichter (üblich in Windenergieanlagen). In Windenergieanlagen sind zwei Arten von Netzfiltern üblich: LCL oder Saugkreisfilter. Beide werden in dieser Arbeit ausgelegt und untersucht. So ist ein direkter Vergleich möglich - auch hinsichtlich der Sensitivität bzgl. Netzresonanzen. Beide Filtertopologien beinhalten Resonanzen welche angeregt werden können. Dies kann zu einer Instabilität der Regelung führen. Hier werden zwei Lösungen verfolgt: Passive Dämpfungsschaltungen oder eine aktive Dämpfung durch die Regelung. In dieser Arbeit werden beide Methoden analysiert. Insbesondere werden verschiedene passive Dämpfungsmethoden verglichen. Es wird festgestellt, dass deutlich unterschiedliche Filterauslegungen für schwache und starke Netze notwendig sind (als Konsequenz aus den Netzanschlussbedingungen). Aus diesem Grund werden zwei unterschiedliche LCL / Saugkreisfilter ausgelegt, zum einen für ein starkes Netz mit einem Kurzschlussleistungsverhältnis des Netzes zur Anlagenleistung von größer als 50 und zum anderen für 10-50.

Mit dem Ziel ein Standard-Netzumrichter-System einer Windenergieanlage auszulegen wird in dieser Arbeit die komplette dq-Strom-Regelung für alle ausgelegten Filter entworfen. Da jede Messung die Kosten erhöht, und eine Messung des Umrichterstroms aus Sicherheitsgründen immer installiert sein muss, wird der Umrichterstrom (und nicht der Netzstrom) geregelt. Es wird erklärt weshalb das symmetrische Optimum und nicht das Betragsoptimum die richtige Wahl für das Startdesign der Stromregler ist. Ein weiterer Fokus liegt auf Messfiltern. Hier wird herausgefunden, dass ein Tiefpassfiltern der Netzspannung Aliasing verhindert und die Stromregelungsbandbreite erhöht. Es wird ein Modell für ein Mittelspannungsnetz mit einer Resonanz entwickelt, das letztlich einem LCL Schaltkreis gleicht.

Im nächsten Schritt wird für alle entworfenen Regelungen eine Stabilitätsanalyse mit variierender Netzresonanz durchgeführt. Das Resultat ist, dass spezifische Netzresonanzen mit einer sogenannten -180° Frequenz des offenen Stromregelkreises stabilitätskritisch sein können. Es wird gezeigt, dass nur mit einem neuen PI Design auch hier stabile Regelungen erreicht werden können. Für die angepassten PI Regler wird weiterhin die in den Netzanschlussbedingungen geforderte Dynamik eingehalten.

Die Filterauslegung, die Reglerauslegung und die Stabilitätsanalyse werden mit einem Per Unit übertragenen Laborsystem validiert. Dies wird für alle vier Filtertopologien durchgeführt. Verglichen mit dem 2 MW System, werden im Laborsystem deutlich niedrigere X/R Verhältnisse

der passiven Komponenten vorgefunden. Dies führt zu einer größeren Dämpfung und daher zu anderen Stabilitätsergebnissen. Als Lösung wird die Wurzelortskurvendarstellung angewendet. Mit der kritischem PI Verstärkung (der niedrigsten PI Verstärkung die zu Instabilität führt) wird der Einfluss auf die Stabilität von verschiedenen Netzresonanzen demonstriert.

In dieser Arbeit werden alle Daten zur Verfügung gestellt um eine direkte Nachbildung der Ergebnisse zu ermöglichen. Der Autor freut sich über Diskussionen und/ oder Kommentare (mail@felix-fuchs.de).

**Schlagworte:**

Netzseitiger Wechselrichter, LCL-Filter, Saugkreis-Filter, Netzresonanz, Resonanz, Regelung, Stromregelung, Stabilitätsanalyse, Dreiphasig, Aktive Dämpfung, Schwaches Netz, Netzfilter Design, 2 MW, Bezogene Größen

**Keywords:**

grid-connected inverter, LCL filter, trap filter, grid resonance, resonance, control, current control, stability analysis, three-phase, active damping, weak grid, grid filter-design, 2 MW, p.u.

*"Make it" !*   (Steven Tyler, 1973)

# Contents

# Style

| | | |
|---|---|---|
| $\underline{Z}$ | - | Complex variable (underlined) |
| $Z$, $S$... | - | Absolute value |
| $\mathbf{R}$, $\mathbf{L}$, $\mathbf{C}$... | - | Related variables (bold) |
| $\hat{I}$ | - | Amplitude |

# Abbreviations

| | | |
|---|---|---|
| -180 frequency | - | Frequency where the phase of the transfer function of the open loop without grid resonance crosses -180 degree |
| abs | - | Absolute value |
| AD | - | Active damping |
| AP | - | Analytical prediction |
| CL | - | Closed loop |
| critical PI gain | - | Minimal gain of PI controller leading to an instable control loop |
| DCE | - | Digital control emulation |
| est. | - | Estimated |
| grid resonance | - | Grid impedance with resonance, LCL type |
| GVFF | - | Grid voltage feedforward |
| HV | - | High voltage |
| inv | - | Inverse |
| int. | - | Intended |
| IP | - | Instable poles |
| LV | - | Low voltage |
| MaxCCppR | - | Maximal converter current peak-to-peak ripple |
| MV | - | Medium voltage |
| OL | - | Open loop |
| PCC | - | Point of common coupling |
| PFCC | - | Power factor correction capacitances |
| PI | - | Proportional plus integral |
| PLL | - | Phase locked loop |
| $p\mu$ | - | Per ten thousand |
| r | - | Reactive |
| resp. | - | Respectively |
| rms | - | Root mean square |
| SCR | - | Ratio of grid short circuit power to converter rated apparent power |
| SO | - | Symmetrical optimum |
| SRF | - | Synchronous reference frame |
| SV(M) | - | Space vector (modulation) |
| TDD | - | Total demanded distortion |
| TF | - | Transfer function |
| TI | - | Triples leading to instability |
| TO | - | Technical optimum |
| X/R ratio | - | Ratio of reactance to resistance of a capacitance or induct. at 50 Hz |

# Symbols

| | | |
|---|---|---|
| $\stackrel{def.}{=}$ | - | Is defined as |
| $\circ$ | - | Degree |
| $\|\|$ | - | Connected in parallel |
| $\star$ | - | Line-to-neutral |
| $A$ | - | Absolute value |
| $C$ | - | Capacitance |
| $\varphi$ | - | Angle |
| $f$ | - | Frequency |
| $f_{-180}$ | - | Angle where the open loop phase crosses -180 degree |
| $G$ | - | Transfer function |
| $I$ | - | Current |
| j | - | Imaginary unit |
| $L$ | - | Inductance |
| $m$ | - | Modulation index |
| $\nu$ | - | Harmonic number |
| $R$ | - | Resistance |
| $s$ | - | Laplace variable |
| $S$ | - | Apparent power |
| $T$ | - | Time |
| $U$ | - | Voltage |
| $X$ | - | Reactance or disturbance |

# Indices

| | | |
|---|---|---|
| 0 | - | Open Loop or no-load or eigenfrequency |
| 1 | - | Closed Loop or fundamental (frequency) |
| 50Hz | - | Value at 50 Hz |
| ab,bc,ca | - | Line-to-line voltage |
| a0,b0,c0 | - | Line-to-neutral voltage |
| approx | - | Approximated |
| base | - | Base value |
| car | - | Carrier |
| crit | - | Critical |
| ctrl | - | Control |
| conv | - | Converter |
| est | - | Estimated |
| f | - | Value at frequency f or filter |
| grid | - | Grid-side (impedance); including transformer and grid impedance |
| int | - | Intended |
| ll | - | Line-to-line |
| lab | - | Laboratory |
| marg | - | Margin |
| max | - | Maximum |

| | | |
|---|---|---|
| mv | - | Medium voltage |
| Nyquist | - | Nyquist (frequency) of sampled system: half of the sampling frequency |
| PI | - | Proportional plus integral controller |
| PLL | - | PLL |
| power | - | Power |
| pp−p | - | Peak-to-peak value related to peak value |
| PWM | - | Pulse width modulation |
| r | - | Rated (nominal) value |
| real | - | Real |
| res | - | Resonance |
| rms | - | Root mean square |
| ser | - | Series connected |
| seriesf | - | Series connected filter |
| shunt | - | Parallel impedance between converter and grid-side inductance |
| thev | - | Thevenin |
| trsf | - | Transformer |
| trap | - | Trap filter |
| trap2 | - | Second trap filter, tuned to $2f_{\text{car}}$ |
| vltg | - | Voltage |

# 1 Introduction

Wind energy is a well acccepted and implemented renewable energy technology. Meanwhile, the energy payback time of a standard multi-megawatt turbine is far below one year [1]. Nearly all wind turbines include converter systems to enable speed-adjustable operation [2]. The grid-side converter controls the grid current to adjust the power injected into the grid. More recently, more and more stability problems with weak grids and decentralised energy sources have been documented (see Chap. 4.4.1). A weak grid leads to a grid voltage at the wind turbine significantly influenced by the wind turbine's operation itself. It is clear that this is a challenging situation for the turbine control.

The intention of this work is to contribute to the solution of such problems. This thesis is particularly dedicated not only to the influence of weak grids, but also of grids containing resonances. Resonances can be evoked by capacitive elements in the grid as cable capacitances or power factor correction capacitances. The aim is to answer the question: Are weak grids containing arbitrary resonances stability critical for standard grid-connected wind turbine converter systems? If yes, what can be done to stabilise the control?

To analyse control and stability issues in proximity to the industry application, the turbine's (electrical) system parameters must be as realistic as possible. Therefore, parameters from converter manufacturers would be the best option. But the idea of open source sharing is with industry data not possible. The second option, to use literature data, is discarded due to uncertainty. In the end a mix of literature review and discussions led to the new grid converter design presented in this thesis.

The thesis is structured as follows: In Chap. 2, the hardware system is defined. Starting from voltage and current levels, switching frequencies, the converter topology and PWM method is discussed and defined. A main part of the chapter deals with the filter design. It was found that different filter topologies are applied in wind turbine converters depending on the manufacturer. Therefore, it was decided to evaluate (and design) both utilised systems (LCL and trap filter). Great effort was put into the filter design, because at least the filter with its resonance plays an important role for the control stability also regarding grids containing resonances. Passive filter damping circuits are usually applied in industry, these were also included in the analysis.

Subsequently, in the Chap. 3, the (current) control system, including for example PLL design, PI design and signal conditioning methods are developed. Three-phase simulations are carried out to validate the designed filter and control. For good interpretability, many signals of the system are shown.

In the next step, in Chap. 4, the last missing element is defined firstly: the arbitrary grid containing a resonance. Then, as the initial aim of the thesis, the transfer function stability analysis for the standard wind turbine regarding grid resonances, is performed. Specific stability critical resonances are found and validated by three-phase simulation results. Control modifications for a stable control are proposed.

In the last Chap. 5 all results, including the filter design results, are validated by experiments.

# 2 Hardware System Design

## 2.1 Overview

In this chapter the hardware system is designed or defined, always trying to be close to realistic industry data. The main part is the grid filter design. LCL as well as trap filters are applied in industry. Therefore, both filter types are considered and designed.
At the end of the chapter, a set of hardware components is defined as the basis for control design and stability analysis.

## 2.2 Analysis of Grid Codes Regarding Harmonics

The filter and control design in this work is carried out according to the German BDEW grid codes [3] and the American IEEE 519 [4]/ 1547 [5] standard [6]. Below, parts of these grid codes are summarised.
The aim of the BDEW grid code is to guarantee a maximum harmonic distortion of the grid voltage evoked by the energy plant. This distortion is defined in percentage of the fundamental grid voltage for odd and even multiples and interharmonics (Tab. 2.1, fourth column). The voltage limits can be converted to the current limits in Tab. 2.1, fifth column, here the normalized values with a factor of $10^6$, (Tab. 2.4.3-1 in [3]). This is done with Eq. 2.2 which is derived from Eq. 2.1. From this derivation it is concluded that the limits are rms values. The current limits

**Table 2.1:** Voltage and current limits for a medium voltage connection according to [3], $v$- harmonic number (grey: not precisely mentioned in [3] but often assumed)

| Property | Harmonic number $v$ | f [Hz] | $u_{v,\max} = U_{\max}/U_{\mathrm{r}}$ [%] | $i^{rms}_{v,\max}/(A \cdot V/MVA)$ |
|---|---|---|---|---|
| odd | 5 | 250 | 0.5 | 580 |
| odd | 7 | 350 | 1 | 820 |
| odd | 11,13,17,19,23,25 | 550-1250 | $11/v$ | $63509/v^2$ |
| odd | $25 < v < 40$ | 1250-2000 | 0.4 | $2500/v$ |
| even & interharm. | $v < 40$ | <2000 | 0.1 | $600/v$ |
| in 200 Hz (Eq. 2.3) | $v > 40$ | >2000 | 0.3 | $1800/v$ |

are dependent on the grid voltage and the short circuit power of the grid.

$$u_{v,\max} \frac{U_{\text{grid}}^{ll,rms}}{\sqrt{3}} = Z_{v,\text{grid}} I_{v,\max}^{rms} \;\rightarrow\; I_{v,\max}^{rms} = \frac{u_{v,\max} U_{\text{grid}}^{ll,rms}}{\sqrt{3} v Z_{\text{grid,50Hz}}} = \frac{u_{v,\max} S_{\text{grid}}}{\sqrt{3} v U_{\text{grid}}^{ll,rms}} \tag{2.1}$$

$$i_{v,\max}^{rms} \overset{def.}{=} I_{v,\max}^{rms} \frac{U_{\text{grid}}^{ll,rms}}{S_{\text{grid}}} = \frac{u_{v,\max}}{v\sqrt{3}} \tag{2.2}$$

$u_{v,\max}$ : p.u. part of fundamental Y voltage; $U_{\text{grid}}^{ll}$ : line-to-line grid voltage; $Z_{v,\text{grid}}$ : grid impedance at harmonic $v$, assumed to be only inductive and linear; $I_{v,\max}$ : maximal current at harmonic $v$; $S_{\text{grid}}$ : short circuit power of the grid; $Z_{\text{grid,50Hz}}$ : grid impedance at 50 Hz.

Limits above the 40th harmonic are only represented by the last row. No distinction between even, odd or interharmonic is made. A measurement bandwidth of 200 Hz must be computed following the definitions according to Eq. 2.3 of the IEC standard [7] Appendix B.

$$I_{B,b} = \sqrt{\sum_{f=b-95Hz}^{b+100Hz} I_{Cf}^2} \tag{2.3}$$

$B$ : number of interval; $b$ : center frequency.
The center frequencies for 50 Hz systems are accordingly b= 2100 Hz, 2300 Hz, 2500 Hz and so on. If SVM is used, four significant voltage (and current) components at $f_{\text{car}} \pm 100Hz$ and $f_{\text{car}} \pm 200Hz$ appear (assuming 50 Hz to be the fundamental converter frequency). If they appear in the same 200 Hz interval the grid code limit has to be decreased by $1/\sqrt{2}$ (according to Eq. 2.3,[6]).
Another harmonic grid code is respresented by the IEEE 519 / 1547 standard which is also shown in the plots in the next sections. Here, also the total demanded distortion (TDD) has to be computed according to Eq. 2.4. It has to be < 5 % for SCR <= 20 and  < 8  % for SCR <= 50.

$$TDD = \frac{\sqrt{\sum_{v=2}^{\infty} I_{dist,v}^2}}{I_L} \tag{2.4}$$

## 2.3 Analysed Wind Turbine System and Overview of Simplifications

This thesis focuses on a 2.2 MVA wind turbine system with full-size converter. Nevertheless, using p.u. values makes it easily transferable to other power ratings. As common assumption, the DC link capacitance is assumed to be big enough to separate the generator and grid dynamics. This leads to the reduction of the turbine model to the grid-side converter system as shown in Fig. 2.1. The paralleled low voltage converters in this power range [8] are assumed to be connected directly together [9] and no interleaved switching is assumed. They are modeled as a single converter. Interlock delay time (blanking time), driver dead time and parasitics of
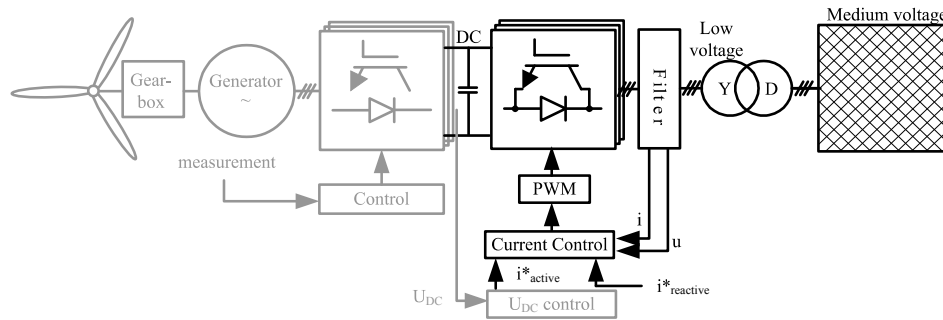
**Figure 2.1:** Simplification (black) of the wind turbine system for grid studies; compared to the schematic, the DC link will be modeled as constant voltage source

**Table 2.2:** Base values for 2 MW system

| Symbol | Description | Value | Unit |
|--------|-------------|-------|------|
| $S_{\text{base}} = S_{\text{r}}$ | Apparent power | $2/0.9 \approx 2.22$ | $MVA$ |
| $U_{\text{base}} = U_{\text{r}}$ | Voltage (l-l, rms) | 690 | $V$ |
| $f_{\text{base}}$ | Frequency | 50 | $Hz$ |
| | Derived values: | | |
| $I_{\text{base}}$ | Current (rms) | $= \frac{S_{\text{base}}}{U_{\text{base}}\sqrt{3}} = 1858$ | $A$ |
| $Z_{\text{base}}$ | Impedance | $= \frac{U_{\text{base}}^2}{S_{\text{base}}} = 0.214$ | $\Omega$ |
| $L_{\text{base}}$ | Inductance | $= \frac{Z_{\text{base}}}{2\pi f_{\text{base}}} = 682$ | $\mu H$ |
| $C_{\text{base}}$ | Capacitance | $= \frac{1}{2\pi f_{\text{base}} Z_{\text{base}}} = 14.9$ | $mF$ |

semiconductor module and converter setup are excluded from this analysis. The DC voltage control is also excluded (the DC link is modeled as constant voltage source). The rated active power is assumed to be 2 MW, while the actual grid codes [3] demand a *cosφ* of 0.9 inductive or capacitive. The rated apparent power then is $S_{\text{r}} = 2/0.9 = 2.22$ *MVA*. As common converter AC voltage in this power range, 690 V / 50 Hz is taken. All base values can be seen in Tab. 2.2. These are the basis for the following analyses. A carrier based modulation scheme is used as standard modulation. Carrier frequencies in the region of several kilohertz ($2-5\ kHz$) are common in this system class [9, 10, 11]. The design of carrier frequency, DC link voltage and grid filter is a complex task and have to be done together. This is done in Chap. 2.8. As an input for the design, the spectrum of the line to midpoint converter voltage is taken. It is assumed that the converter operates at modulation indices of $0.75...2/\sqrt{3}$. Taking the highest part at each frequency, the so-called worst case spectrum is obtained [12],[13][1]. Fig. 2.2 (a) shows the worst case spectrum for a carrier frequency of 2.85 *kHz* and asymmetrical regular sampled (double update) space vector modulation. The BDEW harmonic current limits at 690 V (as presented Chap. 2.2) are shown in Fig. 2.2 (c). The BDEW limits depend on the short circuit power of the connected grid and are valid for all (medium) voltage levels at the primary side of the transformer. For $f > 2\ kHz$ two lines are shown (the lower one is decreased by $1/\sqrt{2}$ corresponding to Chap. 2.2). In (d) the IEEE 514 / 1547 limits are shown.
One design goal of the grid filter is to guarantee that the harmonic (and interharmonic) currents evoked by the converter voltage shown in (a)/(b) are within the limits shown in (c)/(d). For

---

[1] The spectrum is computed by separating the converter output voltage in pulses which are then Fourier transformed (si-function).
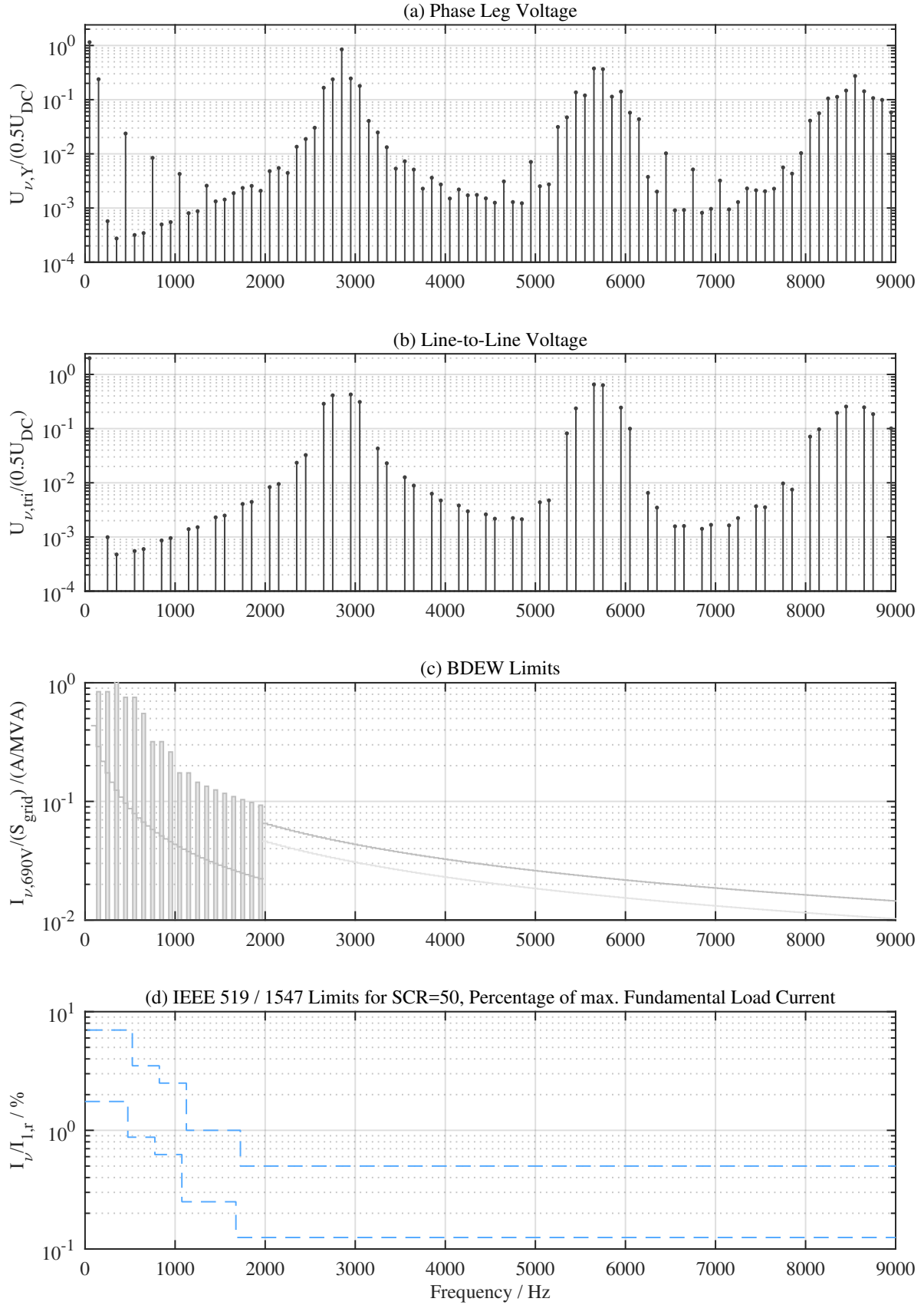
**Figure 2.2:** Harmonic worst case magnitude spectrum ($m = 0.75...2/\sqrt{3}$) of (a) leg and (b) line-to-line voltage for asymmetrical SVM with a carrier frequency of 2.85 $kHz = 19 \cdot 3 \cdot f_1$ divided by half of the DC link voltage (50 $Hz$ value is $2/\sqrt{3}$)) (c) 690 V grid current limits according to [3] resp. Tab. 2.1 related to short circuit power of the medium voltage grid (d) IEEE 514/ 1547 limits [4], upper line for odd, bottom for even harmonics

specific cases, the necessary admittance of the filter from converter voltage to grid current can be calculated.

## 2.4 Carrier Frequency, Converter Voltage Spectrum for Harmonic Current Calculation and Modulation Method

The carrier frequency is chosen to be $2.85\ kHz = 19 \cdot 3 \cdot 50\ Hz$ which is an odd triplen multiple of the fundamental [2] and in the range of actual turbine converters [9, 11, 10]. An odd multiple of the fundamental is chosen. In this case the pulses of the positive and negative part of the sin wave are symmetrical. Several components of the phase leg spectrum are shifted to triplen multiples of the fundamental. They have an equal amplitude and phase for all three leg voltages (common mode). This is validated by an analysis of the line-to-line voltage.

In Fig. 2.2 (a) the spectrum of one inverter leg (according to Chap. 3 in [14]) is shown. To include the effect of the two other phase legs the line-to-line voltage is computed. Therefore, the **complex** phase leg spectra have to subtracted. As result it is observed that all components at the triple of the fundamental and multiples of it cancel out (Fig. 2.2 (b)). This is confirmed by literature ([14] Chap. 5.6.1, see also Fig. 6.10). For the subsequent harmonic current calculation the common mode components are neglected due to the fact that nor the DC link midpoint nor the transformer star point is connected (In wind turbines the transformer is generally Dy type [15, 16].). No phase information is of interest. Therefore, the absolute value of the line-to-line voltage spectrum, divided by $\sqrt{3}$ (line and not delta currents are to be calculated), is taken as input for the filter design.

The SVM method is taken where the voltage according to Eq. 2.5 is added to all three reference voltages (Eq. 6.33 in [14]) [3].

$$u_0^\star(t) = -\frac{max(u_a^\star(t), u_b^\star(t), u_c^\star(t)) + min(u_a^\star(t), u_b^\star(t), u_c^\star(t))}{2} \qquad (2.5)$$

## 2.5 Definition and Calculation of Weak and Stiff Grid Impedance

For converter simulation and controller design, the common approach to model the grid connection is an inductive and resistive impedance with an ideal $50\ Hz$ voltage source as shown in Fig. 2.3. The impedance varies depending on the connected grid. It can be calculated using the short

---

[2] The effect of odd and / or triplen multiples of the fundamental as carrier frequency are discussed in [14] Chap. 5.6.1. In real systems an exact triple-n ratio of the carrier and fundamental frequency cannot be guaranteed (the grid frequency can also change). This is not analysed further in this work.

[3] Other modulation methods as optimized pulse patterns or methods adapting the actual $cos(\varphi)$ are possibly improvements regarding losses and THD. This is not analysed further in this work.
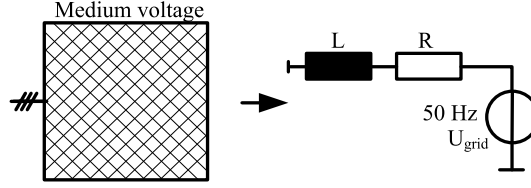
**Figure 2.3:** Simple model of grid connection

**Table 2.3:** Parameters of medium voltage grids and equivalent $R_{grid}$ and $L_{grid}$ in p.u.

|  | Short circuit power | SCR | $L_{grid}(X/R = 20)$ | $R_{grid}(X/R = 20)$ |
|---|---|---|---|---|
| stiff/strong | $> 111\ MVA$ | $> 50$ | $< 2.22\%$ | $< 0.11\%$ |
| weak | $< 111\ MVA$ | $< 50$ | $> 2.22\%$ | $> 0.11\%$ |
| worst case | $22.2\ MVA$ | $10$ | $10\%$ | $0.5\%$ |

circuit power $S_{grid}$ according to Eq. 2.6. Often $S_{grid}$ is provided by the local network operator.

$$S_{grid} = \frac{U_r^2}{Z_{grid}} \longrightarrow Z_{grid} = \frac{U_r^2}{S_{grid}} = \sqrt{R_{grid}^2 + X_{grid}^2} \tag{2.6}$$

Generally, the short circuit powers of medium voltage grids are in the range of 100...500 MVA ([17], p. 28). For the filter design in the next chapter, an extreme minimum case is assumed: a SCR (ratio of the short circuit power of the grid to the rated apparent power of the turbine) of 10. For the analysed 2.22 MVA turbine this leads to a short circuit power of $S_{grid} = 10 \cdot 2.22\ MVA = 22.2\ MVA$. According to literature for medium voltage grids the corresponding X/R ratios are in the range of 5[3]...10[17]..13[3]..30[18]. In this work, it was decided to use SCR=50 ($S_{grid} = 111\ MVA = 50 \cdot S_r$) as the boundary to speak of a weak or a stiff/strong grid. Table 2.3 gives an overview.

## 2.6 Transformer Leakage Inductance

A wind turbine is coupled with a transformer to the medium voltage grid. The simplest model of the grid impedance seen by the turbine is the series connection of the transformer leakage impedance and the grid impedance. The transformer impedance $Z_{trsf}$ is computed according to Eq. 2.7 [19].

$$\underline{Z}_{trsf} = \frac{U_{trsf,r}^2}{S_{trsf,r}} \cdot (u_r + ju_x) \tag{2.7}$$

$U_{trsf,r}$ can be the low voltage or the medium voltage depending on the voltage level of the analysis. $u_k$ and the no-load losses $P_0$ and some load losses are usually available from data sheets. Using $P_0$ and the transformers' rated apparent power $S_{trsf,r}$ $u_r$ and then $u_x$ is calculated with Eq. 2.8.

$$u_r = \frac{P_0}{S_{trsf,r}}; \ u_x = \sqrt{u_k^2 - u_r^2} \tag{2.8}$$

Table 2.4: Typical values of $u_k$ and $u_r$ for transformers[19],[17] p.36

| $S_{trsf}$ /MVA | Voltage | $u_k$ | $u_r$ | Source |
|:---:|:---:|:---:|:---:|:---:|
| 0.63...2.5 | LV/MV | 4...6 % | <1 %, (1..1.5 %[17]) | [19] |
| 2...10 | MV/HV | 8...17 % | <1 % | [19] |
| 2.5...25 | MV/MV | 6...9 % | 0.7..1 % | [17] |
| 25...63 | HV/MV | 10...16 % | 0.6...0.8 % | [17] |
| 12.5...80 | MV/HV | 8...17 % | <0.6 % | [19] |

Generally $u_x/u_r$ is in the range of $25 - 50$ for $2 - 3$ *MVA* transformers (see App. 7.1). Therefore, the approximation $u_x \approx u_k$ is often used. Table 2.4 summarises typical values for the relative short circuit voltage $u_k$ and active part $u_r$ depending on the transformers' rated power and voltage. These values from literature are in line with the additional data sheet analysis done in this work (App. 7.1). Here, all analysed transformers have $u_k = 6\%$, therefore this value is taken for further consideration. As rated apparent transformer power $S_{trsf,r}$ the converter rated apparent power $S_r = 2/0.9 = 2.22$ *MVA* is taken. By doing so, the related transformer inductance is equal to $u_x$ (related variables are bold):

$$L_{trsf}^{[Henry]} = \frac{1}{2\pi 50} \frac{U_{trsf,r}^2}{S_{trsf,r}} u_x \overset{!}{=} \underbrace{\frac{1}{2\pi 50} \frac{U_r^2}{S_r}}_{L_{base}, seeTab.2.2} \cdot u_x \rightarrow \boxed{\boldsymbol{L_{trsf} = u_x \overset{!}{=} 6\%}} \approx u_k \tag{2.9}$$

As a matching value regarding Tab. 7.1 in App. 7.1, an X/R ratio of 40 is taken leading to the series (parasitic ) resistance according to Eq. 2.10. Magnetic core losses and shunt elements are not considered.

$$R_{trsf}^{[Omega]} = \underbrace{\frac{U_{trsf,r}^2}{S_{trsf,r}}}_{Z_{base}} u_r \rightarrow \boxed{\boldsymbol{R_{trsf} = u_r \overset{!}{=} \frac{6}{40} = 0.15\%}} \tag{2.10}$$

## 2.7 Motivation and Literature Review of High Power Grid Filter Design

The general topology of turbine grid filters is shown in Fig. 2.4. The shunt impedance $Z_{shunt}$[4] mainly absorbs high frequency (and little fundamental) current. It can be a capacitance [20], a capacitance with trap filter [21] or one single [22] or several trap filters. In this thesis, two filter designs are considered: 1) an LCL filter and 2) a trap filter configuration, each with active or different passive damping methods. The grid filter design is not a new topic in literature. Therefore the aim of this work was to use suitable publications to design the filter. Hereby,

---

[4] In this work, the name 'shunt' impedance is used to describe all passive elements between the converter and transformer inductances.

it is important to realise that a wide range of different wind turbine converter systems exists. In this work, directly parallel connected low voltage converters are considered. Publications concerning interleaved parallel connected converters or medium voltage converters with low switching frequency (with for example optimized pulse patterns) are less suitable.

Directly adopting parameters from other publications was no option, because the complete analysis stands and falls with the hardware parameters. Therefore, it was decided to design a new filter, always double checking it with literature and industry experience. Below, the corresponding publications for the high power filter design are discussed.

In [23], the design procedure for an LCL filter system is proposed. It is mentioned that the total inductance (converter + grid) should be less than 0.1 p.u., to limit the ac voltage drop. In this thesis, this voltage drop is considered in detail. The operating point including the highest voltage drop is identified and the filter is designed accordingly. The LCL design mainly follows the ideas of this paper.

[24] designs an NPC converter filter with 7 MW rated power. Despite a different topology and switching frequency, the results are similar to those of this work.

In [25], a 125 kW trap and LCL filter system is designed and compared. The trap filter design in this work mainly follows the ideas of this publication. In addition, the voltage drop as well as several passive damping methods are analysed in detail.

[21] designs a trap filter system for a 12 MVA converter system. It is mentioned that for a given series inductance, the voltage drop depends on the necessary reactive power which is injected and this should be included in the filter design.

[12] also designs a high power NPC grid LCL filter with relatively low switching frequencies. Here, parameter variations are considered, too.

Another NPC medium voltage (3.3 kV) LCL grid filter design is carried out in [26]. In this work, an adapted voltage drop consideration to the specific wind turbine operating points is used. A similar approach is used in the present work, also for the trap filter design. In [26], SCR=20 is considered, while in the present work an even weaker grid with SCR=10 is considered.

The design of an LCL grid filter for a 2 MW DFIG wind turbine in [27] shows that the same methods as for full-size converter systems can be applied.

The effectiveness of passive damping circuits for an LCL filter is analysed in [28]. The LCL filter is designed considering converter current ripple and reactive power consumption of the capacitance. The voltage drop across the inductors is mentioned as an argument for low inductor values but is not specifically analysed.

In [29], the LCL-type grid filter for a bidirectional 11 kW drive system is designed. A series resistance damping is applied. The converter-side inductance is designed according to a specific current ripple. Here, [28] is referenced. In this work, grid codes resp. IEEE519 standard is mentioned, but no validation is provided. The voltage drop across the filter during rated operation is neglected.

[30] analyzes the LCL filter design with parallel C-R damping regarding the power losses.
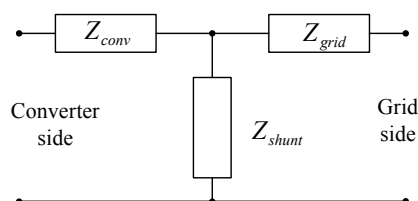


**Figure 2.4:** Single phase equivalent of general type of grid filters

Higher frequency inductor models are applied. In the present work, the losses are not a point of focus. Nevertheless, these are computed (with fundamental passive element values) in order to have an estimation of their magnitude. A 2 MW filter is designed in [31] for parallel connected converters with interleaving. A combination of trap, C and parallel C-R damping is applied. The main focus of this thesis is on the stability analysis with *standard* wind turbine converter systems. Directly paralleled converters are considered as standard [9] and are therefore looked at.

The principle of DC voltage reserve which is utilised here can also be found in [32] (here only for an LCL filter with unity power factor). In the present work, it is also applied for two trap filters and also adapted to specific wind turbine operating points: $cos(\varphi) = 0.9$ overexcited and a grid voltage rise of 10 %.

Concluding the literature review it can be said that the following filter design includes ideas from all mentioned publications and is compared against their results each time (as mentioned below). It is a specific filter design for the intended 2 MW fully-sized converter system, where the following points are included:

- Theoretical validation regarding the grid codes

- Experimental validation with spectra

- Design and comparison of three different passive damping methods for LCL and trap filter system

- Design and comparison of two different filter designs for a weak and a strong grid

- Adaption of the filter design to the presence of the turbine transformer and its leakage inductance (no additional grid-side inductance necessary)

- Inclusion of DC voltage reserve respectively the voltage drop for the specific operating points ($cos(\varphi) = 0.9$)

- Harmonic loss computation

The designed filters are conform to the IEEE 514 / 1547 grid code seen in Fig. 2.2. They are also conform with the BDEW grid code which is not divided by $\sqrt{2}$ (see Chap. 2.2) and have been designed to meet this grid code.

Below, the LCL filter is designed, followed by the trap filter.

## 2.8  Option 1: LCL Filter

### 2.8.1  Design of LCL Filter and DC voltage

The higher damping at high frequencies (compared to an L filter) makes the LCL filter a solution to meet the harmonic grid codes. Its design is an optimising problem with several
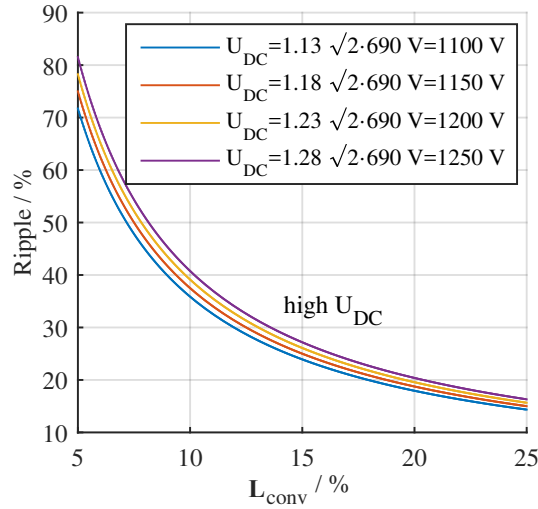
**Figure 2.5:** For SVM: Maximal current ripple (peak-to-peak related to peak current) versus converter side inductance for different DC link voltages

objectives (size, cost, voltage drop, losses in the converter and passive elements, reactive power consumption of the shunt elements...). Several points are not considered here (component size, cost, DC link capacitance and voltage ripple). Nevertheless, the design results in values near to real world systems. It is found that completely different filter designs are necessary for a weak and a stiff grid. This is a result of the fact that the grid code limits inversely proportional decrease with the grid short circuit power (see Fig. 2.2 (c)) but the increased damping of the LCL filter introduced by the higher grid inductance is much less. Therefore two filters are designed, one for a stiff (SCR = 50 and above) and one for a weak grid (SCR=10-50). According to Chap. 4.2, an X/R ratio of 20 is taken. Below, firstly the general design steps are described and then the specific design is carried out.

1. A start *DC link voltage* is determined. For SVM, the minimum DC voltage to generate the rated grid voltage plus a variation is taken: $U_{\mathrm{DC,start}} = 1.1...1.3\sqrt{2}U_r^{ll} = 1.1...1.3\sqrt{2}\cdot 690\,V = 1073...1269\,V$.

2. *Converter side inductance*: The related maximal converter current peak-to-peak ripple (MaxCCppR) for SVM is computed using $\frac{\Delta I_{\mathrm{conv,max}}}{\hat{I}_r} = \frac{U_{\mathrm{DC}}}{6\cdot f_{\mathrm{car}}\cdot L_{\mathrm{conv}}\cdot\hat{I}_r}$ [33] varying the converter side inductance. This is the maximal ripple which is obtained for $m = 2/\sqrt{3}$ [33]. Fig. 2.5 shows that MaxCCppRs in the range of $10-30\%$ lead to converter side inductances in the range of $\approx 10-20\%$. This is valid for all analysed filters, LCL, Trap, weak or stiff grid.

3. *Grid side inductance*: As the voltage drop across the filter should be kept small, it is decided to add no additional inductance to the 6% transformer leakage inductance and the grid impedance ($SCR = 50 -> L_{\mathrm{grid}} \approx 2\%$; $SCR = 10 -> L_{\mathrm{grid}} \approx 10\%$).

4. *Capacitance*: For the range of converter inductances, the minimal capacitance which provides sufficient damping at $f_{\mathrm{car}} \pm 100\,Hz$ is computed. As worst case converter voltage $U_{\mathrm{conv}}^{star}(f_{\mathrm{car}} + 100\,Hz) \approx 0.2384 U_{\mathrm{DC}}/2$ and $U_{\mathrm{conv}}^{star}(f_{\mathrm{car}} - 100\,Hz) \approx 0.2472 U_{\mathrm{DC}}/2$ is assumed (compare to Fig. 2.2 (a)). It is multiplied by the admittance from converter

voltage to grid current (Eq. 2.11) and the absolute value is compared with the grid codes.

$$\underline{Y}(f_{\text{car}} \pm 100Hz) = \frac{1}{(j\omega_{\pm100})^3 L_{\text{conv}}(L_{\text{trsf}} + L_{\text{grid}})C + j\omega_{\pm100}(L_{\text{conv}} + L_{\text{trsf}} + L_{\text{grid}})} \quad (2.11)$$

The results are shown in Fig. 2.6 (a) for the stiff grid and in (b) for the weak grid. It can be seen that the minimal capacitance falls in the range of $\approx 4 - 8\%$ for $SCR > 50$ and $\approx 8 - 18\%$ for $50 > SCR > 10$. The percentage of the capacitance is equal to the percentage of fundamental frequency current consumed by the capacitor.

5. *DC voltage resulting from filter design*: The minimum necessary DC link voltage $U_{\text{DC,min}} = \sqrt{2 \cdot 3} U^\star_{\text{conv,AC,min}}$ is computed for the worst case operating point (grid voltage rise of 10 % and $S_r$ at $cos\varphi = 0.9$ overexcited both at the high voltage side of the transformer[5)]). Fig. 2.6 (c) (strong grid) and (d) (weak grid) show that a minimal DC link voltage ranges between approx. 1100 and 1220 V for both SCRs.

6. *DC voltage reserve.* Each start DC link voltage chosen in point 1 is compared with the corresponding DC link voltage computed in point 5 to receive the important design factor DC voltage reserve. A non negative DC voltage reserve is necessary to keep the converter in the linear PWM range. Here, the DC voltage reserve is computed according to Eq. 2.12.

$$DC \ voltage \ reserve = \frac{U_{\text{DC,start}}}{U_{\text{DC,min,voltagedrop}}} - 1 \quad (2.12)$$

Fig. 2.6 (e) and (f) show that only previously assumed DC voltages of 1250 *V* and 1225 *V* provide a sufficiently positive DC voltage reserve (over the complete range).

7. *Resonance frequency*: For active damping the resonance frequency shown in Eq. 2.13 must be below the Nyquist frequency ($f_{\text{Nyquist}} = 0.5 f_{\text{sample}} \underbrace{=}_{doubleupdate} f_{\text{carrier}} = 2850 \, Hz$).

$$f_{\text{res}} = \frac{1}{2\pi} \sqrt{\frac{L_{\text{conv}} + L_{\text{trsf}} + L_{\text{grid}}}{L_{\text{conv}}(L_{\text{trsf}} + L_{\text{grid}})C}} \quad (2.13)$$

It can be an advantage if it is not too near to characteristic grid harmonics (5*th*, 7*th*, 11*th*, 13*th*..). In Fig. 2.6 (e) and (f) the resonance frequencies are also plotted. For SCR=50, the resonance frequencies vary between $\approx 750 - 1150 \, Hz$ versus the chosen MaxCCrpp. The necessary higher damping for SCR=10 results in lower resonance frequencies of $\approx 430 - 620 \, Hz$.

**Discussion and choice of filter for SCR>50 (Tab. 2.5).** Simulation experience shows that a DC voltage reserve of circa 5 % is a minimum for the control. Tab. 2.5 demonstrates for different MaxCCRppR the corresponding DC link voltages which provide a reserve of 5 %. Also the necessary DC link voltages without a grid voltage rise are shown. In this case they decrease by 100 V. A higher DC link voltage leads to higher semiconductor losses. From this point a lower DC link voltage can be desired. A solution can be to adapt (during operation) the DC link

---

[5)] In App. 7.4, it is explained in detail how the minimal DC link voltage is computed.
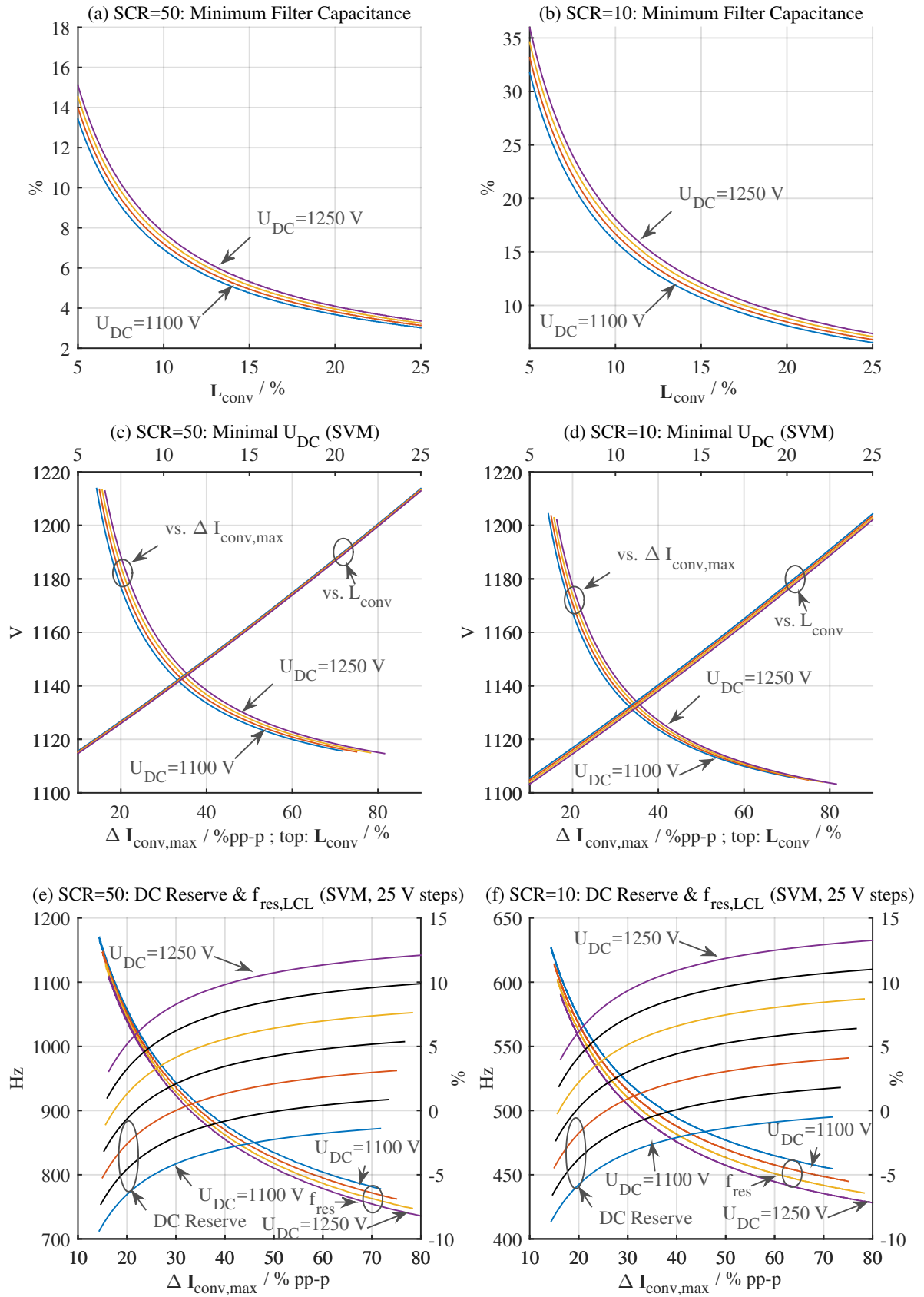
**Figure 2.6:** LCL filter design results for a stiff (left column) and weak grid (right). In (c) and (d), the DC link voltage (result of the worst case voltage drop) is plotted two times versus two horizontal axes. In (e) and (f), two vertical axes are integrated.

**Table 2.5:** LCL Filter for different MaxCCRppR for $SCR >= 50$, $f_{car} = 2.85\ kHz$

| $\Delta I_{conv}^{pp-p}$ / % | $L_{conv}$ / % | $C$ / % | $f_{res}$ / $Hz$ | $U_{DC}$ / $V$ | $U_{DC}$ at $U_r$ / $V$ | $L_{trsf} + L_{grid}$ / % |
|---|---|---|---|---|---|---|
| 20 | 20.4 | 4.0 | 1039 | 1250 | 1150 | 6+2 |
| **25** | **16.0** | **4.9** | **975** | **1225** | **1125** | **6+2** |
| 30 | 13.3 | 5.8 | 926 | 1225 | 1125 | 6+2 |
| 50 | 7.8 | 9.4 | 817 | 1200 | 1100 | 6+2 |

**Table 2.6:** LCL Filter for different MaxCCRppR for $SCR = 10 - 49$, $f_{car} = 2.85\ kHz$

| $\Delta I_{conv}^{pp-p}$ / % | $L_{conv}$ / % | $C$ / % | $f_{res}$ / $Hz$ | $U_{DC}$ / $V$ | $U_{DC}$ at $U_r$ / $V$ | $L_{trsf} + L_{grid}$ / % |
|---|---|---|---|---|---|---|
| 20 | 20.4 | 9.0 | 557 | 1250 | 1150 | 6+10 |
| **25** | **16.0** | **11.2** | **529** | **1225** | **1125** | **6+10** |
| 30 | 13.0 | 13.4 | 510 | 1200 | 1100 | 6+10 |
| 50 | 7.7 | 22.2 | 467 | 1175 | 1075 | 6+10 |

voltage to the grid voltage which results, as mentioned before, in a benefit of 100 V.

In the next step, the MaxCCppR is chosen. In literature, a wide range from $\approx 17\%$ [27] up to 35% [25] and 50% [21] is found. In this work, the MaxCCppR is set to 25%. The corresponding capacitance is 4.9%.

**Discussion and choice of filter for SCR=10-49.** Following the same ideas as mentioned above, the parameters shown in Tab. 2.6 are obtained. For MaxCCRppR =25 %, a higher capacitance of 11.2% is necessary. It also means that 11.2% fundamental current is consumed by the capacitor. This needs to be included when the converter is designed (regarding the current rating).

**General comments.** The obtained DC link voltages are critical for 1700 V IGBTs. Therefore, in practice the DC link voltage possibly has to be reduced. Regarding a grid voltage increase of 10 % this is not possible (no DC voltage reserve left). A solution would be to decrease the low voltage to for example 600V.

The MaxCCppR occurs at maximal modulation degree of $2/\sqrt{3}$. Normally, the converter is designed to operate with at least 5 % DC voltage reserve. This fact (and e.g. no grid voltage rise by 10 %) leads to lower modulation indices than $2/\sqrt{3}$ and therefore lower MaxCCppR. This indicates that the designed MaxCCppR is an absolute worst case value.

The design results for the undamped LCL filter are graphically summarised in Fig. 2.7. A validation of the designed components by using bode diagrams, as well as the dimensioning and selection of the passive damping is the topic of the next section.

## 2.8.2 Design of Several Passive LCL Damping Methods

A damping of the resonance makes sense, because it enables higher control bandwidths (which will be seen below) and higher robustness against possible resonance stimulation from the grid. The LCL resonance can be damped actively (by the control) or passively. To the author's knowledge, for industrial applications manufactures are often not only relying on active methods, since special care needs to be taken if control (and therefore active damping) fails [25, 28, 21,
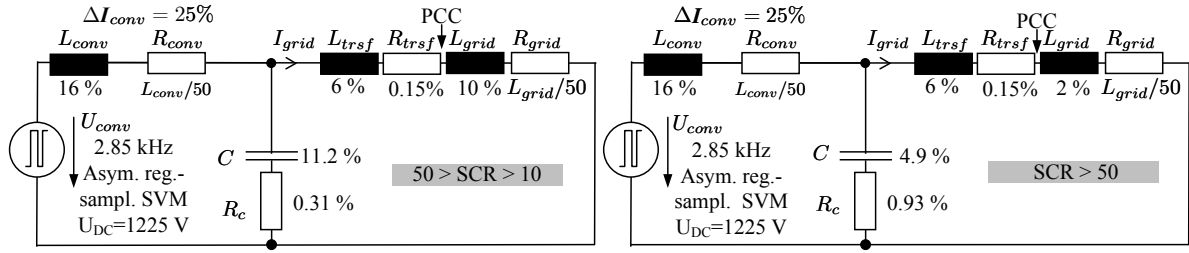
**Figure 2.7:** Graphical presentation of the LCL filter design results; for p.u. based parameters, the X/R ratio of 50 for the inductances transforms to $R = L/50$, for base values see Tab. 2.2
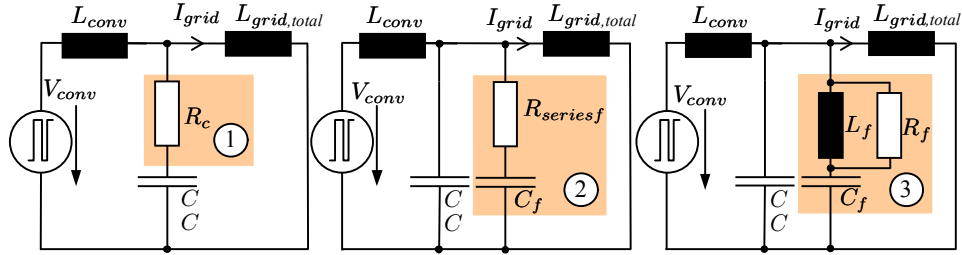


**Figure 2.8:** Passive damping methods for LCL filter[28]: 1) series resistance 2) split capacitance with series resistance (parallel C-R) 3) parallel trap filter tuned to resonance frequency (parallel C-R‖L)

34, 31]. In this case the undamped filter can be excited. Therefore, a passive damping is designed below.

Two points for the damping at resonance frequency are considered. 1) The grid codes must still be met at the resonance frequency. 2) The resonance should be damped to a large extend [6] by the passive damping.

Fig. 2.8 shows several solutions [28] which are explained, designed and analysed below.

1. *Series Resistance*. The series damping resistance is increased until the desired resonance damping is reached. At the same time, the damping at the carrier frequency decreases. This must be compensated by a corresponding increase of the capacitance.

2. *Parallel C-R*. The idea is to split the capacitance into one part with series damping resistance and in one without: $C_{\mathrm{f}} = C \cdot n$. In this way, losses are decreased compared to the first method. The ohmic resistance providing the best damping can be calculated according to Eq. 2.14[7].

$$R_{\mathrm{seriesf}} = \sqrt{\frac{L_{\mathrm{conv}}(L_{\mathrm{trsf}} + L_{\mathrm{grid}})}{(L_{\mathrm{conv}} + L_{\mathrm{trsf}} + L_{\mathrm{grid}})C} \cdot \frac{(2+n)(4+3n)}{2n^2(4+n)}} \tag{2.14}$$

The capacitance $C_{\mathrm{f}}$ respectively $n$ is increased until the desired damping is reached. Similar to the Series Resistance Method, the damping at carrier frequency is affected and has to be compensated by a bigger total capacitance. However, the total increase is lower

---

[6] Precisely it shall be formulated: The maximum point of the admittance $|I_{\mathrm{grid}}/U_{\mathrm{conv}}|$ (at the resonance frequency) should be decreased to large extend.

[7] This formula is an advancement of the $R_{\mathrm{f}}$ dimensioning shown in [35] formula 10.33. In [35], only an LC filter is considered, but no LCL filter.

compared to the first method.

3. *Parallel C-L||R*. Again the capacitance is split into the two branches while the parallel C-L||R trap frequency is tuned to the resonance frequency of the complete LCL filter acoording to Eq. 2.15 [28].

$$L_{\text{f}} = \frac{1}{\omega_{\text{res,LCL}}^2 C_{\text{f}}} \tag{2.15}$$

The damping resistance is tuned manually.

## 2.8.3  Graphical Analysis of Damped and Undamped LCL Filters

Below, the design results are analysed graphically with spectrum plots. In the subsequent Chap. 2.8.4 all data is provided and discussed. The undamped and damped filters are analysed together in Fig. 2.9.

In (a), the line-to-midpoint amplitude spectrum of the converter voltage (computed from the line-to-line voltage as described in Chap. 2.4) for $U_{\text{DC}} = 1225\ V$ is shown (the fundamental is removed). The spectrum is related to the rated amplitude of the grid $690\sqrt{2/3}$ V. In this way, a graphical multiplication with the admittance can be done (shown below).

In (b) and (c), the design results for SCR=50 and in (d) and (e) for SCR=10 are shown. In (b), the admittance $Y_{\text{conv}} = I_{\text{grid}}/U_{\text{conv}}^{\star}$ related to base admittance ($Y_{\text{base}} = 1/Z_{\text{base}}$, compare Tab. 2.2) is plotted in p.u.. P.u. is used here to enable the graphical multiplication. The line styles corresponding to the damping methods are listed. All methods have approximately the same damping near the carrier frequency (2850 Hz). This is correct. For all damping approaches, the resonance frequency is slightly shifted to a lower frequency due to their higher total capacitance.

In (c), the related percentaged current spectrum for all damping methods (the same colors and line style as in (b)) and the related percentaged grid codes are shown. It can be gathered multiplying the percentaged voltage spectrum in (a) with the p.u. admittance in (b) (graphical validation). Here, it is important to remember that the voltage spectrum is for a DC voltage of 1225 V. For the passively damped systems with SCR=10 a slightly higher DC link voltage must be taken. Therefore, the spectrum would increase slightly.

As intended, near the carrier frequency, all filters guarantee currents below the grid code limits. This counts also for the currents near resonance frequency. The TDD is below the demanded values (see Chap. 2.2).

Assuming a variation of the grid inductance, the resonance frequency can migrate. In the worst case, a harmonic can be encountered leading to high harmonic currents. This is an argument to use damping methods.

The results for SCR=10 in (d) and (e) are similar to those for SCR=50 and therefore are not explained in detail.

## 2.8.4  Parameter Analysis of Damped and Undamped LCL Filters

The LCL parameters and some characteristic values are given in the left hand of Tab. 2.7.   The
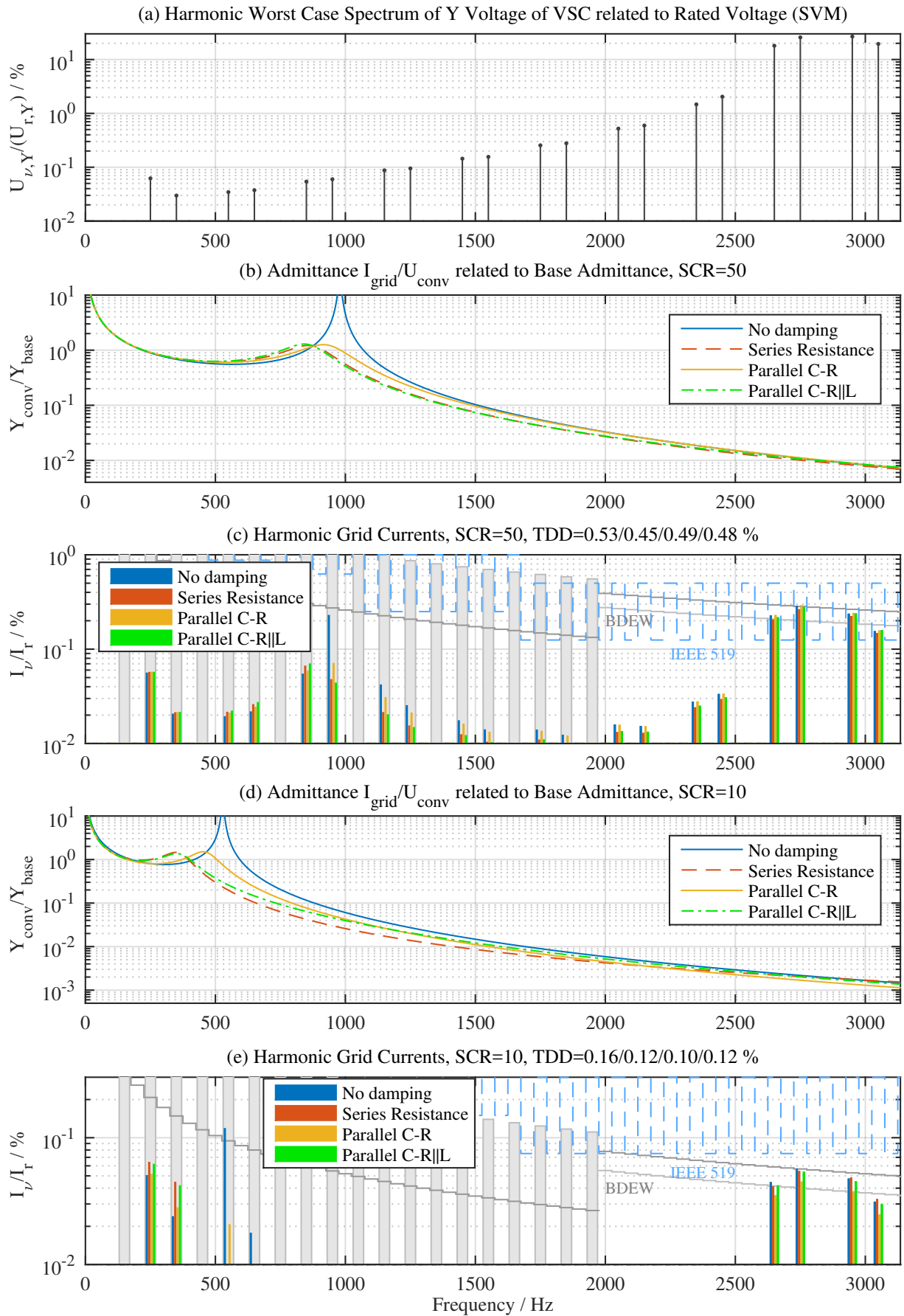
**Figure 2.9:** LCL filter design, the TDD values correspond to no / series resistance / parallel C-R / parallel C-L||R damping

**Table 2.7:** LCL and trap filter data. All values in % except total harmonic losses (according to Appendix 7.5) in ppm, frequencies in Hz, $U_{DC}$ in V and $Y(f_{res})$ in p.u..
Definitions: 'L': LCL; 'T': Trap; '0': no passive damping; '1': series resistance $R_c$ damping; '2': Parallel $C_f - R_f^{ser}$ damping; '3': Parallel $C_f - L_f||R_f$ damping
Base values (according to Tab. 2.2): $S_r = 2.2\ MVA$; $I_r = 1860\ A$; $C_{base} = 14.9\ mF$; $L_{base} = 0.68\ mH$; $R_{base} = 0.21\ \Omega$; $f_{car} = 2.85\ kHz$; SVM

| | L0 | L1 | L2 | L3 | L0 | L1 | L2 | L3 | T0 | T1 | T2 | T3 | T0 | T1 | T2 | T3 |
|---|---|---|---|---|---|---|---|---|---|---|---|---|---|---|---|---|
| $SCR$ | 10 | 10 | 10 | 10 | 50 | 50 | 50 | 50 | 10 | 10 | 10 | 10 | 50 | 50 | 50 | 50 |
| $U_{DC}$ | 1225 | 1250 | 1250 | 1250 | 1225 | 1225 | 1225 | 1225 | 1250 | 1250 | 1250 | 1250 | 1250 | 1250 | 1250 | 1250 |
| $\Delta I_{conv}$ | 25 | 20 | 20 | 20 | 25 | 25 | 25 | 25 | 25 | 25 | 25 | 25 | 25 | 25 | 25 | 25 |
| $L_{conv}$ | 16 | 20.4 | 20.4 | 20.4 | 16 | 16 | 16 | 16 | 16.3 | 16.3 | 16.3 | 16.3 | 16.3 | 16.3 | 16.3 | 16.3 |
| $f_{trap}$ | - | - | - | - | - | - | - | - | 2865 | 2860 | 2870 | 2867 | 2830 | 2825 | 2835 | 2840 |
| $R_{trap}$ | - | - | - | - | - | - | - | - | 2 | 16.9 | 2 | 2 | 2.2 | 37.1 | 2.2 | 2.2 |
| $C_{trap}$ | - | - | - | - | - | - | - | - | 1 | 6.3 | 1 | 1 | 0.5 | 0.7 | 0.5 | 0.5 |
| $L_{trap}$ | - | - | - | - | - | - | - | - | 3 | 0.5 | 3 | 3 | 6.8 | 4.6 | 6.8 | 6.8 |
| $Q_{trp}$ | - | - | - | - | - | - | - | - | 84 | 2 | 84 | 84 | 175 | 7 | 175 | 175 |
| $B_{trp}$ | - | - | - | - | - | - | - | - | 34 | 1731 | 34 | 34 | 16 | 402 | 16 | 16 |
| $P_{trap}^{loss}$ | - | - | - | - | - | - | - | - | 1.9 | 37 | 1.8 | 1.8 | 2.0 | 32.1 | 1.9 | 1.9 |
| $f_{trap2}$ | - | - | - | - | - | - | - | - | 5660 | 5660 | 5660 | 5660 | 5660 | 5660 | 5660 | 5660 |
| $R_{trap2}$ | - | - | - | - | - | - | - | - | 1.9 | 21.9 | 1.9 | 1.9 | 2 | 39 | 2 | 2 |
| $C_{trap2}$ | - | - | - | - | - | - | - | - | 1.1 | 1.1 | 1.1 | 1.1 | 0.3 | 0.5 | 0.3 | 0.3 |
| $L_{trap2}$ | - | - | - | - | - | - | - | - | 0.7 | 0.7 | 0.7 | 0.7 | 2.3 | 1.7 | 2.3 | 2.3 |
| $Q_{trp2}$ | - | - | - | - | - | - | - | - | 43 | 4 | 43 | 43 | 130 | 5 | 130 | 130 |
| $B_{trp2}$ | - | - | - | - | - | - | - | - | 132 | 1523 | 132 | 132 | 43 | 1172 | 43 | 43 |
| $P_{trap2}^{loss}$ | - | - | - | - | - | - | - | - | 1 | 6.6 | 0.9 | 0.9 | 0.8 | 16.6 | 0.8 | 0.8 |
| $f_{res}^{damp}$ | - | - | - | 395 | - | - | - | 875 | - | - | - | 1147 | - | - | - | 1937 |
| $C_f$ | - | - | 5.6 | 9 | - | - | 2 | 4.4 | - | - | 1.7 | 0.9 | - | - | 0.5 | 0.4 |
| $R_{seriesf}$ | - | - | 311.3 | 0.4 | - | - | 405.7 | 0.9 | - | - | 399.6 | 1.9 | - | - | 625.5 | 1.9 |
| $L_f$ | - | - | - | 17.9 | - | - | - | 7.4 | - | - | - | 21.3 | - | - | - | 15 |
| $R_f$ | - | - | - | 90 | - | - | - | 33.9 | - | - | - | 487.7 | - | - | - | 581.2 |
| $Y(f_{res})$ | 43.5 | 1.5 | 1.5 | 1.4 | 20.5 | 1.2 | 1.3 | 1.3 | 20.1 | 1.9 | 0.6 | 0.9 | 15.9 | 1.1 | 0.6 | 0.6 |
| $B_{trp}^{damp}$ | - | - | - | 251 | - | - | - | 231 | - | - | - | 1147 | - | - | - | 1937 |
| $P_{series}^{loss}$ | - | - | 326 | 1 | - | - | 59.1 | 1.3 | - | - | 39.8 | 0.1 | - | - | 14.1 | 0.1 |
| $P_{Rf}^{loss}$ | - | - | - | 10 | - | - | - | 25.8 | - | - | - | 2.3 | - | - | - | 10.1 |
| $P_{RLf}^{loss}$ | - | - | - | 2.3 | - | - | - | 0.2 | - | - | - | - | - | - | - | - |
| $C$ | 11.2 | 21.3 | 11.2 | 9 | 4.9 | 6.1 | 4.7 | 1.7 | - | - | - | - | - | - | - | - |
| $R_c$ | 0.3 | 17.9 | 0.3 | 0.4 | 0.9 | 18.9 | 0.9 | 1.9 | - | - | - | - | - | - | - | - |
| $f_{LCL}$ | 528 | 362 | 408 | 395 | 978 | 875 | 834 | 875 | - | - | - | - | - | - | - | - |
| $P_{Rc}^{loss}$ | 1.7 | 285.9 | 1.6 | 1.3 | 2.2 | 52.2 | 2.1 | 0.7 | - | - | - | - | - | - | - | - |

All shunt capacitance values are equal to the 50 Hz current of the same shunt branch. This also applies for the trap filters. Therefore, fundamental currents are not shown here.

columns are separated in four sectors, the first (from left to right) for the weak grid LCL filter, the second for the strong grid LCL filter, the third for the weak grid trap filter and the fourth for the strong grid trap filter. The nomenclature and units etc. are explained in the caption of the table. Below, the parameters are individually discussed.
The parasitic resistances of inductances are obtained according to App. 7.2, those of the transformer in App. 7.1 and those of the capacitances according to App. 7.3.

- *DC link voltage, MaxCCRpp, converter side inductance.* As previously mentioned, the design aim is 25 % MaxCCRpp. The corresponding DC link voltage is 1225 V for SCR=10 and also for =50 (Tab. 2.5 and 2.6). It is found that for SCR=10 with damping circuits a grid code compliance with an acceptable capacitance (<25 %) can only be reached with an increase of $L_{\mathrm{conv}}$. Therefore, it is decided to decrease the MaxCCRpp to 20%. This would again lead to a higher voltage drop according to Fig. 2.6 (d),(f). Obviously for the worst case +10% grid voltage the 5% DC voltage reserve is not provided ($\approx 3\%$). This could be compensated by a decreased grid voltage as mentioned earlier. The MaxCCRpp ($\Delta I_{\mathrm{conv}}$) and its corresponding inductances for the LCL filter can be taken from the first two sections of the table.

- *Undamped LCL filter.* This is listed as 'L0' in the table. For SCR=50 (strong grid), an acceptable value of 4.9 % for the capacitance is reached. For SCR=10 (weak grid), the capacitance is significantly higher (11.2%). $R_{\mathrm{c}}$ is the parasitic resistance of the capacitances, calculated according to Appendix 7.3. The resonance frequency is 978 respectively 526 Hz. A change of the resonance to characteristic grid frequencies is possible (for example 550 Hz). An active damping method might solve this problem.

- *Series damped LCL filter.* This is listed as 'L1' in the table. A significant increase of the capacitance is necessary to comply with the grid codes ($4.9 \rightarrow 6.1\%, 11.2 \rightarrow 21.3\%$). This leads to lower resonance frequencies. The damping resistances are around 18 % and therefore in the range which is recommended in [36]. The total losses in the damping resistance $P_{\mathrm{R_c}}^{loss}$ (harmonic and fundamental, excluding magnetic core losses) are computed according to Appendix 7.5. It can be seen that the losses are significantly higher than without damping (285.9 ppm =0.29% compared to 1.7 ppm =0.0017% [8] for the undamped filter). For the present system, this corresponds to an acceptable value of 6.4 kW losses in the passive damped filter while the rated apparent power is 2.22 MVA.

- *Parallel $C_{\mathrm{f}} - R_{\mathrm{seriesf}}$ damped LCL filter.* This is listed as 'L2' in the table. For SCR=50 it is found that the total capacitance has to be slightly increased by 10 % compared to series damping. The capacitance separation factor *n* is 0.3. The total harmonic losses $P_{\mathrm{series}}^{loss} + P_{\mathrm{C}}^{loss}$ are greater compared to series damping (61.2 ppm compared to 52.2 ppm). In this case, this method obviously only offers disadvantages.
  SCR=10 is relatively similar concerning the losses (320 ppm compared to 290 ppm). The difference lies in the total capacitance (and the resulting fundamental current consumption) which is significantly reduced (16.8 % compared to 21.3 %). This can be rated as an advantage compared to series damping.

- *Parallel $C_{\mathrm{f}} - L_{\mathrm{f}}||R_{\mathrm{f}}$ damped LCL filter.* This is listed as 'L3' in the table. As mentioned

---

[8] As mentioned in App. 7.5, the loss calculation is only a very rough instrument to get a tendency of the losses.

**Table 2.8:** Selected results from LCL design

| | SCR=10 | | | | SCR=50 | | | |
|---|---|---|---|---|---|---|---|---|
| | L0 | L1 | L2 | L3 | L0 | L1 | L2 | L3 |
| $L_{\text{conv}}$ / % | 16 | 20.4 | 20.4 | 20.4 | 16 | 16 | 16 | 16 |
| Total capacitance / % | 11.2 | 21.3 | 16.8 | 18 | 4.9 | 6.1 | 6.7 | 6.1 |
| Total losses / ppm | 1.7 | 285.9 | 327.6 | 14.6 | 2.2 | 52.2 | 61.2 | 28 |
| Admittance at $f_{\text{res}}$ in p.u. | 43.5 | 1.5 | 1.5 | 1.4 | 20.5 | 1.2 | 1.3 | 1.3 |

above, the resonance frequency of the trap damping circuit $f_{\text{res}}^{damp}$ is the LCL filter resonance $f_{\text{LCL}}$. For SCR=50, the same total capacitance as used in series damping is used. It is split into the undamped and damped path. The total losses (in this case $P_{\text{series}}^{loss} + P_{\text{R}_f}^{loss} + P_{\text{R}_L f}^{loss} + P_{\text{R}_c}^{loss}$) are significantly reduced to 28 ppm. A 7.4 % inductance has to be introduced, which needs to be designed to the -quite small- shunt current.
For SCR=10, the capacitance can be slightly decreased compared to series resistance damping (18% compared to 21.3 %). The total losses are 14.6 ppm.

For a direct comparison, some results are summarised in Tab. 2.8.
 **Conclusion for SCR>=50.** All designed filters , with or without passive damping, are solutions to meet the harmonic grid codes. Compared to the undamped case, series resistance and parallel C-R‖L need 1.25 higher total capacitance, while parallel C-R needs an even higher value of 1.38 times the capacitance of the undamped case. For all passive damping methods, the filter capacitance is around 5-7 %. Values from this range are, according to [25], considered as good values. The damping at resonance frequency is approximately the same for all passively damped filters (see Tab. 2.8 or Fig. 2.9). The parallel C-R method has higher total losses and a greater total capacitance than series R and is therefore estimated as unsuitable. The best passive damping method seems to be parallel C-R‖L with the lowest losses.
**Conclusion for 50>SCR>=10.** Compared to the strong grid filter, the capacitance (and 50 Hz current consumption) is higher (11.2%-21.3%). As a consequence, the resonance frequencies are relatively low. For passive damping approaches, the converter inductance has to be increased to 20.4 %. A reduction of the low voltage to, for example, 600 V seems to be the only option to handle the necessary high DC voltage with 1700 V IGBTs. The damping at resonance frequency is similar for all passive damping methods (Fig. 2.9 (d)). Again the parallel C-R‖L method is the most advantageous method concerning total losses. A similar study in [28] also favours the parallel C-R‖L method.

## 2.9  Option 2: Trap Filter

### 2.9.1  Design of Trap Filter and DC voltage

A trap filter in the shunt path is an alternative to a capacitance [22, 37, 38, 21, 25, 39, 40]. The minimum of the trap filter impedance is tuned to the carrier frequency of the converter. As for the LCL filter in the previous section, the converter inductance is designed to a MaxCCRpp of
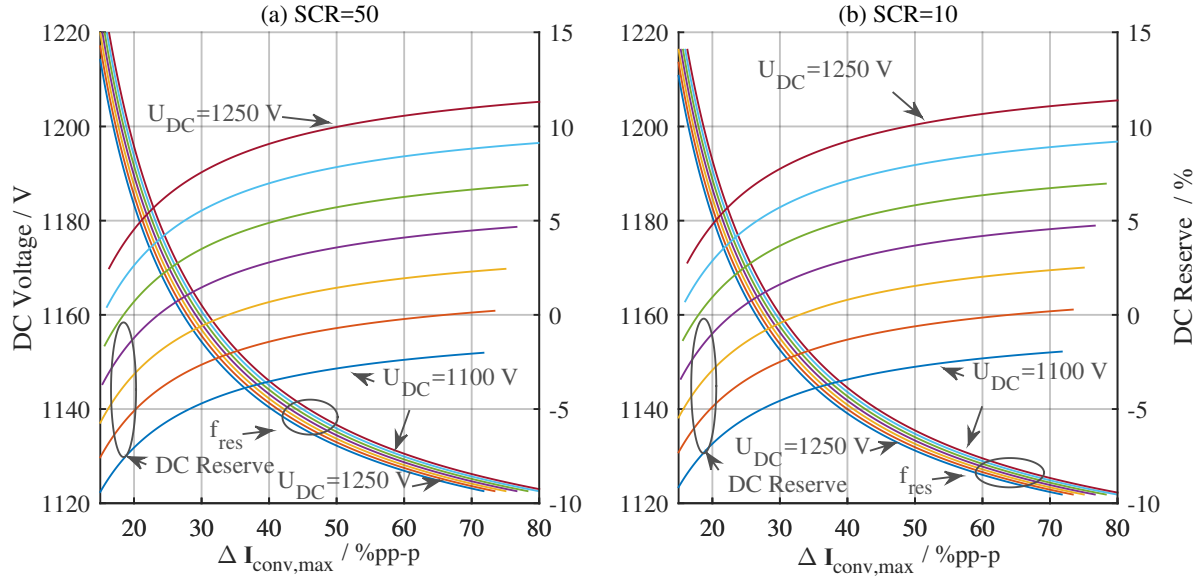
**Figure 2.10:** Minimal DC voltage calculation for the two trap filter designs. (A grid voltage rise of 10 % and cos $\varphi$=0.9 overexcited at rated apparent power is assumed)$f_{\mathrm{car}} = 2850\,Hz$

25 %, and no additional (apart from the transformer and grid impedance) grid side inductance is added. In anticipation of the following trap filter design, the minimum DC link voltage for a 5 % voltage reserve is calculated. Fig. 2.10 shows the minimal DC link voltages computed with the trap filters developed below. For both SCRs, 1250 V is a sufficient DC link voltage providing 5% DC voltage reserve. As for the LCL filter, this is computed at rated apparent power and $cos\varphi = 0.9$ overexcited with a grid voltage rise of 10 % according to App. 7.4.

The grid codes cannot be met at $2f_{\mathrm{car}}$ with only one trap filter tuned to $f_{\mathrm{car}}$. Therefore, a second trap filter tuned to $2f_{\mathrm{car}}$ is introduced. Below, the trap filter tuned to $f_{\mathrm{car}}$ is called *first* and the one tuned to $2f_{\mathrm{car}}$ is called *second* trap filter. The design is done as follows:

- A start capacitance $C_{\mathrm{trap}}, C_{\mathrm{trap2}}$ [9] is taken (for example 1%). With the defined trap frequency, the inductance $L_{\mathrm{trap}}, L_{\mathrm{trap2}}$ can be calculated using $L_{\mathrm{trap}} = 1/(\omega_{\mathrm{trap}}^2 C_{\mathrm{trap}})$ .

- The corresponding grid current spectrum is computed. The capacitance (resp. trap bandwidth) is adjusted until the current sidebands at $f_{\mathrm{car}}$ and $2f_{\mathrm{car}}$ exactly meet the grid codes[10]. As series resistance, only parasitic resistances of the components are considered (computed according to Appendix 7.2 and 7.3). A graphical and data analysis of the undamped trap filter will be done at the same time as the following passive damping circuits.

The design results for the undamped trap filter are graphically summarised in Fig. 2.11.

---

[9] Related variables are in bold.

[10] Sometimes, it is necessary to increase the capacitance of the second trap filter to a larger extent. This results from the fact that at frequencies $> 2f_{\mathrm{car}}$ the grid codes are not met. The present designs meet the grid codes at all frequencies.
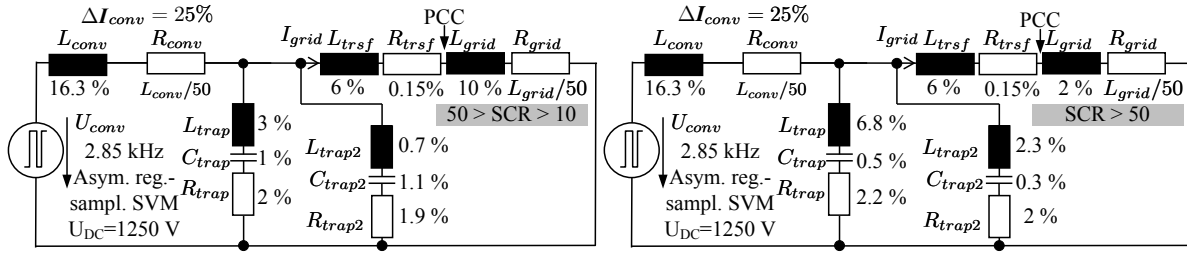
**Figure 2.11:** Graphical presentation of the trap filter design results

## 2.9.2 Design of Several Passive Trap Damping Methods

Just like the LCL filter, the trap filter also evokes a resonance in the admittance $I_{\mathrm{grid}}/U_{\mathrm{conv}}$. Both trap filters have a resonance frequency below their trap frequency. Only the resonance of the trap filter tuned to $f_{\mathrm{car}}$ is found to be critical. This resonance can be damped actively, passively or both. It is observed that this resonance can also be above $0.5 f_{\mathrm{car}}$. In this case, active damping methods must be operated with double update (double edge) PWM to get the frequency in the Nyquist range. Below, the same passive damping methods as for the LCL (Fig. 2.8) filter are developed. Again, first the methods are explained, then the graphical results are discussed followed by the data.

1. *Series resistance damping.* The series resistance is increased until the grid current meets the grid codes at *resonance* frequency. At the same time, the trap filter capacitance has to be increased in order to reach the same damping at $f_{\mathrm{car}}$. The trap inductance has to be decreased to keep the intended trap frequency.

2. *Parallel C-R.* In contrast to the LCL filter, the parallel C-R capacitance is chosen to be an additional capacitance increasing the total amount of the shunt capacitance [11]. For SCR=10 a value of 1.44 and for SCR=50 a value of 1.62 times the sum of the trap capacitances $(C_{\mathrm{trap}} + C_{\mathrm{trap2}})$ is found to be suitable. In both cases the series resistance is designed according to $R_{\mathrm{seriesf}} = \sqrt{\frac{L_{\mathrm{conv}}(L_{\mathrm{trsf}}+L_{\mathrm{mv}})}{(L_{\mathrm{conv}}+L_{\mathrm{trsf}}+L_{\mathrm{mv}})C_{\mathrm{shunt,total}}} \cdot \frac{(2+n)(4+3n)}{2n^2(4+n)}}$ [12].

3. *Parallel C-R||L.* This additional trap filter is tuned to the critical resonance frequency of the first trap filter. As mentioned before, this resonance frequency is calculated with symbolic maths software. The result is too complex to be shown here. The capacitance is designed following the same principle as for the main trap filters. If the bandwidth (explained in Chap. 2.9.3) of the trap is not high enough, which means in this case the resonance is not damped sufficiently, the capacitance is increased. Here, 55 % for SCR=10 and 42 % for SCR=50 of $C_{\mathrm{trap}} + C_{\mathrm{trap2}}$ turns out to be suitable. The inductance again is computed using $L_{\mathrm{f}} = 1/((\omega_{\mathrm{trap}}^{res,trap1})^2 C_{\mathrm{f}})$. As damping resistance, a value of the filter inductance reactance at $\omega_{\mathrm{res,trap1}}$ is found to provide good damping: $R_{\mathrm{f}} = \omega_{\mathrm{res,trap1}} L_{\mathrm{f}}$. For low frequencies, the inductance bypasses the resistance and thus minimises losses [28].

---

[11] why? because: It will be seen that the introduced passive damping has no great influence near the carrier frequency. Therefore, if the capacitance of the already designed trap filters were to be reduced, the grid codes would not be met any longer.

[12] This dimensioning was explained and developed in the LCL filter section. It also delivers a very good damping for the trap filter.

### 2.9.3 Graphical Analysis of Damped and Undamped Trap Filters

Fig. 2.12 is constructed like the figure of the LCL filter. The frequency range is increased to $2.1 f_{\text{car}}$. In (b) and (d), it can be seen that the trap frequencies of both filters are placed well at $f_{\text{car}}$ and $2 f_{\text{car}}$. The undamped trap filters (blue line) damp the currents at their trap frequencies correctly to meet the grid codes ((c) and (d)). At the resonance frequency of the first trap filter, the grid codes are not met for SCR=10. The series resistance damping (red dashed line) seems to have a stronger effect on the damping at $f_{\text{car}}$ than at the intrinsic aim, the resonance frequency. For SCR=10, it even flattens the admittance at the trap frequencies. The increased capacitance leads to a lower resonance frequency compared to the other damping methods. An advantage of parallel C-R (continuous orange) and parallel C-R∥L (green dash-dotted) damping is that both do not deteriorate the damping at the trap frequencies. For SCR=10, a higher damping for the C-R∥L method could not be found. Both methods lead to grid code compliant currents.

For trap filter analysis, the Q-factor (Quality factor) will be used. References from power engineering are used here ([18, 41]). The higher the value of Q, the more pronounced is the valley at the trap frequency [18]. This is defined as Eq. 2.16 ([18], Chap. 20.8.1). In [18], values for Q from 20-100 are mentioned. Additionally, the bandwidth of the trap filter can be calculated from the quality factor (Eq. 2.17, [41] Table 6.1).

$$Q = \frac{\omega_{\text{trap}} L_{\text{trap}}}{R_{\text{trap}}} = \frac{1}{\omega_{\text{trap}} C_{\text{trap}} R_{\text{trap}}} = \frac{\sqrt{L_{\text{trap}}/C_{\text{trap}}}}{R_{\text{trap}}} \tag{2.16}$$

$$B = f_{\text{trap}}/Q_{\text{trap}} = f_{\text{trap}} R_{\text{trap}} \sqrt{C_{\text{trap}}/L_{\text{trap}}}] \tag{2.17}$$

### 2.9.4 Parameter Analysis of Damped and Undamped Trap Filters

All data is shown in Tab. 2.7 in the last two column sections. Below, the parameters are discussed.

- *DC link voltage, MaxCCRpp, converter inductance.* As already mentioned, the MaxCCRpp is set to 25 %. This leads to slightly different converter inductances (compared to the LCL filter) for SCR=10 and 50 due to the different DC link voltages.

- *Undamped filter.* In the table, this is listed as 'T0'. The resonance frequencies $f_{\text{trap}}, f_{\text{trap2}}$ of the undamped filters are set near $f_{\text{car}}$ and $2 f_{\text{car}}$. Both trap filters are only damped by their parasitic resistances computed according to App. 7.2 and 7.3. For SCR=10, their capacitances $C_{\text{trap}}, C_{\text{trap2}}$ have to be increased. Consequently their quality factors decrease in comparison to SCR=50. The quality factors are still in the range as mentioned in literature. Their defined bandwidths ($B_{\text{trap}}$ & $B_{\text{trap2}}$) are 16 and 43 Hz for SCR=50 and 34 and 132 Hz for SCR=10. For SCR=50, it could be considered to increase the bandwidth, as possible parameter variations could lead to a violation of the grid codes.

- *Series resistance damping.* In the table this is listed as 'T1'. The series resistance damping is applied for the first and the second trap filter. To keep the same carrier frequency damping, their capacitances $C_{\text{trap}}$ are increased compared to the undamped case (for the
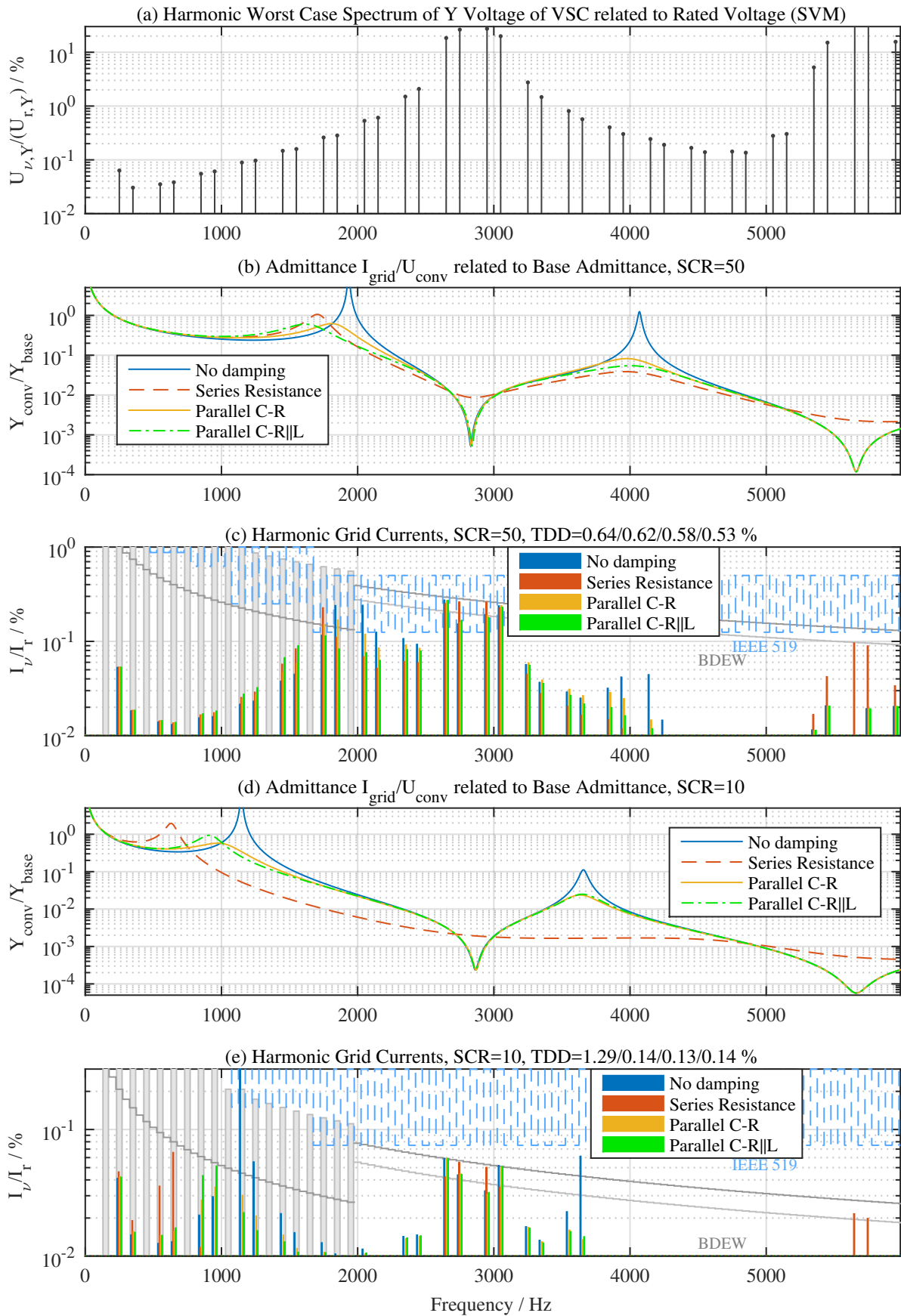
**Figure 2.12:** Trap filter design with different passive damping strategies

**Table 2.9:** Selected results from trap design

| | SCR=10 | | | | SCR=50 | | | |
|---|---|---|---|---|---|---|---|---|
| | L0 | L1 | L2 | L3 | L0 | L1 | L2 | L3 |
| $L_{\text{conv}}$ / % | 16.3 | 16.3 | 16.3 | 16.3 | 16.3 | 16.3 | 16.3 | 16.3 |
| Total capacitance / % | 2.1 | 7.4 | 3.8 | 3 | 0.8 | 1.2 | 1.3 | 1.2 |
| Total losses / ppm | 2.9 | 43.6 | 42.5 | 5.1 | 2.8 | 48.7 | 16.8 | 12.9 |
| Admittance at $f_{\text{res}}$ in p.u. | 20.1 | 1.9 | 0.6 | 0.9 | 15.9 | 1.1 | 0.6 | 0.6 |

first trap filter factor 6.3 (SCR=10) and factor 1.4 (SCR=50)). The quality factor decreases significantly (for the first trap filter) while its inverse, the bandwidth, increases. The total losses ($P_{\text{trap}}^{loss} + P_{\text{trap2}}^{loss}$) increase significantly by approximately factor 18.

- *Parallel C-R.* In the table, this is listed as 'T2'. As mentioned before, the first and second trap filter remain unchanged compared to the undamped case (except for a slight change of the trap frequency). For SCR=10, the total losses ($P_{\text{trap}}^{loss} + P_{\text{trap2}}^{loss} + P_{\text{series}}^{loss}$) are in the same range as for series resistance damping. For SCR=50, the total losses are decreased significantly to $\approx$ 35 % compared to series resistance damping.

- *Parallel C-R∥L.* In the table, this is listed as 'T3'. Again the first and second trap filter remain unchanged. As described above, the trap frequency of the damping C-R∥L circuit is set to the resonance frequency of the first trap filter. For both SCRs, this method has the lowest total losses ($P_{\text{trap}}^{loss} + P_{\text{trap2}}^{loss} + P_{\text{series}}^{loss} + P_{\text{R}_\text{f}}^{loss}$).

**Conclusion for SCR>=50 and 50>SCR>=10.** All passive damping methods need an increased total shunt capacitance compared to the undamped filter (see Tab. 2.9). For series resistance damping, the quality factor of the trap filters decreases. This is no problem due to the fact that the 'trap valley' still is 'deep enough' to meet the grid codes. The highest losses occur at series resistance damping with 43.6 ppm (SCR=10) and 48.7 ppm (SCR=50). In absolute values, this is in the range of 1 kW at 2.22 MVA rated apparent power. The parallel C-R∥L method is an option to reduce these losses to the range of 300 W. Regarding additional passive components, the series resistance damping is the most advantageous (and simplest) method. But it has to be considered that the damping of this method at resonance frequency is less than the damping achieved with the other methods (Fig. 2.12 b), d) and value $Y_{\text{fres}}$ in Tab. 2.7). For SCR=10, the parallel C-R∥L method also provides a sufficient resonance damping in the medium range. The best option seems to be parallel C-R damping for SCR=50 (providing the highest resonance damping) and parallel C-R∥L for SCR=10 due to the lower losses.

# 2.10  Analysis and Comparison of both LCL and Trap Filters

## 2.10.1  Robustness of LCL and Trap Filters Against Grid Impedance Variations

An aspect, which has not been considered so far, is the sensibility of resonance and switching damping regarding grid impedance variations.

In Fig. 2.13, the admittance $I_{\mathrm{grid}}/U_{\mathrm{conv}}$ varying the grid impedance for LCL ((a)-(d)) and trap ((e)-(h)) filter is shown. No damping circuits are included. On the left side the weak grid, on the right side the strong grid design respectively the SCR interval is analysed. For all filters the resonance frequency increases with decreasing grid impedances (increasing SCRs). For the LCL filter, it is obvious that the admittance at carrier frequency of 2850 Hz increases with an increasing SCR (in (c) and (d), the interesting frequency range is zoomed in.). The lowest (continuous blue) line is the admittance resulting from the previously shown filter design and therefore meets the grid codes. For an increasing SCR the admittance increases also, therefore, higher grid currents near the carrier frequency are evoked. The harmonic current grid codes proportionally rise with the SCR (see Fig. 2.2 (b)). Consequently the increased admittance must be below SCR/10 respectively SCR/50 times the not increased admittance to still guarantee grid conformity. This is the case for the shown admittances and also for the trap filters shown in (g) and (h). A graphical validation can be done.

The resonance of the trap filters and LCL filters on the other hand migrates with a varying grid impedance. In the worst case, it could happen that the designed damping circuit no longer damps the migrated resonance appropriately. Especially for the parallel C-R‖L damping circuit, which is tuned to the resonance frequency, this might be a problem. This is an argument against the parallel C-R‖L circuit. Regarding the LCL filter, the same phenomenon occurs.

## 2.10.2  Harmonic Grid Currents of the LCL and Trap Filters Regarding Distorted Grid Voltages

To evaluate the influence of a distorted grid voltage, the admittance $I_{\mathrm{grid}}/U_{\mathrm{grid}}$ is calculated with Matlab and plotted in Fig. 2.14. $U_{\mathrm{grid}}$ is defined as the grid voltage source at no load, compare Fig. 2.3. This admittance is important if the grid voltage contains harmonics. Assuming only fundamental current control of the converter, the grid currents are calculated by multiplying the possible grid voltage spectrum with the shown admittance. In contrast to the previously analysed admittances $I_{\mathrm{grid}}/U_{\mathrm{conv}}$, a zero point below the first resonance frequency appears. This is a good property due to the fact that here less harmonic currents can be evoked. If the admittance is below 0 dB, for example a 5% harmonic voltage evokes less than 5% harmonic currents at its frequency. The resonance on the other hand amplifies the value of percentaged harmonic voltage when the harmonic current is calculated. Active or passive damping methods need to prevent this. It is assumed that the grid voltage can especially contain 5th, 7th, 11th and 13th harmonics (250, 350, 550 and 650 Hz). In Tab. 2.10, an analysis considering these characteristic points is given. A value of the admittance below one is considered to be not critical. For SCR=50, all filter admittances (also the undamped ones) are for the critical frequencies below 0 dB (see third
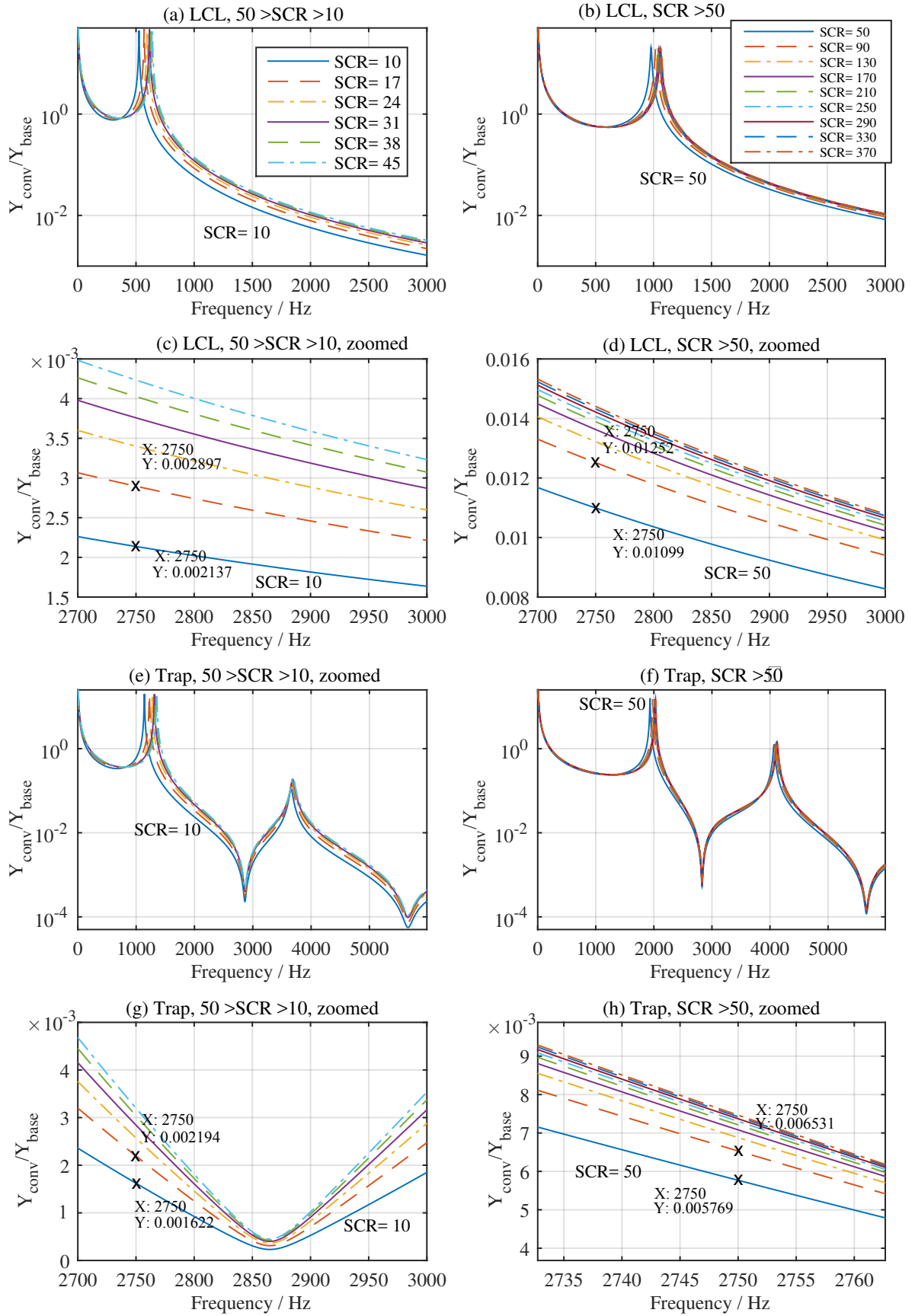
**Figure 2.13:** Magnitude plots of the admittance $Y_{\text{conv}}(j\omega) = I_{\text{grid}}/U_{\text{conv}}$ related to base admittance for all analysed filters and SCRs
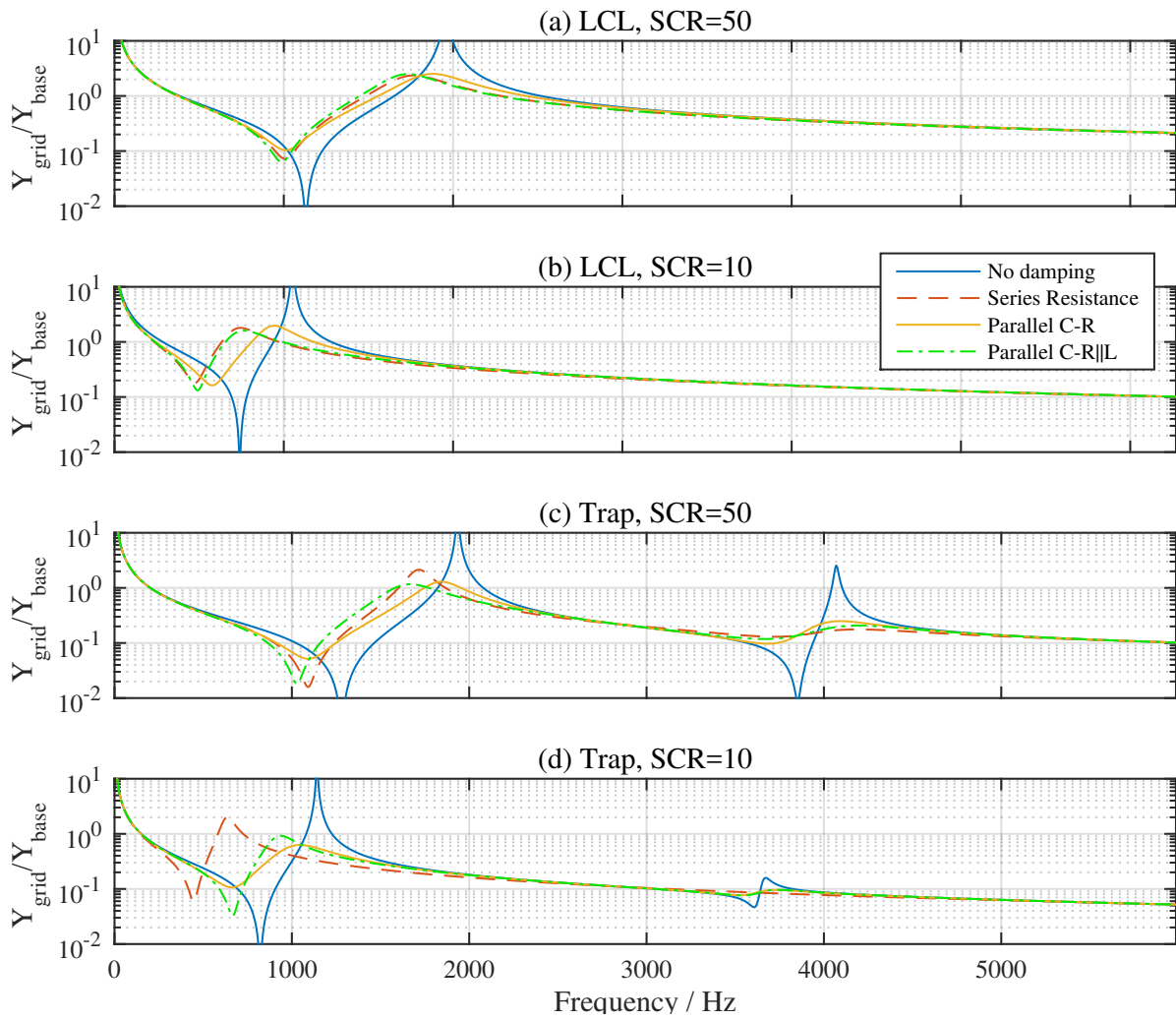
**Figure 2.14:** Admittance $I_{\text{grid}}/U_{\text{grid}}$ magnitude plots to evaluate the grid voltage influence

**Table 2.10:** Analysis of related admittance $I_{grid}/U_{grid}$ at characteristic grid voltage distortion frequencies (0)-no damping; (1)-Series resistance (2)-C-R (3)-C-R‖L

| Frequency / Hz | LCL SCR=10 | LCL SCR=50 | Trap SCR=10 | Trap SCR=50 |
|---|---|---|---|---|
| 250 | all<1 | all<1 | all<1 | all<1 |
| 350 | *(0),(3)<1;(1),(2)≈5-8* | all<1 | all<1 | all<1 |
| 550 | *(0)»1;(3)≈3;(1),(2)<1* | all<1 | all<1 | all<1 |
| 650 | all<1 | all<1 | *(1)≈10;(0),(2),(3)<1* | all<1 |

column). Also from this point no passive damping is necessary. For SCR=10, the resonance is closer to the critical frequencies. For the LCL filter, all combinations deliver at some points admittances above 0 dB. In contrast, for the trap filter design only the series resistance damping method violates the criterion. It is concluded that the trap filters for SCR=10 are less critical. As next step the harmonic impedance $I_{grid}/U_{grid}$ including the converter control should be analysed [42]. This goes beyond the scope of this work.

## 2.10.3  Comparison of LCL and Trap Filter Solutions

The LCL filter solution seems to be the most easy-to-design method. Moreover it is more flexible due to the fact that the trap filters are limited to a fixed carrier frequency. Both methods require (worst case: cos$\varphi$=0.9 overexcited, grid voltage rise of 10%) relatively high DC link voltages. If passive damping methods are desired for SCR=10, the trap filter only needs 81% of the converter inductance of the LCL filter. At the same time, the trap filters need 25 V higher DC link voltages. The total capacitances of the trap filters are significantly less than those of the LCL filter (SCR=10: 19,35,23,17 % of the corresponding LCL filter, SCR=50: 16,20,19,20 % of the corresponding LCL capacitance). The lower capacitances (and reactive current consumption of the shunt branches) are an argument for the trap filters.

The trap filters have more shunt inductance than all corresponding LCL filters. This is a drawback. Nevertheless, it is assumed that shunt inductance at least does not play such a big role in the complete design process, because it only has to be designed to a fraction of the rated turbine current.

If the grid codes are only valid until 9 kHz, the second trap filter could be omitted (with an increased switching frequency). This would probably make the trap filter again more advantageous compared to the LCL filter.

In this work, the control and stability analysis will be performed for both filter types. Nevertheless, the results of the present analysis rather suggests to take trap filters than LCL filters for the grid connection.

## 2.10.4 General Comments

Several aspects have not been paid attention to during the filter design. These aspects are for example: Component availability and costs, magnetic core losses, losses in the converter (only indirectly by DC link voltage, low carrier frequency and converter current ripple), DC link capacitance and current ripple, high frequency models of the component etc..

Concerning the grid code limits, the trap filters can be critical also for frequencies higher than $2f_{car}$ [39]. In contrast to the LCL filter, the admittance $I_{grid}/U_{conv}$ does not only decrease above the trap frequency. Due to this fact the capacitance of the second trap filter has to be increased more than it is necessary for the damping at $2f_{car}$. Still, compared to the LCL filter, it is a very small capacitance. In this way, the present filters meet the grid codes at all frequencies.

Additional improvements to the existing trap filters can be a parallel resistance to their inductances. This can lead to a better damping at higher frequencies providing the possibility to decrease the capacitance of the second trap filter. In this work, this is not considered.

During the passive damping circuit design, several times try-and-error methods have been applied to find for example the best damping configuration. In a recent publication [43] general methods have been developed for their design.

It is interesting that the LCL filter with C-R∥L damping resembles the trap filter with C-R damping. The idea, that in the end the same filter designs are analysed is disproved by comparing their filter data in Tab. 2.7. The C-R∥L circuit is always tuned to resonance frequency while the trap filters are tuned to carrier frequency (always different).

# 3  DQ Grid Current Control Design and Analysis

## 3.1  Overview

In this chapter the current control of the grid connected converter is defined and designed. First, the general structure is described, then, all specific parts are explained. As the main objective is the current control stability analysis regarding specific grids, high effort is put into the current control design and analysis, representing the main part of the chapter. Specific aspects, for example anti aliasing filters, are discussed. At the end, three-phase simulations validate the successful completion of the design process for the 2 MW grid-connected wind turbine.

## 3.2  Current Control Scheme

A common current control method in a rotating space vector reference frame is implemented: dq current control (see for example [44]). In this way, active and reactive power of the converter can be controlled. The control schematic is shown in Fig. 3.1 and explained below. The control part is drawn in grey while the hardware components are black. The measured abc converter currents are transformed into the grid voltage oriented dq frame. The active current reference $i_{d,ref}$ generally originates from the DC voltage control. Due to the fact, that a constant DC voltage source is assumed, $i_{d,ref}$ and $i_{q,ref}$ can be set arbitrarily. The dq grid voltage angle is obtained with a Sychronous Reference Frame (SRF) PLL. Therefore the line-to-line voltages are measured. As the control is performed with line values, the line-to-line voltages are transformed to line signals. An analogue lowpass filter is implemented. The currents are controlled with discrete PI controllers. They are decoupled with an approach described in the following sections. The converter reference voltage is transformed back to the abc frame. A unit delay is introduced (only in the simulation model) to model the computation delay. After processing the Space Vector (SV) modulation, the switching signals for the IGBT drivers are obtained. The converter imposes an ideally switched voltage to the filter and grid connection.
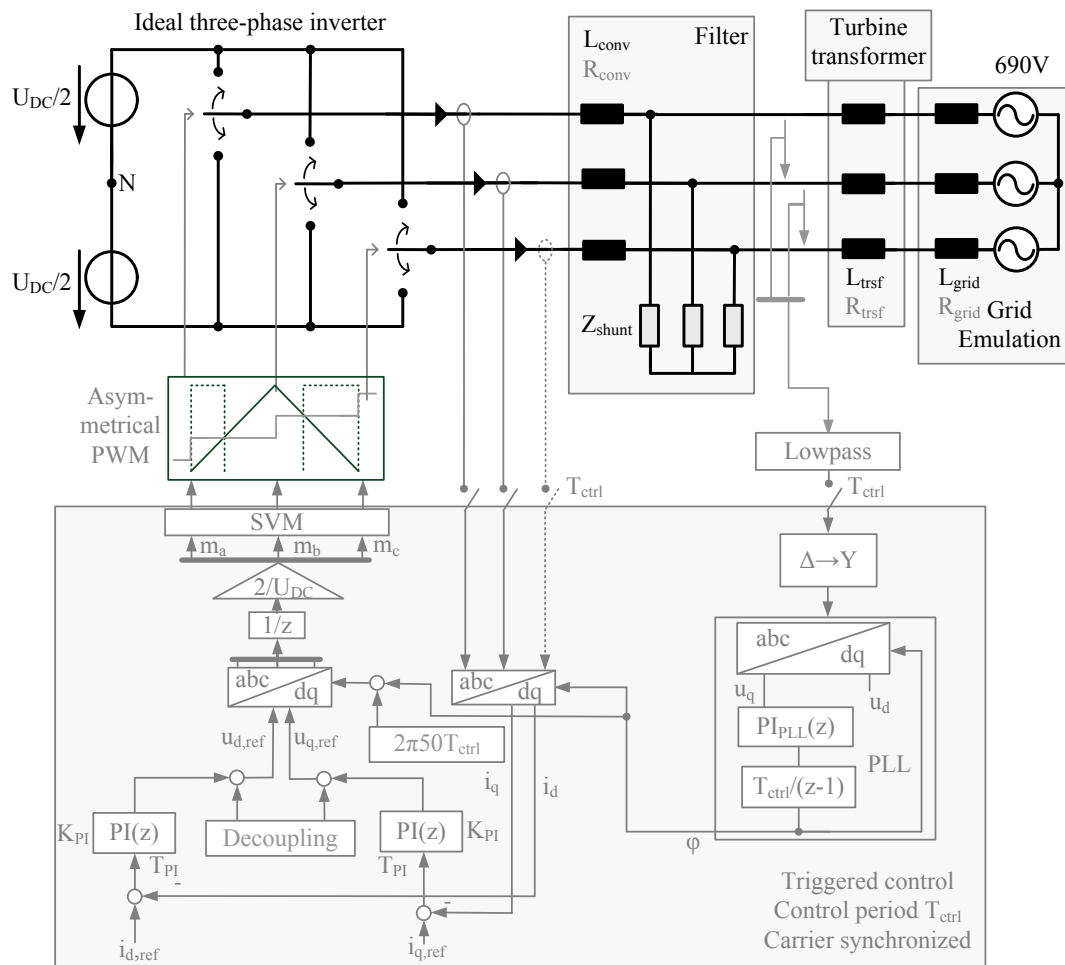
**Figure 3.1:** Complete control and hardware simulation model (for LCL filter)
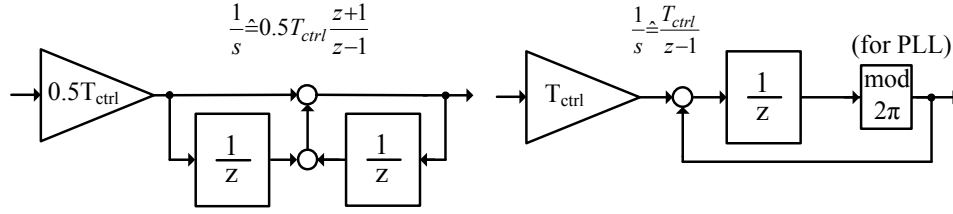
**Figure 3.2:** Implemented discrete integrators: left: Tustin method, right: forward Euler method (the modulo $2\pi$ operation is implemented for the PLL integrator to prevent integrator overflow)
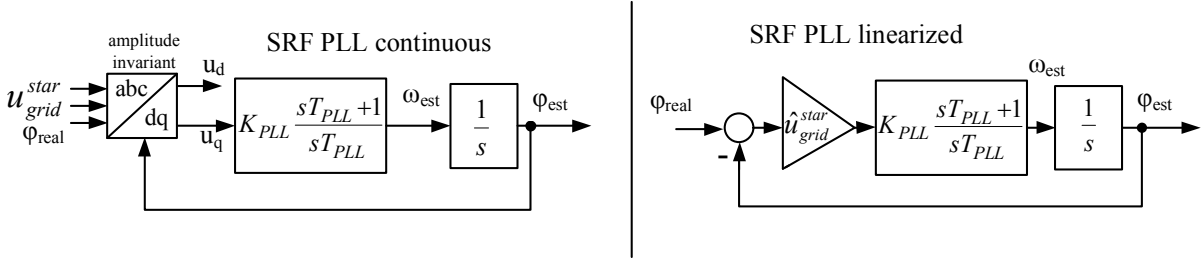


**Figure 3.3:** Synchronous reference frame PLL. left: schematic; right: linearised model; est=estimated

## 3.3 Anti-Windup and Discretisation

*PI controller anti-windup.* As the converter is operated with only a 5 % DC voltage reserve, the anti-windup is important. For rated current reference steps, the control goes in saturation. The implemented anti-windup sets the integrator input to zero if the absolute value of the dq reference converter voltage is higher than its theoretical (linear) maximum for SVM ($2/\sqrt{3}U_{\text{DC}}$). *Discretisation.* In [45] Chap. 3.2.3, the problem and solution of discrete approximation of PI controllers / integrators is explained. It is shown that the Tustin discretisation has the smallest discretisation error, therefore it is utilised in this work (see Fig. 3.2). Obviously this discrete integrator has a direct feed through. If there are no loops in the control, this poses no problem. The SRF PLL has a loop closing directly behind its integrator. This algebraic loop is prevented by using forward Euler discretized integrators, seen in Fig. 3.2 on the right.

## 3.4 Phase Locked Loop Design

An important part of the current control is the grid synchronization which is done by using a standard synchronous reference frame (SRF) phase locked loop (PLL) [46]. A schematic is shown in Fig. 3.3 on the left. Below, the PLL PI controller is designed. A linearised model of the PLL is utilised [47, 48]. With the addition theorem and assuming a symmetrical input voltage and small angle deviations, the linearised model is obtained [48] (Fig. 3.3 on the right). Below $\hat{u} = \hat{u}_{\text{grid}}^{\star}$ is used. Comparing the closed loop transfer function with its general form (Eq.
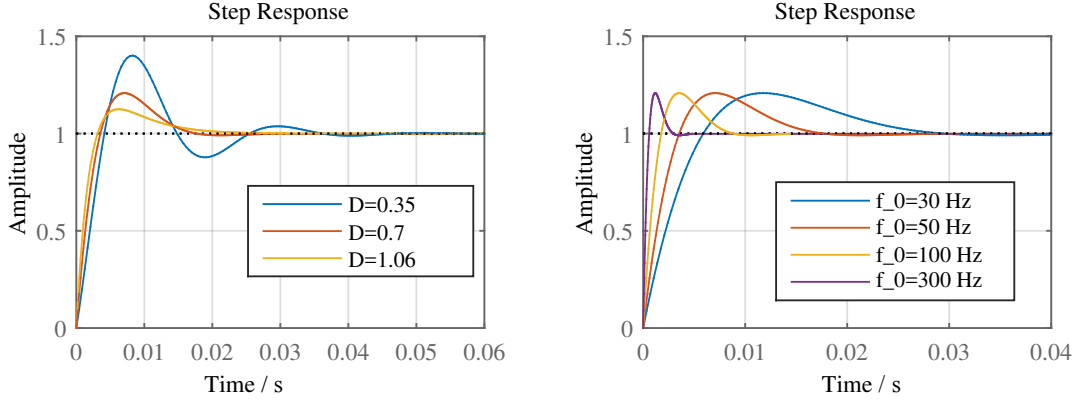
**Figure 3.4:** Step response of SRF PLL transfer function. left: Variation of the damping D with $\omega_0 = 2\pi 50$; right: variation of $\omega_0$ with $D = 1/\sqrt{(2)}$

3.1), the cut-off frequency $\omega_0$ and damping $D$ can be expressed (Eq. 3.2,[48]).

$$\underline{G}_{\text{SRF}}(s) = \frac{\varphi_{\text{est}}(s)}{\varphi_{\text{real}}(s)} = \frac{s \cdot \hat{u} \cdot K_{\text{PLL}} + \frac{\hat{u} \cdot K_{\text{PLL}}}{T_{\text{PLL}}}}{s^2 + s \cdot \hat{u} \cdot K_{\text{PLL}} + \frac{\hat{u} \cdot K_{\text{PLL}}}{T_{\text{PLL}}}} = \underbrace{\frac{s2D\omega_0 + \omega_0^2}{s^2 + s2D\omega_0 + \omega_0^2}}_{\text{general form}} \quad (3.1)$$

$$\Rightarrow \omega_0 = \sqrt{\frac{K_{\text{PLL}} \cdot \hat{u}}{T_{\text{PLL}}}}; \ D = \frac{K_{\text{PLL}} \cdot \hat{u}}{2\omega_0} = \frac{\sqrt{T_{\text{PLL}} \cdot K_{\text{PLL}} \cdot \hat{u}}}{2} \quad (3.2)$$

The controller parameters are then derived according to Eq. 3.3.

$$\Rightarrow K_{\text{PLL}} = \frac{2 \cdot D \cdot \omega_0}{\hat{u}}; \ T_{\text{PLL}} = \frac{K_{\text{P}} \cdot \hat{u}}{\omega_0^2} = \frac{2 \cdot D}{\omega_0}. \quad (3.3)$$

In Fig. 3.4, the step responses of the PLL resp. Eq. 3.1 are plotted. With $\varphi_{\text{real}} = 1/s \cdot \omega_{\text{real}}$ and Fig. 3.3 the transfer function $\omega_{\text{est}}(s)/\omega_{\text{real}}(s)$ can be calculated. It is identical to Eq. 3.1. Therefore, the step responses can also be understood as response to a frequency change. According to Fig. 3.4 on the left, $D$ is set to $D = \frac{1}{\sqrt{2}} \approx 0.707$. The cut-off frequency $\omega_0$ defines the dynamic of the PLL as it is seen on the right. For controlling 50 Hz currents, the reaction time of the PLL should also be in this range (20 ms). In the following sections $\omega_0$ will be called the 'bandwidth' of the PLL and is adjusted together with the current control.

## 3.5 PI Controller Design and Loop Analysis for All Designed Filters

### 3.5.1 Start Design: Symmetrical Instead of Technical Optimum

The current controller design can be done in many ways optimising different properties of the control (for example settling time or overshoot of the step response or robustness via for

**Figure 3.5:** Simplified current control loop for control design

example phase and gain margin). For example [42] analyzes the distance of the closed loop poles to the imaginary axis to choose the PI gain. Additionally 'simulation and experimental techniques' are applied to find an adequate PI time constant. Also [49] uses a pole placement strategy.
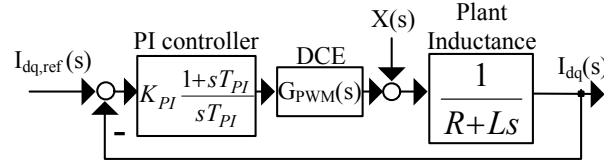
More direct ways are the well-known approaches for simple plants, the technical (TO) and symmetrical optimum (SO) (see e. g. [50]). Often, also in actual publications the TO is taken as current controller design criterion in literature [36, 32, 51, 46]. This stands in contrast to what was found - that the PI time constant of the TO for converter current control with filters generally is too high ([52], from 1997!). A bad disturbance reaction is the result. As a solution the SO is proposed [52, 50]. A similar controller design is used in [53]. Below, it is shown that also for the present system the TO results in a too high PI time constant. Then the SO design is derived and taken as start control design. The development is carried out according to [50] (in [50] for motor current control).

The TO is valid for a plant consisting of two first order systems. For the dq current controller design, it is common to simplify the plant transfer function to the two demanded first order systems by neglecting dq couplings and the shunt impedances ([44], [46] Chap. 12.6). Eq. 3.4 shows the resulting open loop transfer function.

$$\underline{G}_0(s) = \underbrace{K_{\mathrm{PI}}\frac{1+T_{\mathrm{PI}}s}{T_{\mathrm{PI}}s}}_{\text{PI}} \cdot \underbrace{\frac{1}{1+1.5T_{\mathrm{ctrl}}s}}_{\text{PWM; discrete control}} \cdot \underbrace{\frac{\frac{1}{R}}{1+\frac{L}{R}s}}_{\text{Plant}} \tag{3.4}$$

$R, L$: *total* series resistance/ inductance including converter, transformer and grid impedance; $T_{\mathrm{ctrl}}$: control (sampling) period

The TO design eliminates the slowest time constant $T_{\mathrm{PI}} = L/R$ of the plant and adjusts a damping of $D = 1/\sqrt{2}$ of the closed loop by setting $K_{\mathrm{PI}} = L/(2 \cdot 1.5T_{\mathrm{ctrl}})$. Hereby, the closed loop has the general form of Eq. 3.5 (see for example [54] Eq. 4.3.48 and Fig. 4.3.16).

$$\underline{G}_1(s) = \frac{V}{\frac{s^2}{\omega_{\mathrm{x}}^2} + \frac{2Ds}{\omega_{\mathrm{x}}} + 1} \tag{3.5}$$

The result is a very simple open loop transfer function (Eq. 3.6).

$$\underline{G}_{0,\mathrm{TO}}(s) = \frac{1}{(1+1.5T_{\mathrm{ctrl}}s)3T_{\mathrm{ctrl}}s} \tag{3.6}$$

Concerning TO, [50] says that the time constants of the two first order systems must not differ more than a factor 4, if the disturbance response is important ([50] p.50).

This is the case for the present system (for example ($S_{\mathrm{r}}$=2.2 MVA, 690 V, SCR=50, Trap, C-R‖L damping): $L/R = 130$ ms$>> 4 \cdot 1.5T_{\mathrm{ctrl}} = 1.1$ ms). It is obvious that $L/R$ is dependent on the

X/R ratio of the inductances. As is explained in appendix 7.2, the X/R ratio of commercially [1] available inductances is crucial dependent on their current rating. For low current ratings ( 20 A), ratios of 10-15 are found, while for high currents (400-1000 A) the ratios are around 50. Therefore, for low current inductances the time constant precondition has to be checked again. This is done exemplarily for an X/R ratio of 10. The calculation results approximately in a times four smaller time constant $L/R$ but in the same conclusion ($L/R = 32$ ms$>> 4 \cdot 1.5 T_{ctrl} = 1.1$ ms). It can be concluded that the present system with TO tuned controllers would eliminate disturbance influences very slowly (see for example [50] Fig. 3.16). The question is: what is the disturbance, and is it important to be eliminated quickly? In [50], the disturbance is an added input between the two first order systems of the plant (X(s) in the dq control loop in Fig. 3.5). In the present case, it is the grid voltage. In normal stationary operation $x_d = U_r \sqrt{2/3}$; $x_q = 0$ is valid. Having a fast disturbance elimination now means that the control can handle sudden grid voltage changes. This can be a desired property.
There are two aspects against the TO:

- As described before, the grid voltage disturbance elimination is poor.

- The PI time constant of the TO is dependent on the parasitic resistance of the series inductance $T_{PI,TO} = L/R$. This is assumed to be a disadvantage, because the parasitic resistance is difficult to determine and not exactly known for the grid impedance. This is a second argument against the TO.

The *Symmetrical Optimum* (SO) results in a controller design being independent from $R$ and fast elimination of disturbances and steady-state deviations. Originally, this is applied for plants including an integrator (in the present case the digital PWM control approximation) and a first order system. In [50] on page 69 & 70 correction factors for plants with a first order system instead of an integrator are presented. The aim is to obtain the same dynamics as for the SO with an integrator in the plant. For the given case, it can be concluded that regarding p. 69 in [50] that these correction factors deviate only slightly from 1 for the high power case. Therefore, considerations can be given towards using the correction factors only in the case of the low power system. Here, they are neglected.
The SO controller tuning can be found in Eq. 3.7. For the analysed system, the time constant of the controller is much smaller than the TO time constant $T_{PI,TO} = 130$ *ms* $> T_{PI,SO} = T_{PI,start} \approx$ 2.4 *ms*.

$$T_{PI,start} = a^2 1.5 T_{ctrl}; \; K_{PI,start} = \frac{L}{a 1.5 T_{ctrl}}; \; a = 3 \tag{3.7}$$

$L$: complete series inductance including converter, transformer leakage and grid inductance
To reduce the overshoot of the controlled current step response, a reference prefilter (first order hold with time constant $T_{prefilter}$) is implemented (Eq. 3.8) [50]. The control can be run with or without the prefilter. In literature, ramps are also mentioned as prefilters. In practice, both are be applied. For the present analysis, the first order hold is taken due to the fact that it can be easily described in the frequency domain.
For now a standard controller tuning is performed which is utilised as start controller design. The shunt elements of the filter are neglected. In the following section, the PI controller is

---

[1] In principle, the X/R ratio can be influenced by the winding diameter and magnetic core structure. Nevertheless, commercially available (and utilised) inductances are of interest.

analysed and improved incorporating the shunt elements.

$$\underline{G}_{\text{prefilter}}(\underline{s}) = \frac{1}{1 + T_{\text{prefilter}}\underline{s}} \tag{3.8}$$

## 3.5.2 Digital Control Emulation for Stability Analysis and Simplification for Control Design

Today, converter control is performed digitally [45]. The rest of the control loop has continuous properties. Two options arise for control design and for stability analysis, the continuous Laplace domain or the discrete domain using the z transformation. Historically, control was first implemented in an analog / continuous way. The continuous Laplace domain seems to be a method where cause and effect are more evident to see. Therefore in this work, the Laplace domain is applied. The PI start design of the previous chapter is used in the continuous domain where the digital control and PWM delay is modeled with a PT1 element according to Eq. 3.9.

$$\underline{G}_{\text{PT1}}(\underline{s}) = \frac{1}{1 + T_{\text{PT1}}\underline{s}} \tag{3.9}$$

The following controller improvement and stability analysis regarding resonances is then performed with a more advanced model for the digital control and PWM delay. Eq. 3.10 is a way to emulate digital control in the continuous Laplace domain ([55] p.145,[56] p.56, [57]).

$$\underline{G}_{\text{PWM}}(\underline{s}) = \frac{1}{T_{\text{ctrl}}} \cdot \underbrace{\frac{1 - e^{-\underline{s}T_{\text{ctrl}}}}{\underline{s}}}_{\text{Zero Order Hold}} \cdot \underbrace{e^{-\underline{s}T_{\text{ctrl}}}}_{\text{Delay}} \tag{3.10}$$

For a control that is updated one time per switching period, $T_{\text{ctrl}} = T_{\text{sample}}$ applies, for a double update $T_{\text{ctrl}} = 0.5\,T_{\text{sample}}$. $G_{\text{PWM}}$ can be simplified to the commonly used PT1 element: Concerning frequencies far below the control frequency $f_{\text{ctrl}}$, the zero order hold can be simplified to a delay with half the control period, multiplied by $T_{\text{ctrl}}$ ([56] p. 57). The resulting delay of 1.5 $T_{\text{ctrl}}$ then can be approximated with the first two elements of the Taylor series of $e^x$. This leads to the common approximation for digital converter control design (Eq. 3.11):

$$\underline{G}_{\text{PWM}}(\underline{s}) \approx \frac{1}{T_{\text{ctrl}}} \cdot \underbrace{T_{\text{ctrl}}\,e^{-s\,0.5T_{\text{ctrl}}}}_{\text{ZOH approx.}} \cdot e^{-sT_{\text{ctrl}}} = e^{-s1.5T_{\text{ctrl}}} \approx \frac{1}{1 + 1.5T_{\text{ctrl}}s} = D_{\text{approx}}(s) \quad (3.11)$$

This PT1 element with a 1.5 $T_{\text{ctrl}}$ approximation is in line with literature ([46], p. 351 or [52]). In order to analyse the differences between the PT1 and exponential description, in Fig. 3.6, their Bode plots and step responses are compared. The PT1 element with time constant $T_{\text{ctrl}}$ is also analysed, due to the fact that its step response is also similar to the one of the exponential description. The Bode plots show that at approximately $0.02f_{\text{ctrl}}$ the magnitude responses of the first order approximations begin to drift away from the perfect exponential description. The same applies for the phase while the 1.5 control period approximation does not differ before $0.06f_{\text{ctrl}}$. For frequencies near to the control frequency, both approximations are insufficient. [57] analyzes other rational approximations of $G_{\text{PWM}}(s)$. Here, the complete analysis will be performed using the exponential representation. Nevertheless, regarding the curves in Fig.
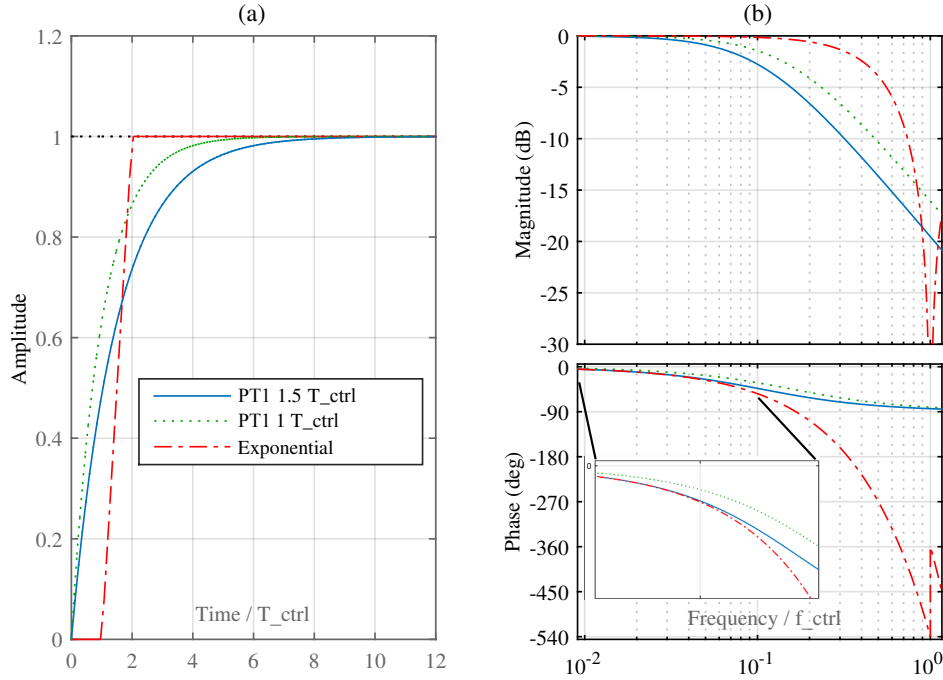
**Figure 3.6:** Comparison of digital control emulator: (a) step response (b) Bode diagram

3.6 it can be queried whether the first order hold with $T_{\text{ctrl}}$ or $1.5T_{\text{ctrl}}$ should be applied for controller design. Especially regarding the settling time of the step response, the one with $T_{\text{PT1}} = T_{\text{ctrl}}$ is closer to the one of the exponential response. The following analysis validates that $T_{\text{PT1}} = 1.5T_{\text{ctrl}}$ is the right choice.

A closed loop analysis is performed. As described in the previous chapter, the controller is tuned according to the symmetrical optimum with a varying optimising factor $a^2 = 2, 4, 9$. The design and analysis is performed for $T_{\text{PT1}} = T_{\text{ctrl}}$ and $T_{\text{PT1}} = 1.5T_{\text{ctrl}}$. Fig. 3.7 shows the resulting step responses of the closed loop using the exponential (considered as best) and first order hold (assumed for control design) presentation for $\underline{G}_{\text{PWM}}(s)$ in the loop equation according to Fig. 3.5. The first order hold step responses (red lines) in the first row ((a)-(c)) for $T_{\text{PT1}} = T_{\text{ctrl}}$ do not differ from those in the second row ((d)-(f)) except for the settling time. This is a logic consequence of the lower time constant in the first order approximation of $\underline{G}_{\text{PWM}}(s)$ and PI design equations.

For the blue lines, $\underline{G}_{\text{PWM}}(s)$ is replaced by the more realistic and precise exponential description (Eq. 3.10). The step responses drift away from those in red that were initially designed by the symmetrical optimum. For all values of a, the approximation with $T_{\text{PT1}} = 1.5T_{\text{ctrl}}$ reproduces the symmetrical optimum dynamic in a more precise way. Especially for $a^2 = 2$ ((a) and (d)), this is obvious. The previously stable adjusted step response is instable with the exponential description (or three-phase system). Therefore, it is concluded that for controller design, $T_{\text{PT1}} = 1.5T_{\text{ctrl}}$ is the better choice, which is in line with literature. For $a^2 = 9$ the difference is not significant. Here, also the modeling with $T_{\text{PT1}} = T_{\text{ctrl}}$ could be taken.
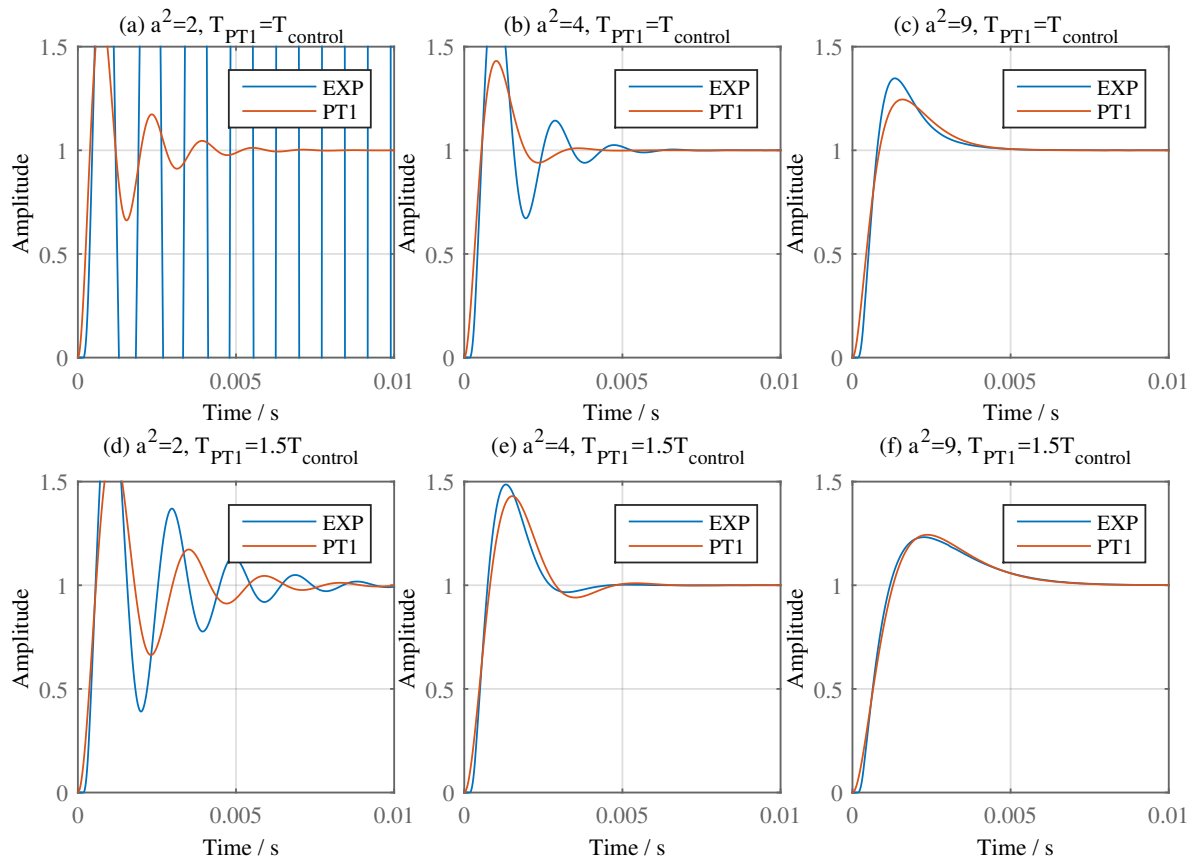
**Figure 3.7:** Comparison of control design with $T_{\text{PT1}} = T_{\text{ctrl}}$ and $T_{\text{PT1}} = 1.5T_{\text{ctrl}}$ for SO tuning for different factor a considering an inductive plant. The exponential step responses can be expected in simulation and laboratory.
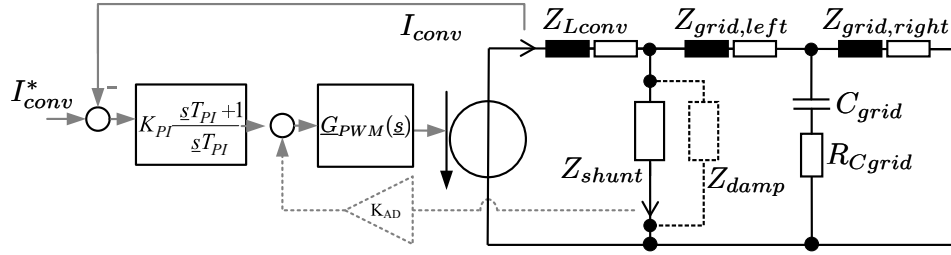
**Figure 3.8:** Control loop for analysis. $Z_{\text{shunt}}$ can be the capacitor or trap filter.

### 3.5.3 Fine Tuning of the PI Controllers: Bode and Characteristic Parameter Analysis

**General Comments.** The start control design (Eq. 3.7) is derived neglecting the shunt components. For the subsequent fine tuning of the design parameters, the shunt components are included in the loop analysis. The analysed loop is shown in Fig. 3.8. The grid capacitance is neglected in this chapter.

In this work, it is decided to perform the analysis in the continuous domain with Bode plots and step responses. Bode plots provide the possibility to directly evaluate the performance at specific frequencies. Step responses are a direct link to the real (current) control behaviour. The Bode plots and step responses are obtained using the transfer function tool of Matlab. [2]

It is assumed, that the preconditions to utilise the well-known (simple) Nyquist criterion and its characteristic parameters such as phase and gain margin, are fulfilled ([54], Chap. 6.4.1 or [58] Chap. 8.5). In many publications, this point is not considered. The precondition is that all poles of the open loop transfer function are in the left s-half plane or one or two at s=0 [54]. For a specific case, this is validated in the root locus in Fig. 5.18(For k=0 the poles of the open loop can be estimated.). Additionally, this is validated with a short analysis in App. 7.6.

In Fig. 3.9, a *general* Bode plot of the open loop transfer function $\underline{G}_0(s)$ is shown. All subsequent Bode plots resemble the one shown in the figure. The (classical) phase margin $\varphi_{\text{marg}}$ at gain 1 and gain margin $A_{\text{marg}}$ at -180° and the phase and gain margin at resonance frequency $\varphi_{\text{marg}}^{res}$ and $A_{\text{marg}}^{res}$ are analysed. Often dB scales are utilised. In this work, the absolute value is taken. The gain margin is the factor by which the open loop can be multiplied to achieve a gain of one ([59] Chap. 5.3.1, p. 126). Eq. 3.12 and 3.13 show recommendations from books ([54, 59]). Even if these recommendations are for plants without resonances, they are taken as reference values.

$$A_{\text{marg}} > \begin{cases} 4...10 \ (equivalent\ to\ G_{0,-180°} < \frac{1}{4}...\frac{1}{10}) & command\ action \\ 2...3 \ (equivalent\ to\ G_{0,-180°} < \frac{1}{2}...\frac{1}{3}) & disturbance\ action \end{cases} \tag{3.12}$$

$$\varphi_{\text{marg}} = \begin{cases} 40°...60°[54]; \ > (50°...60°)[59] & command\ action \\ 20°...50°[54]; \ \ > 30°[59] & disturbance\ action \end{cases} \tag{3.13}$$

If the absolute value at the resonance frequency is above 1, the phase margins $\varphi_{\text{marg2}}$ and $\varphi_{\text{marg3}}$ are additionally calculated (Fig. 3.9).

Experience shows that for the weak grid, the control fine tuning has to be done together with the

---

[2] Sometimes, the *minreal* command must be used in Matlab to eliminate numerical problems.
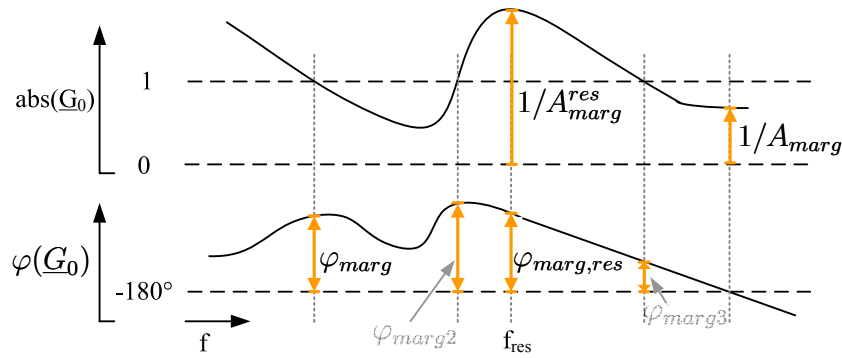
**Figure 3.9:** Explanation of characteristic parameters of the open loop

three-phase simulation. The grid synchronization (including grid voltage signal conditioning) is not included in the transfer function modeling. Nevertheless, for weak grids it has a non-negligible influence on the control performance. Approaches including PLL dynamics result in complex equations [60] which are difficult to handle and interpret. The analysis in this work shows that a sufficient predictability is reached without including PLL dynamics in the loop.
For slow PLLs, it is not sufficient to analyse only the current control. It is possible, that while the current control seems to be in steady state, the PLL still (slowly) tracks the dq reference frame angle, resulting in a poor power control dynamic. Therefore, for the control analysis in three-phase simulation domain, a characteristic time constant $T_{power}$ is introduced. This is defined as the time after a current step until the mean (active and reactive) power remains in an interval of 0.5 % (of $S_r$). $T_{power}$ is determined manually.
It is found that d (active) current steps are less critical than q (reactive) current steps. If the q current step is more oscillatory than the d step, it can be improved by a decrease of the PLL bandwidth, always keeping $T_{power}$ in mind. This is validated with the three-phase active and reactive power respectively $T_{power}$. $T_{power} < 20 \ ms$ is assumed to be a well-designed control when also considering the grid codes (Chap. 2.2).
As a characteristic parameter for the closed loop, its bandwidth $f_{-3dB}$ is utilised. This is defined as the frequency where the closed loop magnitude reaches $-3 \ dB \hat{=} 10^{-3/20} \approx 0.707$ [54]. It is assumed that a closed loop bandwidth $f_{-3dB} > 50 \ Hz$ is sufficient. Nevertheless, the more important factor is $T_{power}$.
Below, always one controller design is given and developed for the different filters (LCL SCR=50; Trap SCR=50; LCL SCR=10; Trap SCR=10). It is found that the control dynamic of each of the four filter types is very similar for all passive damping circuits developed in Chap. 2. This is no surprise, as their admittances are very similar (Fig. 2.9 and Fig. 2.12). Another set of controller parameters is developed for the active damping in the next section 3.5.4. For the undamped filter, no specific controller parameters are developed.

**LCL, SCR>50 (stiff grid)**

Graphical design results are shown in Fig. 3.10 and 3.11, and the characteristic parameters are listed in Tab. 3.1. If an interval is specified for a parameter, it is the interval in which the values of the different passive damping circuits are located.
For LCL SCR=50, the figures with the Bode diagrams and step responses are explained in detail. For all other designs, this is omitted. The figures are arranged as follows: In the left column
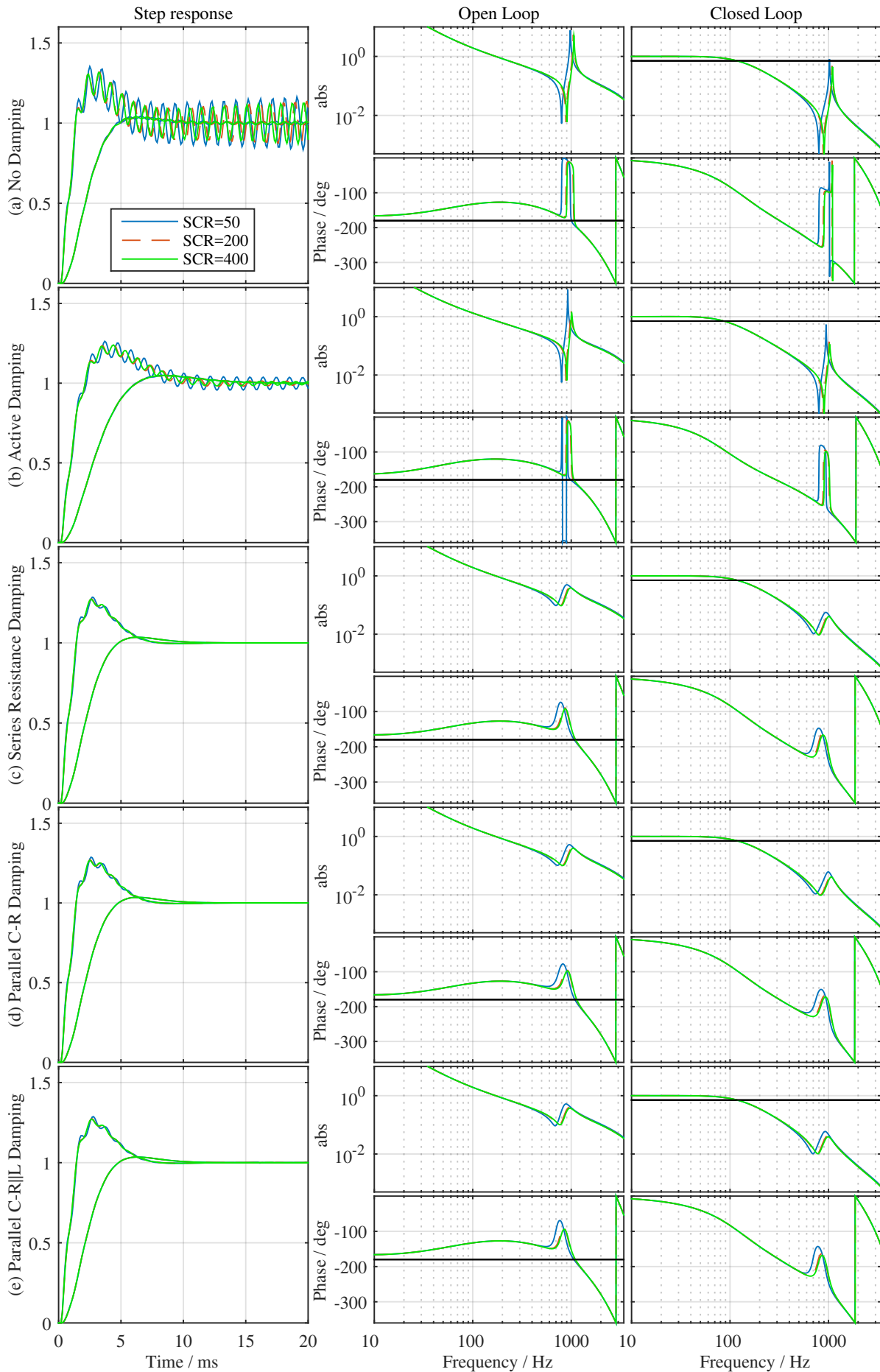
**Figure 3.10:** LCL strong grid system: command transfer function $\underline{I}_{\mathrm{conv}}(\underline{s})/\underline{I}_{\mathrm{conv,ref}}(\underline{s})$ analysis
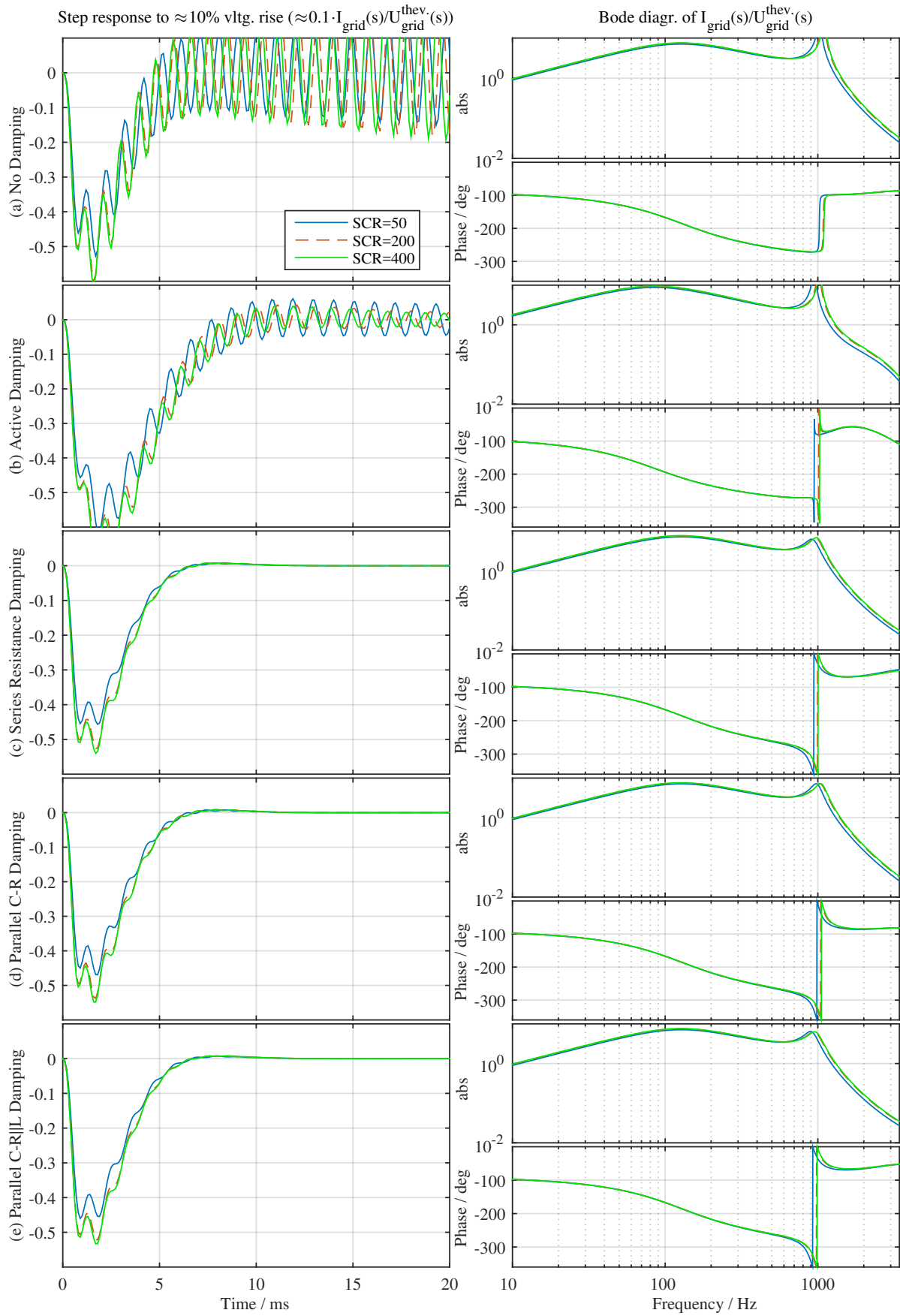
**Figure 3.11:** LCL strong grid system: disturbance transfer function $\underline{I}_{\text{conv}}(\underline{s})/\underline{X}(\underline{s})$; $\underline{I}_{\text{conv,ref}}(\mathbf{s}) = 0$ analysis

**Table 3.1:** Controller and characteristic parameter for LCL, SCR>50

| $K_{\text{PI}}$ | $T_{\text{PI}}$ | $T_{\text{prefilter}}$ | $f_{\text{PLL}}$ |
|---|---|---|---|
| $0.8\frac{L_{\text{total}}}{4.5 T_{\text{ctrl}}}$ | $13.5 T_{\text{ctrl}}$ | $12 T_{\text{ctrl}}$ | $50\ Hz$ |

| $A_{\text{marg}}$ | $\varphi_{\text{marg}}$ | $A_{\text{marg}}^{res}$ | $\varphi_{\text{marg}}^{res}$ | $A_{\text{marg}}^{res,G_1}$ | $f_{-3\text{dB}}$ | $T_{\text{power}}$ |
|---|---|---|---|---|---|---|
| $2.7-3.1$ | $53°$ | $1.9-2$ | $48...57°$ | $1.2..1.4$ | $114\ Hz$ | $\approx 18\ ms$ |

the step responses, in the middle column the corresponding open loop and in the right hand column the closed loop Bode diagrams are shown. In every phase diagram, -180° is highlighted with a reference line. The Bode diagrams are limited to 10-3200 Hz (slightly above the Nyquist frequency of 2850 Hz). Each row stands for a specific passive damping method, as designed in Chap. 2. Additionally, active damping results are shown in row (b). Active damping is designed in the next section and hence not relevant here. All plots contain the results for three different SCRs. Here the PI gain is always adapted to the SCR, as its definition contains the total series inductance. In addition the step responses' subplots in Fig. 3.10 contain two lines per SCR: one of the closed loop with reference prefilter (without overshoot) and another one without the prefilter (with overshoot).

In the Bode plots of the open and closed loop in Fig. 3.10, the effect of the passive damping circuits can be seen clearly. The LCL resonance near 1 kHz is damped significantly. The control without passive damping in the first row is instable, which is directly seen looking at the step response. The instability can also be validated with the open loop Bode diagram. A $-180°$ phase crossing is found near the resonance frequency of $\approx 1$ kHz while the magnitude is above 0 dB. For the undamped system, the same controller parameters are used as for the passively damped systems. This demonstrates that with passive damping circuits, a higher control bandwidth is possible. The passively damped systems are designed as follows.

The start controller design (Eq. 3.7) without a prefilter leads to slightly oscillating step responses (Fig. 3.12). Although this is hardly not seen when the reference prefilter is used, it is decided to be disadvantageous. A decrease of the PI gain to $0.8\,K_{\text{PI,SO}}$ attenuates this oscillation (see Tab. 3.1 and Fig. 3.10 (c), (d) and (e)) and leads to a 30 % higher gain margin at resonance frequency $A_{\text{marg}}^{res}$. From this fact it could be concluded that a minimum value of two is good for the gain margin at resonance frequency. $A_{\text{marg}}$ with 2.7-3.1 is well-defined according to the mentioned disturbance action in Eq. 3.12. $\varphi_{\text{marg}}$ with $53°$ is also acceptable regarding Eq. 3.13.

A PLL time constant according to Chap. 3.4, 1/(50 Hz) is found to be a good value. The control design is carried out alongside with the three-phase simulation. The PLL is only modeled in simulation. Simulation results will be provided in Chap. 3.7.

A prefilter is used to attenuate the overshoot. While this lowers the overshoot, it also reduces the control bandwidth. It is also assumed that rather no overshoot is favoured. Therefore, a (relatively big) time constant of $T_{\text{prefilter}} = 12 T_{\text{ctrl}}$ is chosen. This results in $f_{-3\text{dB}} = 114\ Hz$ (see Fig. 3.10 (c)(d)(e) CL, the -3dB line is marked in black) and $T_{\text{power}} \approx 18\ ms$ which can be checked by analyzing the simulation results (Fig. 3.24). It is obvious that the current control even with reference prefilter is significantly faster ($\approx 10$ ms, see for example Fig. 3.10 (c)).

According to [50], the disturbance transfer function $\underline{I}_{\text{dq}}(s)/\underline{X}(s)$; $I_{\text{dq,ref}} = 0$ (see Fig. 3.5) including the LCL/trap filters is analysed (Fig. 3.11). Since $I_{\text{dq,ref}} = 0$, the reference prefilter has no influence, and only one curve per SCR is included in all plots. The step response is multiplied by 0.1 to obtain the response to a 10% grid voltage rise. The disturbance is compensated after a negative deviation before 10 ms. This is also validated in the three-phase simulation in Fig.
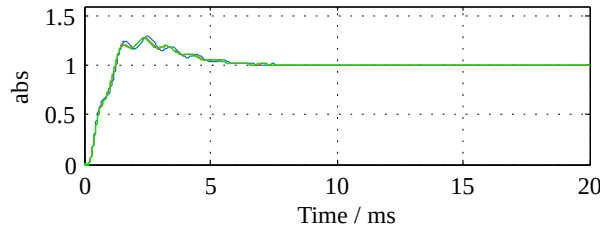
**Figure 3.12:** Slightly oscillating step response for start controller design (here parallel C-R damping, similar for other damping methods)

3.24 (at t=0.13 s), which is explained in detail in Chap. 3.7. The undamped disturbance is left instable (like the command response) to demonstrate the effectiveness of the active damping.

### Trap, SCR>50 (stiff grid)

The parallel C-R and C-R∥L damping methods are found to be suitable. For series resistance damping $A_{\mathrm{marg}} = 1.5$ is valid. Here, the control should be optimized. Due to the fact that this damping method is not utilised in the rest of this work, this is not considered in detail. The graphical design results are shown in Fig. 3.13 and the characteristic parameters are listed in Tab. 3.2. As can be seen for the LCL SCR>50 system, the disturbance reaction (Fig. 3.11) largely resembles the result of the command reaction (Fig. 3.10 ). This is also the case for all subsequent systems, and therefore their disturbance reactions are not shown. The start control

**Table 3.2:** Controller and characteristic parameter for trap filter, SCR>50

| $K_{\mathrm{PI}}$ | $T_{\mathrm{PI}}$ | $T_{\mathrm{prefilter}}$ | $f_{\mathrm{PLL}}$ | | | |
|---|---|---|---|---|---|---|
| $\frac{L_{\mathrm{total}}}{3T_{\mathrm{ctrl}}}$ | $9T_{\mathrm{ctrl}}$ | $9T_{\mathrm{ctrl}}$ | $50\ Hz$ | | | |
| $A_{\mathrm{marg}}$ | $\varphi_{\mathrm{marg}}$ | $A_{\mathrm{marg}}^{res}$ | $\varphi_{\mathrm{marg}}^{res}$ | $A_{\mathrm{marg}}^{res,G_1}$ | $f_{-3\mathrm{dB}}$ | $T_{\mathrm{power}}$ |
| $2.6 - 2.9$ | $43°$ | $2.3 - 2.5$ | $-10...-40°$ | $0.9; 2.3; 2.1$ | $179\ Hz$ | $\approx 14\ ms$ |

design (Eq. 3.7) without a prefilter results in a small settling time of around 5 ms, practically no oscillations, but with a high overshoot of 30 %. As for the LCL filter, the overshoot is eliminated by using a prefilter with $T_{\mathrm{prefilter}} = 9T_{\mathrm{ctrl}}$. The gain margin at resonance frequency fulfills the previously derived condition $A_{\mathrm{marg}}^{res} > 2$. As mentioned before, this is not the case for series resistance damping. Oscillation of the resonance frequency can be seen in its step response (Fig. 3.13 (c)). The classical gain margin $A_{\mathrm{marg}}$, PLL bandwidth $f_{\mathrm{PLL}}$ and $T_{\mathrm{power}}$ are acceptable. With the same PI parameters, the undamped system is instable again.

### LCL, 50>SCR>10 (weak grid)

The control design is valid for all damping methods. The graphical design results are shown in Fig. 3.14, and the characteristic parameters are listed in Tab. 3.3. As already mentioned, the control design for the weak grid must be done together with the three-phase simulation
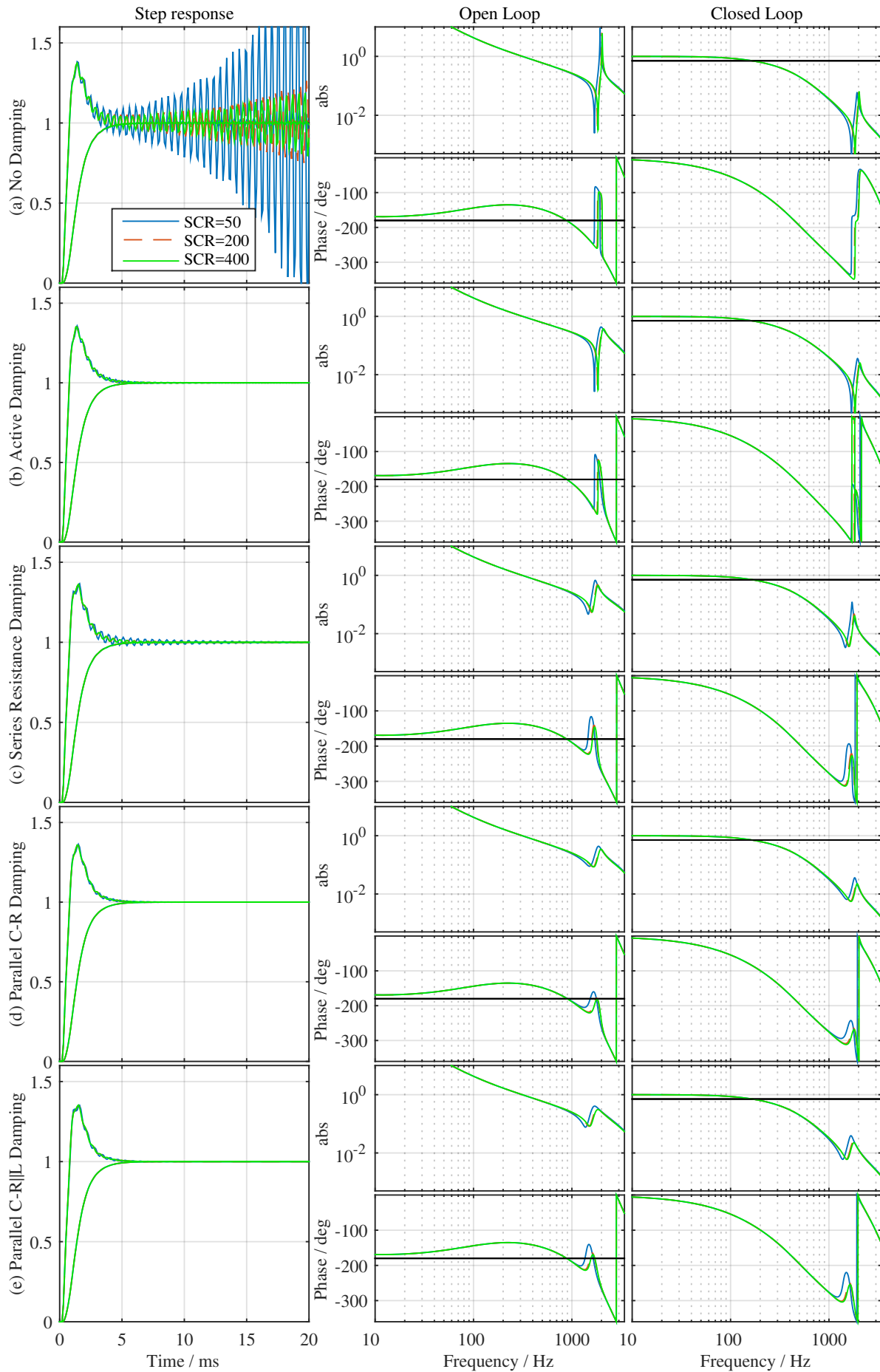
**Figure 3.13:** Trap strong grid system: command transfer function $\underline{I}_{\text{conv}}(\underline{s})/\underline{I}_{\text{conv,ref}}(\underline{s})$ analysis

**Table 3.3:** Controller and characteristic parameter for LCL filter, 50>SCR>10

| $K_{\mathrm{PI}}$ | $T_{\mathrm{PI}}$ | $T_{\mathrm{prefilter}}$ | $f_{\mathrm{PLL}}$ | | | |
|---|---|---|---|---|---|---|
| $\dfrac{L_{\mathrm{total}}}{A_{\mathrm{res,start}}3T_{\mathrm{ctrl}}}$ | $10T_{\mathrm{ctrl}}$ | $15T_{\mathrm{ctrl}}$ | $28\,Hz$ | | | |
| $A_{\mathrm{marg}}$ | $\varphi_{\mathrm{marg}}$ | $A_{\mathrm{marg}}^{res}$ | $\varphi_{\mathrm{marg}}^{res}$ | $A_{\mathrm{marg}}^{res,G_1}$ | $f_{-3\mathrm{dB}}$ | $T_{\mathrm{power}}$ |
| $3.8-4.5$ | $43-44°$ | $1$ | $94-98°$ | $1.2;1.1;1.2$ | $110\,Hz$ | $\approx 22\,ms$ |

(adjusting the PLL dynamic). The problem is: Due to the high grid impedance, the converter current significantly influences the grid voltage in phase and amplitude. A fast reacting PLL tries to track the varying grid voltage. At the same time, it 'shakes' the dq reference frame causing the dq current control less able to work well. Therefore, the logical consequence is a decrease of the PLL dynamic. Here, it must be considered that an excessively slow PLL leads to a slow steady-state error elimination of the power. For control design, two tactics may now be pursued:

The first is to slow down the current control without disturbing the PLL by high di/dts. Due to the fact that the current controller should be able to eliminate disturbances in parts of the fundamental, this will be done by adjusting the prefilter to a settling time of 20 ms. The PLL dynamic should be reduced only, if necessary.

The second is to design a relatively fast current control with the aim that the (slowed down) PLL has a longer time period to eliminate the steady-state error. This tactic is pursued below. For the start design, the magnitude at resonance frequency $A_{\mathrm{res,start}}$ of the resulting open loop Bode plot is determined. $K_{\mathrm{PI,start}}$ is divided by it to receive a gain of one at resonance frequency [36]. A higher damping could also be realized, but would result in a higher overshoot. Looking at the OL phase near the resonance frequency in Fig. 3.14 (c)(d)(e), it can be seen that it is not near -180° (black solid line). The step response without a prefilter also contains practically no oscillations. Therefore, it is assumed that here, a magnitude of one at the resonance frequency is sufficient. In the next step, $T_{\mathrm{PI,start}}$ is adjusted optimising the step response and the stability characteristics. $T_{\mathrm{PI}} = 10T_{\mathrm{ctrl}}$ is found to be a good compromise. As for the other designs, a reference prefilter (first order with time constant $15T_{\mathrm{ctrl}}$) is implemented to prevent an overshoot. The classical gain and phase margins are well-designed. As previously mentioned, the PLL bandwidth $f_{\mathrm{PLL}}$ is reduced to 28 Hz. Nevertheless, $T_{\mathrm{power}}$ is only slightly above 20 ms which is considered to be still acceptable. Here, again, it has to be said that the SCR of 10 is an extreme case.

As can be derived from Fig. 3.4, the slowed down PLL theoretically tracks the angle in approx. $1/28\,Hz = 36\,ms$. This stands slightly in contrast to the observation in simulation which is analysed in Chap. 3.7. $T_{\mathrm{power}} \approx 22\,ms < 36ms$ is observed. Here, it has to be said that after 36 ms the control is completely in steady state. Before, approximately 0.5 % of $S_{\mathrm{r}}$ (11.1 kVA) is tracked in the time period from 22 to 36 ms. This is considered here to be acceptable.

**Trap, 50>SCR>10 (weak grid)**

For all designed damping methods, different control designs are necessary. The graphical design results are shown in Fig. 3.15, and the characteristic parameters are listed in Tabs. 3.4,3.5,3.6. *Parallel C-R Damping.* Similar to the LCL filter, for the weak grid the PI gain of the start design
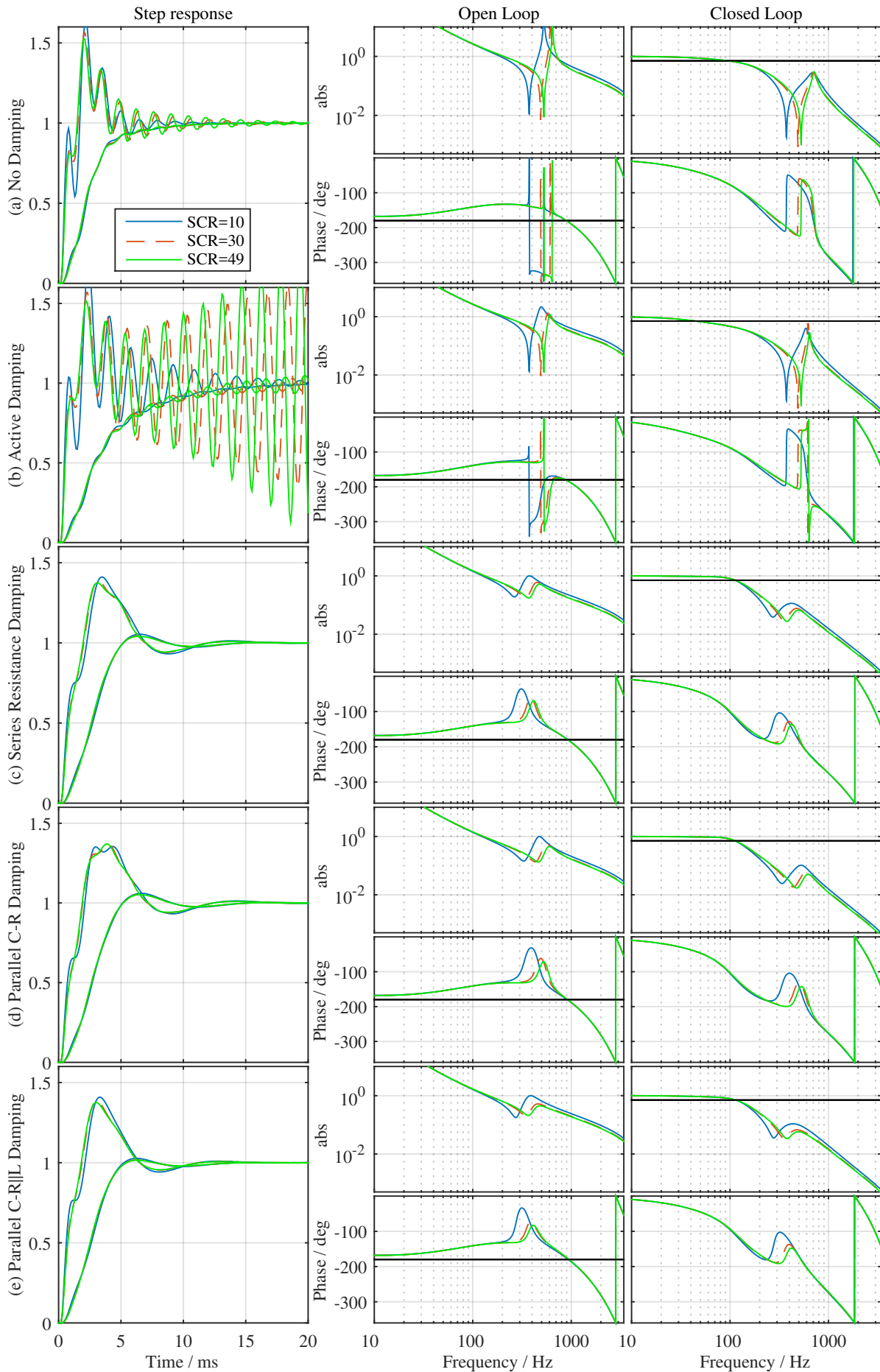
**Figure 3.14:** LCL weak grid system: command transfer function $\underline{I}_{\mathrm{conv}}(\underline{s})/\underline{I}_{\mathrm{conv,ref}}(\underline{s})$ analysis
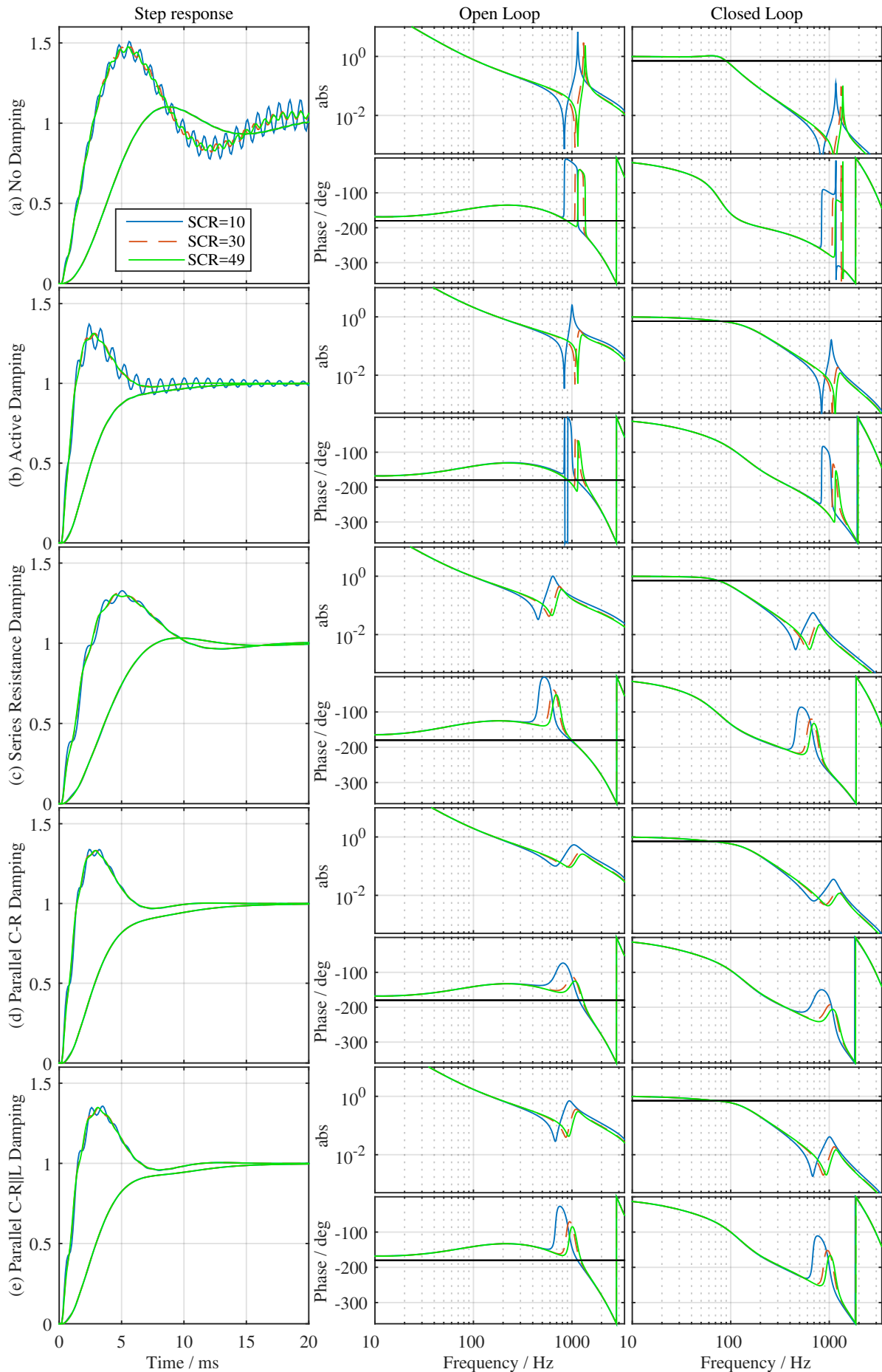
**Figure 3.15:** Trap weak grid system: command transfer function $\underline{I}_{\mathrm{conv}}(\underline{s})/\underline{I}_{\mathrm{conv,ref}}(\underline{s})$ analysis

**Table 3.4:** Controller and characteristic parameter for trap filter with parallel C-R damping, $50 >$ SCR $> 10$

| | $K_{\mathrm{PI}}$ | | $T_{\mathrm{PI}}$ | $T_{\mathrm{prefilter}}$ | $f_{\mathrm{PLL}}$ | |
|---|---|---|---|---|---|---|
| | $0.54\dfrac{L_{\mathrm{total}}}{A_{\mathrm{res,start}}3T_{\mathrm{ctrl}}}$ | | $10T_{\mathrm{ctrl}}$ | $21T_{\mathrm{ctrl}}$ | $40\,Hz$ | |
| $A_{\mathrm{marg}}$ | $\varphi_{\mathrm{marg}}$ | $A^{res}_{\mathrm{marg}}$ | $\varphi^{res}_{\mathrm{marg}}$ | $A^{res,G_1}_{\mathrm{marg}}$ | $f_{-3\mathrm{dB}}$ | $T_{\mathrm{power}}$ |
| $\approx 2.3$ | $46°$ | $\approx 1.9$ | $43°$ | $0.9$ | $58\,Hz$ | $\approx 20\,ms$ |

with $a = 3$ is divided by the OL amplitude at resonance frequency. This *still* leads to (slight) oscillations in the step response comparable to the those in Fig. 3.12. Note that these oscillations are only critical for SCR=10. They are attenuated for example for SCR=30. Therefore, the gain is reduced further to attenuate the oscillations. A value of 0.54 at resonance frequency seems to be a good compromise. If the gain is decreased too much, the overshoot and PLL interaction for reactive current steps is too heavy. To minimize the PLL interactions, its bandwidth is slightly reduced to 40 Hz. The prefilter time constant is chosen to be large enough to prevent overshoots. The gain margin at resonance $A^{res}_{\mathrm{marg}}$ is near to the previously found good range ($>2$). The classical gain margin $A_{\mathrm{marg}}$ is in the recommended range for disturbance action (2-3).

**Table 3.5:** Controller and characteristic parameter for trap filter with series resistance damping, $50>$SCR$>10$

| | $K_{\mathrm{PI}}$ | | $T_{\mathrm{PI}}$ | $T_{\mathrm{prefilter}}$ | $f_{\mathrm{PLL}}$ | |
|---|---|---|---|---|---|---|
| | $\dfrac{L_{\mathrm{total}}}{A_{\mathrm{res,start}}3T_{\mathrm{ctrl}}}$ | | $15T_{\mathrm{ctrl}}$ | $21T_{\mathrm{ctrl}}$ | $40\,Hz$ | |
| $A_{\mathrm{marg}}$ | $\varphi_{\mathrm{marg}}$ | $A^{res}_{\mathrm{marg}}$ | $\varphi^{res}_{\mathrm{marg}}$ | $A^{res,G_1}_{\mathrm{marg}}$ | $f_{-3\mathrm{dB}}$ | $T_{\mathrm{power}}$ |
| $\approx 4.7$ | $49°$ | $1$ | $99°$ | $0.8$ | $76\,Hz$ | $\approx 20\,ms$ |

*Series resistance damping.* The PI gain can only be adjusted to $A_{\mathrm{res}} = 0\,dB$. Despite the passive damping, a high resonance (see Fig. 2.12 (d)) is apparent. A good performance of the control cannot be designed. An overshoot and coupling is present. This is not critical, as has already been mentioned the series resistance damping is not practicable for SCR=10 with the trap filter. *Parallel C-R∥L damping.* As can be seen in Fig. 2.12 (d), the damped resonance for the parallel C-R∥L damping is higher than for the parallel C-R damping. Therefore, the control design again is more difficult. The start design with damped resonance leads to oscillations in the step response without a prefilter. Therefore, it is damped further (0.7). The shown design leads to acceptable dynamics. Generally, a higher attenuation of the resonance by passive damping (as

**Table 3.6:** Controller and characteristic parameter for trap filter with parallel C-R∥L damping, $50>$SCR$>10$

| | $K_{\mathrm{PI}}$ | | $T_{\mathrm{PI}}$ | $T_{\mathrm{prefilter}}$ | $f_{\mathrm{PLL}}$ | |
|---|---|---|---|---|---|---|
| | $0.7\dfrac{L_{\mathrm{total}}}{A_{\mathrm{res,start}}3T_{\mathrm{ctrl}}}$ | | $10T_{\mathrm{ctrl}}$ | $21T_{\mathrm{ctrl}}$ | $50\,Hz$ | |
| $A_{\mathrm{marg}}$ | $\varphi_{\mathrm{marg}}$ | $A^{res}_{\mathrm{marg}}$ | $\varphi^{res}_{\mathrm{marg}}$ | $A^{res,G_1}_{\mathrm{marg}}$ | $f_{-3\mathrm{dB}}$ | $T_{\mathrm{power}}$ |
| $\approx 2.7$ | $45°$ | $1.4$ | $72°$ | $0.7$ | $75\,Hz$ | $\approx 21\,ms$ |

for parallel C-R damping) is assumed to be advantageous for the control.

### 3.5.4  Active Damping

Active damping (AD) of filter resonances is a separate research field. As this is not the main focus of this work, it is investigated to choose and design a *standard* AD approach.
The shunt current or voltage can be used for AD [53]. For the current a proportional, for the voltage a derivative feedback are the options [53]. A variant with less implementation effort would be to utilise the voltage, because it is already measured for grid synchronization. As is described in Chap. 3.6.2, an analog low pass filtering of the grid voltage with a cut-off frequency of 1 kHz is utilised. Using higher cut-off frequencies leads to stability problems. Therefore, with AD only resonances clearly below 1 kHz could be damped. As it is decided to analyse only one active damping method, voltage active damping is excluded. The necessary (digital) derivation is also an argument against voltage active damping, as derivations can lead to high gains due to measurement noise. Only the current active damping method is designed and analysed. Fig. 3.8 shows that this method is very simple: the three-phase shunt current is measured, multiplied by a gain $K_{AD}$ and added to the converter reference voltage.
Active damping is designed for the system without passive damping circuits. Combinations of passive and active damping could be reasonable, but are not analysed in this work.
Regarding the shunt *current* measurement, it is important to remember that this consists mainly of 'ripple' current and no fundamental current. The utilised filter design (Chap. 2) allows maximum peak-to-peak current ripples related to the amplitude of the nominal current of 25 %. In contrast to the grid voltage, this ripple current can be sampled symmetrically with the carrier (at the minima and maxima of the triangular carrier) eliminating the carrier frequency components. Components at other frequencies than the carrier frequency, especially the filter resonance frequency, are visible. A case simulation for the trap and LCL filter with SCR=50 is performed. In Fig. 3.16 (a), the shunt current (capacitor current) for the LCL filter is shown. The sampled shunt current (in this case for the LCL SCR>50 system) contains an oscillation which is not the carrier frequency (and not the fundamental). As mentioned in the filter design section, a fundamental component of 4.9 % (value of the capacitance, see Tab. 2.7) is observed. The adjusted maximum current ripple of 25% $\equiv$ 0.25 $p.u.$ can also be seen.
For the trap filter, it is different. Despite the synchronization, frequency components with carrier frequency appear in the sampled signal. In the dq currents, their amplitude is approximately 2-3 %. The effects are decreased to approximately 1 % by measuring only the first trap filter current (its resonance is also the one which must be damped). On the other hand, three-phase simulation results show that the higher aliasing with the total shunt current is not critical. It is the opposite: the critical PI gain (leading to an instable loop) of AD with *total* shunt current is approximately twice the one with single shunt current. Therefore, the total shunt current is taken for AD with trap filters. Alternatives to eliminate the ripple component are sigma delta circuits or analog low passes. In these cases, the challenge is to stabilise the control despite the integrated delay. To the author's knowledge no publications concerning active damping for trap filter systems exist. Following [53], gain values $K_{AD}$ for the proportional feedforward of the shunt current can be found which stabilise the control. This is performed here regarding the open loop Bode plots varying the gain factor. The factor resulting in the highest resonance damping is considered as optimal gain.
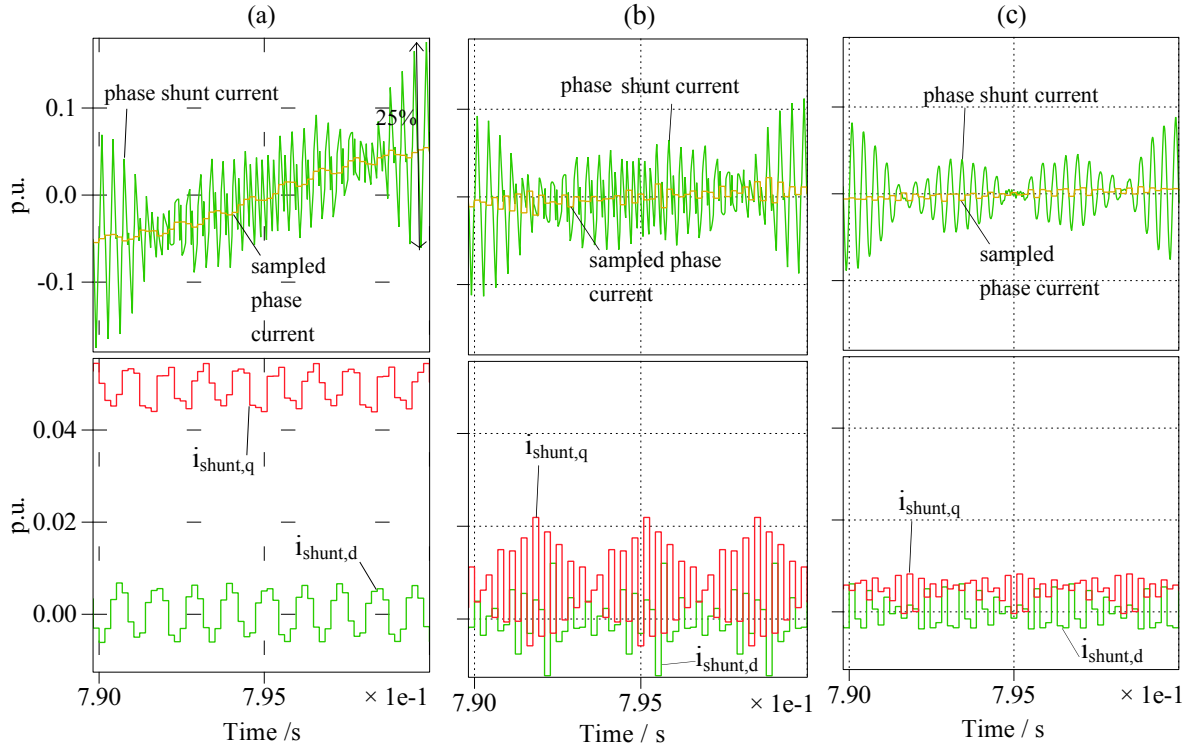
**Figure 3.16:** Simulative analysis of switching frequency ingredient of sampled shunt current (carrier synchronised, asymmetrical PWM) for passively *undamped* filters in steady state for SCR=50 (with active damping)
(a) LCL, (b) Trap measuring complete shunt current, (c) Trap measuring shunt current of trap filter tuned to carrier frequency

### LCL, SCR>50 (stiff grid)

The graphical design results are shown in Fig. 3.10 (b) and 3.11 (b) and the characteristic parameters are listed in Tab. 3.7. As optimal gain factor $K_{AD}$ for the active damping, 0.08 is

**Table 3.7:** Controller and characteristic parameter for LCL filter with active damping, SCR>50

| $K_{PI}$ | $T_{PI}$ | $T_{prefilter}$ | $f_{PLL}$ | $K_{AD}$ |
|---|---|---|---|---|
| $9\dfrac{L_{total}}{A_{res,start}4.5T_{ctrl}}$ | $18.9T_{ctrl}$ | $15T_{ctrl}$ | $40\,Hz$ | $0.083$ |

| $A_{marg}$ | $\varphi_{marg}$ | $A_{marg}^{res}$ | $\varphi_{marg}^{res}$ | $A_{marg}^{res,G_1}$ | $f_{-3dB}$ | $T_{power}$ |
|---|---|---|---|---|---|---|
| $2.4$ | $59°$ | $0.1$ | $91°$ | $1.9$ | $84\,Hz$ | $\approx 20\,ms$ |

found (trial and error in simulation). Independently from this, 0.083 is theoretically found - for a different system- in literature [61]. The feedback shunt current has to be **added** to the reference voltage (also done in [53]). Command and disturbance steps with the PI parameters designed for the passively damped filters (Tab. 3.1) are stable, but contain $\approx 13\,\%$ oscillation with the resonance frequency with decay in several fundamental periods. A decrease of the PI gain improves this. The lower the gain chosen, the more oscillatory the *simulation*. This is in contrast to transfer function analysis. Sampling effects are assumed to be the cause, because the model runs stably (as theoretically predicted) when a non switching model for the converter is

utilised. Therefore, only a slight reduction of the gain (from 0.8 for the passive damping case to $9/A_{\text{res,start}} \approx 0.6$) is adjusted. The time constant is slightly increased resulting in a faster decay of the resonance oscillations. The utilised prefilter prevents overshoots and the excitation of the mentioned oscillations. Nevertheless, they occur for the disturbance response (grid voltage rise) in simulation. The critical PI gain (bringing the control loop to instability) is equal for transfer function analysis and simulation.

The designed active damping stabilizes the current control which is instable without the active damping branch. Nevertheless, it is worthy of discussion, if the oscillations in the step resonse (Fig. 3.10 (b)) are acceptable. For higher SCRs, the oscillation / the resonance is further attenuated (which can be seen in the Bode diagram) and is not that critical.

**Trap, SCR>50 (stiff grid)**

The graphical design results are shown in Fig. 3.13 (b) and the characteristic parameters are listed in Tab. 3.8. The controller parameters remain unchanged compared to the passive damped

Table 3.8: Controller and characteristic parameters for trap filter with active damping, SCR>50

| | $K_{\text{PI}}$ | $T_{\text{PI}}$ | $T_{\text{prefilter}}$ | $f_{\text{PLL}}$ | $K_{\text{AD}}$ | |
|---|---|---|---|---|---|---|
| | $\frac{L_{\text{total}}}{3T_{\text{ctrl}}}$ | $9T_{\text{ctrl}}$ | $9T_{\text{ctrl}}$ | $50\,Hz$ | $0.25$ | |
| $A_{\text{marg}}$ | $\varphi_{\text{marg}}$ | $A_{\text{marg}}^{res}$ | $\varphi_{\text{marg}}^{res}$ | $A_{\text{marg}}^{res,G_1}$ | $f_{-3\text{dB}}$ | $T_{\text{power}}$ |
| $3.09$ | $44°$ | $2.3$ | $-31°$ | $27.8$ | $163\,Hz$ | $\approx 15\,ms$ |

cases. The active damping gain of $K_{\text{AD}} = 0.25$ is found to be optimal. Comparing the OL Bode diagrams of the undamped loop in Fig. 3.13 (a) with the active damped OL in (b), the resonance attenuation introduced by the AD is obvious (the controller parameters remain unchanged). In comparison to the previously designed LCL AD, here practically no oscillations appear.

**LCL, 50>SCR>10 (weak grid)**

The graphical design results are shown in Fig. 3.14 (b), and the characteristic parameters are listed in Tab. 3.9.

The control is already stable without active damping and the passive damping controller parameters (Fig. 3.14 (a)). The active damping with K=0.083 shows simulated worse behaviour than without AD which is visible in Fig. 3.14 (b). Therefore, no active damping is included.

Table 3.9: Controller and characteristic parameters for LCL filter without damping, 50>SCR>10

| | $K_{\text{PI}}$ | $T_{\text{PI}}$ | $T_{\text{prefilter}}$ | $f_{\text{PLL}}$ | |
|---|---|---|---|---|---|
| | $0.66\frac{L_{\text{total}}}{3T_{\text{ctrl}}}$ | $10T_{\text{ctrl}}$ | $24T_{\text{ctrl}}$ | $50\,Hz$ | |
| $A_{\text{marg}}$ | $\varphi_{\text{marg}}$ | $A_{\text{marg}}^{res}$ | $\varphi_{\text{marg}}^{res}$ | $A_{\text{marg}}^{res,G_1}$ | $f_{-3\text{dB}}$ | $T_{\text{power}}$ |
| $1.8$ | $47°$ | $0.02$ | $136°$ | $3.5$ | $88\,Hz$ | $\approx 20\,ms$ |

Only the design for undamped system is fine tuned. Compared to the passive damped parameters in (a), a reduction of the gain by 33% is necessary for robustness (step response etc., not shown). The prefilter prevents overshoot. The PLL dynamic can be increased to 50 Hz. The parameters can be found in Tab. 3.9.

**Trap, 50>SCR>10 (weak grid)**

The graphical design results are shown in Fig. 3.15 (b), and the characteristic parameters are listed in Tab. 3.10. Simulation tests again result in an optimal AD gain of 0.25. The PI design

**Table 3.10:** Controller and characteristic parameter for trap filter with active damping, 50>SCR>10

| $K_{PI}$ | | $T_{PI}$ | $T_{prefilter}$ | $f_{PLL}$ | $K_{AD}$ |
|---|---|---|---|---|---|
| $2.5\frac{L_{total}}{A_{res,start}3T_{ctrl}}$ | | $10T_{ctrl}$ | $18T_{ctrl}$ | $50\,Hz$ | $0.25$ |

| $A_{marg}$ | $\varphi_{marg}$ | $A^{res}_{marg}$ | $\varphi^{res}_{marg}$ | $A^{res,G_1}_{marg}$ | $f_{-3dB}$ | $T_{power}$ |
|---|---|---|---|---|---|---|
| $\approx 2.1$ | $49°$ | $0.4$ | $88°$ | $6.2$ | $79\,Hz$ | $\approx 19\,ms$ |

leveling the resonance to 1 excites an excessively strong overshoot in combination with the PLL. An increase by factor 2.5 solves this problem. The power time constant is below 20 ms. Only for SCR=10, slight oscillations with resonance frequency can be seen in the non-prefiltered step response in Fig. 3.15 (b). These are not seen using the prefilter. Nevertheless, if they are not desired, a lower gain can be chosen (resulting in higher $T_{power}$).

**General Comments**

For the stiff and weak grid trap filter, the designed active damping could replace the passive damping circuits. For the LCL strong grid system, the current AD stabilizes the control, but cannot prevent slight oscillations. For the weak grid system, the designed current AD is not applicable. An adaption of the controller parameters results in a stable design. The influence of the grid voltage which could excite the filter resonance was also analysed by using the previously developed disturbance transfer function. As it resembles the command function for all designed filters, it is only shown for the stiff grid LCL system. The effect of driver deadtime and parasitic properties of all parameters on the active damping is neglected in this design section. This is automatically included in the analysis with the experimental setup (Chap. 5).

## 3.6 Practical Aspects of Current Control

In this work, 8th order Bessel filters are used as signal conditioning filters similar to those shown in [62] p. 322,[63]. Bessel filters have a sharp magnitude decay at their cut-off frequency. In contrast to R-C filters, their phase shift is linear, decreasing to minus infinity. This leads to a frequency independent group delay time, which is easy to compensate with the control.
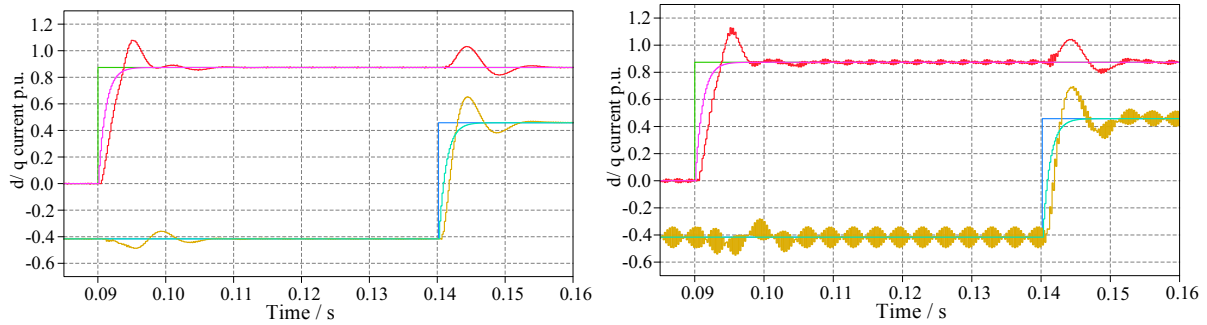
**Figure 3.17:** Example simulation to demonstrate the effect of current anti-alias filter: left: d and q current in p.u. without current signal filtering; right:d and q current in p.u. with Bessel 8th order low pass filtering for current signal (corner frequency 10 kHz) (Trap filters, SCR=50, parallel C-R damping, no active damping, 1 kHz Bessel voltage low pass, $f_{\text{car}} = 2.85\ kHz = 0.5 f_{\text{ctrl}}$)

### 3.6.1 Converter Current Signal Filtering

The converter current is sampled synchronously with the triangular carrier (at the minima and maxima, see for example [62] Fig. 4.4 (c), p. 99). No low pass filter to eliminate the switching ripple is necessary ([45] Chap. 3.1.2). Nevertheless, filters omitting higher frequency noise can be desirable. Simulative analysis including such a filter (Bessel 8th order and also first order with cut-off frequency 10 kHz) in the current path hinders the carrier synchronised sampling to 'mask' the switching ripple ([64] Chap. 9). This can be directly seen looking at Fig. 3.17. On the left the d and q currents of a complete converter control without, on the right, with the filter is shown. A solution could be to further increase the cut-off frequency. In this work no signal filter is implemented for the current control.

### 3.6.2 Voltage Signal Filtering

As mentioned in [65] p.36, the measured (grid) voltage should be low pass filtered due to aliasing problems. No literature regarding this point could be found. Using a control updated twice per switching period (usually the case), the lower sidebands near the carrier frequency are below the Nyquist frequency. In this case unwanted frequency components, not resulting from aliasing, are also present. As is seen in Fig. 3.1, the grid voltage is only utilised in the PLL (for synchronization). In this work, a simple SRF PLL structure is utilised. Its single aim is to detect the fundamental grid angle. From this point, a low pass filtering of the grid voltage is not critical. In contrast, simulative analysis showed that even for the present system it is essential to filter the grid voltage. Without the voltage low pass filter the control proves to be less robust: the critical PI gain (see Chap. 5.6) is significantly lower. This is not analysed further in this work, only the need of a voltage signal filter is found. A cut-off frequency of 1 kHz is found to be a good value. The phase shift at fundamental frequency must then be compensated. This is done by adding the delay angle $\varphi_{\text{delay,bessel}} = 2\pi f_1 / f_{\text{bessel}}$ to the detected angle of the PLL. Fig. 3.18 demonstrates the explained case. No signal filter (a), a Bessel filter with cut-off frequency of $f_{\text{car}} = 2850\ Hz$ (b) and a Bessel filter with cut-off frequency of $f_{\text{car}} = 1000\ Hz$ (c) is plotted. In the bottom plot of (a), the effect of sampling the unfiltered voltages can be seen. As there are

still ripple components in (b), the low pass Bessel filter of 1 kHz seen in (c) is decided as the best filtering option. This effect is independent of the SCR due to the fact that the grid codes define a maximum (SCR independent) voltage distortion (see Chap. 2.2).

In Fig. 3.18 (c), the significant fundamental phase delay introduced by the Bessel filter can be seen. The *compensated* grid angle is also plotted. It can be seen that the maximum of the unfiltered grid voltage (phase a) is met very well by the angle ($2\pi$-switching), even when filtered voltages are utilised (see Chap. 3.4). For a good comparison, the dq voltages of the PLL are shown in the bottom plots. Additionally, it can be seen that using no low pass filter the correct amplitude of the fundamental grid voltage (which is slightly *above* 1 p.u.) is not met. The shown sampling problems are probably also a problem for control methods where the voltage is used as disturbance compensation (direct summation to the converter reference voltage).

Using harmonic current control, for example, with the aim to improve the voltage quality, voltage lowpass filtering can be a disadvantage. Nevertheless, in general the harmonics usually to be compensated are below 1 kHz (5th, 7th ...). More complex PLL techniques must be used in this case. The phase shift of the low pass filter at the desired frequencies would have to be taken into account, too.
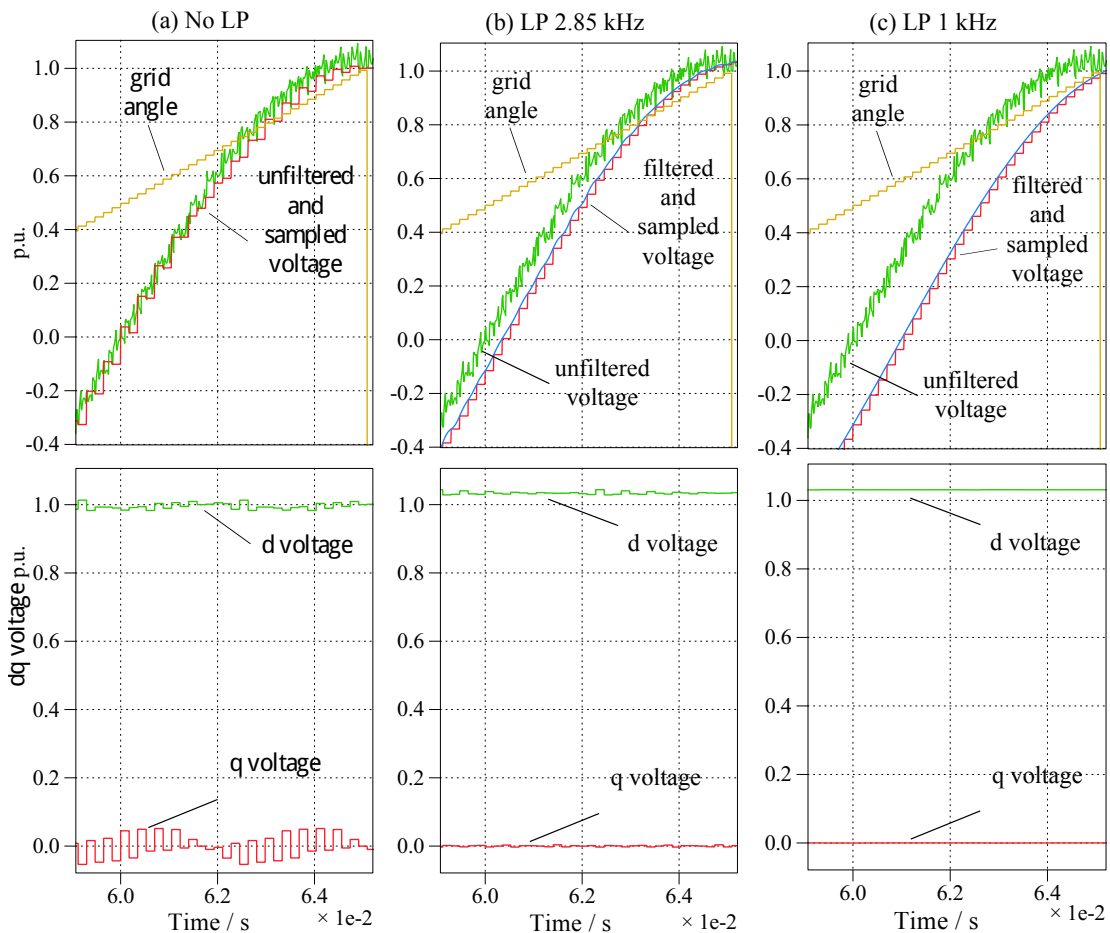


**Figure 3.18:** Comparison of different voltage low pass cut-off frequencies (8th order Bessel filter) and their effect on the dq voltage for grid code compliant voltage distortion. (star voltage phase a at low voltage side of transformer, grid filter type: trap, SCR=50, parallel C-R damping, no active damping, no low pass for current measurement, Nyquist & carrier frequency: 2.85 kHz (asymmetrical PWM))
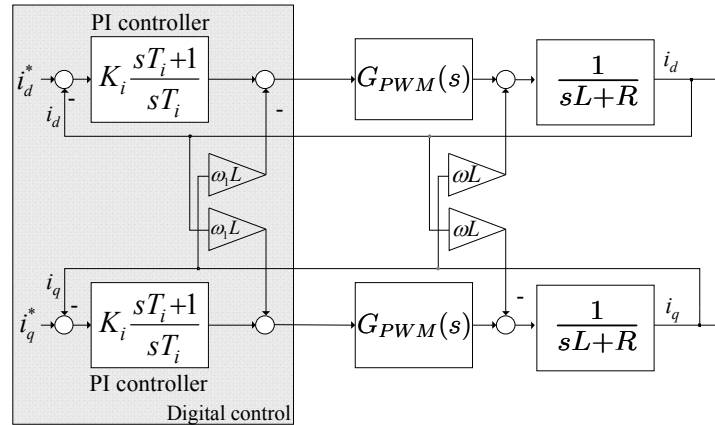
**Figure 3.19:** Standard current control decoupling method assuming a purely inductive plant

### 3.6.3 Grid Voltage Measurement: Line-to-line or Line-to-neutral

The grid voltage can be measured line-to-line or line-to-neutral (for example to the star point of the low voltage side of the transformer). If no zero voltage is needed, only two sensors are necessary, the third voltage can be calculated using the fact that the sum of all voltages is zero. When a line-to-line measurement is utilised, a transformation to star voltages can be performed using Eq. 3.14 (assuming a symmetrical voltage system). This transformation can be performed within the control at control frequency. The line-to-line voltage measurement eliminates the need of the neutral point as measurement point. The line-to-line voltage is $\sqrt{3}$ times higher than the star voltages (approx. 1000 V peak against 600 V). This can be a (cost) argument for a star voltage measurement. In this work, the line-to-line voltage measurement with transformation to star voltages is utilised.

$$u_{a0}(t) = \frac{u_{ab}(t) - u_{ca}(t)}{3}; \quad u_{b0}(t) = \frac{u_{bc}(t) - u_{ab}(t)}{3}; \quad u_{c0}(t) = \frac{u_{ca}(t) - u_{bc}(t)}{3} \tag{3.14}$$

### 3.6.4 Decoupling of Current Control

In general, active and reactive currents cannot be controlled completely independently from each other. The decoupling circuit of the d and q axes in the current control loop improves the decoupled (active and reactive) power control. The following control loop analysis assumes that the d and q axes are perfectly decoupled. In this work, an advanced decoupling approach is implemented. The shunt branches are neglected for decoupling. A standard decoupling method is shown in Fig. 3.19 ([66]). A further developed method for a technical optimum tuned controller assuming so-called multivariate controllers is shown in Fig. 3.20 [67, 68, 69]. This approach is based on a modeling of the dq current control in the complex (space vector) domain. The coupling between the axes can be modeled with the additional imaginary part $j\omega L$. It is proposed to compensate this in the PI controller by adding this imaginary part, resulting in the decoupling scheme in the figure. When the controller is tuned to eliminate the plant time constant $T_{PI} = L/R$ (technical optimum) the adjustment of the factor $K = T_{PI}$ guarantees a good
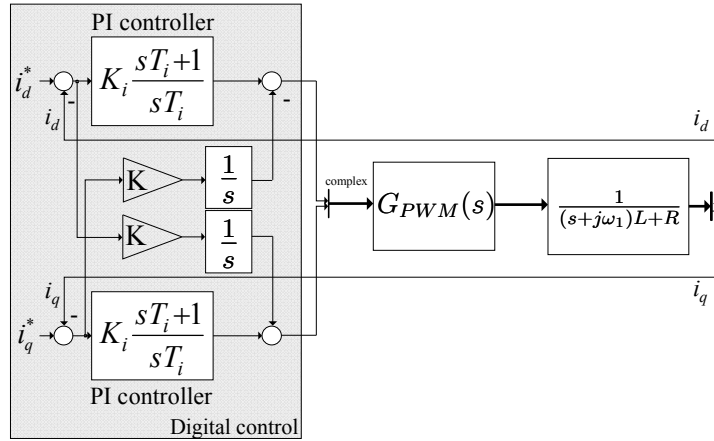
**Figure 3.20:** Decoupling using a multivariate approach

decoupling. This can be understood regarding Eq. 3.15 ($\underline{G}_{\mathrm{PWM}}$ is neglected here).

$$\underline{G}_0(\underline{s}) = K_{\mathrm{PI}} \underbrace{\frac{(\underline{s}T_{\mathrm{PI}} + j\omega_1 K) + 1}{\underline{s}T_{\mathrm{PI}}}}_{Controller} \cdot \underbrace{\frac{1/R}{(\underline{s} + j\omega_1)L/R + 1}}_{Plant} \tag{3.15}$$

$\omega_1$: *actual fundamental grid frequency;* K: *decoupling factor*; $\underline{G}_0$: *Open loop transfer function;* $K_{\mathrm{PI}}, T_{\mathrm{PI}}$: *PI controller parameters; L, R: plant parameters*

In this work, for the present system, it was found that the time constant of the controller has to be set to a much smaller value (see Chap. 3.5.1). Therefore, the presented decoupling approach obviously cannot yield perfect results. Nevertheless, varying factor K an optimum value can be found which decouples the current control much better than the conventional approach.

## 3.6.5 Transformation of DQ Grid Current References to Converter Current References

In normal operation, the active current reference results from the DC link voltage control and the reactive current reference can be set arbitrarily (see for example [66]). Often specific $cos\varphi$ are demanded by the grid operator resulting in correspondent reactive current reference values. It has to be considered that (in this work) the *converter* current (and power) is controlled. Regarding the DC link voltage control, this is the appropriate parameter. Regarding the demanded $cos\varphi$ at the *high* voltage side of the wind turbine transformer, the reference values have to be converted from grid current references. The reactive control will work with transformed current references. Since the active power consumption of the filter and transformer between converter and grid currents is negligible, the DC link voltage resp. active power control is also capable of running with grid current references. So from the control design point of view, it is not necessary to integrate the current reference transformation in this work.

From the filter design point of view, it is necessary: the voltage drop in Chap. 2.8.1 and 2.9.1 was computed assuming rated apparent power of $S_{\mathrm{r}} = 2.22\ MVA$ at $cos\varphi = 0.9$ overexcited at the high voltage side of the transformer. Therefore, for example to validate the accuracy of the filter design, power setpoints at high voltage side of transformer have to be adjustable. The
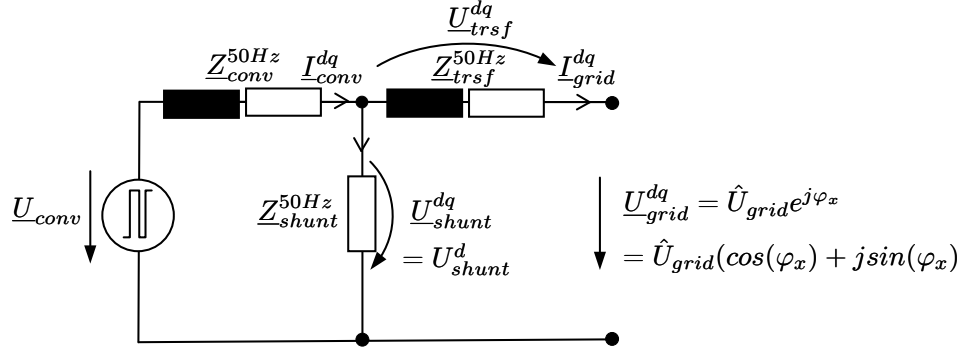
**Figure 3.21:** Schematic for converter current reference calculation with grid current reference in dq frame oriented at shunt voltage

converter current references are calculated according to Fig. 3.21 and Eq. 3.16, Eq. 3.17 and Eq 3.18.

$$\underline{i}_{\text{dq,conv.}}^{ref} = \underline{i}_{\text{dq,grid}}^{ref} + \frac{U_{\text{shunt}}^{d}}{\underline{Z}_{\text{shunt,50Hz}}} = \underline{i}_{\text{dq,grid}}^{ref} + \frac{R_{\text{trsf}}i_{\text{grid,d}}^{ref} - \omega_1 L_{\text{trsf}}i_{\text{grid,q}}^{ref} + \hat{U}_{\text{grid}}cos(\varphi_{x})}{\underline{Z}_{\text{shunt,50Hz}}} \quad (3.16)$$

$$sin(\varphi_{x}) = \frac{R_{\text{trsf}}i_{\text{grid,q}}^{ref} - \omega_1 L_{\text{trsf}}i_{\text{grid,d}}^{ref}}{\hat{U}_{\text{grid}}} \quad (\Im - part\ equation) \quad (3.17)$$

$$cos(\varphi_{x}) = \sqrt{1 - sin^2(\varphi_{x})} \quad (3.18)$$

$\varphi_{x}$: angle of the primary side transformer voltage in the shunt voltage dq frame

Fig. 3.22 shows a case validation for the transformation. The absolute value of the reference grid currents $|\underline{i}_{\text{dq,grid}}^{ref}|$ is easiliy reached by the shown abc grid currents although the converter currents are controlled. It is clear that this transformation needs precise model parameters.
In practice a power control would be probably applied. This control would smooth the converter current references preventing the possibility of evaluating the current control (with step responses). For this reason, the presented reference value transformation is done here, also enabling the possibility for validation of critical power operating points.
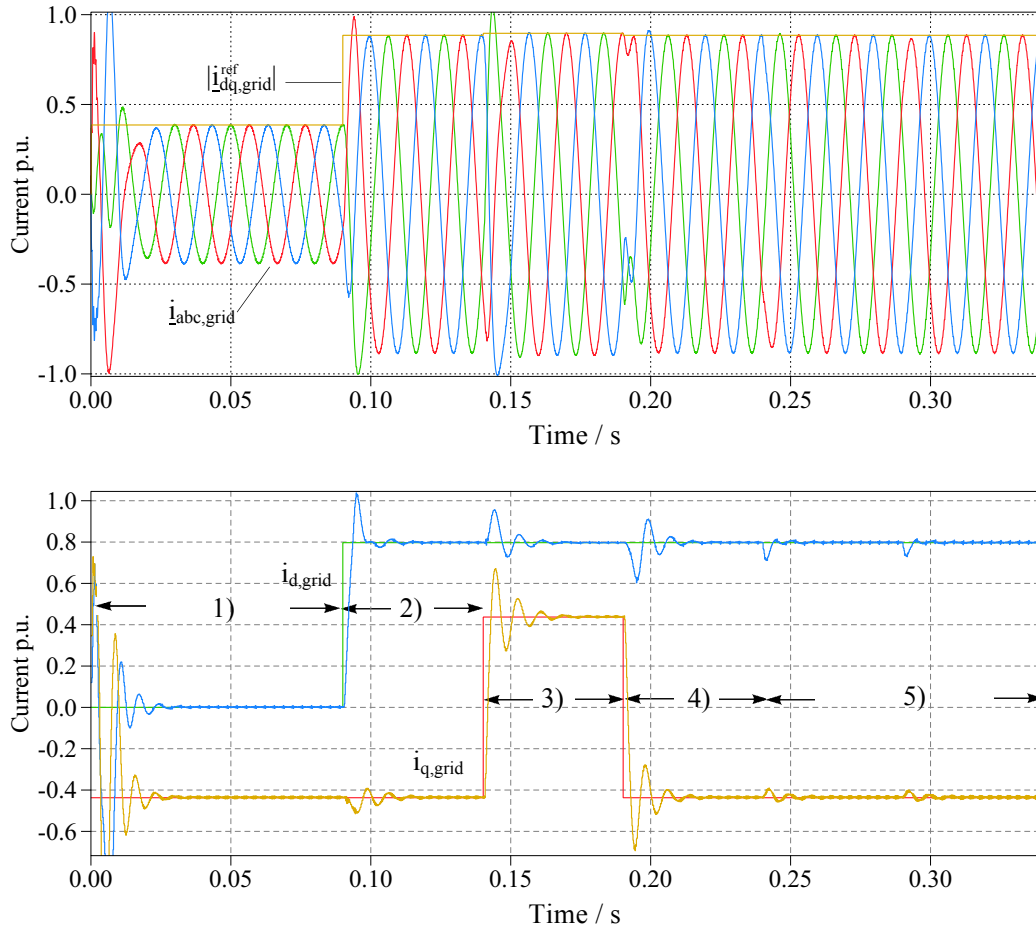
**Figure 3.22:** Case validation of converter current reference transformation at several operating points: 1) only reactive current, 2) $cos\varphi = 0.9$, 3) underexcited, 4) $cos\varphi = 0.9$, 5) t>0.24 s: $S_r$ at $1.1U_r$ at the high voltage side of transformer
(abc currents are unfiltered, grid filter type: trap, SCR=50, parallel C-R damping, no active damping, no current measurement low pass, Nyquist & carrier frequency: 2.85 kHz (asymmetric PWM))

## 3.6.6 Simulative Realisation of 10% Grid Voltage Rise at Primary Side of Transformer

The turbine is forced to stay connected to the grid at $U_{grid,mv} = U_{r,mv}(1 \pm 0.1)$. Considering the simulation, this grid voltage rise is realized by an increase of the (ideal) 50 Hz voltage 'behind' the grid impedance (see Fig. 3.1). Here, it has to be made sure that the grid voltage at the high voltage side of the turbine transformer rises by 10 %. Especially for SCR=10, an increase of the ideal 50 Hz voltage by 10 % would lead at rated turbine operation to a higher transformer voltage rise. This is considered by using Eq. 3.19 for the 50 Hz grid voltage rise. It is added to the 50 Hz voltage, seen in Fig. 3.1.

$$U_{grid50Hz}^{rise} = abs(1.1\frac{Ur}{\sqrt{3}} - \underline{Z}_{grid}\frac{I_r}{1.1}e^{-j\varphi}); \quad \varphi > 0 \tag{3.19}$$

## 3.7 Three-Phase Simulation Results

The control design in Chap. 3.5 also uses three-phase simulation results. These results are shown here for parallel C-R damping. For the other passive damping methods, the control dynamics are similar (compare the step responses in Chap. 3.5). A simulation model in Matlab Simulink Plecs according to Fig. 3.1 is set up for all systems. As previously mentioned, no current signal conditioning is applied, and the grid voltage is low pass filtered with a Bessel filter with a cut-off frequency of 1 kHz. The simulation results are plotted in p.u. values. The control is tested starting from stationary equilibrium commanding active and reactive current steps. The previously mentioned reference prefilters are included. Nevertheless, all controls without a prefilter are also stable according to the step responses in the previous design section. Additionally, the grid voltage rise of 10 % is tested. To validate the MaxCCPPR, the grid voltage is increased even more to bring the converter to its maximum modulation index. The test sequence is equal for all four filters and can be seen in Fig. 3.23.
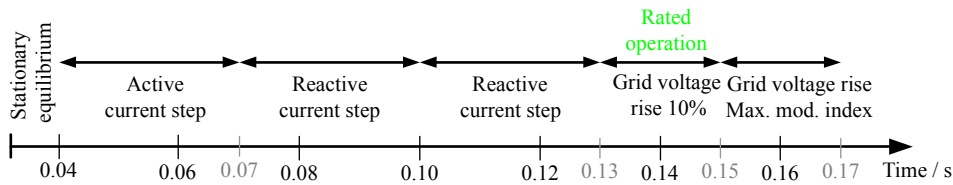


**Figure 3.23:** Test sequence for the simulation results

Below, the plot for LCL SCR=50 (Fig.3.24) is explained in detail. This is omitted for the other plots. Several signals of the simulation are shown. In general, the title of each plot directly explains what can be seen. Here, only additional information is given. In the title of (a), an anti-windup switch is mentioned. This is the output of the antiwind up. If it is one, the control is not in saturation. If it is zero, the anti-windup sets the input of the PI integrator to zero. This is explained in Chap. 3.3. In (b), the grid voltage at the low voltage side of the transformer is plotted. As already mentioned, the voltage is Bessel low pass filtered (Chap. 3.6.2). The unfiltered and filtered voltage is plotted. The fundamental phase delay is clearly seen. The compensated PLL angle according to Chap. 3.6.2 is also shown. Only by graphical analysis, the phase angle being correctly in phase with the unfiltered (green) grid voltage can be validated. For clarity reasons, phase b and c are not plotted. In (c), the dq transformed voltages are seen. It is obvious that the amplitude invariant transformation is used. The 10 % grid voltage rise can be validated at t=0.13 s. In (d), in addition to the reference dq currents the output of the reference prefilter according to Eq. 3.8 is shown. The shown converter current references result from the transformation from grid current reference values, as described in Chap. 3.6.5. They are sampled with the control frequency $1/(2 \cdot 2850) \approx 0.18 \; ms$. For the trap filters, the shunt current in (g) is the current of both trap filters. In (i), the online calculated instantaneous powers and $cos(\varphi)$ are plotted according to Eq. 3.20, 3.21 and 3.22.

$$p(t) = u_{a0}(t)i_a(t) + u_{b0}(t)i_b(t) + u_{c0}(t)i_c(t) \tag{3.20}$$

$$q(t) = \frac{1}{\sqrt{3}}(u_{bc}(t)i_a(t) + u_{ca}(t)i_b(t) + u_{ab}(t)i_c(t)) \tag{3.21}$$
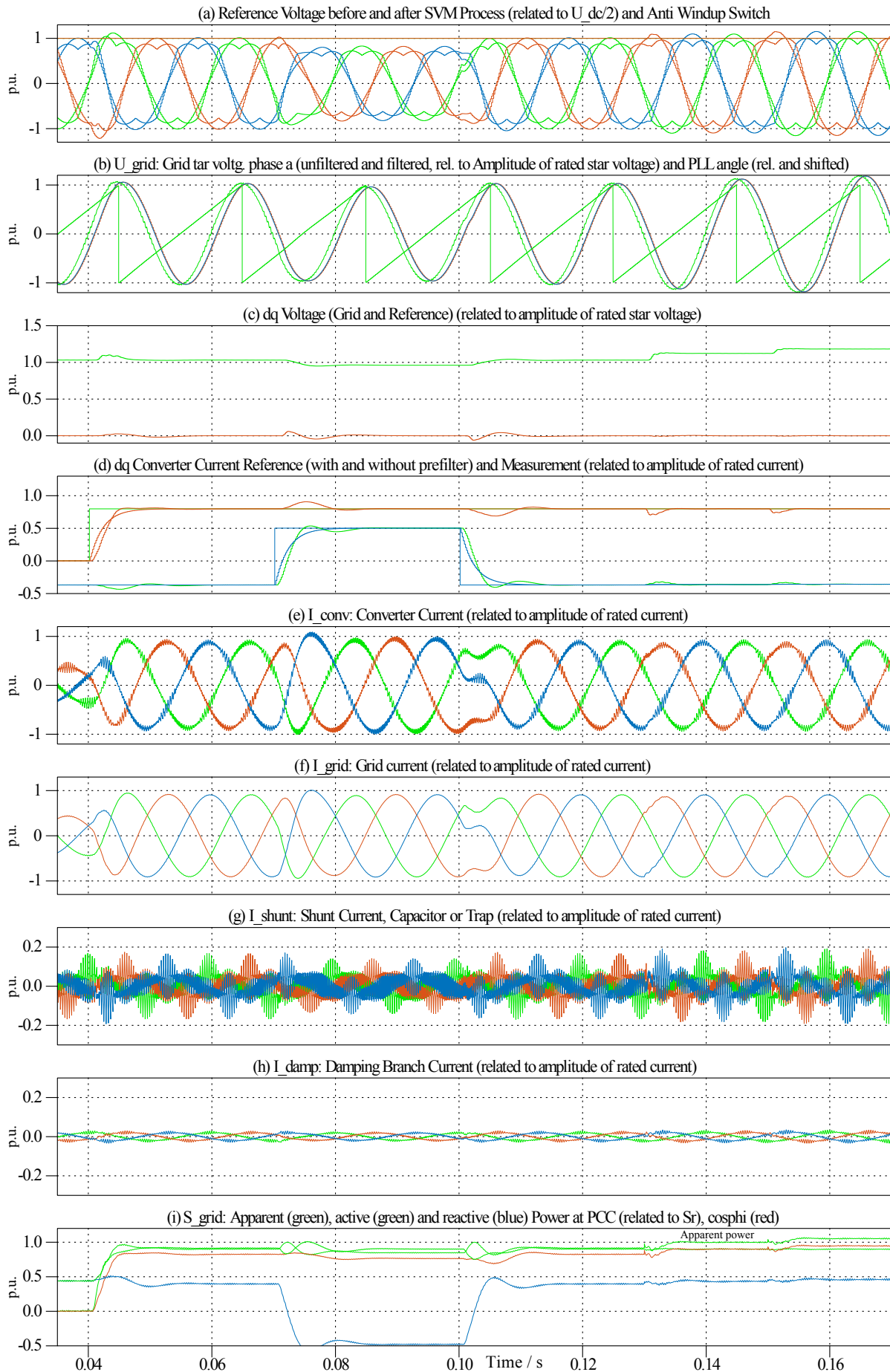
**Figure 3.24:** Simulation of strong grid LCL filter with parallel C-R damping method including reference prefilter SCR=50; $\hat{I}_r = 2628\,A$; $\hat{U}_r^\star = 563\,V$ (for all base values see Tab. 2.2)

$$s(t) = \sqrt{p^2(t) + q^2(t)}; \quad cos(\varphi)(t) = p(t)/s(t) \tag{3.22}$$

### 3.7.1 LCL, SCR>50 (Stiff Grid)

The grid currents in (f) have no visible 'ripple' component. The dq current step responses resemble the transfer function responses in Fig. 3.10 (d). The reactive current step has a slight undershoot in contrast to the active current step response. Especially with the reactive step, dq couplings are present. At t=0.13 s, the reaction of the control to a grid voltage rise of 10% is tested. It can be seen that the response resembles the one of the disturbance response shown in Fig. 3.11 (d). From t=0.13 s to t=0.15 s, the system is additionally at rated apparent power with $cos(\varphi) = 0.9$ overexcited (see (i)). The control handles this operating point without problems. The designed DC voltage enables the operation below modulation index 1 which can be seen in (a). Nevertheless, SVM is necessary, as the sinusoidal reference is already above one.

To validate the designed worst case converter current ripple, the grid voltage is further increased. The maximal ripple appears for the highest modulation index [33]. This can be validated graphically at t>0.15 s. Most of the ripple part of the converter current is trapped by the capacitance current in (g). It can be seen that here the highest current ripple appears with approximately 25 % which is the designed MaxCCppR.

In Chap. 3.5.3, the time constant for the power is introduced. This is obtained by graphical analysis of the simulation results. All three simulated current steps are analysed, and the highest value is taken as $T_{\text{power}}$. For the present strong grid LCL results, $T_{\text{power}}$ is found to be 18 ms which can be validated with Fig. 3.24 (i).

### 3.7.2 Trap, SCR>50 (Stiff Grid)

The results can be found in Fig. 3.25. For the active current step, the control is shortly in saturation which can be seen at the anti-windup switch in (a). This is not critical for the step response seen in (d). Compared to the stiff grid LCL system, the control dynamics are not changed significantly. The step response from the transfer function analysis in Fig. 3.13 (d) is met very well for active as well as for reactive current steps. The dq couplings are decreased. Compared with the stiff grid LCL filter the fundamental current consumption of the shunt branches (g) and (h) is significantly reduced due to lower capacitances in the shunt path.

### 3.7.3 LCL, 50>SCR>10 (Weak Grid)

The results can be found in Fig. 3.26. Compared to the stiff grid LCL system, the modulation index significantly decreases for the positive reactive current at t=0.08 s. This is clearly the effect of the higher grid impedance. Additionally, a significantly increased fundamental current consumption can be seen in (g) and (h). This is the result of the increased filter capacitance
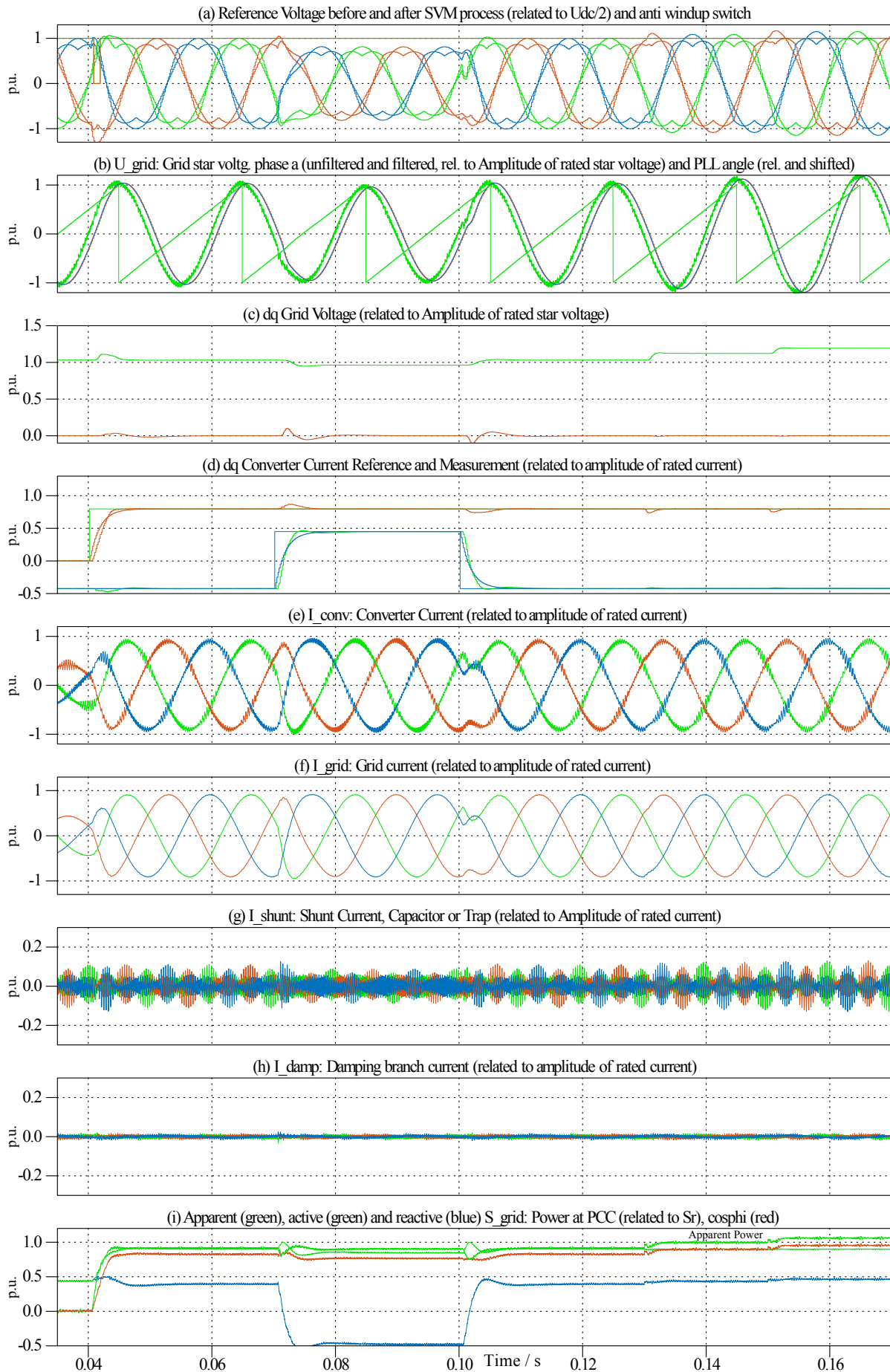
**Figure 3.25:** Simulation of strong grid trap filter with parallel C-R damping method including prefilter SCR=50, $\hat{I}_r = 2628\ A$; $\hat{U}_r^\star = 563\ V$ (for all base values see Tab. 2.2)

**Figure 3.26:** Simulation of weak grid LCL filter with parallel C-R damping method including prefilter SCR=10, $\hat{I}_r = 2628\ A$; $\hat{U}_r^\star = 563\ V$ (for all base values see Tab. 2.2)

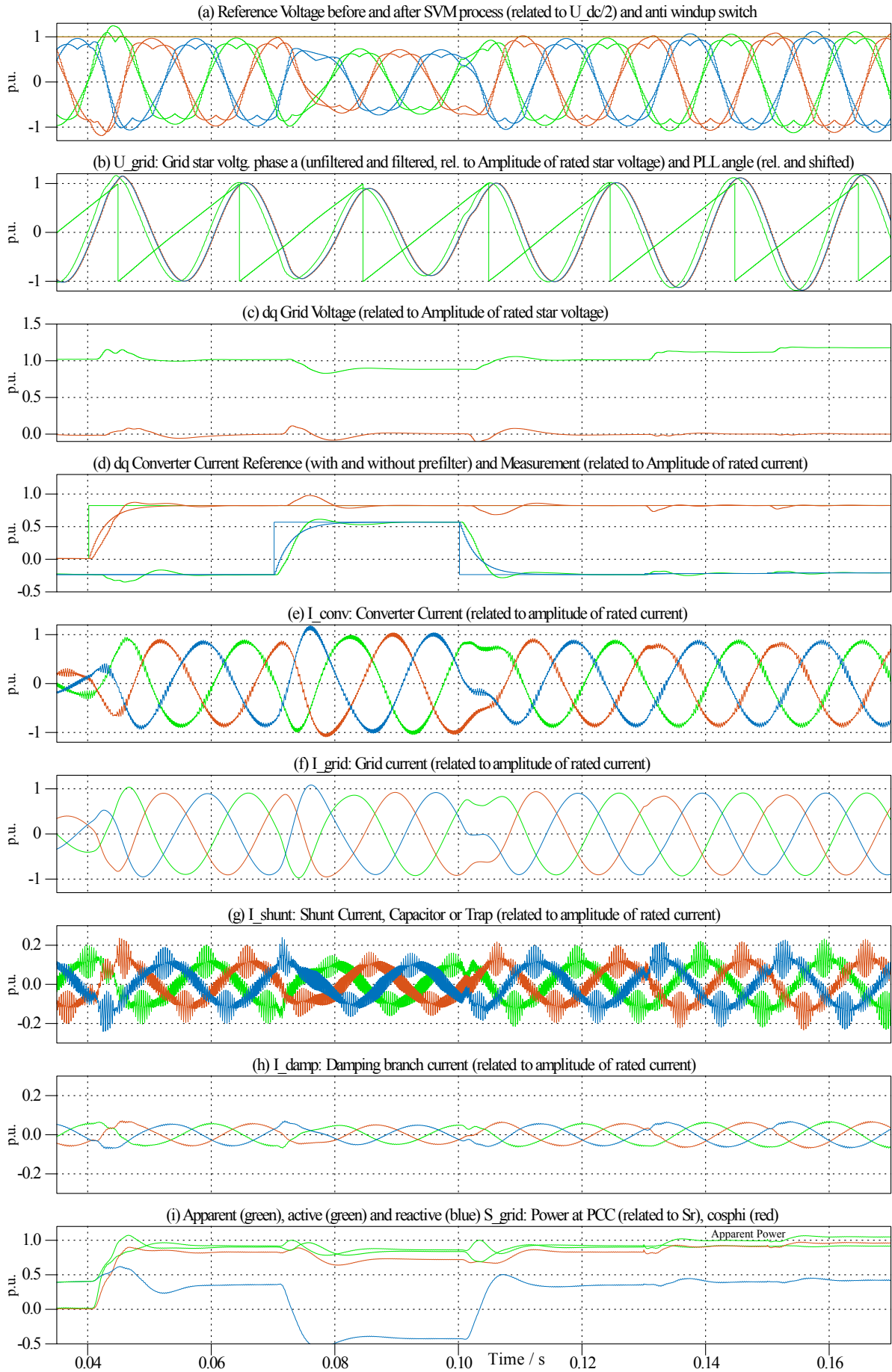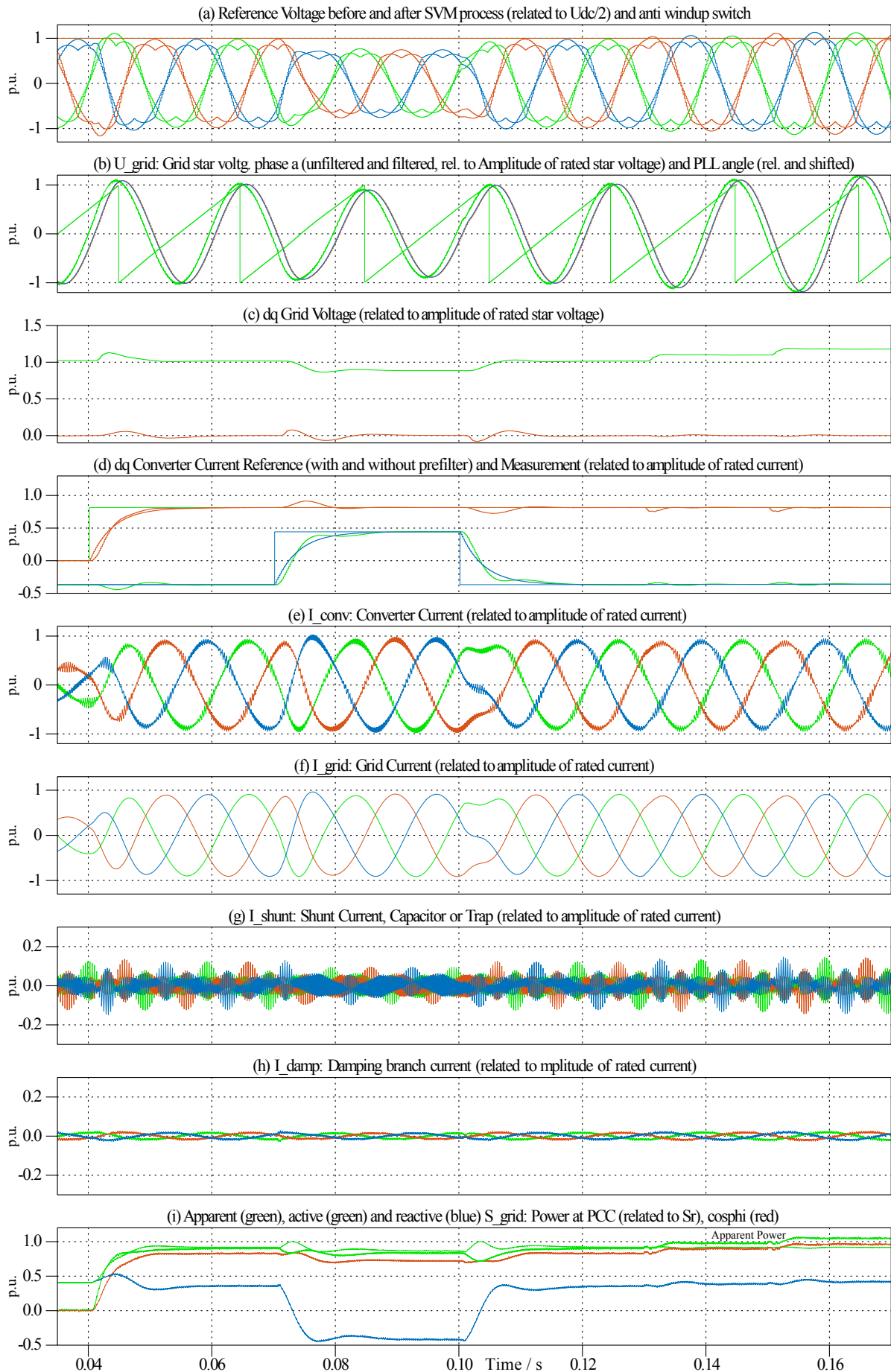**Figure 3.27:** Simulation of weak grid trap filter with parallel C-R damping method including prefilter SCR=10, $\hat{I}_r = 2628\ A$; $\hat{U}_r^\star = 563\ V$ (for all base values see Tab. 2.2)

of 11.2 % and the damping capacitance of 5.6 % (see Tab. 2.7). The designed step response according to Fig. 3.14 (d) is met well.

### 3.7.4  Trap, 50>SCR>10 (Weak Grid)

The results can be found in Fig. 3.27. Again, compared to the LCL filter system, the fundamental shunt current consumption is significantly lower. The step responses are met well (Fig. 3.15 (d)).
All four filter designs in combination with their current control are designed and validated by simulation. In the next chapter, their robustness against grids including resonances is validated. Before, the main findings of this chapter are summarised.

## 3.8  Summary of Main Findings

- The single loop, continuous frequency domain model of the current control is a precise instrument to predict and analyse the three-phase switching system.

- For the synchronised converter current sampling method, analog low pass filters must have a very high cut-off frequency.

- It is advantageous to low pass filter the grid voltage (at the low voltage side of the transformer) to avoid switching frequency components. This should be done for double update control with corner frequencies clearly below the Nyquist/carrier frequency (here with $0.35 f_{\text{Nyquist}}$).

- As standard PI start design, the Symmetrical Optimum method proved to be the most appropriate (and not the Technical Optimum). In the next step, this start design must be fine tuned with regards to the resonances of the plant.

- For the weak grid SCR=10, the control design must be done together with the dynamic of the PLL.

- As an active damping method, the designed proportional feedforward of the shunt current stabilizes the (passively) undamped systems. The described aliasing problems, when sampling the shunt current, do not carry significant weight.

# 4 Grid Resonance and Converter Control

## 4.1 Overview

Below, the robustness of the previously designed filters and controls is analysed with respect to a grid with capacitive elements leading to resonances. Generally, it could be assumed that these grid resonances[1)] are damped by a resistance that increases with frequency due to the skin effect, thus not being critical for stability. This is disproved in the first part of this chapter by comparing several skin effect models for grids and the turbine transformer. In the next step, a simple model for a grid impedance including a resonance (LCL-type) is developed. Finally, the transfer function stability analysis is performed and validated with three-phase simulations. In the last step, current controls that are robust regarding the grid resonance are designed.

## 4.2 Skin Effect for Grid Components

### 4.2.1 Grid Impedance

On the right hand side in Fig. 4.1, a simple high frequency model of the grid impedance is shown. In this section only the factor which changes the resistance $R(f)$ is analysed. The higher the frequency, the more the current tends to flow near the surface of the conductor [70]. This effect, the skin effect, leads to higher equivalent resistances. It also leads to decreasing inductances of the conductor at higher frequencies [70]. This is neglected here, due to the fact that it only shifts the resonance frequency, but does not significantly change the characteristics of the grid impedance. Besides precise modeling of the skin effect (by Bessel functions [71]), transmission system operators use approximations by means of correction factors to the fundamental resistance [72]. Eq. 4.1 presents a general correction factor for overhead lines and Eq. 4.2 for
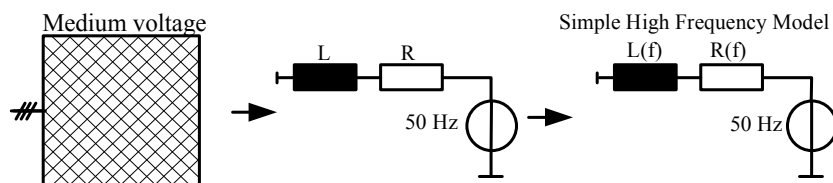


**Figure 4.1:** Frequency dependent L-R model of the grid impedance

---

[1)] In this chapter, the term 'grid resonance' is utilised for simplicity reasons. Strictly speaking, this is not exact. Grid resonance means a grid impedance including capacitive and inductive elements leading to a resonance.
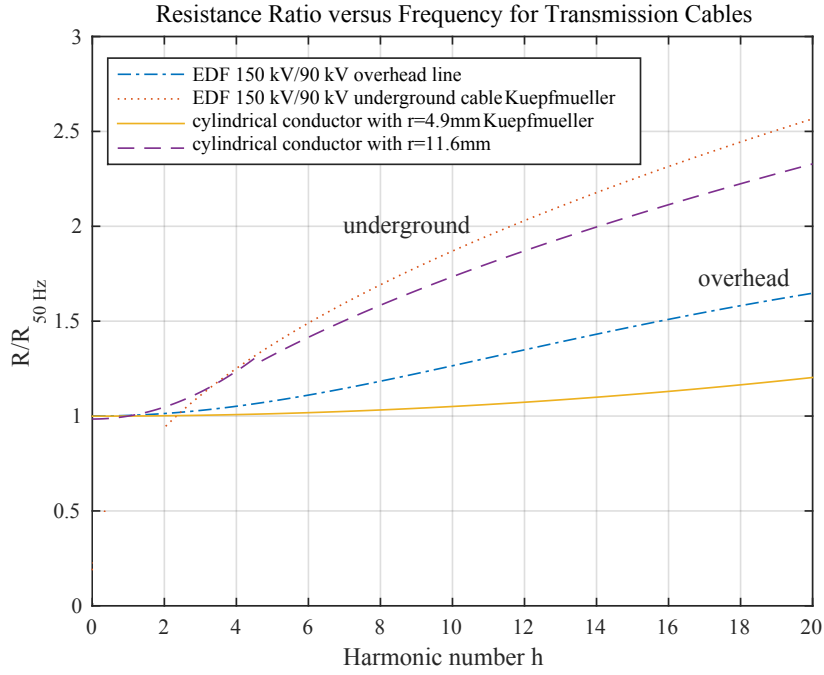
**Figure 4.2:** Skin resistance correction factors

underground cables in the high voltage domain ([72], source: EDF, the French transmission system operator).

$$R_{\text{overhead}}^{EDF} = R_1\left(1 + \frac{0.646h^2}{192 + 0.518h^2}\right) \tag{4.1}$$

$$R_{\text{underground}}^{EDF} = R_1(0.187 + 0.532\sqrt{h}); \ h \geq 2 \tag{4.2}$$

$h$: harmonic number; $R_1$: ohmic resistance at fundamental frequency

According to [70], the skin effect on the resistance of a cylindrical conductor can be approximated using Eq. 4.3.

$$R = R_{\text{DC}} \cdot \begin{cases} \left(1 + \frac{1}{3}x^4\right) & x < 1 \\ \left(\frac{1}{4} + x + \frac{3}{64x}\right) & x > 1 \end{cases}; \quad x = \frac{r}{2}\sqrt{\pi f \kappa \mu} \tag{4.3}$$

$r$ - radius of conductor; $\kappa$ - conductor conductivity; $\mu$ - permeability

Most of the medium voltage cables have aluminium cores [73]. Therefore the following data is taken ($\kappa_{\text{Al}} = 33 \cdot 10^6 \ S/m$, $\mu_{\text{Al}} = \mu_0\mu_r = 4\pi \cdot 10^{-7} \ Vs/Am$, $r_{\text{conductor}}^{33kV} = 4.9 \ mm...11.6 \ mm$ [74]). In Fig. 4.2, these approximation methods are plotted up to 1 kHz (h=20). It can be seen that the increase of resistance for overhead lines is less than for underground cables. The resistance for common conductor sizes in the medium voltage range [73] is in a similar range. As highest resistance increase, the EDF underground cable equation is found. At 1 kHz, the fundamental frequency resistance is increased by the factor of 2.5.

In Chap. 4.3, it is shown that an increase in this range is not high enough to level possible grid resonances. Additionally, it is assumed that -for the present analysis- it is not important to model the frequency dependency of the resistance. The 50 Hz resistance will be used. For specific
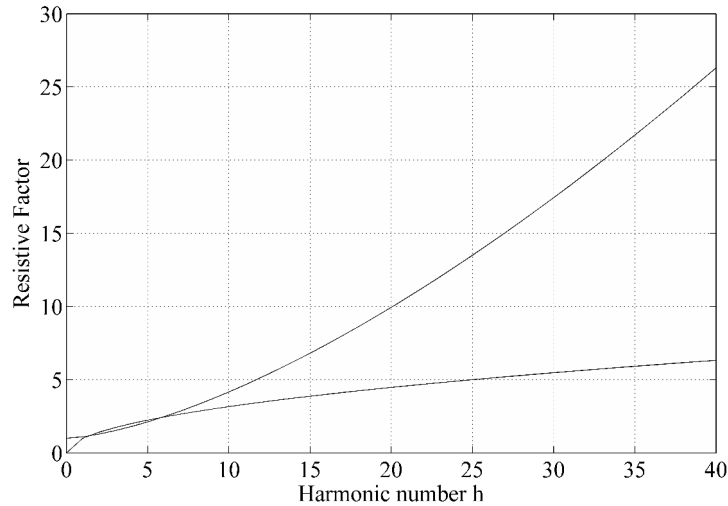
**Figure 4.3:** Resistive factor of two approximation methods

cases, it will be analysed, if the increase by an appropriate factor has a stabilizing effect.

## 4.2.2 Transformer

Higher frequency transformer models can be arbitrarily complex. Considering possible grid resonances, it is important to see how they can be damped by an increased ohmic resistance of the transformer. Therefore, a higher frequency model of the series resistance is analysed. The IEEE Standard 399 [75] recommends $R = R_{\mathrm{DC}}(1 + 0.1h^{1.5})$, while [72] proposes $R_1\sqrt{h}$. Both factors are plotted in Fig. 4.3. The models differ significantly especially for the higher frequency range. As seen later the interesting grid resonances are near 1 kHz. According to the models here an increased fundamental resistance by factor 5-10 seems to be realistic. As for the grid model, first (as worst case) the fundamental frequency resistance is taken for the complete frequency range. Later, regarding specific grids, the influence of an increased resistance due to the skin effect is discussed.

## 4.3 Grid Impedance with Resonance

Resonances in the electrical grid, especially in grids with renewable energy sources, are analysed in several power engineering publications. Due to the fact that this topic is not common for power electronics engineers, a short overview is given below. It has to be stated that impedance analysis in publications is mostly based on computer simulation and not on measurements.
In [76, 77] Bode plots demonstrate the time dependence of resonances. A related IEEE working group summarises similar results in several publications [78]. CIGRE working groups are dealing with this topic [79]. Specific resonance problems and hardware solutions (trap filters, active filters) for a wind park are documented for example in [80] and in [81]. Examples for varying resonances are documented in [82]. Analysis especially for a wind park is done in [83]. In [51] Chap. 7.1.1, the higher frequency grid impedance is measured and emulated by
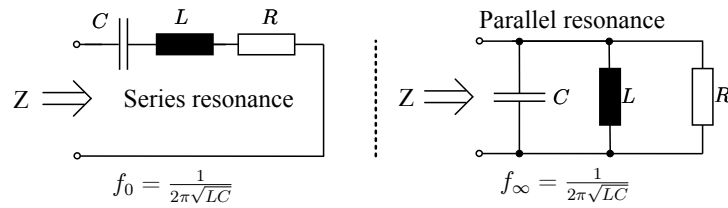
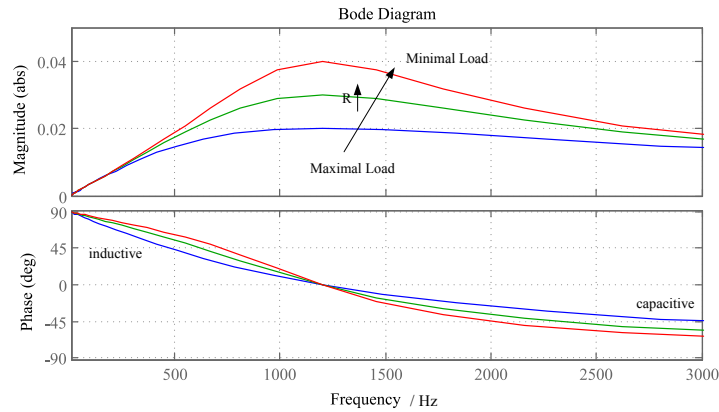**Figure 4.4:** L-R-C circuit for modeling grid impedance resonance



**Figure 4.5:** Bode plot of grid impedance for different load conditions (parallel resonance)

interpolation with electric components. Power engineering books are dedicated to this issue addressing on the one hand resonances caused by power factor correction capacitances (PFCC) [84, 72, 18] and on the other hand by cable capacitances [85, 86]. PFCC are often switchable, leading to abruptly changing grid impedance resonances [17, 72]. When PFCC are implemented, care is taken that possible series or parallel resonant circuits do not have resonance frequencies at harmonic frequencies of the fundamental. To make the resonance frequency more independent from the actual grid situation, often an inductance is implemented in series to the PFFC [86]. In this work the general model of a grid resonance including a PFCC without inductance is analysed.

## 4.3.1  Series and Parallel Resonance

In power engineering, resonance phenomena in grids are separated in series and parallel resonances [17]. A series resonance leads to a decrease, a parallel resonance to an increase of the grid impedance at resonance frequency. The series or parallel resonance can be modeled as a series or parallel R-L-C circuit having the same resonance frequency (Fig. 4.4). For example, the modeling of a grid impedance as shown in [77, 76, 78] can be done using an L-R-C parallel circuit. The load-varying characteristic can then be reproduced by varying the parameters. Setting the resonance frequency to 1.2 kHz and varying the resistance leads to the Bode plot shown in Fig. 4.5. It can be seen that in the lower frequency domain below the resonance frequency the impedance has an inductive characteristic ($\varphi$ near 90°). Crossing the resonance frequency, a capacitive characteristic is observed. As a consequence from the grid layout, series and parallel resonances appear at the same time [84]. Therefore, the analysis here is performed for a grid impedance including a series and a parallel resonance.

A specific resonance analysis including data is given in [72] p.145. The reactive power of a
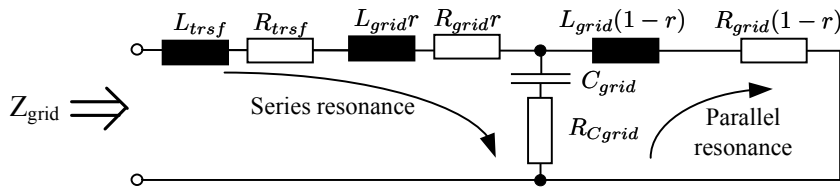
**Figure 4.6:** Grid impedance utilised for analysis (including parallel and series resonance)

six-pulse rectifier of an iron-sand mining plant on a long cable is compensated by a PFCC. The following development of the grid impedance including resonances is based on this example.


## 4.3.2 Resonance with Power Factor Correction Capacitor


A medium voltage grid including a single resonance resulting in an LCL type grid impedance (Fig. 4.6) is analysed. The capacitance $C_{\mathrm{grid}}$ is assumed to represent a PFCC. Both LCL inductances represent the grid's inductance resulting from cables, overhead lines, transformers etc.. By splitting the grid inductances into one part before the PFCC ($rL_{\mathrm{grid}}$) and one behind ($(1-r)L_{\mathrm{grid}}$), a distance between the turbine and the PFCC shall be emulated. The PFCC rating is chosen in a range typical for medium voltage grids (0.05-15 MVAr) [41] p.111 [72]. Experience shows that very low capacitances, which are not usual for PFCC, can also lead to problems. In this case, it should be interpreted that $C_{\mathrm{grid}}$ rather models a cable capacitance rather than a PFCC. As mentioned in [41] p.111, the X/R ratio of PFC capacitor banks is in the order of 5000. As a simplification for the following stability analysis, the PFCC is considered without resistive parts. For simulation the mentioned X/R ratio is taken for a series resistance $R_{\mathrm{Cgrid}}$. No parallel resistances are considered.

The developed LCL type grid impedance contains a series and parallel resonance, as is shown in Fig. 4.6. Fig. 4.7 shows the Bode plot of the grid impedance at the low-voltage side of the transformer varying the different parameters. In (a), the distance factor r, in (b) the short circuit power of the grid, in (c) the size of the PFCC and in (d) the X/R ratio of the inductances is varied. It can be seen that (a)-(c) are possible parameters to change the resonance frequency while particularly (c) also has an influence on the maximum point of the impedance. With the X/R ratio the resonance can be damped.


# 4.4 Stability Analysis Regarding Grid Resonances


## 4.4.1 Literature Review


The stability of decentralised energy sources regarding grid impedances going beyond the simple R-L model is a topic of great actuality. Most of the publications analyse full-sized converter systems [87, 22, 88, 89]. Stability problems (and solutions) in a wind park originating from grid resonances are documented in an early publication with industrial background [37, 38]. An equivalencing method from power engineering according to [90] is utilised for
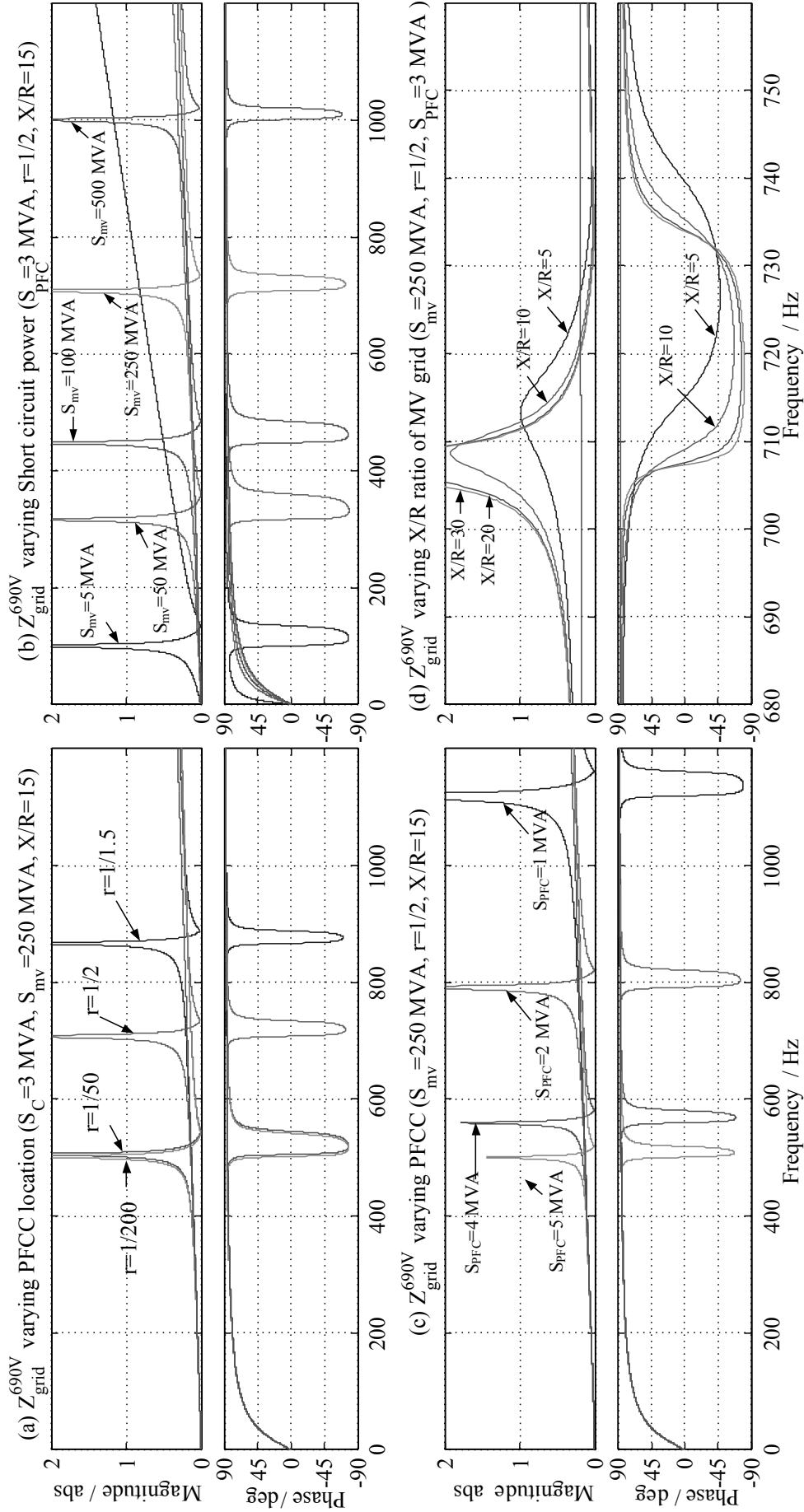
**Figure 4.7:** Variation of different parameters of the grid impedance including resonance (including the transformer impedance)

the wind park collector system to obtain an equivalent grid impedance. It is not clear if this method is applicable to gain a concentrated model for a windpark for a single turbine control stability analysis. The current control of the other turbines is not included. The same author holds a patent regarding the topic [22]. A dq current control is improved to withstand grid impedance resonances by introducing a digital notch filter which is tuned according to the grid resonance frequency. Unfortunately, no analysis regarding the controller parameters is provided. Additionally, no current control parameters are given. In [88], this approach is also applied and further developed with an adaption of the grid resonance frequency. [89] extends the analysis to two grid-connected converters using impedance models. As rather high switching frequencies are chosen (20 kHz), the analysis rather corresponds to solar converters. Solar converters with grid resonances, resp. high harmonic currents, are analysed in [91]. In a more recent publication, [87] proposes a lead lag compensator with current input to handle grid resonances while the converter filter is one inductor. This is comparable to [52] where a lead lag filtering of the voltage is used for LCL filter stabilisation. It is mentioned that the introduction of this element is the alternative to an adaption of the current control parameter. This, however, seems not to be an option, because its bandwidth is not allowed to be changed. In this chapter, it is shown that adapted control parameters can stabilise the control regarding grid resonances with a sufficient control bandwidth. Grid resonance problems have also been a topic in railway applications [92]. Specific problems concerning resonances in the grid of a railway tunnel are documented in [93]. In recent literature, more and more impedance-based methods for stability analysis were proposed. Regarding the railway grids, an impedance criterion called ESCARV (similar to the Nyquist criterion) for the impedance of (single-phase) controlled train converters has been established [94]. Based on a stability criterion of Middlebrook [95], an impedance-based stability criterion for three-phase grid-connected converters is proposed in [96] and applied in [97]. This approach originates from the power engineering side. Controlled grid connected converters are relatively new grid participants still with a lack of appropriate models (for example for harmonic analysis). The mentioned publication is a contribution to this problem. Additionally, the PLL dynamic is included resulting in complex equations. [98] also includes the PLL in the analysis regarding two different dq frames: one of the control (as a result of the PLL) and one of the real grid.

In the present work, the stability analysis is performed from the wind turbine's point of view. A classical current control loop analysis is performed. It will be seen that the simple dq frame current control loops neglecting couplings or PLL dynamics is sufficient to predict instabilities and enable a better controller design.

Generally, there exist two points of view. Firstly, the problem is how to prevent high harmonics in the resonant grid which are critical for all components? This question arises mainly for the grid operator respectively power engineering side. Solutions can be the placement of trap filters tuned to the desired frequencies in the grid [81] or converter-based elements like a Statcom [99],[80]. Secondly, the question for the turbine control design engineer is how a stable control can be designed in the face of a grid resonance. This is the question which is answered in this thesis.

Regarding the state of the art of the literature, the next step is to combine the theoretical analysis which is mostly performed for the low power laboratory systems with the intended high power wind turbine analysis. This is carried out in this work, as all theoretical analysis is performed for the designed 2 MW system. Only the experimental validation is done in the low power domain. The important differences between the two domains are identified. Against the usual praxis, all data is provided.

It seems that often complex approaches are analysed and developed without starting with a

simple configuration. In this thesis, a basic system was defined, using the simplest current control and PLL. At the beginning, it was expected that the limitations of this approach would be seen during the analysis. This was not the case. In the end, a stable operation could be reached, with this simple control structure, even for extremely weak grids containing grid resonances.

An novelty of this thesis is to consider a general grid impedance including resonances. In this way, the stability respective instability regarding changing resonance frequencies and dampings can be validated. Additionally, stability critical grid resonances can be identified.

In previous publications [100, 101], current control methods with grid voltage feedforward (GVFF) were also analysed. The analysis in Chap. 3.6.2 showed that the grid voltage with a grid-compliant filter can only be measured using (analog) low pass filters. Low pass filters in a possible GVFF feedforward path deteriorate the GVFF significantly. Due to the fact that a stable high performance current control can be designed for all grid situations without GVFF, the GVFF is not considered in this work.

Even if deciding that a simple control loop stability analysis is the best choice, there exist many criteria and tools [54]. For the current control fine tuning in Chap. 3.5.3, the Nyquist criterion with Bode plots was utilised. A method which can more easiliy be automated is to check whether the closed loop poles are in the left s half plane. Below, the pole computation is utilised. For specific cases, their Bode plots are shown.

## 4.4.2 Closed Loop Pole Analysis

For computing the poles of the continuous closed loop a precise linear approximation of the exponential digital control emulator (Eq. 3.10) is needed. The second order Padé approximation shown in Eq. 4.4 is utilised leading to a significant increase in precision compared to a simple first order representation ([57],[102] p. 34f.).

$$\underline{G}_{\mathrm{PWM}}(\underline{s}) = e^{-\underline{s}T_{\mathrm{ctrl}}} \cdot \frac{1 - e^{-\underline{s}T_{\mathrm{ctrl}}}}{\underline{s}T_{\mathrm{ctrl}}} \underbrace{\approx}_{e^{-\underline{s}T_{\mathrm{ctrl}}} \approx \frac{12 - 6T_{\mathrm{ctrl}}\underline{s} + T_{\mathrm{ctrl}}^2\underline{s}^2}{12 + 6T_{\mathrm{ctrl}}\underline{s} + T_{\mathrm{ctrl}}^2\underline{s}^2}} 12\frac{12 - 6T_{\mathrm{ctrl}}\underline{s} + T_{\mathrm{ctrl}}^2\underline{s}^2}{(12 + 6T_{\mathrm{ctrl}}\underline{s} + T_{\mathrm{ctrl}}^2\underline{s}^2)^2} \tag{4.4}$$

An analytical closed loop pole computation where the grid resonance parameters are symbolic values would be the best solution. In this way, for all poles the real part could be analysed in dependance of the grid parameters. Unfortunately this analytical equation is not solvable with standard mathematic software. Due to this fact the real parts of the poles are analysed numerically for a wide range of grid resonances and shown below.

The stability of the *closed* current control loop according to Fig. 4.8 is analysed regarding a possible resonance within the grid. For the analysed grid resonance in Fig. 4.6, four parameters are varied: the location factor $r$, the short circuit power of the grid $S_{\mathrm{grid}}$ (leading to a specific SCR), the grid capacitance $C_{\mathrm{grid}}$ (resp. the reactive power of the capacitance $S_{\mathrm{Cgrid}}$) and the X/R ratio of the grid inductances. The transformer leakage impedance is always kept at 6 %. The parameter intervals are summarised in Tab. 4.1. As explained in Chap. 2.5 the short circuit power ratio SCR distinguishes between a stiff and weak grid. The grid capacitance is calculated
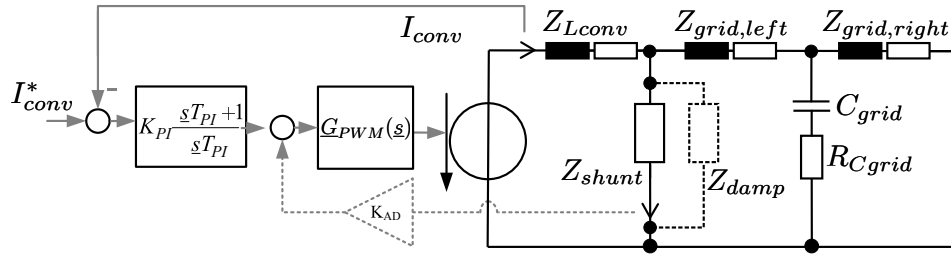
**Figure 4.8:** Control loop for analysis. $Z_{\text{shunt}}$ can be the capacitor or trap filter.

**Table 4.1:** Search intervals of grid resonance

|  | Stiff Grid | Weak Grid |
|---|---|---|
| SCR | 10-49.9 | 50-500 |
| X/R | 30 | 30 |
| $S_{\text{Cgrid}}$ / MVAr | 0.05-15 | 0.05-15 |
| $R_{\text{Cgrid}}$ / % | 0 | 0 |
| r | 0-0.99 | 0-0.99 |

from its reactive power with Eq. 4.5.

$$C_{\text{grid}} = \frac{S_{\text{Cgrid}}}{2\pi 50 U_{1-1}^2} \tag{4.5}$$

### 4.4.3 Descriptive Case Analysis

In Fig. 4.9, an exemplary analysis for the strong grid LCL filter is shown. In the first row the location factor r, in the second the SCR, in the third the grid capacitance $C_{\text{grid}}$ (resulting from the reactive power $S_{\text{Cgrid}}$ of the capacitance) and in the fourth the X/R ratio is varied. For all step and Bode analyses, also the present, the exponential description of $G_{\text{PWM}}$ is utilised. For the pole zero map, Eq. 4.4 is used. The pole zero map is reduced to the positive complex half plane. All poles and zeros which are not on the real axis have conjugate complex equivalents. For a direct link to the Bode diagram, the axes' units are set to Hertz and not to rad/s. The readability is additionnally improved using a logarithmic x axis scale. The frequency range is limited to frequencies near the Nyquist frequency of approximately 2.85 kHz. By doing so one pole for all pole zero maps at $s \approx -4.4 \; kHz$ is not shown. Additionally, a pole zero pair for r=0.99 (in the first row) at $s/2/\pi = -0.85 + j6309 \; Hz$ is omitted.

 **Analysis of the effects introduced by the grid resonance.** This analysis is done with the last row (d). An SCR of 50, a grid capacitance reactive power of 0.7 MVAr and a location factor of 0.32 is analysed. The X/R ratio is varied between 5 and 30. The step response diagram (left column) shows that all combinations remain stable. Compared to the step response without grid resonance in Fig. 3.10 (d) oscillations appear. They are not leading to instability. In the open loop (OL) Bode plot (middle) it can be seen that an additional maximum point and minimum point appear compared to the OL Bode without grid resonance (Fig. 3.10 (d)). The new introduced maximum point is higher than the OL transfer function at LCL resonance frequency (around 1 kHz). The closed loop pole zero map in the right column shows that the two corresponding
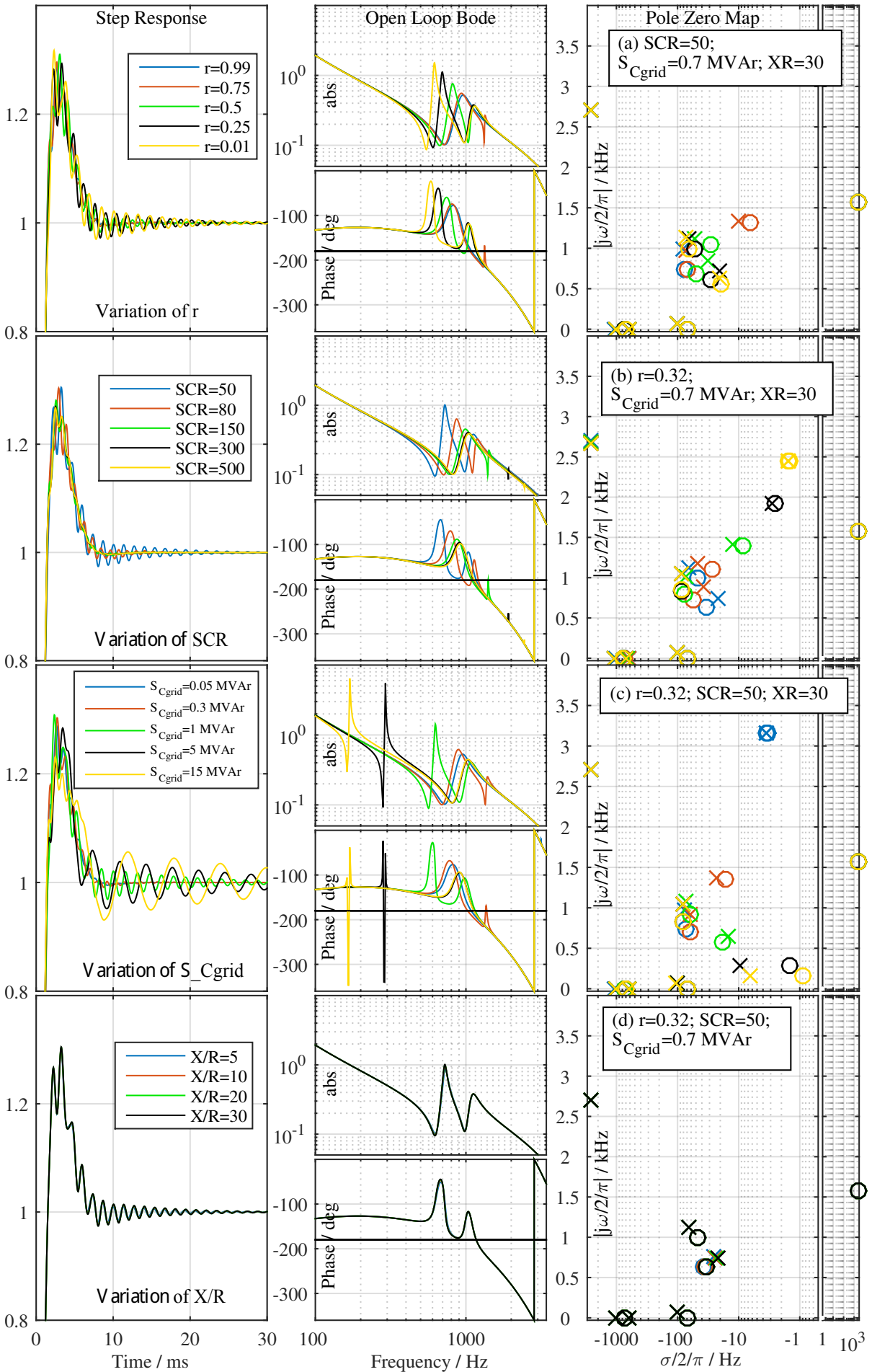
**Figure 4.9:** Loop analysis for strong grid LCL system with passive parallel C-R damping method for varying grid resonance parameters

poles (and zeros) near 1 kHz remain in the left s half plane.

**Effects of varying grid resonance.** Regarding a varying X/R ratio no significant differences in the system behaviour can be seen. The control remains stable. In the third row (c) the grid capacitance is varied. The LCL filter resonance pole near $s/2/\pi = -80 + 1000j\ Hz$ is not changed significantly. The additional pole introduced by the grid resonance varies from 100 Hz to 3.2 kHz. The zero follows the pole. This can also be observed in the corresponding OL Bode plot in the middle. When the SCR is varied a similar behaviour is observed (second row, (b)). For increasing SCR respectively lower grid inductances the grid zero is nearer to the pole. The varying of the location factor in the first row (a) again mainly only varies one pole (and zero). When the grid capacitance is far away (r=0.99) the pole zero combination is moved to the not shown range $\underline{s}/2/\pi = -0.85 + j6309\ Hz$.

**Findings regarding stability.** For the analysed combinations the introduced grid resonance does not bring the current control to instability. When it is assumed that the simple Nyquist criterion (instability: OL -180 degree phase crossing at magnitude >1) can be applied it could be assumed that grid resonances below the frequency where the OL phase crosses -180 degree cannot bring the control to instability: The grid resonance increases the phase, which is anyway above -180 degree. Therefore, in this frequency range a grid resonance moves the Nyquist curve away from the critical point -1. In the phase diagram of third row (c) this can be observed (the wrongly visible -180 crossing is only a result of limiting the range to $[-360...0°]$). The following pole zero stability analysis for the complete grid resonance range validates this thesis.

### 4.4.4 General Pole Analysis

The poles of the command transfer function are computed while varying the grid resonance properties (SCR=[10..49.9] resp. [50...500], $S_{\mathrm{Cgrid}}$=[0.05...15]MVAr, r=[0...0.99], X/R=30). A resolution of 60 samples per quantity is chosen leading to a computation time of approximately three days (the filters and damping methods are computed in parallel). All combinations having poles with a real value greater than zero are stored.

**LCL system[2].** For the *passively damped* LCL systems, no instable poles are found. This is in line with the previously shown results in Fig. 4.9. The developed *active damping* for the strong grid LCL system becomes instable at several grid resonances. For the weak grid LCL system, no active damping was designed, as it is stable without passive damping (see Fig. 3.10 (a)). The *undamped* system has also several destabilising grid resonances.

**Trap system.** The strong grid trap system has several destabilising grid resonances for all damping methods. The weak grid system has several destabilising grid resonances for *active damping*, 24 instabilities for *series resistance damping* and no instabilities for *parallel C-R* and *parallel C-R|L damping*.

The stability analysis results are summarised in Tab. 4.2. The only passively damped system sensitive to grid resonances is the strong grid trap system. For example, for parallel C-R damping method its instable poles are in the following intervals: (f=996-1326 Hz; r=0- 0.74; SCR 50-149; $S_{\mathrm{Cgrid}}$=0.3-0.81 MVAr). As predicted in the previous section, this is in the frequency range where the phase of the OL crosses -180 degree (see Fig. 3.13). For series resistance damping, some parts of the IP have a frequency >1.6kHz (2342).

---

[2]  Below, the term 'system' is used to describe the complete system of designed filter and corresponding current control.

**Table 4.2:** Number of instable poles (IP) of the current control loop with a 60 sample grid resonance variation

| Damping method | LCL strong | LCL weak | Trap strong | Trap weak |
|---|---|---|---|---|
| Active damping | 1700 IP | - | 530000 IP | 255000 IP |
| No damping | - | 1304 IP | - | - |
| Series resistance | no IP | no IP | 10000 IP | 24 IP |
| Parallel C-R | no IP | no IP | 626 IP | no IP |
| Parallel C-R‖L | no IP | no IP | 4022 IP | no IP |

**Case analysis strong grid trap system with parallel C-R damping.** In Chap. 2, the parallel C-R damping method was found to be the most advantageous for the strong grid trap system, so it is chosen to be analysed in detail. In Fig. 4.10, the same graphical analysis as for the strong grid LCL system is provided. In (d), it can be seen that the X/R ratio of the grid inductances has a significant influence on the stability. With decreasing X/R ratio, the destabilising poles in the right s half plane move towards the imaginary axis. For X/R=5, the system even becomes stable. In the third row (c), the assumption, that only grid resonances near the $-180°$ crossing of the OL phase can be critical to stability, is validated. The very low frequency grid resonances (yellow and black) lead to a stronger oscillation in the step response (left column), but not to instability. The pole zero map validates that also grid resonances with higher frequency than the $-180°$ phase crossing frequency lead to a stable system (only the red pole is instable). In the second row (b), this fact is supported, while here the grid resonance is shifted to higher frequencies by the varying SCR. In the first row (a), it is seen that location factors of 0.01, 0.25 and 0.5 lead to the critical grid resonances near $-180°$ crossing. Especially for the trap filters, the active damping has many instable poles. This is not analysed further in this work.

**Visualisation of critical combinations.** For a deeper understanding which grid resonances are stability critical, the combinations of r, SCR and $S_{\text{Cgrid}}$ leading to a pole frequency near the $-180°$ crossing frequency are computed. As an analytical computation of the poles of the complete closed loop is not possible, first the poles of $\underline{Y}_{\text{conv}}(s) = \underline{I}_{\text{conv}}(s)/\underline{U}_{\text{conv}}(s)$ are computed analytically. All resistances and passive damping circuits are set to zero. The analytical solution for the grid resonance pole is rearranged to the grid capacitance power: $S_{\text{Cgrid}} = f(s_{\text{inf,gridres.}}, r, SCR)$. The r factor and SCR are varied in the known range while $s_{\text{inf,gridres.}}$ is set to the $-180°$ crossing frequency minus 100 Hz and plus 500 Hz. The corresponding $S_{\text{Cgrid}}$ is computed. This is visualised in a 3D plot shown in Fig. 4.11. The z axis is the reactive power of the grid capacitance, the x and y axes the location factor r and the SCR of the grid. Two planes are drawn: One for an equal pole frequency of $f_{-180} - 100\,Hz$ (corresponding to a higher grid capacitance, therefore the upper plane) and one in $f_{-180} + 500\,Hz$ (the bottom plane). This is done for all four (undamped) filter types: LCL strong (a); LCL weak (b); Trap strong (c); Trap weak (d). The properties of the equal frequency planes are similar for all filter types: The grid capacitance respectively the grid capacitance power on the z axis must be increased with increasing SCR (which means decreasing grid inductances) to keep the pole frequency constant. Similarly, it has to be increased with increasing location factor r. Despite the fact that different filters are used for strong and weak grid, the planes for the weak grid ((b),(d)) are approximately the prolongation of the planes for the strong grid in (a) and (c). It can be seen that the power of the grid capacitance $S_{\text{Cgrid}}$ is in the range (0.03...100 MVAr) to shift the grid resonance frequency to the control critical frequency. For strong grid systems (left column), most of the plane is
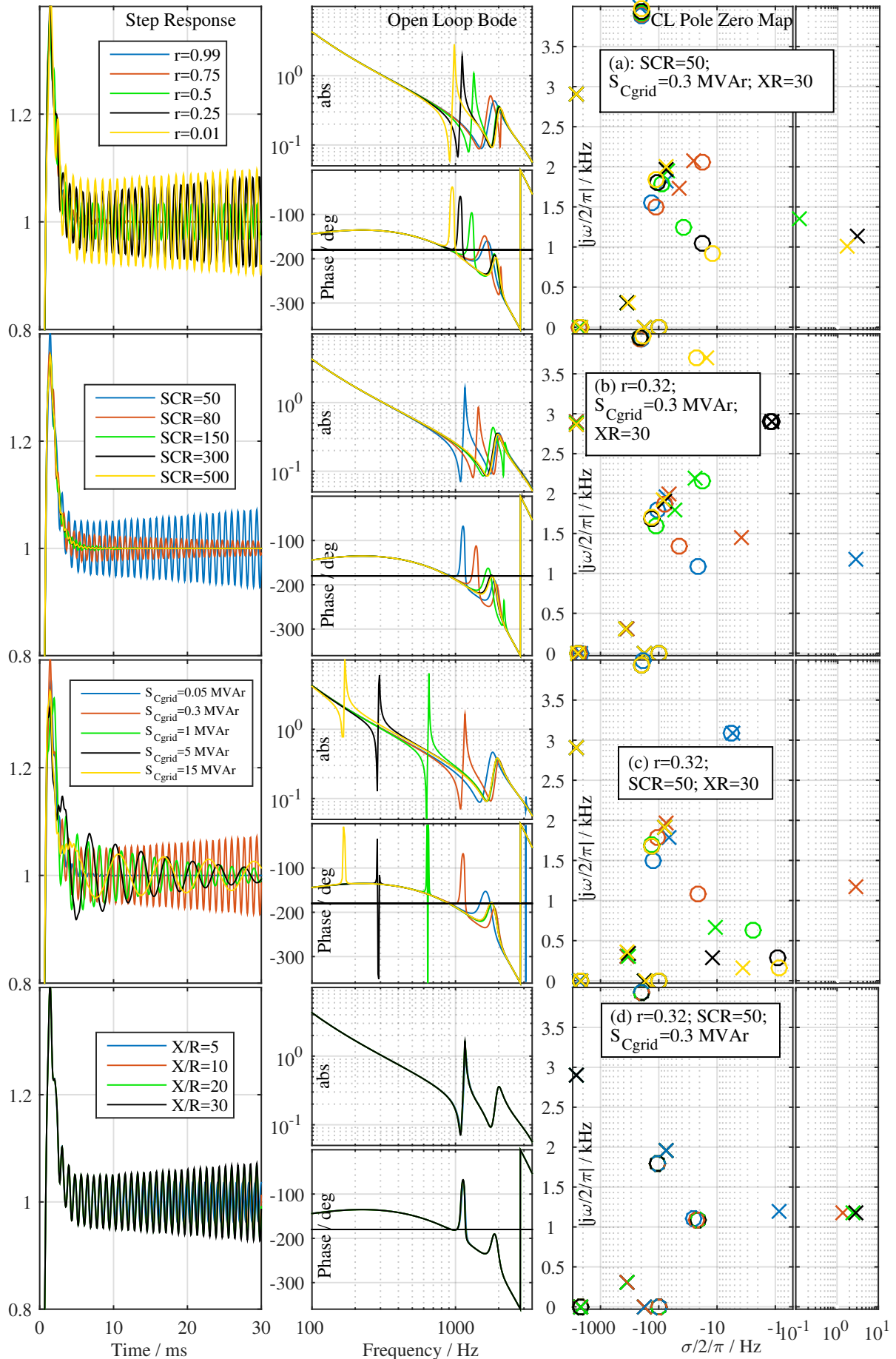
**Figure 4.10:** Loop analysis for strong grid trap system with passive parallel C-R damping method
for varying grid resonance parameters
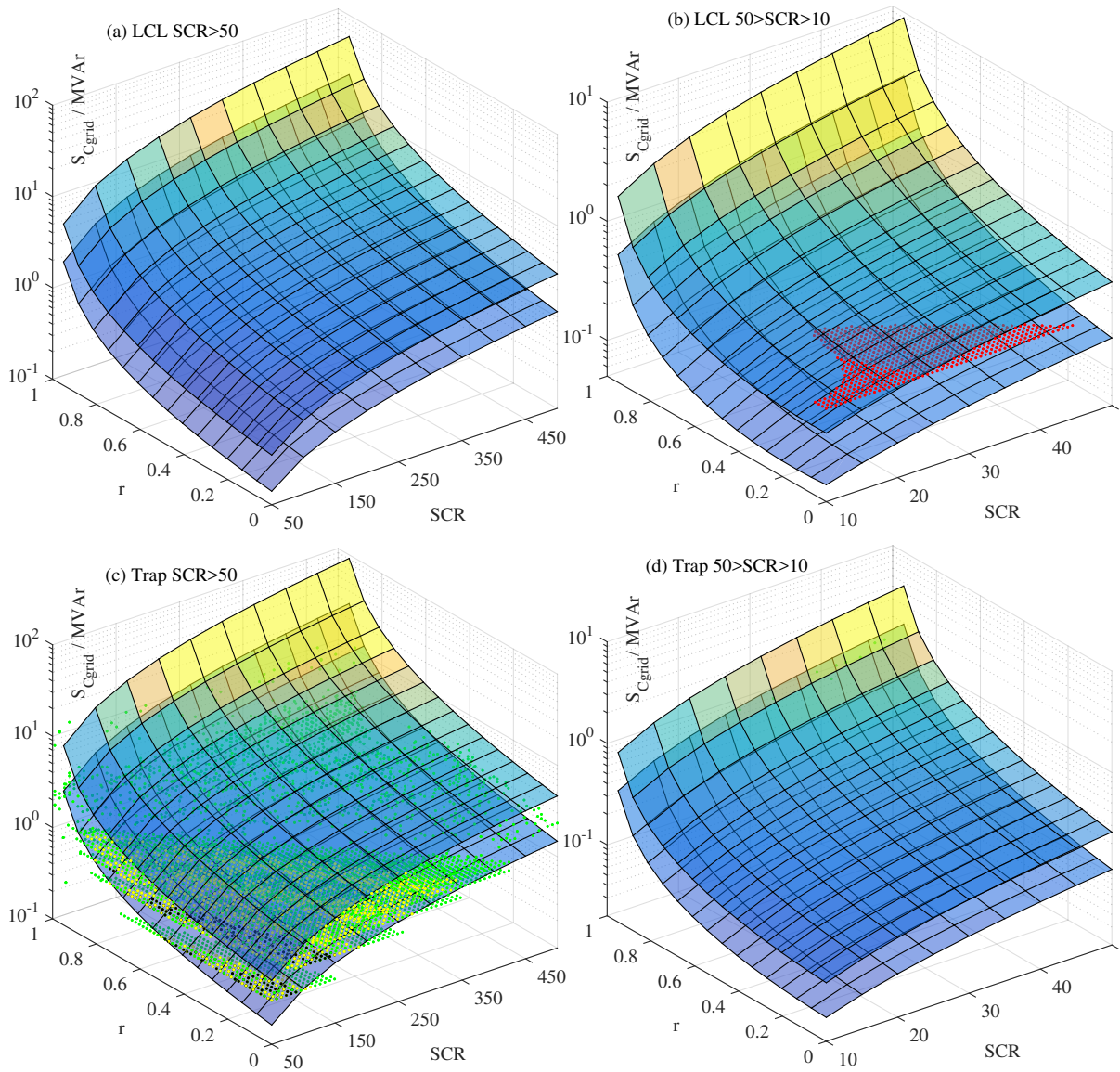
**Figure 4.11:** Planes where r, SCR and $S_{\text{Cgrid}}$ lead to equal pole frequencies (top plane: $f_{-180} - 100\,Hz$; bottom plane: $f_{-180} + 500\,Hz$) and triples leading to instability (dots); red: no damping; green: series resistance; black: parallel C-R; yellow: parallel C-R‖L $f_{-180}$ is set to the frequency where the OL phase of the parallel C-R damping system crosses -180 degree. It is found as $f_{-180,\text{LCL,strong}} = 1077\,Hz$, $f_{-180,\text{LCL,weak}} = 891\,Hz$, $f_{-180,\text{Trap,strong}} = 880\,Hz$, $f_{-180,\text{Trap,weak}} = 1200\,Hz$.

below 10 MVAr which seems to be realistic. When the location factor r approaches 1, higher $S_{\text{Cgrid}}$ are necessary to keep the pole frequency fixed. Here it has to be analysed specifically, if a PFCC of for example 50 MVAr next to a wind turbine is a realistic scenario. The weak grid systems on the right column even need lower $S_{\text{Cgrid}}$ below 10 MVAr.

Additionally, the triples of r, SCR and $S_{\text{Cgrid}}$ of the grid impedance which lead to instable poles are marked for all developed systems except for the active damping system. The large amount of active damping IP would be spread over all plots and bring no information. Below, these points are named as triples leading to instability (IT). As previously mentioned, the weak grid LCL system has several IP/IT for the undamped system. They are marked as red dots in Fig. 4.11 (b). Their range is approximately r=0...0.4; SCR=10...45; $S_{\text{Cgrid}} = 0.03$ $MVAr$. Instabilities occur only for a very small range of $S_{\text{Cgrid}}$. This is validated by time simulation for SCR=22.7; r=0.14; $S_{\text{Cgrid}} = 0.21$ $MVAr$, which is not shown here (another simulation result is provided below). The frequencies of the IP belonging to the IT are within 919-1130 Hz. The planes are chosen to be 1391 Hz for the bottom and 791 Hz for the top. The fact that not all triples are between the two planes (for lower SCR near 10) shows that the pole frequency of the admittance $Y_{\text{conv}}$ (for which the planes are representative) are not exactly the same as for the closed current control loop poles (which represent the ITs).

In Fig. 4.11 (c), the sampling distance of the IP search regarding $S_{\text{Cgrid}}$ is directly seen for the green dots/IT (0.05; 0.168; 0.286...MVAr). The green dots stand for IT of the series resistance, the black for parallel C-R and the yellow for parallel C-R‖L damped system. The black and yellow IT all remain between the top and bottom planes which here stand for bottom $f_{\text{pole}} = 1380$ $Hz$ and top for $f_{\text{pole}} = 780$ $Hz$. Several green IT are below the bottom plane. A limiting line, as also seen in (b), appears going from r=0 and SCR=423 to r=0.87 SCR=50. As already mentioned, the black ITs (parallel C-R) are located within (f=996-1326 Hz; r=0- 0.74; SCR 50-149; $S_{\text{Cgrid}}$=0.3-0.81 MVAr). The yellow ITs (parallel C-R‖L) are spread over a wider range: 924-1403 Hz SCR 50-340 r 0-0.85 $S_{\text{Cgrid}} = 0.3 - 1.32$ $MVAr$. The green series resistance ITs are again located in a wider range. Additionally, ITs are found at higher $S_{\text{Cgrid}}$. For the weak grid trap system in (d), the ITs are located at r=0.99 SCR=28...49 $S_{\text{Cgrid}}$=0.81...1.32 and are hardly visible in the graphic.

**Findings regarding stability.** The strong grid trap system is sensitive to the analysed grid resonance. The weak grid LCL system has triples of r SCR and $S_{\text{Cgrid}}$ leading to instability only for series resistance damping . Most of the developed systems are stable, even though during their design possible grid resonances have not been considered. This is a confirmation that the control design is robust.

**Simulative validation.** Several critical and non-critical resonances and their corresponding converter systems have been simulated for validation of these theoretical stability results. Due to space limitation, only a single result is shown here. The *strong grid trap system* with SCR=50 (X/R=30), r=0.32, $S_{\text{Cgrid}} = 0.3$ $MVAr$ is selected. Its result from transfer function analysis has already been plotted in Fig. 4.10 (c) in red. Different solver types for the Matlab simulations are investigated: Dormand Prince (ode45) with variable step size where the maximum step size is set to $1\mu s$ . For stiff systems, stiff solvers are recommended [103]. To exclude unwanted solver effects, the same simulation is performed with the stiff ode23s Mod. Rosenbrock solver. No significant differences are observed. This is also valid for the Dormand Prince solver (ode45) without maximum step size (which is significantly faster).

Fig. 4.12 shows the simulation results obtained with the ode45 solver. The order of signals is the same as in the simulation results shown in Chap. 3.7 and therefore is not explained again. At first, the simulation is started without grid capacitance (its current shown in (i) is zero). The converter runs stably. At t=0.05 s, the grid capacitance is connected. The grid capacitance
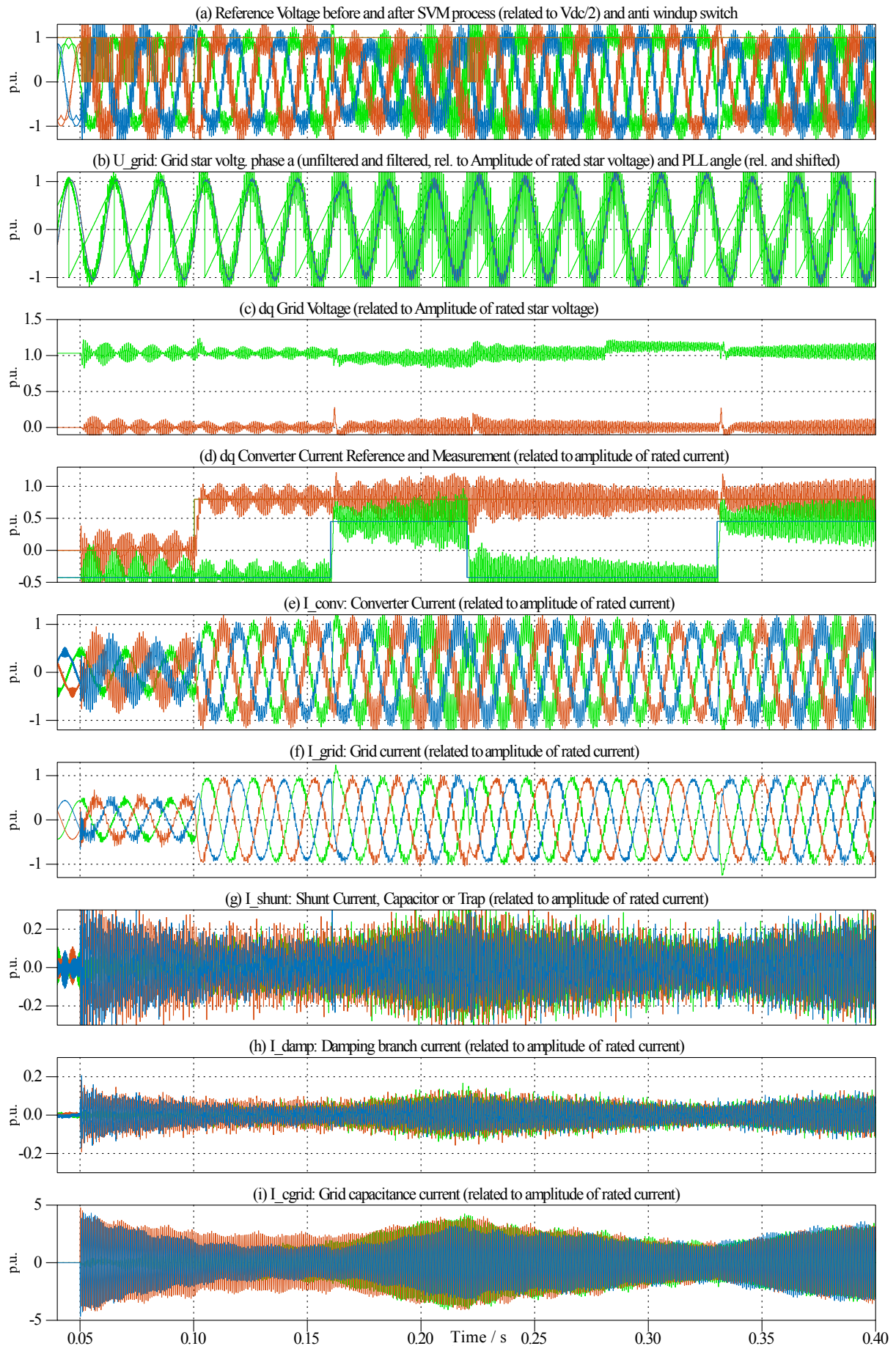
**Figure 4.12:** Simulation of strong grid trap system with parallel C-R damping with grid impedance including capacitance, connected at t=50 ms (SCR=50 (X/R=30), r=0.32, $S_{\text{Cgrid}} = 0.3\ MVAr$) (for p.u. values see Tab. 2.2)

current in (i) starts oscillating with the resonance frequency of the IP: 1.14 kHz. It is an oscillating current between two phases (b and c) while the third current phase a remains near zero. This is a result of the connecting time related to the fundamental voltage phase angle. Near t=0.2 s, the grid capacitor current of phase a resembles the others. It is assumed that the hard connecting of a PFCC is a worst case event. In practice, preloading resistances could be a solution to prevent overcurrents. Here hard switching is shown as worst case. The mentioned asymmetry is consequently observed in other currents. Only phase b and c of the converter current in (e) are oscillating. This leads to the 100 Hz beat in the dq currents (d). It is interesting that the grid current is not very strongly affected. At t=0.05 s, the control is in saturation which is seen at the anti-windup signal in (a). When it is zero, the PI integrator input is set to zero. During most of the simulation, the control is not in saturation. At t=0.1 s, an active current step is controlled. The control runs without the reference prefilter. Regarding the instability, this makes no difference. In contrast, the changing of the reactive current setpoint at t=0.16 s has a destabilising effect. Notably the grid voltage in (b) begins to oscillate stronger. Consequently, the grid capacitance current follows in (i). Interestingly, this operating point does not lead to total instability. If no reference changes are commanded at t=0.19 s (and also at t= 0.329 s and t=0.42 s), the converter remains at this critical stable point. At t=0.22 s, the reactive current setpoint is changed again. A slightly more stable operation appears, while an increase of the grid voltage of 10% at t=0.28 s leads to a further decrease of the oscillations. A second setpoint change of the reactive current at t=0.35 s increases the oscillations again. As already mentioned, the operating point at the end of the simulation is stationary, and the control is not in saturation. **Interpretation.** This simulation partly validates the predicted instability. The designed control changes to an unacceptable operating mode caused by the introduced grid capacitance. Nevertheless, in contrast to the prediction, it does not become instable. Here, an interesting observation is made. When exactly the same simulation is run without a converter, which means that the digital control output is not put to the PWM modulator but to ideal voltage sources, the control immediately becomes completely instable. As the PWM switching is not included in the linear transfer function analysis this shows that the prediction is correct. In this case, obviously the PWM switching has a stabilizing effect.

The effect of the PLL is also analysed. In Fig. 4.13, the input of the PLL, the grid voltage in (b) is heavily oscillating at t=0.2 s. As mentioned in Chap. 3.6.2 the grid voltage is low pass filtered. In Fig. 4.13, it can be seen that due to the low pass filter the oscillation is greatly damped in the sampled voltage of the PLL. This results in the assumption that the PLL has less influence. This assumption is supported by the fact that a simulation with a 'sawtooth' as angle (instead of the PLL) gives very similar results. It can be concluded that the predicted instability is not validated as complete instability but as unacceptable operating point and therefore has to be avoided.

### 4.4.5 Design for Grid Resonance Robust Control

In the previous section, destabilising grid resonances for the strong grid trap and weak grid LCL system are found. Going back to the control design chapter section 3.5.3, it can be seen that for the strong grid trap system, in contrast to all other systems, the PI gain is not decreased compared to the symmetrical optimum start design. Nevertheless, the magnitude at the (trap) resonance frequency $1/A_{\mathrm{marg}}^{res}$ is the lowest of all designed controls. Therefore, in the previous chapter it was assumed that a further decrease of the PI gain is not necessary. Concerning grid resonances, this is not the case. When dividing the PI gain by 2, all instabilities disappear, while
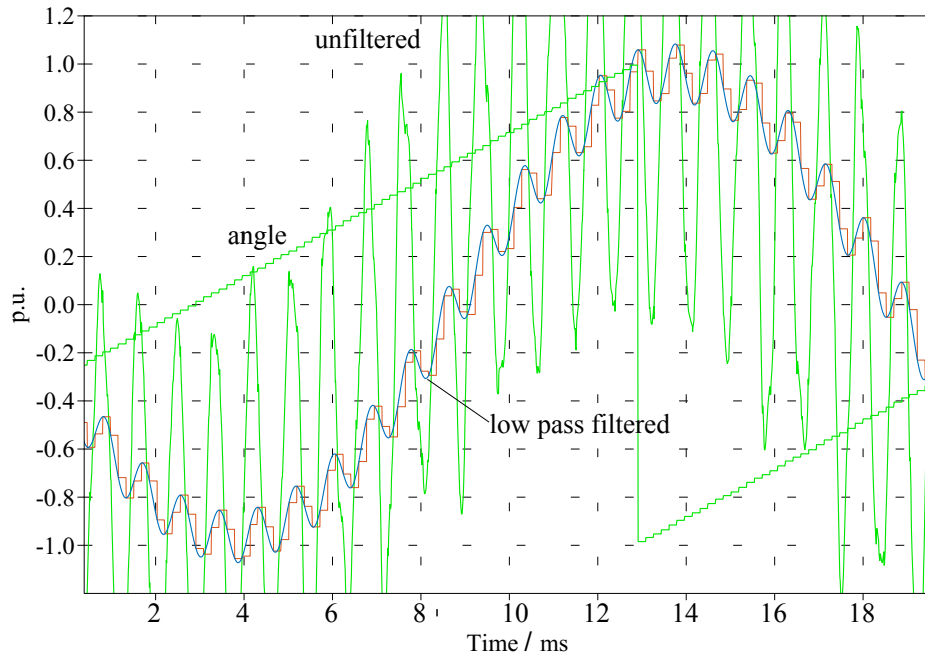
**Figure 4.13:** Corresponding grid voltage: unfiltered, filtered, sampled and angle detected by PLL (for p.u. values see Tab. 2.2)

the control dynamic is still sufficient (20 ms power adjustment, overshoot etc.).

This shows that *only* by a PI control design adapted to the grid resonance, all developed passive damped systems (and the undamped weak LCL system) are robust against the *complete* grid resonance range. Compared to literature, the system designed in this work does not need stabilizing methods as for example notch filters tuned to resonance frequency or lead lag filters (which increase the complexity) to remain stable.

Moreover the analysis of the increased resistance due to skin effect should be mentioned. For example, the case analysis in Fig. 4.10 (d) shows a clear stabilizing effect of the grid resistance. This can be related to the increased grid resistance due to the skin effect analysed in Chap.4.2. It is found that the 50 Hz resistance of the grid impedance is increased by factor 2.5 at 1 kHz. It would decrease the X/R to for example 30/2=15. Additionally, the transformer resistance is increased by approximately factor 4. As the transformer impedance is 6% and the grid impedance 2% (strong grid), this is a significant increase of the damping which could already stabilise the case. This is different for example for a control with symmetrical modulation (single update). Here, the frequency of stability critical grid resonances would be decreased. Accordingly, the resistance increase due to skin effect is smaller.

## 4.5 Summary of Main Findings

- From power engineering, simple models to increase the 50 Hz resistance in consideration of the skin effect can be a first step to improve the high frequency grid impedance model.

- The continuous closed loop pole analysis with second order Padé approximation of the digital control emulator provides sufficient predictability of the three-phase simulation

stability.

- Mainly grid impedance resonances with frequencies near the $-180°$ crossing frequency of the OL without grid resonance are stability critical.

- An adaption of the PI parameters is sufficient to stabilise the current controls that are initially instable due to the grid resonance. No complex stabilizing methods are necessary.

- A rough estimation shows that according to the power engineering models (skin effect), the increased grid resistance already has stabilizing effects for the specific case.

# 5 Experimental Validation

## 5.1 Overview

The following chapter presents the experimental validation of the previously developed theoretical results. First, the utilised laboratory setup is described in detail. An explanation is given of how the p.u. transformation is utilised to obtain suitable laboratory values. General functionalities of the setup are validated with time plots. All four LCL and trap filters are described in detail. Their performance regarding harmonics mitigation is validated with current spectra. In the next step, the designed current controls are validated. It is shown that no PI controller parameter adaption needs to be carried out to gain the same dynamics as in simulation. Finally, the most important aspect is validated: the stability regarding introduced LCL-type grid resonances. Here, the stability limit is tested with the so-called critical PI gain. The chapter concludes with a summary of the main findings.

## 5.2 Setup Description - P.U. Transformation of the 2 MW Parameters

The schematic of the setup is shown in Fig 5.1. A converter system from industry with $S_\mathrm{r} =$ 20.8 $kVA$ (1%) is taken for the analysis [104], integrating the drivers, power modules, DC link and snubber capacitances as well as the air cooling system. The driver signals for the six IGBTs of 0...15 V are the input for the system. The utilised dSPACE 1103 system does not support an asymmetric PWM, hence, the modulation is performed using a commercial dSPACE FPGA extension (FPGA.Comm) [105]. A level shifter increases the FPGA output voltage to 0...15 V. In Chap. 2, the filters for the 2 MW system were designed (Tab. 2.7). For the parallel C-R damping, they are transformed to laboratory dimensions (Tab. 5.1). To do this, the base values of the laboratory setup have to be defined. The base values are not set to the rated parameters of the converter. This provides the opportunity for adapting the resulting filter parameters with respect to availability. 400 V, 230 V and 115 V are possible grid voltages/ base voltages. They can be handled with the converter's maximum DC voltage (750 V). The available DC source is 440 V DC, therefore, 230 V AC is taken as the base voltage. The base current is adapted for all filters with consideration to the availability of inductances and capacitances. As seen in Tab. 5.1, this varies between 7.9 and 13.77 A. In the upper part of the table, the intended (on the left side, from 2 MW filter design) and the resulting values, implemented in the laboratory, can be seen. All filter parameters are discussed in detail in the following section. The damping resistances are realized with slide resistances and are therefore adaptable. As can be seen later, the selected
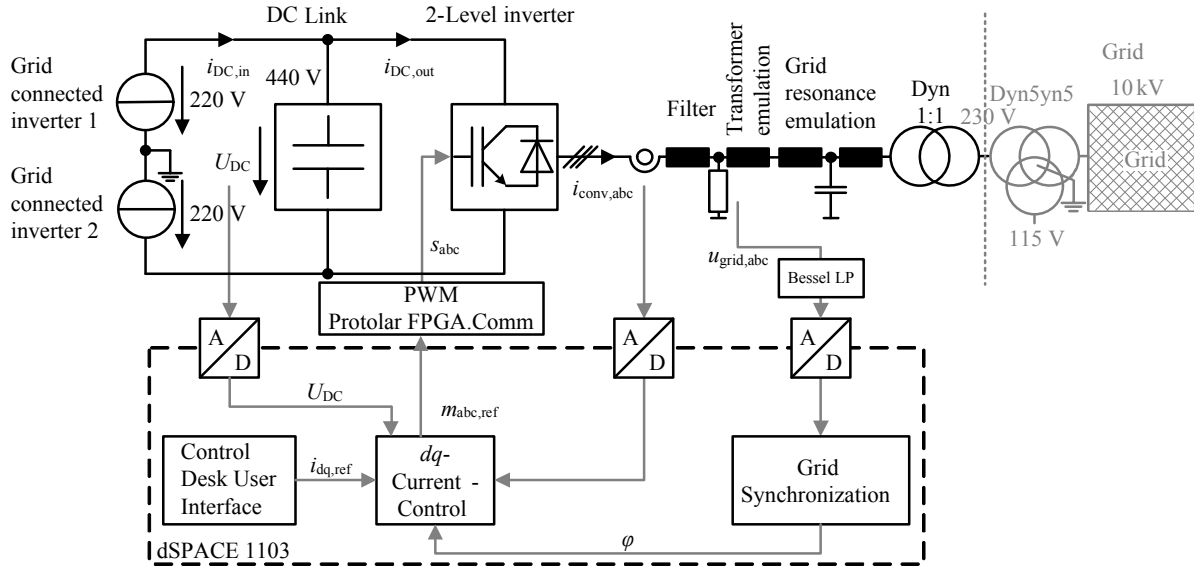
**Figure 5.1:** Schematic of the laboratory setup (single phase equivalent of three-phase system)

parameters are sufficiently close to the real ones to achieve a similar dynamic behaviour. $L_{grid}$ for the weak grid LCL filter is approximately 1.27 too high due to availability. The galvanically isolating 1:1 Dyn5 transformer (see Fig. 5.1) has a $u_k$ of 2.1%, according to the type plate. Its rated current is 72 A at 400 V. Its leakage inductance and resistance is included in $L_{grid}$ and is computed according to Eq. 5.1 assuming an X/R ratio of 15.

$$Z_{trsf,lab,leakage} = u_{k,trsf,lab} \frac{U_{r,trsf,lab}^2}{S_{r,trsf,lab}} = 0.021 \frac{(400V)^2}{\sqrt{3} \cdot 400V \cdot 72A} = 67.4 \text{ m}\Omega$$

$$R_{trsf,lab,leakage} = \frac{Z_{trsf,lab,leakage}}{\sqrt{(X/R)^2 + 1}} = 4.5 \text{ m}\Omega$$

$$L_{trsf,lab,leakage} = \frac{X/R \cdot R_{trsf,lab,leakage}}{2\pi 50} = 0.214 \text{ mH} \tag{5.1}$$

The additional three winding transformer, connecting the 10 kV grid, has a high power rating (170 kVA). Compared to the other inductances its leakage inductance is small. Therefore, it is neglected during the transformation process from high to low power. The DC voltage for all designed systems is a little too high due to availability. This is considered in the experimental filter design evaluation in Chap. 5.4. Regarding the control, this is not critical, as in rated operation PWM saturation is practically not reached (compare the anti wind up signals in Fig. 3.24, 3.25, 3.26, 3.27 each (a)). The PWM carrier frequency remains 2850 Hz, as for the 2 MW system. The PI control parameters are adapted to the new base values of each corresponding filter (see Eq. 5.2).

$$K_{PI,lab} = K_{PI,2MW} \cdot \frac{Z_{base,lab}}{Z_{base,2MW}}; \quad T_{PI,lab} = T_{PI,2MW} \tag{5.2}$$

This shows that the designed controls are easily transferable to all desired power levels. The PLL PI parameters are computed with Eq. 3.3. Compared to the 2 MW system parameters, only the lower grid voltage has to be adapted.

**Table 5.1:** Laboratory: Intended (int.) and real parameters of LCL and trap filter for the analysed parallel C-R damping method and corresponding base values. For the undamped and active damping, *only* the following intended parameters are changed: LCL weak grid $L_{\text{conv,int}} = 16\%$ instead of 20.4% and LCL strong grid $C_{\text{int}} = 16\mu F$ instead of $15\mu F$; $C_{\text{trap2}}$ and $L_{\text{trap2}}$ for weak grid trap filter cannot be realized and are therefore marked in grey (see text).

| | LCL weak | | LCL strong | | Trap weak | | Trap strong | |
|---|---|---|---|---|---|---|---|---|
| | int. | real | int. | real | int. | real | int. | real |
| $U_{\text{DC}}$ /V | 417 | 440 | 408 | 440 | 417 | 440 | 417 | 440 |
| $L_{\text{conv}}$ /% | 20.4 | 20.4 | 16 | 16 | 16.3 | 16.3 | 16.3 | 16.3 |
| $C_{\text{trap}}$ /% | | | | | 1.03 | 1.52 | 0.46 | 0.61 |
| $L_{\text{trap}}$ /% | | | | | 2.96 | 1.95 | 6.83 | 4.98 |
| $C_{\text{trap2}}$ /% | | | | | 1.09 | 1.52 | 0.34 | 0.3 |
| $L_{\text{trap2}}$ /% | | | | | 0.72 | 0.54 | 2.28 | 2.54 |
| $C_{\text{f}}$ /% | 5.6 | 5.6 | 2 | 2 | 1.67 | 1.51 | 0.5 | 0.61 |
| $R_{\text{seriesf}}$ /% | 311 | 311 | 406 | 406 | 400 | 400 | 625 | 625 |
| $C$ /% | 11.2 | 11.2 | 4.7 | 4.7 | | | | |
| $f_{\text{car}}$ /Hz | 2850 | 2850 | 2850 | 2850 | 2850 | 2850 | 2850 | 2850 |
| $L_{\text{trsf}} + L_{\text{grid}}$ /% | 6+10 | 20.3 | 6+2 | 7.98 | 6+10 | 16.3 | 6+2 | 8.1 |
| $S_{\text{base,lab}} = S_{\text{r,lab}}$ /kVA | | 4.45 | | 5.34 | | 3.15 | | 5.86 |
| $U_{\text{base,lab}} = U^{ll}_{\text{r,rms,lab}}$ /V | | 230 | | 230 | | 230 | | 230 |
| $f_{\text{base,lab}}$ /Hz | | 50 | | 50 | | 50 | | 50 |
| $I_{\text{base,lab}} = I_{\text{r,rms,lab}}$ /A | | 11.18 | | 13.4 | | 7.9 | | 13.77 |
| $Z_{\text{base,lab}}$ /$\Omega$ | | 11.9 | | 9.9 | | 16.8 | | 9.6 |
| $L_{\text{base,lab}}$ /mH | | 37.8 | | 31.5 | | 53.5 | | 30.7 |
| $C_{\text{base,lab}}$ /mF | | 0.268 | | 0.321 | | 0.189 | | 0.33 |

Exactly the same Simulink control model as in the simulation is utilised with the dSPACE system. Only the delay block at the output voltages is omitted (see Chap. 3.3) .

The converter current is measured with 30 Arms current probes [106]. All other current measurements are done with 150 Arms current probes [107]. The cable is wound five times to increase the measurement precision. The voltage is measured using two different types of differential probes [108, 109]. Photos of the setup can be found in App. 7.9. The implemented filters are described in detail in App. 7.8. A validation of the functionality of the Bessel signal filter is given in App. 7.7.
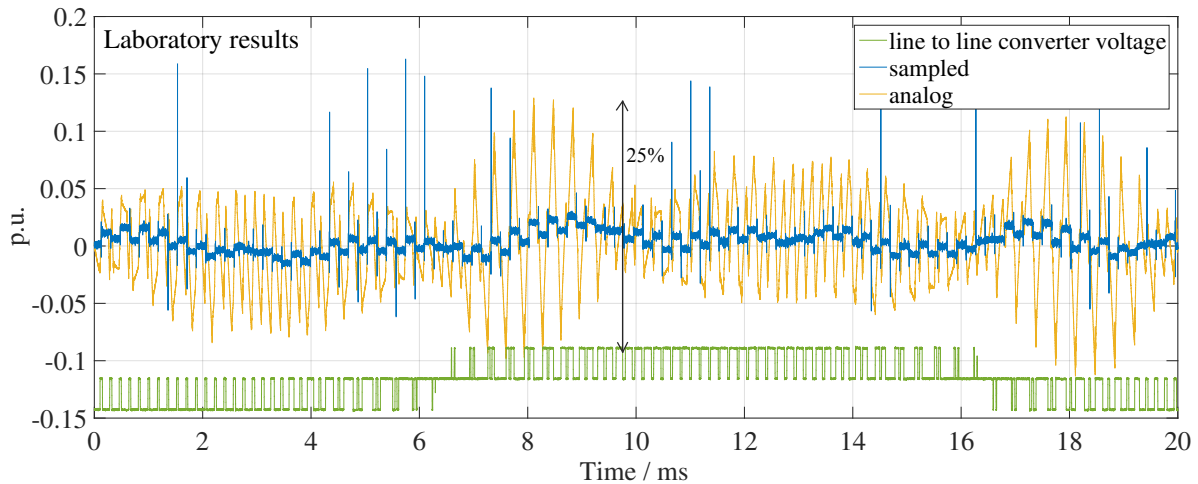
**Figure 5.2:** Laboratory (strong grid trap): converter current phase a related to amplitude of rated current with its sampled equivalent $\hat{I}_{\text{r,lab}} = 19.5\,A$ and converter voltage (qualitative)

## 5.3 Validation of Designed Converter Current Ripple and Carrier Synchronised Sampling

The measured converter current (phase a) and its sampled equivalent are recorded with an oscilloscope. The time range of a fundamental period of 20 ms in steady state is taken. Two operating points are analysed: zero converter current and operation near to the rated current values. This is carried out for the strong grid trap and the weak grid LCL system. In Fig. 5.2, the results for the trap system are shown. In Chap. 2, Tab. 2.7, the maximum peak-to-peak converter current ripple is designed to 25 % of the amplitude of the rated fundamental current. This is highlighted with an arrow in the figure. Fig. 5.3 shows a more detailed view. Generally, the worst case (highest) ripple appears when the corresponding modulation index is at its maximum [33]. Due to the fact that no currents are injected here, the converter is not at its maximum modulation index. This can be validated regarding the converter line-to-line voltage which is also shown in the figures. A slight ripple increase is expected when the modulation index increases.

It can be seen that the carrier synchronised sampling does not sample the ripple current. Nevertheless, slight jumps between each sample appear. This does not deteriorate the fundamental current control. As will be seen in the following sections, characteristic grid harmonics such as the fifth or seventh are present in the current. In Fig. 5.2, higher harmonic currents can be seen. For the rated operation (Fig. 5.4), the modulation index is near to its maximum. This can be validated with the qualitative plot of the converter line-to-line voltage. Again, the sampled current hardly contains the ripple current.

In Fig. 5.5, 5.6 and 5.7 the same operating points as for the previously analysed strong grid trap filter are shown for the weak grid LCL filter system. As seen in Tab. 2.7, the designed MaxCCRpp is only 20%. This can easily be validated by analyzing the analog converter current in Fig. 5.6 near t=9.25 ms. As for the trap filter, slight jumps between two sequent samples appear. The current ripple is hardly sampled. The sampled current exhibits slight harmonic currents (Fig. 5.5). In Fig. 5.7, a high modulation index operating point is shown (see converter voltage). A visual comparison with the equivalent trap filter Fig. 5.4 shows less harmonic distortion in the sampled LCL currents. This is a result of the higher grid inductance.
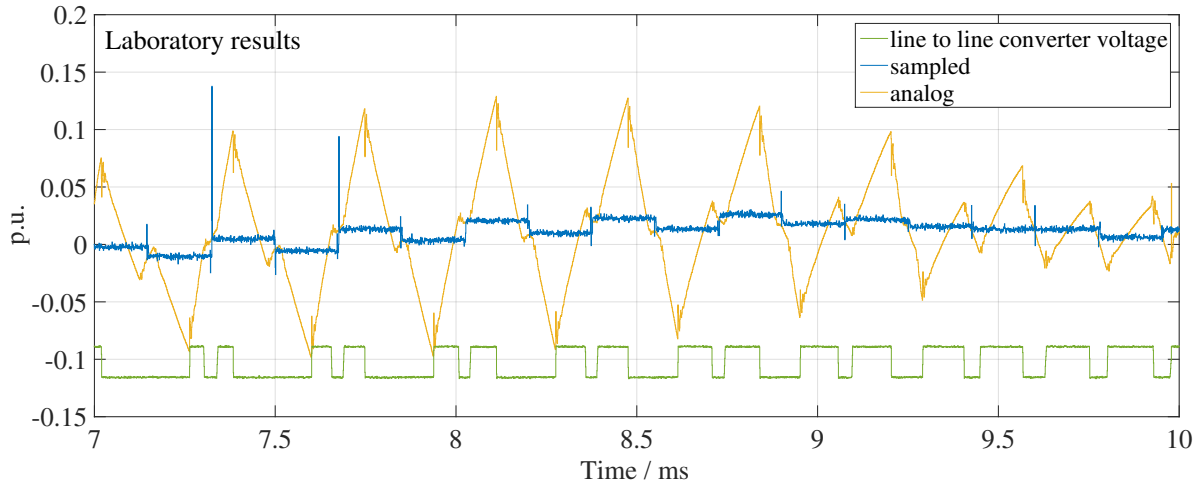
**Figure 5.3:** Laboratory (strong grid trap) zoomed: converter current phase a related to amplitude of rated current $\hat{I}_{r,lab} = 19.5\,A$ with its sampled equivalent and converter voltage (qualitative)



**Figure 5.4:** Laboratory (strong grid trap): converter current phase a related to amplitude of rated current ($\hat{I}_{r,lab} = 19.5\,A$) with its sampled equivalent and converter voltage (qualitative)



**Figure 5.5:** Laboratory (weak grid LCL): converter current phase a related to amplitude of rated current ($\hat{I}_{r,lab} = 15.81\,A$) with its sampled equivalent and converter voltage (qualitative)

**Figure 5.6:** Laboratory (weak grid LCL) zoomed: converter current phase a related to amplitude of rated current $\hat{I}_{r,lab} = 15.81\ A$ with its sampled equivalent and converter voltage (qualitative)
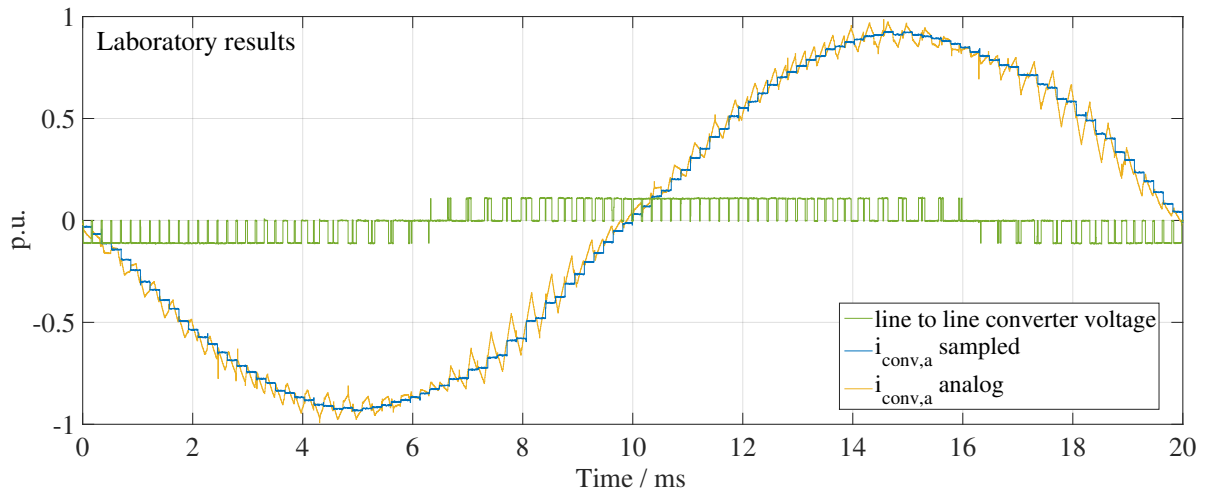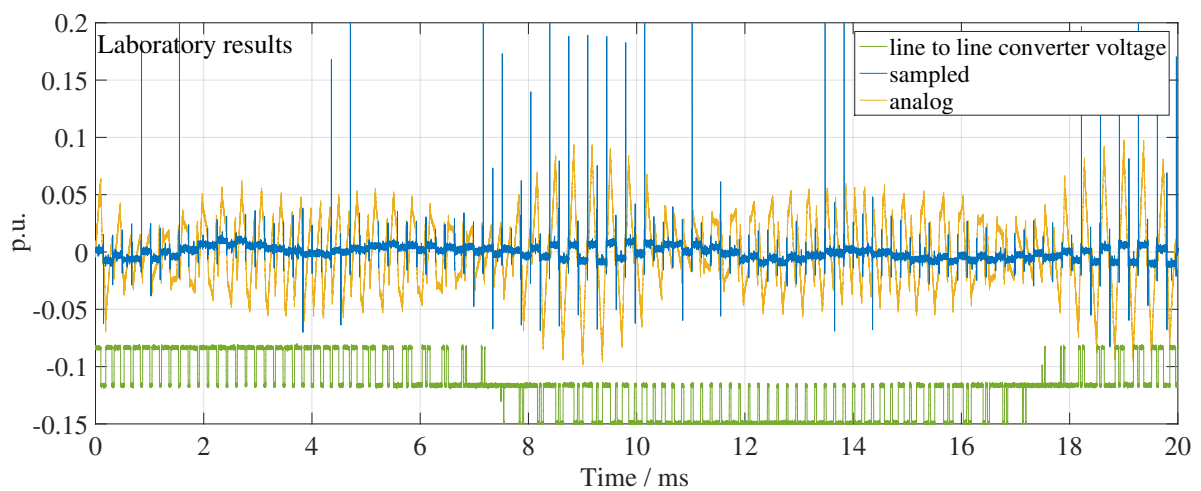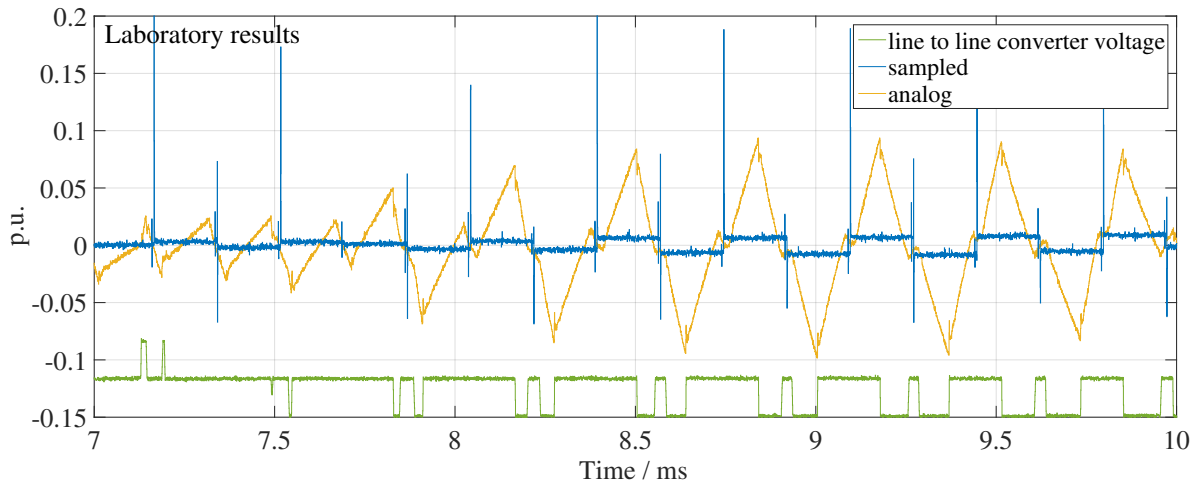


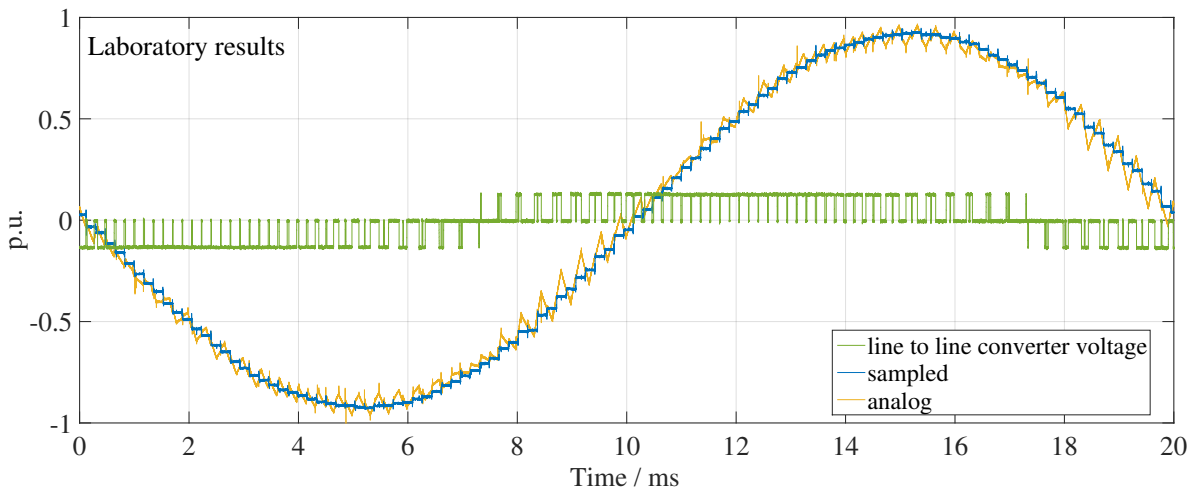**Figure 5.7:** Laboratory (weak grid LCL): $i_{conv,a}$ related to amplitude of rated current $\hat{I}_{r,lab} = 15.81\ A$ with its sampled equivalent and converter voltage (qualitative); $U_{DC} = 417\ V$
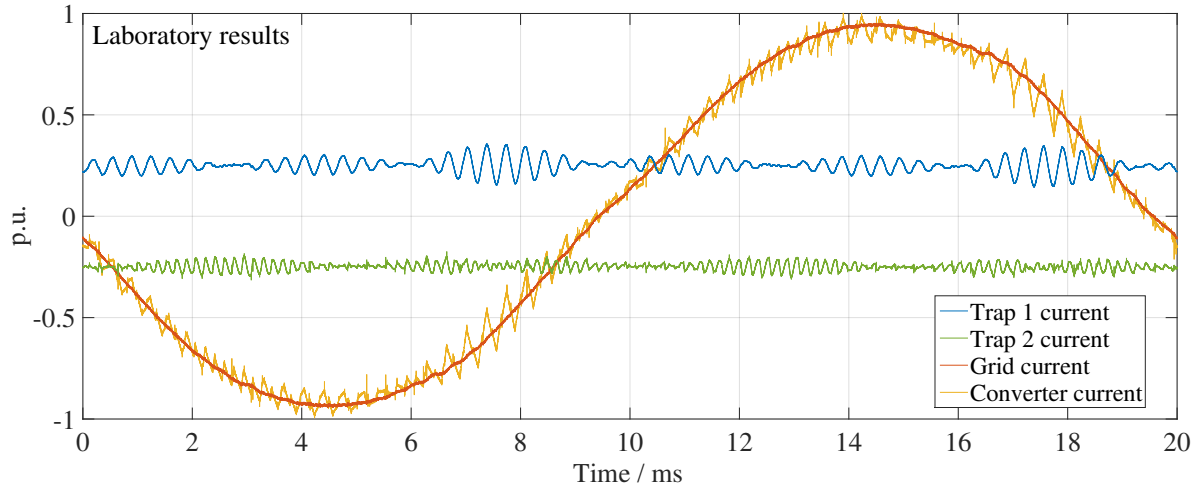
**Figure 5.8:** Laboratory: Strong grid trap filter with parallel C-R damping phase a currents related to the amplitude of the rated current $\hat{I}_r = 19.47\ A$; to improve visibility both trap currents are shifted from zero.

All filters are tested at several operating points. To visualize the filter effect, for the strong grid trap system the different currents are plotted versus time. The converter, first trap (tuned to $f_{car}$), second trap (tuned to $2f_{car}$) and the grid current of phase a are shown in Fig. 5.8. It can be seen that the first trap filter takes the frequency components near to $f_{car}$ and for the second trap filter the frequency components near to $2f_{car}$ of the converter current. Both trap filter currents are shifted from zero for better readability. Below, the resulting grid current is analysed regarding the harmonic grid codes.

## 5.4 Validation of Filter Design Concerning Harmonic Grid Codes

For the filter design and also for the current control validation, no grid resonance is taken into account. The current spectrum is computed and recorded with a 12-bit oscilloscope [110]. Several spectrum measurements are taken and automatically averaged. The frequency resolution is set to 0.1 Hz. The spectrum is recorded in dBm. Below, the spectra are shown as $I/I_r$ in %. This is in line with the filter design in Chap. 2. Here, the rated current is of course not 1858 A but in between 7-13 A for all four filters. The rated voltage is $U_r = 230$ V. This demonstrates the practicability of p.u. resp. % values when comparing different power systems. The current spectrum is dependent on the modulation index of the converter. The filter was designed with a worst case spectrum, where the highest frequency peaks with respect to a modulation index interval were taken. In the laboratory, only a few operating points can be analysed. Four setpoints are adjusted to receive an approximation of the worst case spectrum. The operating points are shown in Tab. 5.2. For the strong grid trap filter, a DC voltage of 417 V is intended (see Tab. 5.1). Due to availability, the measurement is performed with 440 V DC. This is considered in the following spectra by decreasing them accordingly. Generally, the factor has less influence because for example $U_{DC,intended}^{trap,strong}/U_{DC,real}^{trap,strong} = 0.95$ is valid.

**Table 5.2:** Operating points to achieve the worst case grid current spectrum

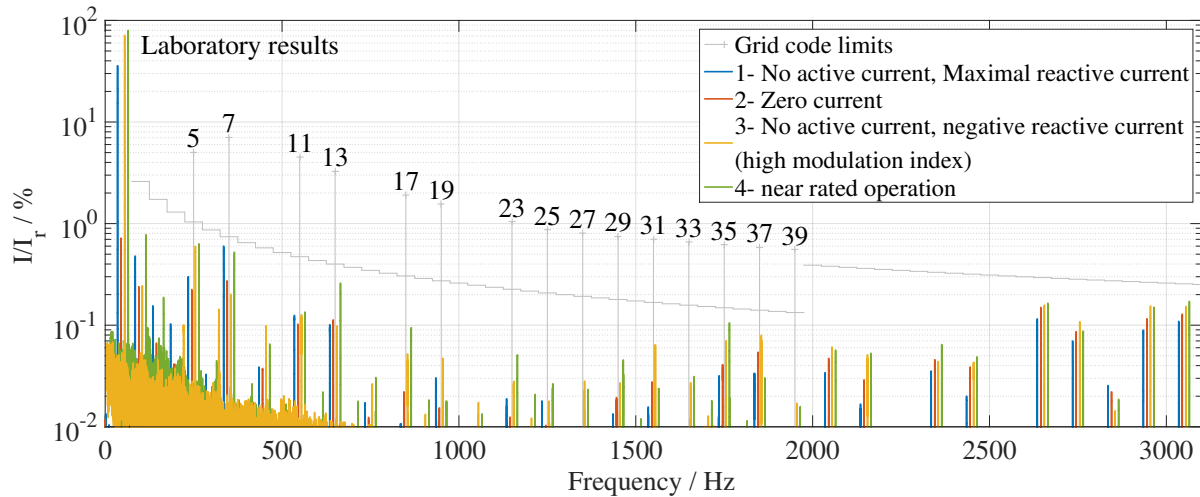| Number | $i_{\text{conv,d,ref}}$ | $i_{\text{conv,q,ref}}$ | m |
|--------|-------------------------|--------------------------|-----------------|
| 1 | 0 | 50% | $\approx 0.7$ |
| 2 | 0 | 0 | |
| 3 | 0 | -max. | near to 1(1.15) |
| 4 | $\hat{I}_{\text{r,lab}}0.9$ | $-\sqrt{\hat{I}_{\text{r,lab}}^2 - i_{\text{conv,d}}^2}$ | |



**Figure 5.9:** Laboratory (strong grid trap, parallel C-R): Grid current spectrum ($I_{\text{r,lab}} = 13.77\,A$) for four different operating points adapted to increased DC voltage ($U_{\text{DC,real}}/U_{\text{DC,int.}} = 417V/440V$) with harmonic grid codes

An example analysis for the strong grid trap filter is shown in Fig. 5.9. To improve visibility, the spectra of the four different operating points are slightly horizontally shifted against each other. In this way, specific components can be compared. It can be seen that the spectral components differ from operating point to operating point. This underlines the need for measuring all operating points. At $f = 50$ Hz, the adjusted fundamental currents can be validated. For operating point 3 and 4, the fundamental current is around 70 to 80 % of the rated current. For operating point 2, its percentage is near to zero ($\approx 1\%$). Especially, 5th, 7th, 11th and 13th harmonics appear. These frequencies are the characteristic distortion frequencies for a grid. A spectral analysis of the grid voltage validates this assumption. Nevertheless, the current harmonics remain conform to the grid code. In contrast to the prediction, triplen multiples of the fundamental appear. The most significant part can be observed at the carrier frequency of 2850 Hz. It is assumed that the cause is parasitic impedances to earth. This also gives rise to the question if the theoretical converter voltage spectrum, derived in Chap. 2.4, has to be extended. This goes beyond the scope of this work.

In the following analysis, the worst case spectrum is always shown. This means that only the highest current amplitude at each frequency is shown. Two filter designs are analysed: the parallel C-R damping and the undamped filters.
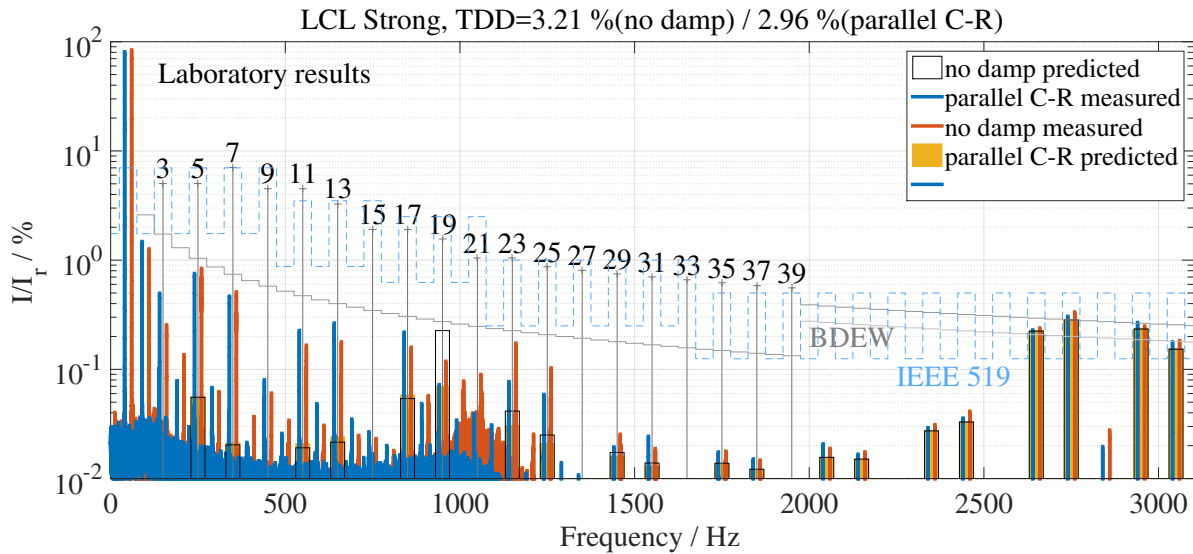
**Figure 5.10:** Laboratory (strong grid LCL system): Worst case grid current spectrum related to the rated current ($I_{r,lab} = 13.4\ A$) with harmonic grid codes and calculated currents for parallel C-R damping and undamped system

## 5.4.1 Strong Grid LCL Filter

The worst case grid current spectra are shown in Fig. 5.10. The predicted currents of Fig. 2.9 are also plotted. For the undamped system, higher currents are visible at around 1050 Hz. Obviously the hardware resonance frequency is slightly shifted compared to the designed resonance frequency of 978 Hz (see Tab. 2.7). As the intended parameters are met very well for the strong grid LCL system (Tab. 5.1), it is assumed that component tolerances lead to this deviation. For the parallel C-R damped system in blue, the resonance is damped to a greater extent. Generally, both analysed current spectra approximately meet the harmonic grid codes. The predicted currents are given in orange for parallel C-R damping, and black framed boxes symbolize the undamped case. Near the carrier frequency, the measured worst case currents approximately match the predicted ones. At 2850 Hz, a common mode component appears for both filters. As previously mentioned, it is likely that parasitic capacitances to earth are the cause.

The spectrum exhibits significant components at the characteristic grid harmonics. They are evoked by the grid and therefore not seen in the predicted currents. Nevertheless, they still conform to the grid code. The TDD (see Chap. 2.2) is below its limits.

## 5.4.2 Strong Grid Trap Filter

The worst case grid current spectra are shown in Fig. 5.11. As calculated for parallel C-R damping in Chap. 2, the predicted currents are taken from Fig. 2.12 (c). As the second trap filter which is tuned to approximately 5700 Hz shall also be validated, the frequency range is extended to 6 kHz. The predicted and measured currents near 5700 Hz are in a similar range. Again, a not predicted common mode component appears at 5700 Hz. The resonance evoked by the second trap filter can be seen near 4 kHz. Compare also the corresponding admittance
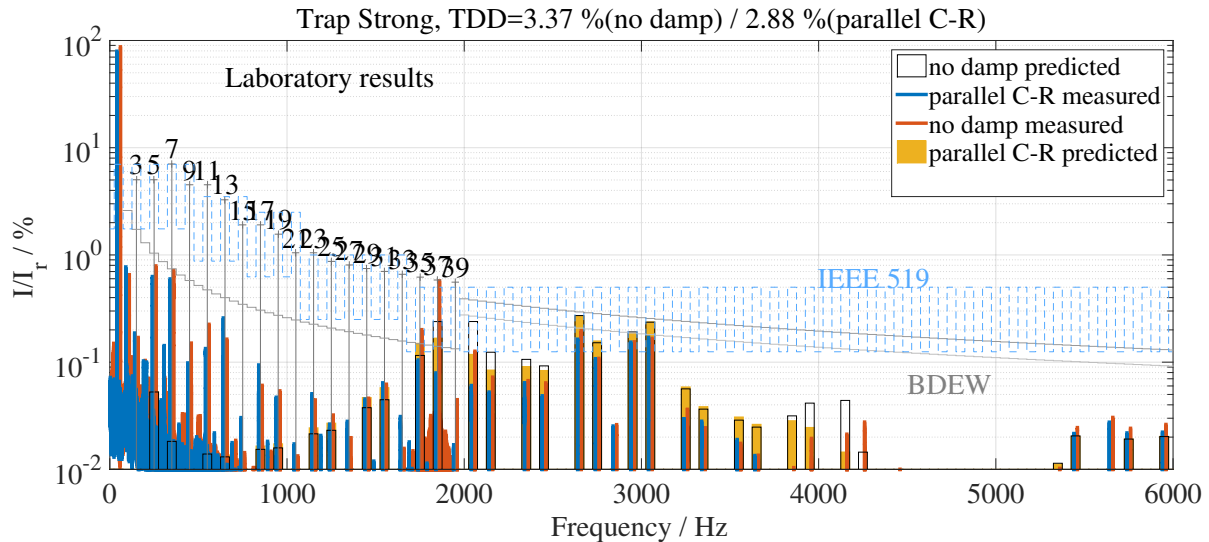
**Figure 5.11:** Laboratory (strong grid trap system): Worst case grid current spectrum related to the rated current ($I_{r,lab} = 13.77\,A$) with harmonic grid codes and calculated currents for parallel C-R damping and undamped system

plot in Fig. 2.12 (b). It is only partly validated by the measurement. Obviously, the laboratory resonance frequency is slightly higher. For the parallel C-R damped system, the resonance is damped well. No current components of the parallel C-R damped system can be seen near 4 kHz.

Near the carrier frequency of 2850 Hz, the predicted and measured currents are in a similar range both for the parallel C-R and the undamped system. Increased currents, especially for the undamped system, can be observed at the resonance frequency evoked by the first trap filter near 1850 Hz. This is near to the resonance seen in the designed admittance in Fig. 2.12 (b). At the 37th harmonic, the undamped system current has a high peak. This peak would be grid code critical. For the parallel C-R damped system, this resonance is damped, nevertheless, it is also seen in the currents. This is in accordance with the design, as they remain slightly below the predicted currents. As for all designed filters, 5th 7th... harmonics appear. Although they are not grid code critical, they could be compensated by a harmonic current control.

### 5.4.3 Weak Grid LCL Filter

The worst case grid current spectra are shown in Fig. 5.12. Corresponding to the lower SCR, the grid code current limits are decreased compared to SCR=50. The currents near the carrier frequency correspond to the predicted ones. As previously mentioned, a common mode component appears at 2850 Hz. The resonance frequency near to 500 Hz, see Fig. 2.9 (d), is partly validated. Due to availability, a significant higher grid inductance is used (see Tab. 5.1). According to Eq. 2.13, this additionally decreases the resonance frequency. In the present case, the influence of the characteristic grid harmonics and the converter harmonics can hardly be separated. High but still grid code conformal currents occur at the 5th, 7th, 11th and 13th harmonic. For most of the frequencies the damped currents are not significantly below the undamped ones. This is in line with the theoretically predicted currents, where damped and undamped currents are also relatively similar.
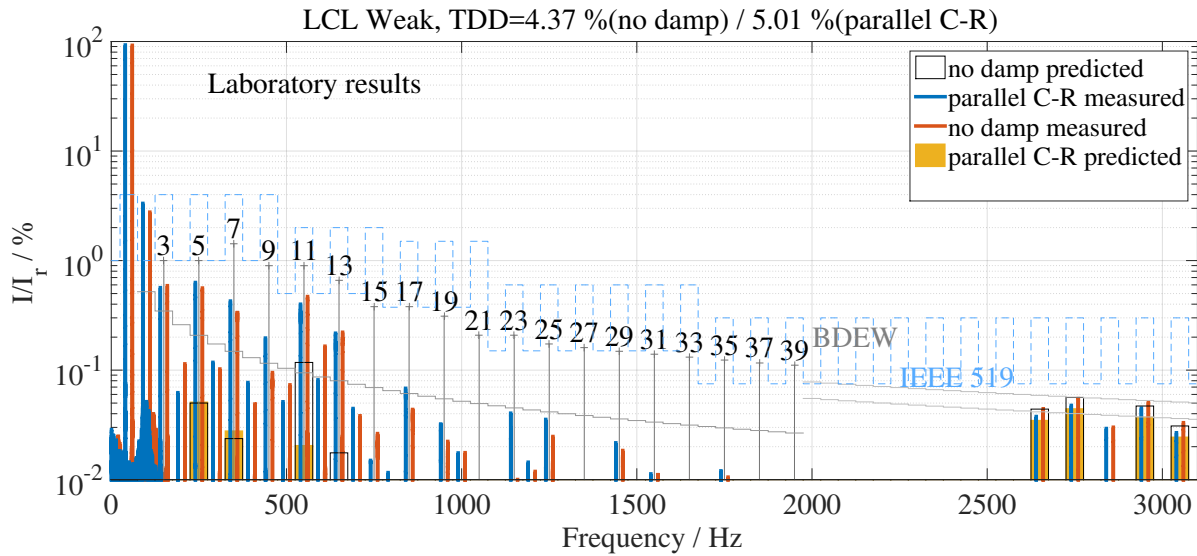
**Figure 5.12:** Laboratory (weak grid LCL system): Worst case grid current spectrum related to the rated current ($I_{r,lab} = 11.18\,A$) with harmonic grid codes and calculated currents for parallel C-R damping and undamped system

## 5.4.4 Weak Grid Trap Filter

The worst case grid current spectra are shown in Fig. 5.13. Again, the frequency range is extended to 6 kHz. The lack of the second trap filter (as mentioned in Chap. 7.8.4) is clearly visible. Near 5700 Hz, high spectral components can be seen for the damped and undamped system. Consequently, the resonance evoked by the second trap filter near 3.5 kHz (compare Fig. 2.12 (d)) is also not observable in the currents. As for the other filter designs, the spectrum near the carrier frequency of 2850 Hz is in the range of the predicted currents. The resonance evoked by the first trap filter is obviously near the 29th=1450 Hz. As for the other filters, this is a deviation from the initially adjusted one (near 1150 Hz). The significant deviation is a result of the changed capacitance of the first trap filter due to availability, see Tab. 5.1. The current components of the parallel C-R damped system in blue do not show a significant rise near this frequency. The passive damping works well.

## 5.4.5 General Comments

The filter design method with theoretically calculated worst case converter voltage spectra is validated experimentally. Although only fundamental frequency inductance and capacitance models are utilised, the current spectra obtained from laboratory are similar to the predicted ones. Nevertheless, a safety margin to the grid code limits should be included in the filter design to increase to the probability of complying with the grid codes.
As seen in this section, several measurements at different operating points are necessary to get the real worst case spectrum.
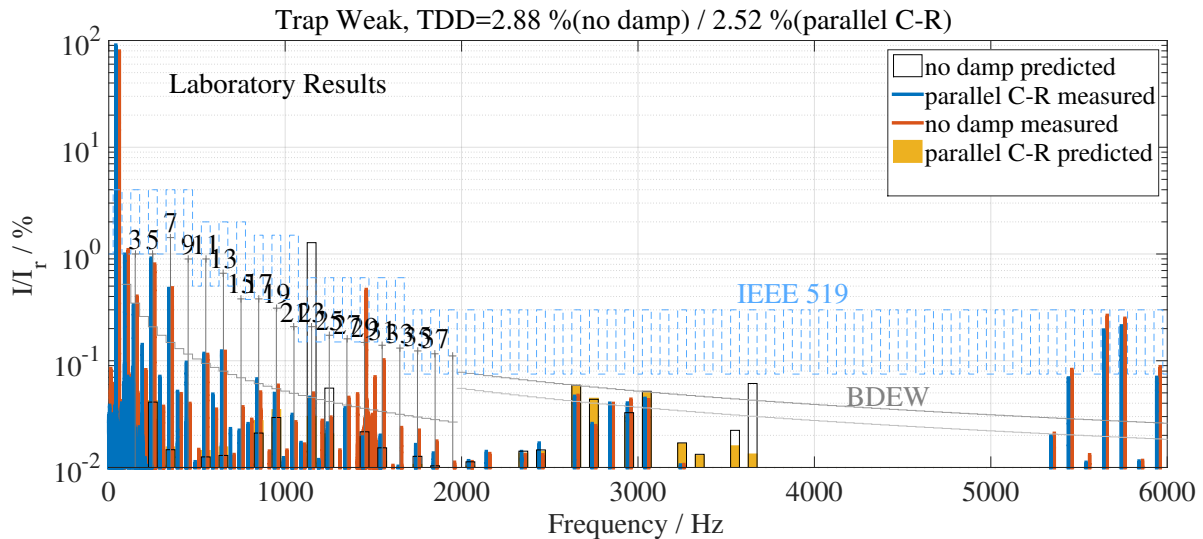
**Figure 5.13:** Laboratory (weak grid trap system): Worst case grid current spectrum related to rated current ($I_{r,lab} = 7.9\,A$) with harmonic grid codes and calculated currents for parallel C-R damping and undamped system

## 5.5 Valdidation of Current Control Design with Parallel C-R Damping for all Filters

As in the simulation, only the parallel C-R damped system results are shown. Similar reference dq current steps, as explained in Fig. 3.23, are taken for the experimental setup. The control is designed to work with a reference lowpass prefilter according to Eq. 3.8. The shown plots contain the signals including the prefilter. From the experiment without a prefilter the d and q currents are included in the (same) figures to demonstrate the proper functioning. The three-phase power values, which can be seen in the following plots, are computed according to Eq. 3.20. The current controller parameters according to Chap. 3.5.3 are adapted following Eq. 5.2. The PLL parameters are adapted according to the new grid voltage using Eq. 3.3.

1) Strong Grid Trap Filter

The experimental results can be seen in Fig. 5.14. In contrast to the simulation in Fig. 3.25, no grid voltage rise is analysed. At t=0 s, an active current step is imposed. The reference currents are only included for the experiment with prefilter. In (d), it can be seen that the step responses generally show the same dynamics as in the simulation (Fig. 3.25) and in the transfer function step response in Fig. 3.13 (d). This counts for active and reactive current steps. The control is also stable without a reference prefilter.

2) Weak Grid Trap Filter

The weak grid trap filter results are shown in Fig. 5.15. According to the designed control and prefilter, the settling time for the step responses is higher but still below one fundamental period ($\approx 10 - 15\,ms$). The power settling time $T_{\text{power}}$, as defined in the control design chapter, is near 20 ms. The results are very similar to the simulation and transfer function plots (Fig. 3.27 and Fig.3.15 (d)). The control without a reference prefilter has a high overshoot and strong couplings (only be seen in (d)). Nevertheless, it is stable.

3) Strong Grid LCL Filter

The results can be seen in Fig. 5.16. Again, they are very similar to the transfer function results in Fig. 3.10 (d) and the corresponding simulation results in Fig. 3.26. For the grid current only

**Figure 5.14:** Laboratory (strong grid trap): Control results from Control Desk except the converter, total shunt and grid current from oscilloscope ($\hat{I}_{\text{base}} = 19.5$ A, $\hat{U}_{\text{base,star}} = 188$ V), for all base values see Tab 5.1 (blue/red/yellow - phase a/b/c)
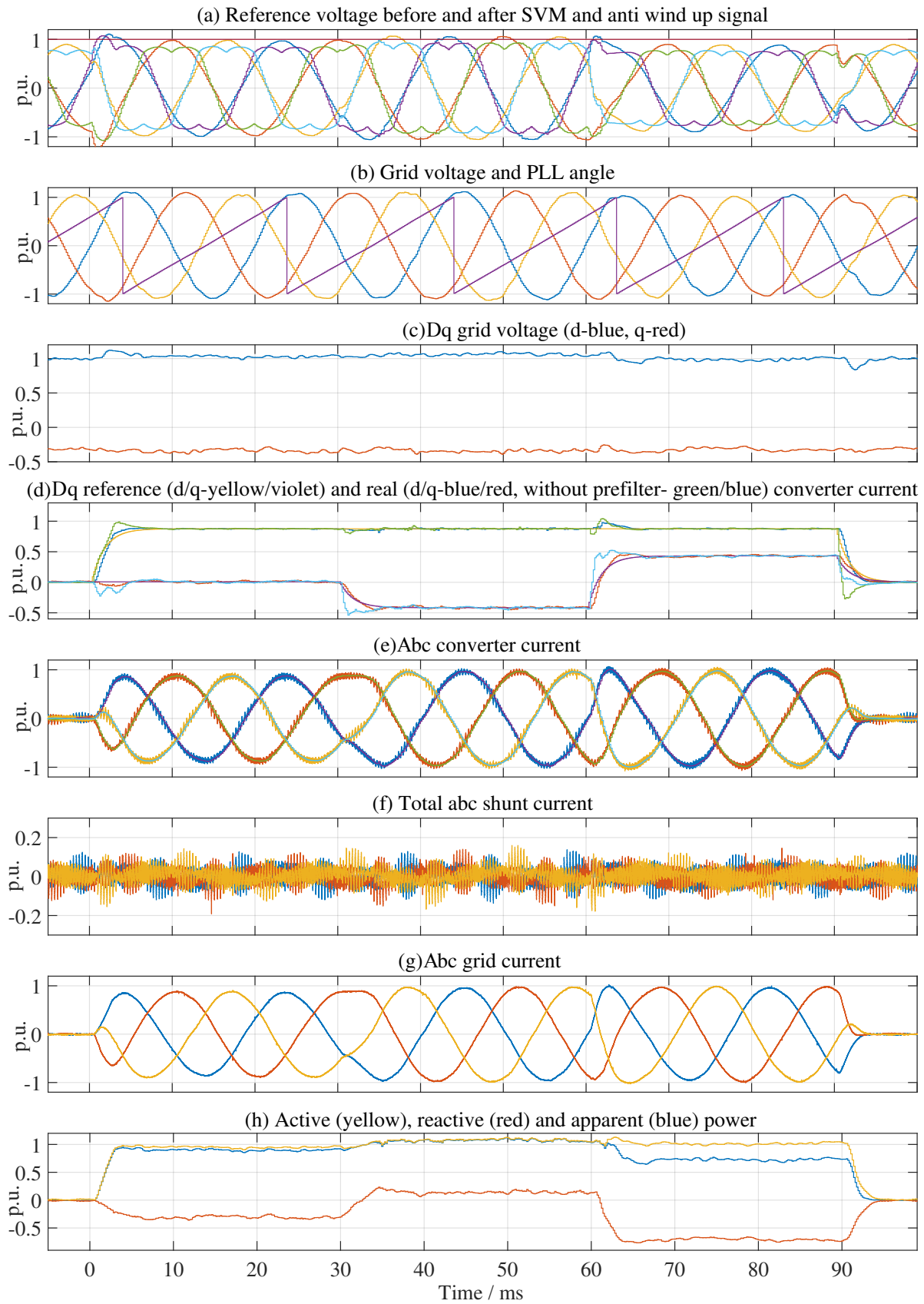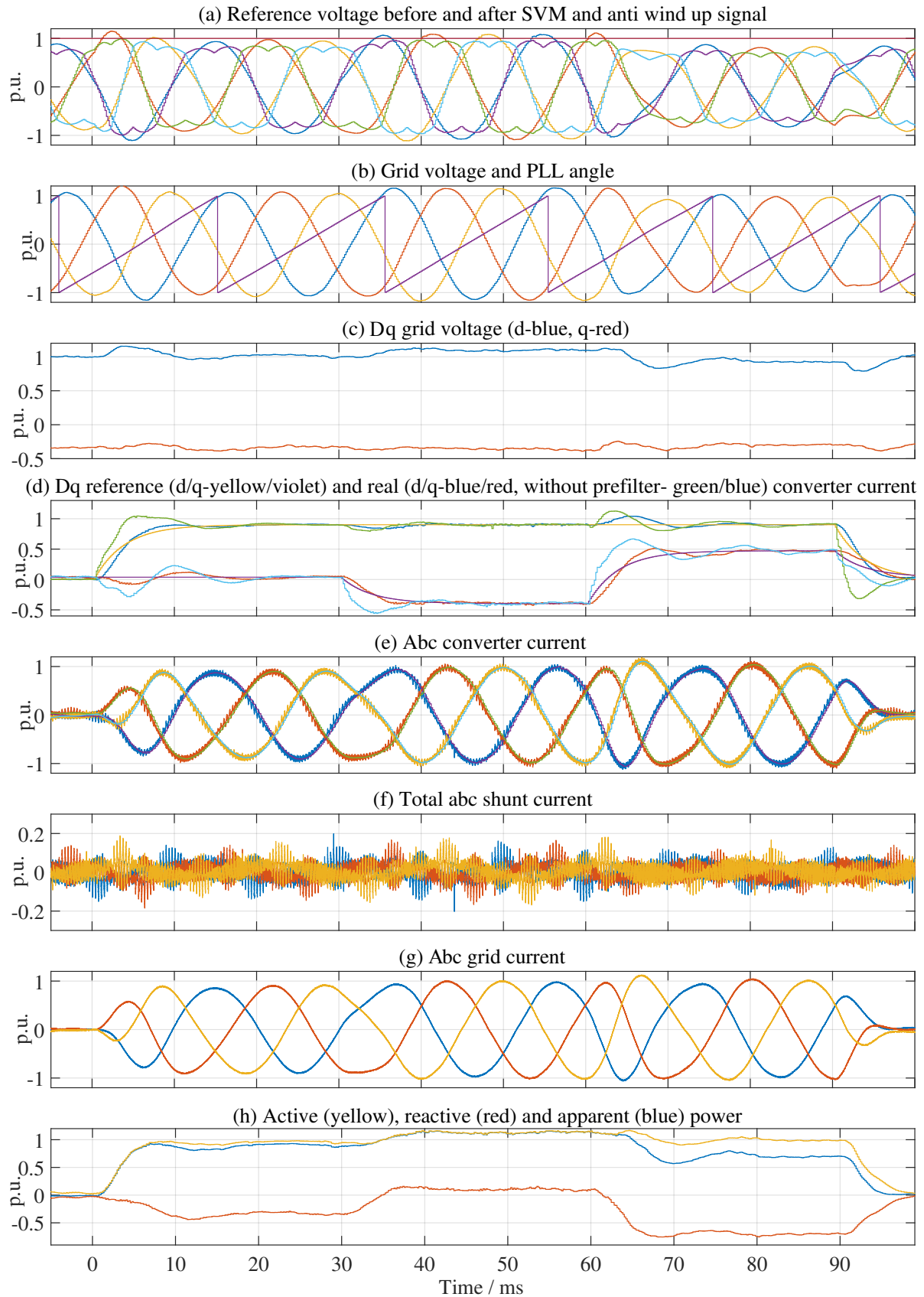
**Figure 5.15:** Laboratory (weak grid trap): Control results from Control Desk except the converter, total shunt and grid current from oscilloscope ($\hat{I}_{base}$ =11.2 A, $\hat{U}_{base,star}$ =188 V), for all base values see Tab 5.1(blue/red/yellow - phase a/b/c)

**Table 5.3:** Laboratory PI gains p.u. transformed from the 2 MW parameters according to Chap. 3.5.3

|  | Strong LCL | Strong Trap | Weak LCL | Weak Trap |
|---|---|---|---|---|
| $K_{\mathrm{PI,lab,base,parallelC-R}}$ | 7.46 | 14.17 | 7.55 | 9.09 |
| $K_{\mathrm{PI,lab,base,noDamp}}$ | 7.46 | 14.17 | 6.22 | 3.42 |
| $K_{\mathrm{PI,lab,base,activedamp}}$ | 5.57 | 14.17 | not utilised | 9.77 |

the measurement of one phase is available.

4) Weak Grid LCL Filter

As for the trap filter, the weak grid LCL control is designed with a higher settling time. Significant overshoots are seen for the experiment without a prefilter (see (d)). The control dynamics are again very similar to the simulation (Fig. 3.26) and transfer function step responses (Fig. 3.14).

The single-loop transfer function analysis, the three-phase simulation and the experimental setups result in very similar step responses. Therefore, it can be concluded that the simulation and transfer function models are sufficiently precise for the subsequent stability analysis.

## 5.6 Validation of the Filter Resonance Damping by Critical PI Gain Analysis

In Chap. 5.4, the designed systems are already validated regarding harmonic grid codes. In Chap. 5.5, the performance regarding current step responses of the parallel C-R damped systems is demonstrated. In this section, the intial task of the designed damping methods is validated. It is shown that for the damped systems, it is much more difficult to excite the filter resonance compared to the undamped system. Selected filter systems are analysed regarding the lowest PI gain, which brings the control loop to an oscillatory state. This PI gain is named the *critical PI gain*. For this analysis, all other parameters are left unchanged (especially the PI time constant). For a stable running control loop, the PI gain is increased until it becomes instable. The corresponding PI gain and the oscillation frequency of the (critically stable) currents are stored.

This method corresponds to a root locus analysis of the control loop [54]. The root locus shows the poles of the closed loop in dependency of the open loop gain, which corresponds to the PI gain. The critical PI gain is reached when a pole crosses the imaginary axis. Its frequency corresponds to the frequency of the measured currents at critical PI gain. A zoomed view of the root locus with second order Padé approximation of $\underline{G}_{\mathrm{PWM}}$ according to Eq. 4.4 can be seen in Fig. 5.18 (a). It is only provided for the strong grid trap system with parallel C-R damping. The pole evoked by the second trap filter near the top of the figure is not stability critical, because it stays in the left s half plane. One critical pole near 900 Hz and one near 1.8 kHz exist. Both cross the imaginary axis at similar PI gains. Below, it will be shown that in the experiment both frequencies are visible at the critical PI gain corresponding to the laboratory resistances in Fig. 5.18 (b). In Tab. 5.3, the nominal PI gains for the four filter types are listed.
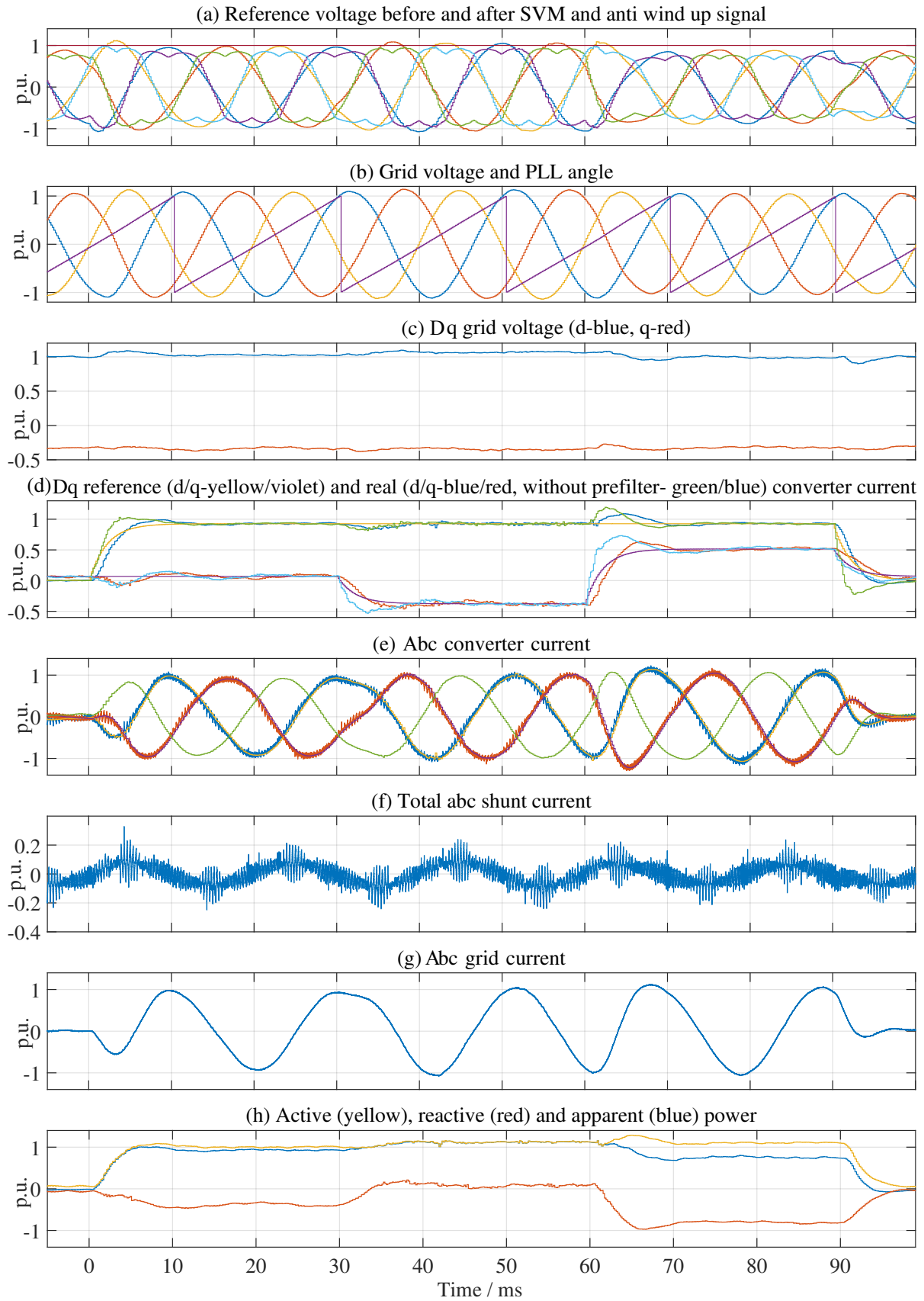
**Figure 5.16:** Laboratory (strong grid LCL): Control results from Control Desk except the converter, total shunt and grid current from oscilloscope ($\hat{I}_{\text{base}}$ =19 A, $\hat{U}_{\text{base,star}}$ =188 V), for all base values see Tab 5.1(blue/red/yellow - phase a/b/c)
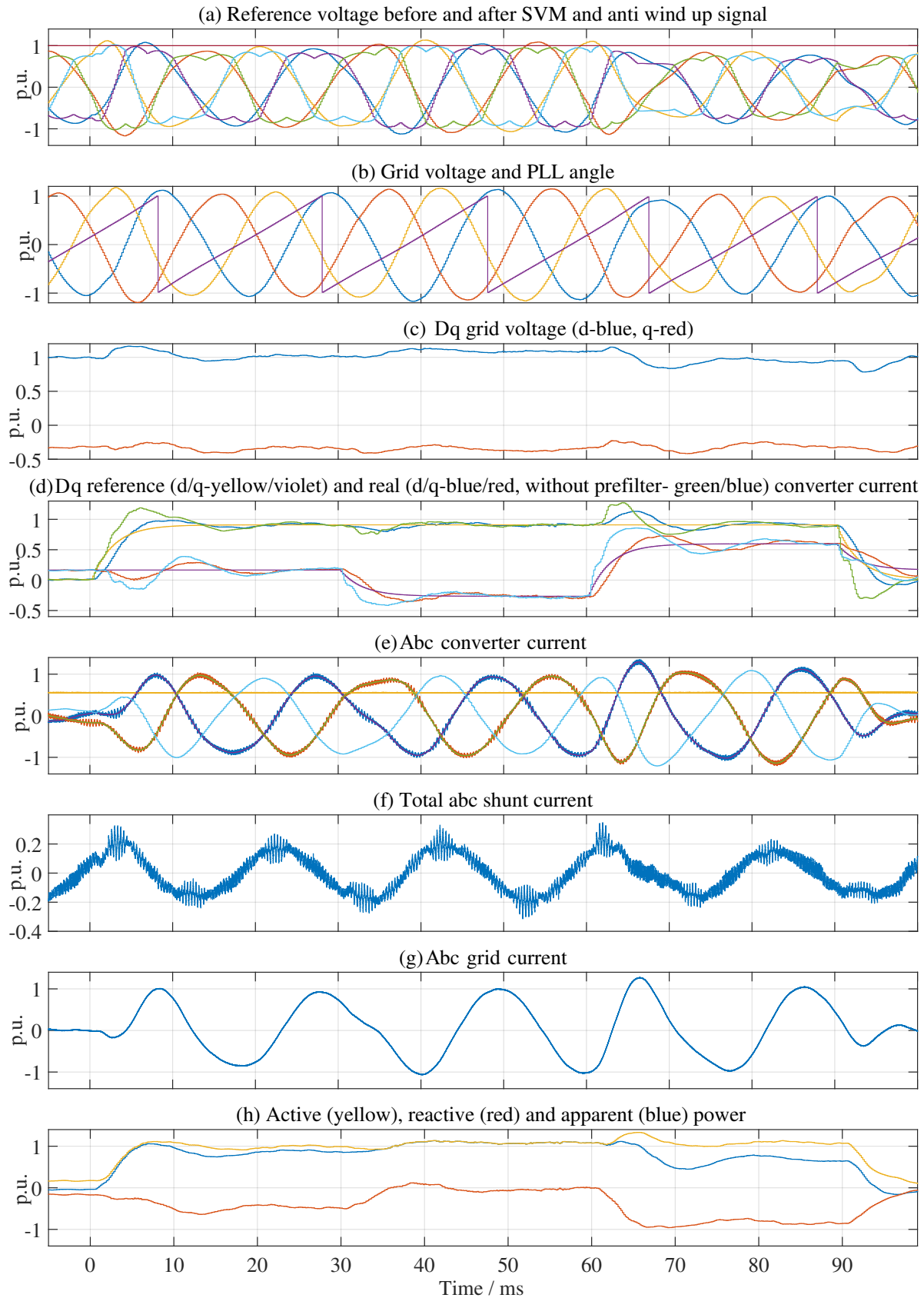
**Figure 5.17:** Laboratory (weak grid LCL): Control results from Control Desk except the converter, total shunt and grid current from oscilloscope ($\hat{I}_{\text{base}} = 15.8$ A, $\hat{U}_{\text{base,star}} = 188$ V), for all base values see Tab 5.1 (blue/red/yellow - phase a/b/c)
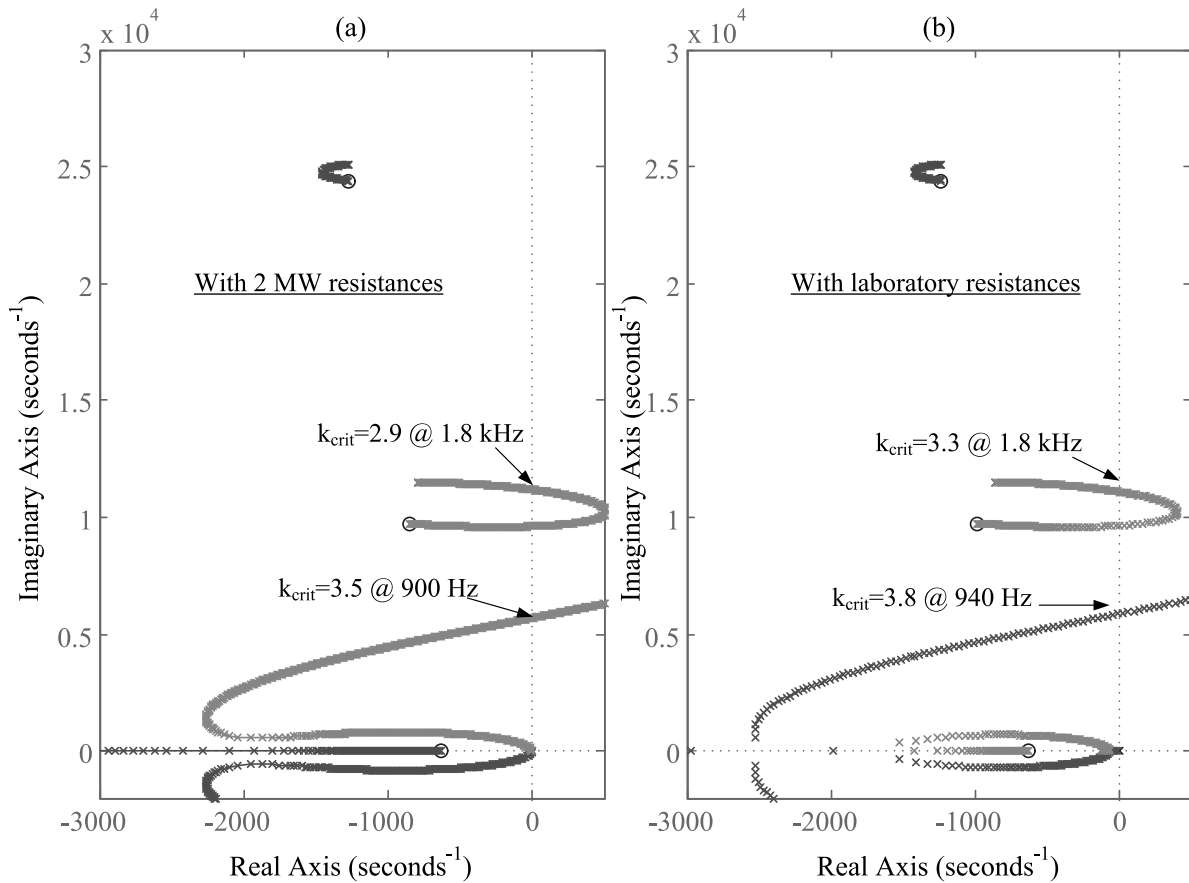
**Figure 5.18:** Zoomed view of the poles of the closed current control loop with varying PI gain (root locus) with normalised PI gain values ($k = 1$ corresponds to $k_{PI} = k_{PI,base}$) for strong grid trap system with parallel C-R damping with (a) 2 MW resistances and (b) laboratory resistances (SCR=50)

## 5.6.1 Validation of Passive Damping (Parallel C-R)

The analysis is discussed in detail for the strong grid trap system. Firstly, three-phase simulative results for the undamped and damped system are discussed and then compared to the experimental ones.

As seen in the control design section, the strong grid trap current control *without passive damping* is instable (first row in Fig. 3.13). It can be stabilised by decreasing the PI gain. It is found that in the simulation, the critical PI gain of the p.u.-transformed 2 MW undamped system is near 7 (Eq. 5.3).

$$K_{\mathrm{PI,undamped,critical}} = 7 \approx 0.5 K_{\mathrm{PI,lab,base,parallelC-R}} \tag{5.3}$$

In the simulation, the *parallel C-R damped* p.u.-transformed 2 MW system has a higher critical PI gain ($>> K_{\mathrm{PI,lab,base,parallelC-R}} = 14.17$).

This is intended to be validated in the laboratory. As seen in Tab. 2.7, the trap components remain the same for parallel C-R damping or no passive damping. Therefore, in the experimental setup, only the damping C-R branch has to be removed for the undamped system. A general finding is that the critical PI gains in the laboratory are significantly higher than in the simulation. Due to this fact no absolute validation is possible. Nevertheless, the findings can be validated in a comparative way. The critical PI gain of the damped system should be higher than the one of the undamped system. This is the case: For the undamped system, the critical PI gain is found to be $\approx 28 = 2 K_{\mathrm{PI,lab,base,parallelC-R}}$ while the damped system is $\approx 48 \approx 3.4 K_{\mathrm{PI,lab,base,parallelC-R}}$. The results for the parallel C-R damped system can be found in the next section in Fig. 5.23. In this section, only the experimental results for the undamped system are shown: In Fig. 5.19, the PI gain in (a) and the abc grid currents (b) are plotted. The PI gain is increased during operation. A value of approximately 34 (= twice the base PI gain) brings the control loop to instability. This can be seen from the rising oscillation in the three-phase currents. A reset of the PI gain to 26 stabilizes the control. As mentioned before, 28.1 is the critical PI gain. If the shown procedure is performed with 28.1, it will take significantly longer time to bring the control to oscillations. For better visibility, a slightly higher PI gain is chosen.

The effectiveness of the passive damping is validated. The low-power experimental setup has a higher critical PI gain with the passive damping branch than without. An *absolute* validation of the 2 MW control design is not possible, as the laboratory damping, resp. the laboratory ohmic resistances are much higher than the (p.u. transformed) 2 MW values. This is validated with the root locus, where the laboratory ohmic resistances are updated. The measured ohmic resistances, seen in Fig. 7.4, are included in the analysis. The ohmic resistances were measured for different frequencies. The values near the grid resonance frequency are taken at 1 kHz. Fig. 5.18 (b) shows the resulting root locus. It can be seen that the critical PI gain is increased to approximately $3.3 k_{\mathrm{PI,base}}$ which is in line with the experimental results.

The analysis is also carried out for the strong grid LCL, and the weak grid trap and LCL system. The results (Tab. 5.4) validate that the passively damped systems all have a higher critical PI gain than the undamped systems.
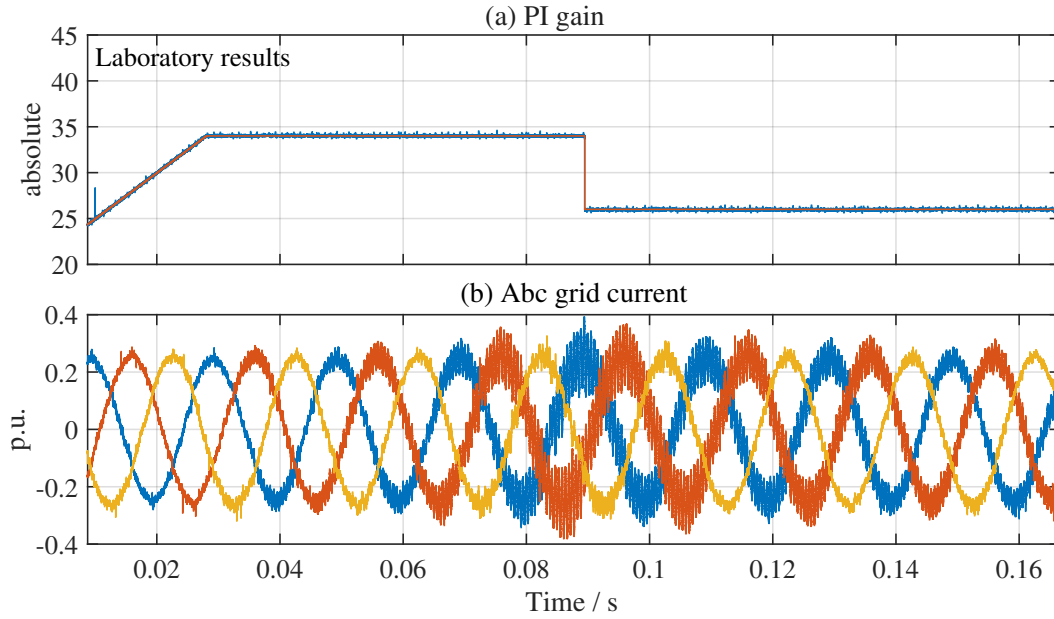
**Figure 5.19:** Critical stability test for the strong grid trap system without active nor passive damping

### 5.6.2 Validation of Active Damping

Again, as an example, the strong grid trap system is described. The results for the other systems are then summarised in a table. The current active damping method designed for the strong grid trap system is analysed with the laboratory setup. An adaption of the proportional factor to the experimental setup is necessary according to Eq. 5.4.

$$K_{\text{capIactiveDnew}} = K_{\text{capIactiveD}} \cdot \frac{Z_{\text{base,lab}}}{Z_{\text{base,2MW}}} \tag{5.4}$$

The new active damping coefficient is 11.24 compared to the 2 MW value of 0.25. This is first analysed by a laboratory simulation. Here, as a further improvement of the simulation model, not the p.u. transformed resistances, but those measured at the highest frequency available, are taken for the simulation. These resistance values can be found in the single-phase equivalent circuit (Fig. 7.3). The result is a simulative critical PI gain of $\approx 40 \approx 2.9K_{\text{PI,base}}$ which is higher (2.9 compared to 2) than the one of the undamped system. This validates that the active damping is implemented well. Due to the updated resistances, approximately the same factor is validated experimentally (Fig. 5.20). The hardware system is unchanged compared to the undamped system, only the active damping is introduced in the software. Due to availability, the converter currents are shown. The critical PI gain is significantly higher than for the undamped system. This validates the effectiveness of the designed active damping. Additionally, the spectrum of the converter current with active damping at critical PI gain is shown in Fig. 5.21. It can be seen that the most significant resonance frequency is around 900 Hz with almost 0.8 A amplitude. In addition, a resonance is evoked near 1750 - 2000 Hz.

The same procedure as for the strong grid trap system with active damping is carried out for all three other filters. The results are shown in Tab. 5.4. It can be seen that all active damping methods provide higher PI gains compared to the undamped system. This validates that the active damping is implemented well.

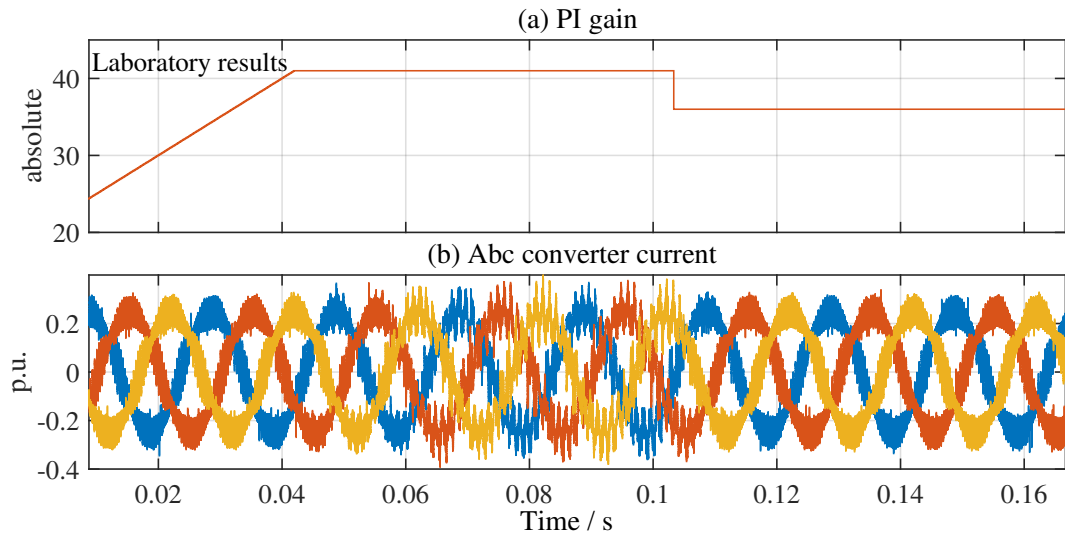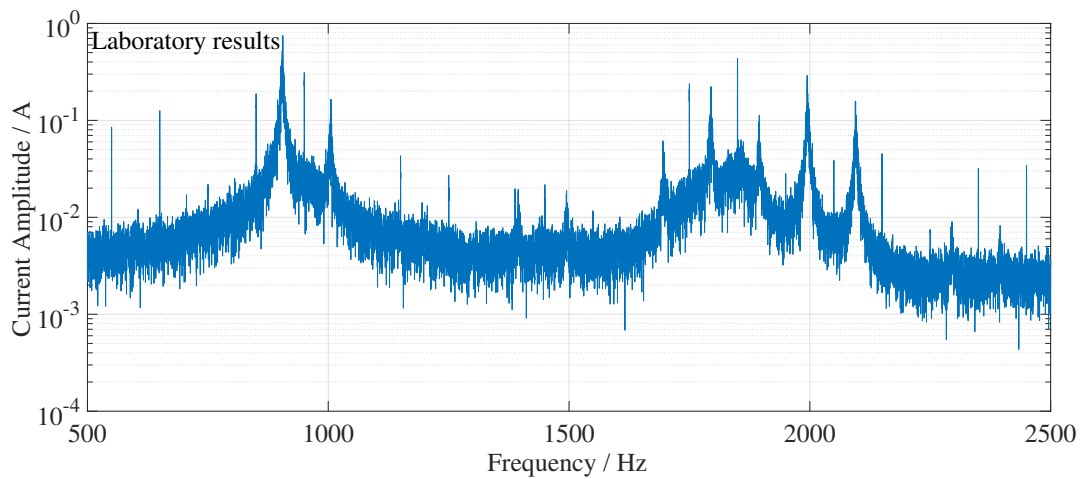**Figure 5.20:** Critical stability test for the strong grid trap system with active damping: Increased critical PI gain



**Figure 5.21:** Spectrum of converter current for strong grid trap system with active damping for critical PI gain of 39.9

**Table 5.4:** Critical PI gains (absolute values) in the laboratory with corresponding oscillating frequency

|                | Strong LCL     | Strong Trap          | Weak LCL      | Weak Trap      |
| -------------- | -------------- | -------------------- | ------------- | -------------- |
| undamped       | 15.1 @ 1103 Hz | 28.1 @ 1820 Hz       | 26.9 @ 915 Hz | 17.4 @ 1470 Hz |
| active damped  | 22.5 @ 1083 Hz | 39.9 @ 900 & 2000 Hz | not utilised  | 48.8 @ 1450 Hz |
| parallel C-R   | 19 @ 1118 Hz   | 47.8 @ 920 & 2000 Hz | 35.9 @ 930 Hz | 48.2 @1350 Hz  |

The designed active (shunt current feedforward) and passive (parallel C-R) damping methods can be compared regarding their critical PI gains. In the table, no clear tendency is seen as to whether the passive or active damping has higher critical PI gains. Both methods result in clearly higher gains compared to the undamped case and are therefore suitable damping methods.

# 5.7  Validation of Critical Stability Regarding Grid Resonance

In Chapter 4.4, the poles of the closed current control loop were analysed with respect to an LCL type grid impedance. Corresponding to Fig. 4.6, three grid parameters can be changed: the short circuit power of the connected grid SCR, the distance factor r for the location of the grid capacitance and the capacitance itself. In this way, a wide range of possible grid resonances is analysed, finding that most of the designed current controls remain stable. Specific combinations lead to instable loops. In the laboratory, only a few grid resonances can be analysed. If the experimental setup behaves as predicted for these cases, it is assumed to be the same for all other resonances.

The decrease of the X/R ratio (increased ohmic resistances) especially for (commercial) inductances leads to an unwanted high damping for the laboratory setup, compared to the 2 MW system. Consequently, critical PI gains are higher. Customised passive elements could approximate the 2 MW X/R ratios. This high effort is not necessary because: 1) The theoretical loop analysis can be validated by an increase of the resistances in the simulation and the transfer function analysis. 2) Destabilising grid resonances can be identified by a significant decrease of the critical PI gain compared to the system without grid resonance.

The stability analysis found, that grid resonances with resonance frequency near the -180° crossing frequency (frequency where the phase of the open loop transfer function crosses -180 degree) of the open control loop can be stability critical. Therefore, such grid resonances are analysed in the laboratory for the strong grid trap and for the weak grid LCL system. On the other hand, the non-critical operation with a grid impedance with a significant *lower* grid resonance frequency is also analysed. This is performed for the strong grid LCL system.

## 5.7.1  Strong Grid Trap Filter

Three different dampings are analysed: the parallel C-R damped, the undamped and the actively damped system.
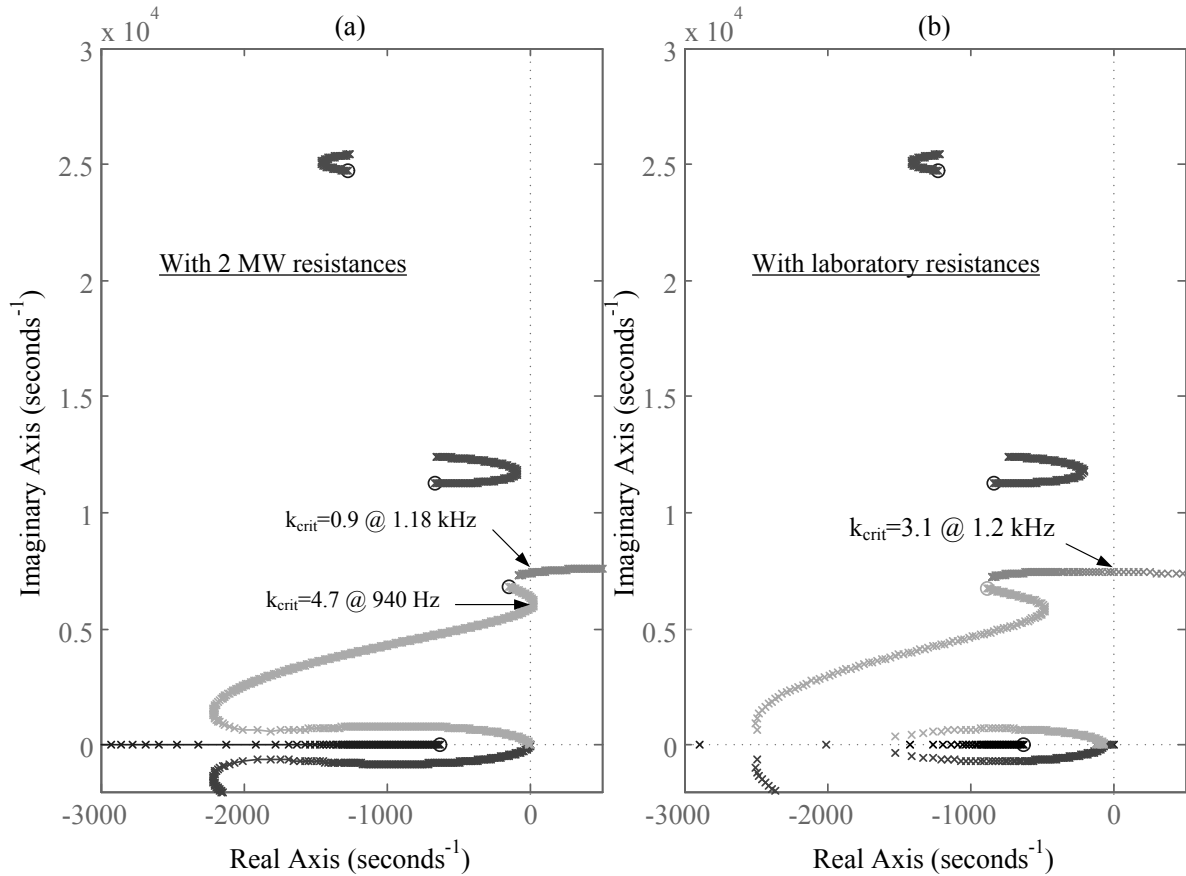
**Figure 5.22:** With grid resonance: Zoomed view of the poles of the closed current control loop with varying PI gain (root locus) with normalised PI gain values ($k = 1$ corresponds to $k_{PI} = k_{PI,base}$) for strong grid trap system with parallel C-R damping with 2 MW resistances (a) and with laboratory resistances (b) (SCR=50, r=0.32 and $S_{Cgrid} = 0.3$ *MVAr*

### Parallel C-R Damped System

The critical grid resonance with SCR=50, r=0.32 and $S_{Cgrid} = 0.3$ *MVAr* is realized in the experimental setup according to Fig. 7.4. It was also analysed in Fig. 4.12. This grid impedance evokes a resonance frequency of the open current control loop near the -180° frequency. This can be validated regarding Fig. 4.11 (c).

For the parallel C-R damped system, again, a root locus analysis is done. This is shown in Fig. 5.22. Compared to the root locus without grid resonance in Fig. 5.18, the lower branch is separated in two branches. The bottom branch crosses the imaginary axis at a significantly higher PI gain than the top branch. Below, it is shown that for the experimental critical PI gain test only the 1.2 kHz oscillatory frequency, resulting from the top branch, is seen. This is in line with the root locus analysis with updated laboratory resistances in Fig. 5.22 (b). Here, only one branch crosses the imaginary axis, which is the branch with 1.2 kHz.

In Fig. 5.23, the critical stability test for the system *without grid resonance* is shown. The PI gain is plotted in (c). Again, the converter and grid current are measured with the oscilloscope. The total shunt current in (f) is the result of the subtraction of converter and grid current. Near $t = 0.02$ *s*, the control is stable. Up to approximately $t = 0.04$ *s*, the PI gain is increased. The control remains stable, but slight oscillations are visible in the reference voltages in (a). In the following few milliseconds, the control becomes critically stable. This can be seen at the
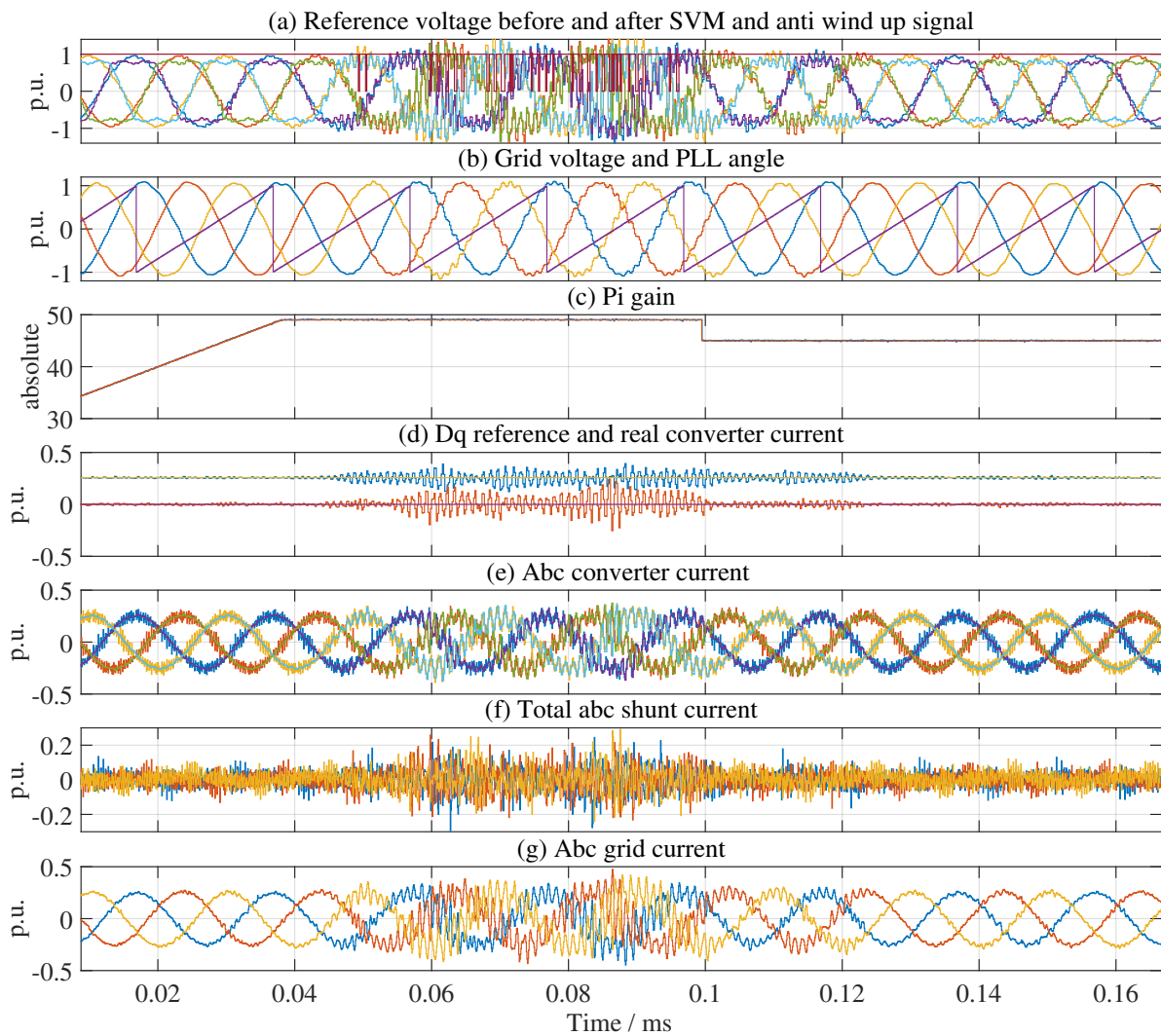
**Figure 5.23:** Without grid resonance: stability test for strong grid trap system with parallel CR damping
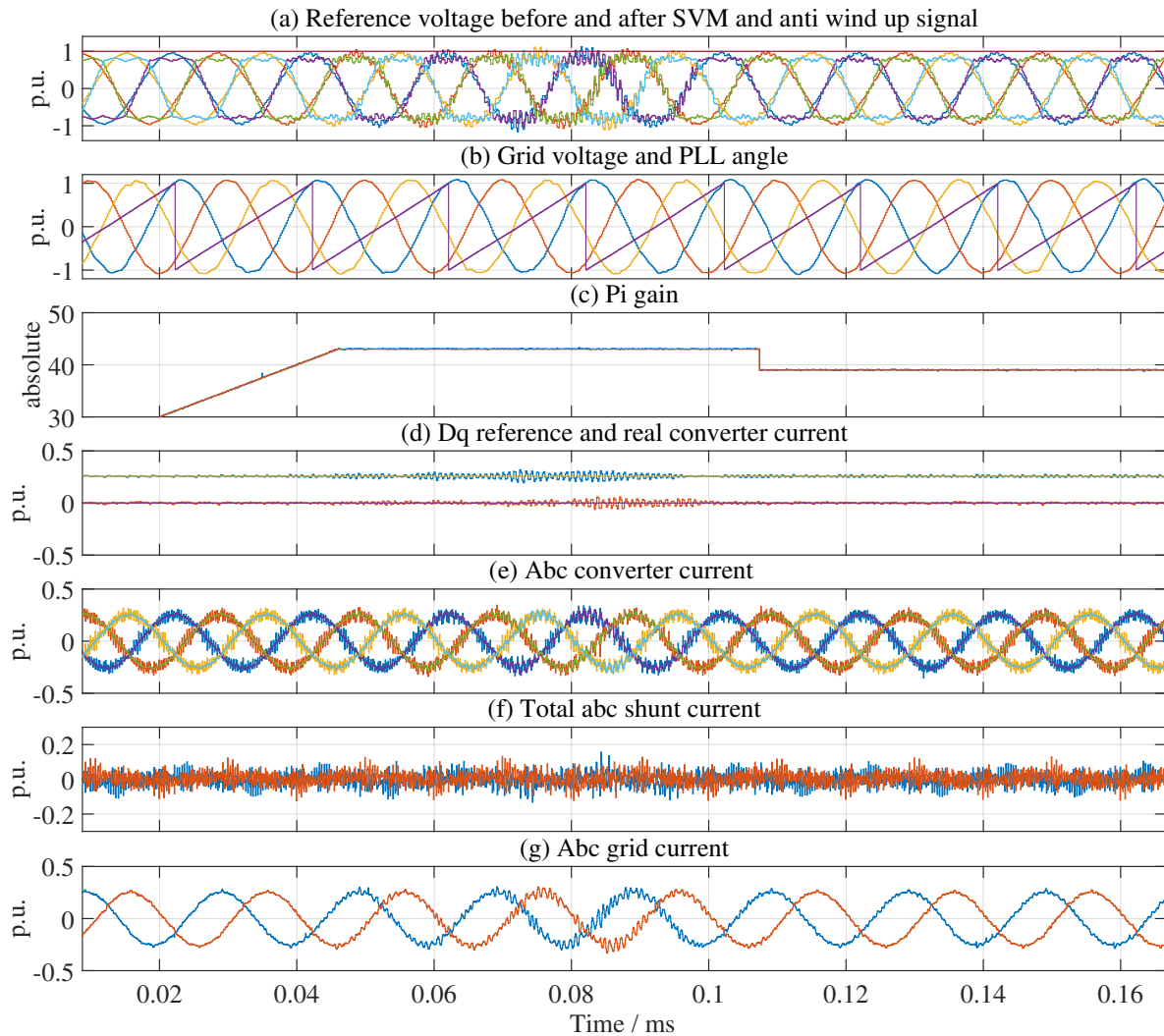
**Figure 5.24:** With grid resonance: stability test for strong grid trap system with parallel CR damping

converter currents in (d) and (e), the grid currents in (g) and, especially, in the reference voltages in (a). The control partly goes into saturation: the anti windup signal in (a) jumps temporarily to zero. It does not become totally instable. At $t = 0.1\ s$, the PI gain is slightly reduced to localize the critical PI gain. It can be seen that this slight reduction leads to a stable control.

The same procedure is performed *with grid resonance* (Fig. 5.24). Principally, the same behaviour is observed. The only difference is that the PI gain leading to instability is decreased compared to the system without grid resonance. To further validate that the introduced grid resonance leads to this decreased critical PI gain, the spectra of the converter currents are analysed.
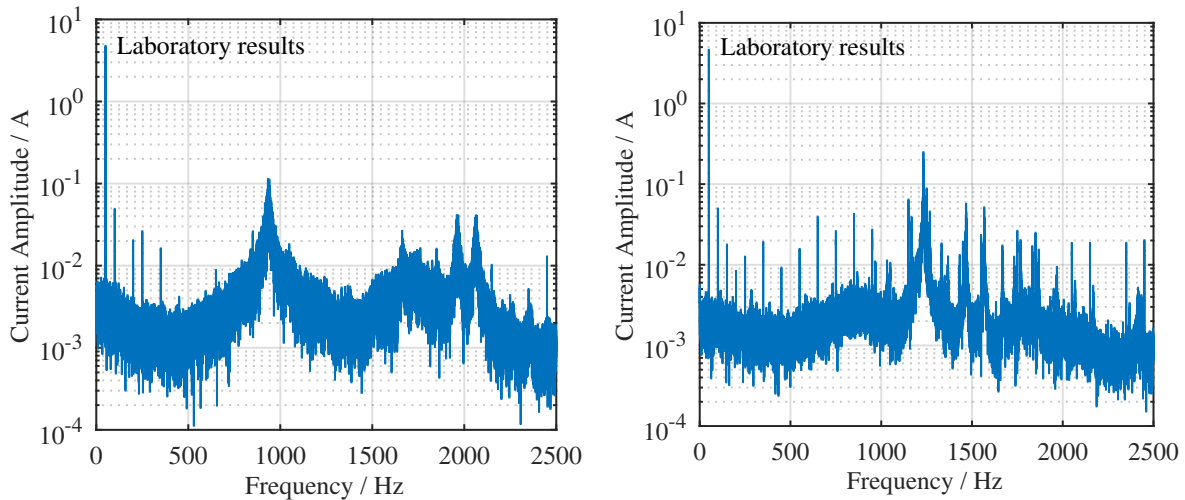
**Figure 5.25:** Converter current spectra at critical stability for strong grid trap system with parallel C-R damping. left: without grid resonance right: with grid resonance

The converter current spectra for the critical stability operating point for the system both with and without grid resonance are shown in Fig. 5.25. For the case *without grid resonance* (on the left side), a high peak appears near 950 Hz. As can be seen in Fig. 3.13, (d) this is the -180° frequency. Two additional peaks can be found near 2 kHz. This is the resonance frequency of the impedance $I_{grid}/U_{conv}$ of the first trap filter (compare Fig. 2.12 (b)). High current spectrum parts near 2 kHz have already been seen in the filter design section in Fig. 5.11 where the control is not instable. Also the corresponding magnitude-frequency plot of the open and the closed loop (Fig. 3.13 (d)) have a maximum point near 2 kHz. Both corresponding poles can also be seen in the root locus analysis in Fig. 5.18.

The converter current spectrum for the case *with grid resonance* on the right side shows, in contrast, high current components near 1250 Hz. Fig. 4.10 shows that this frequency correponds to the resonance frequency of the open loop including the grid resonance. The root locus analysis in Fig. 5.18 results in a similar frequency (1.2 kHz).

Below, a *comparison with the theoretical stability predictions regarding the p.u. transformed PI gain* is provided. A simulation for the laboratory setup including the grid resonance is performed with the updated passive element values (capacitances and inductances). Their ohmic resistances are left as calculated from the p.u. transformation. The critical PI gain is found to be approx. $1.07K_{PI,base}$ ($K_{PI,base} \approx 14$). For the 2 MW system, the designed control was already instable with $K_{PI,base}$, therefore its critical PI gain is below $K_{PI,base}$. This shows that already slight differences from the p.u. values change the stability performance.

As presented in Fig. 7.4, ohmic resistance measurements were performed for all passive elements for 50 Hz and 1 kHz. It can be seen that the intended resistances (blue) resulting from p.u. transformation of the 2 MW system are always smaller than the measured ones. Additionally, a frequency dependency is observed. The grid resonance in consideration is slighty above 1 kHz. Using in the simulation the 1 kHz resistances also leads to a higher critical PI gain of $2.5K_{PI,base}$. A similar critical gain is observed in the laboratory ($\approx 2.8K_{PI,base}$). Both in the simulation and in the experiment, the oscillating frequency is 1250 Hz (for lab see the left plot in Fig. 5.25). Therefore, the intention of the experimental analysis is reached: Predicted instabilities are also found in the three-phase measurement. Nevertheless, for 2 MW validation the X/R ratios have to be kept in mind.

**Undamped and Active Damped System**

Generally, it could be assumed that the undamped system would be deteriorated to a larger extent than the parallel C-R damped by the grid resonance. This is not the case: Including the grid resonance increases the critical PI gain from 28.1 to 45. This is supported by the frequency analysis of the converter current: No grid resonance frequency of 1250 Hz is found, only the -180° frequency and the filter resonance frequency. This shows that the specific grid resonance only deteriorates the parallel C-R damped system. The same applies to the actively damped system. The critical PI gain is increased compared to no grid resonance, and no grid resonance frequency part is found in the oscillating current.
The critical PI gains and corresponding oscillating frequencies are shown in Tab. 5.5. For the actively damped, undamped and parallel C-R damped system, the rated current and voltages are the same. Also their hardware components, except the additional parallel C-R damping branch, are identical. Therefore, their PI gains are comparable.

## 5.7.2 Strong Grid LCL Filter

For the strong grid LCL system, the -180° frequency is slightly above 1 kHz for all damping methods (see Fig. 3.10). Near 200 Hz, the phase margin is at its maximum. A grid resonance at 200 Hz is chosen to be analysed:

$$f_\infty = 200\,Hz \approx \frac{1}{2\pi}\sqrt{\frac{(L_{\text{trsf}} + rL_{\text{grid}}) + (1-r)L_{\text{grid}}}{(L_{\text{trsf}} + rL_{\text{grid}}) \cdot (1-r)L_{\text{grid}}C_{\text{grid}}}} \tag{5.5}$$

An SCR of 50 with r=0.2 and $S_{\text{Cgrid}} = 15$ MVAr would result in a resonance frequency near 200 Hz. The problem is that the resulting capacitance is 675 % of the rated capacitance and equals to 2.2 mF. The fundamental current in the capacitance would increase up to $6.75/\sqrt{3} \cdot I_{\text{r}} = 6.75/\sqrt{3} \cdot 13.4A = 52\ A$. The implemented sytem with cables, inductances and precharging resistances etc. has a maximum current of 20-30 A. Therefore, it is decided to implement a smaller capacitance of $330\mu F$ leading to a fundamental current of $I_{50,\text{Cgrid}} = 230\sqrt{1/32\pi50 \cdot 330\mu F} = 13.8\ A$. The resulting grid resonance frequency with r=0.16 is 448 Hz. This is still far below the -180° frequency of all damping methods (see Fig. 3.10) and therefore very acceptable regarding the intended validation. The resulting grid capacitance corresponds to 2.22 MVAr PFC power in the 2 MW world. This is in a realistic range (see Chap. 4.3.2).

**Parallel C-R Damped System**

Here, the question is: Is it correct that the analysed grid impedance with low resonance frequency is less stability critical than the ones with resonance frequencies near the -180° frequency? This is again validated by the critical stability test. In Fig. 5.26 and 5.27, it can be seen that the introduced resonance even increases the critical PI gain of the control ($\approx 23$ compared to $\approx 19$). The converter current spectrum only has a peak at the -180° frequency and no peak at
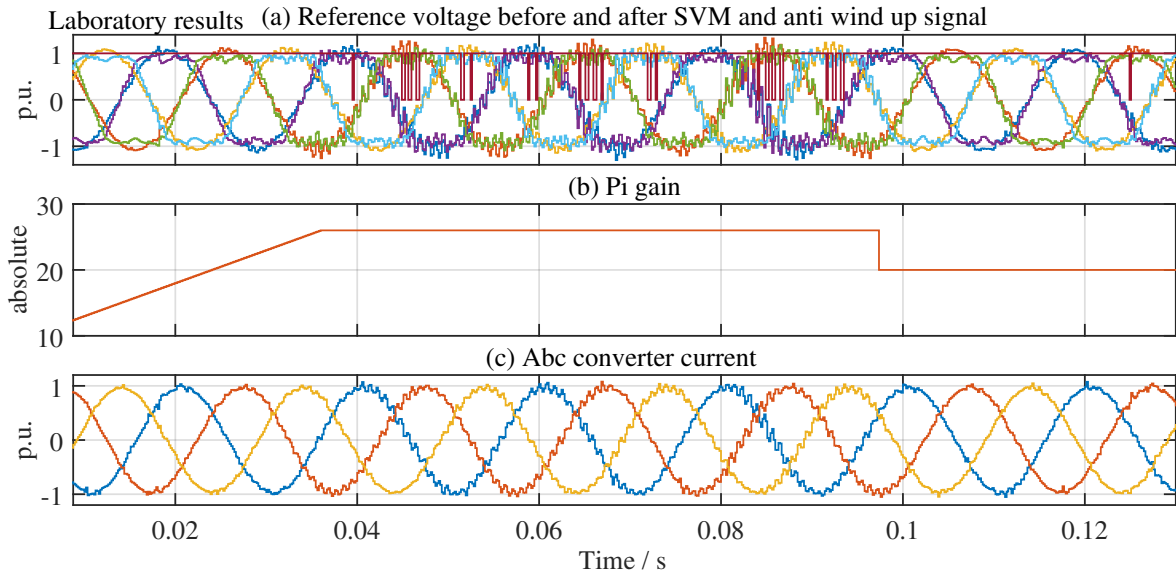
**Figure 5.26:** Stability test with grid resonance; strong grid LCL system with parallel C-R damping
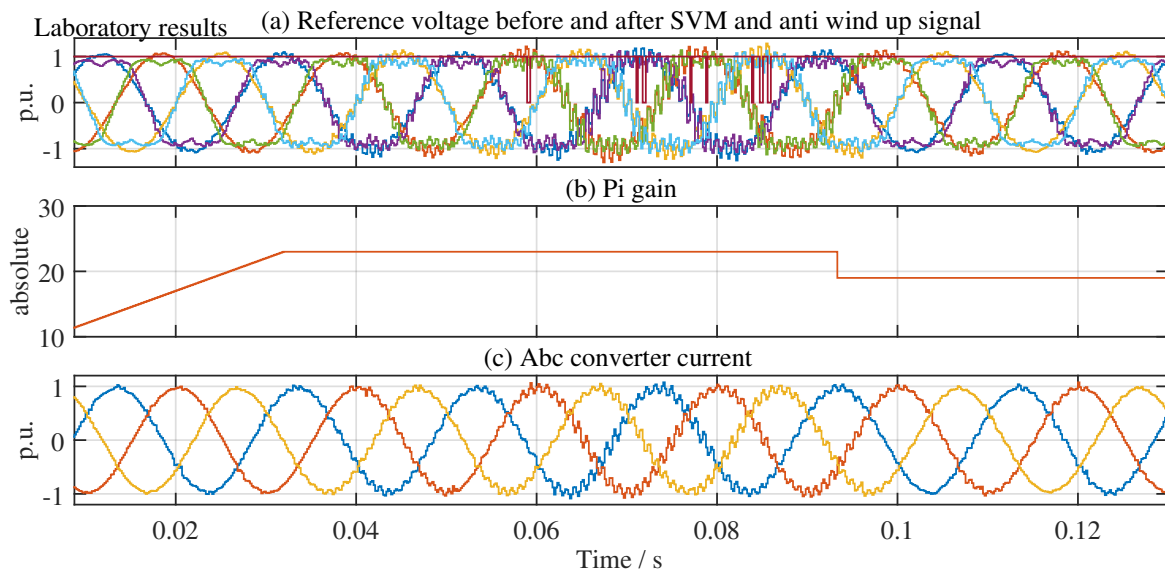


**Figure 5.27:** Stability test without grid resonance; strong grid LCL system with parallel C-R damping

the grid resonance frequency, see also Tab. 5.5. This supports the assumption that low frequency resonances are less stability critical than those with a resonance frequency near the -180° frequency of the control loop.

**Undamped and Actively Damped System**

The critical PI gain rises from approximately 14 (undamped system) to approximately 25 only by introducing the active damping. The active damping also enables higher PI gains with the grid resonance. Still no grid resonance frequency can be found in the oscillating currents.

### 5.7.3  Weak Grid LCL Filter

A grid resonance frequency, which is higher than the -180° crossing frequency of the OL, is chosen. Regarding Fig. 4.11, a combination of SCR=10, r=0.72, and $S_{\text{Cgrid}} = 0.21$ *MVAr* is taken. It results in an grid resonance frequency of 1062 Hz. The -180° frequency is 908 Hz.

**Parallel C-R damped System**

The analysed grid resonance is similar to the strong grid trap filter system where the -180° frequency is 905 Hz and the grid resonance frequency is 1324 Hz. The results are not similar: For the strong grid trap system, the critical PI gain is decreased by the introduced grid resonance. Here, for the weak grid LCL system, the critical PI gain is slightly increased (35.9 to 37) and the oscillating frequency is still the -180° frequency ($\approx 930$ *Hz*). This is supported by the stability analysis in Fig. 4.11 where significantly less instable poles are found for the weak grid LCL system in (b) than for the strong grid trap system in (c).

**Undamped System**

For the 2 MW design, the parallel C-R damping system has a higher converter-side inductance than the system designed without damping. In the laboratory, the converter side inductance must be reduced to 6.05 mH. Only a 6.16 mH is available. The undamped system shows the same behaviour. The grid resonance increases the critical PI gain (26.9 to 28) while the oscillating frequency approximately remains the -180° frequency of 915 Hz.

For the weak grid trap system, no grid resonance operation is analysed.

## 5.7.4 Overview and Conclusion

All critical PI gains and their corresponding oscillating frequencies for the systems with and without grid resonance are summarised in Tab. 5.5. The grid resonance frequencies, computed according to Eq. 5.5, are added as well as the -180° frequencies. The -180° frequencies are taken from the open loop plots in Chap. 3.5.3. The grid resonance frequencies are listed for the p.u. transformed and the real laboratory components. Moreover, the maximum point frequency $f_{\mathrm{mag}}$ of the open loop magnitude plots is added. The table also includes the base PI gains resulting from the p.u. transformation.

Based on the stability analysis in Chap. 5.7, the first intention was to validate the instabilities found for the strong grid trap system. In the laboratory, it was found that the configuration with the p.u. transformed PI gain was stable - in contrast to the 2 MW simulation and analysis. The higher damping of the laboratory setup was identified as the cause. A solution to estimate the robustness of the control is provided with the introduction of the critical PI gain. For the strong grid trap system, the critical PI gain is much higher than the p.u. transformed PI gain (47.8 compared to 14.17), which is summarised in the table. The result of the stability analysis was: the strong grid trap system is sensitive to grid resonances with a frequency near the -180° frequency. This is validated with the experimental setup: Only for the strong grid trap system, the critical PI gain is decreased with introduction of the grid resonance. In addition, the oscillating frequency changes to the grid resonance frequency.

For all other systems, the analysed grid resonances are not stability critical: For the strong grid LCL system, a grid resonance with 448 Hz resonance frequency was analysed. It even increases the critical PI gain, while no grid resonance frequency is visible. For the weak grid LCL system, the critical PI gain is also slightly increased.

**Table 5.5:** Summary of control-related experimental results. $K_{\text{PI,base}}$: PI gain resulting from p.u. transformation; $K_{\text{PI,crit}}$ experimental critical PI gain; $K_{\text{PI,crit,res.}}$ experimental critical PI gain for system with grid resonance; $f_{-180}$ frequency where the corresponding open loop phase (without grid resonance) crosses $-180°$; $f_{\text{max}}$ frequency of the maximum point of the open loop magnitude response (without grid resonance) ; $f_{\text{res,grid,p.u.}}$ grid resonance frequency (Eq. 5.5) computed with p.u. transformed values; $f_{\text{res,grid,lab}}$ grid resonance frequency computed with laboratory values

| | | Strong LCL | Strong Trap | Weak LCL | Weak Trap |
|---|---|---|---|---|---|
| Undamped | $K_{\text{PI,base}}$ | 7.46 | 14.17 | 6.22 | 3.42 |
| " | $K_{\text{PI,crit}}$ | 15.1 @ 1103 Hz | 28.1 @ 1820 Hz | 26.9 @ 915 Hz | 17.4 @ 1470 Hz |
| " | $K_{\text{PI,crit,res.}}$ | 14 @ 1173 Hz | 45 @ 930 Hz & 2000 Hz | 28 @ 915 Hz | - |
| Active D. | $K_{\text{PI,base}}$ | 5.57 | 14.17 | not utilised | 9.77 |
| " | $K_{\text{PI,crit}}$ | 22.5 @ 1083 Hz | 39.9 @ 900 & 2000 Hz | not utilised | 48.8 @ 1450 Hz |
| " | $K_{\text{PI,crit,res.}}$ | 25 @ 1150 Hz | 45 @ 930 & 2000 Hz | not utilised | - |
| Parallel C-R D. | $K_{\text{PI,base}}$ | 7.46 | 14.17 | 7.55 | 9.09 |
| " | $K_{\text{PI,crit}}$ | 19 @ 1118 Hz | 47.8 @ 920 & 2000 Hz | 35.9 @ 930 Hz | 48.2 @ 1350 Hz |
| " | $K_{\text{PI,crit,res.}}$ | 23 @ 1192 Hz | 41 @ 1200 Hz | 37 @ 928 Hz | - |
| " | $f_{-180}$ | 1089 Hz | 905 Hz | 908 Hz | 1183 Hz |
| " | $f_{\text{max}}$ | 957 Hz | 1863 Hz | 474 Hz | 1047 Hz |
| $f_{\text{res,grid,p.u.}}$ | | 442 Hz | 1281 Hz | 1070 Hz | |
| $f_{\text{res,grid,lab}}$ | | 448 Hz | 1324 Hz | 1062 Hz | |

## 5.8 Summary of Main Findings

The main findings of this chapter are summarised below:

- A low power simulation model is sufficiently precise to model the control behaviour of the laboratory hardware setup. The simulation's parameters have to be adapted to the laboratory values, particularly the resistances. In this case, critical PI gains and the control dynamic are very similar.

- The low power (20 kVA) setup is suitable (with some limitations) for validating results intended for a 2.2 MVA system. Generally, it needs to be kept in mind that the X/R ratios are higher and therefore methods as root locus have to be applied for a relative comparison.

- The instable operating point for the 2.2 MVA strong grid trap system, seen in Fig. 4.12, can also be found in the laboratory set up. It can be shown that this specific grid resonance decreases the critical PI gain of the system.

- The 2.2 MVA filter design results are compared and validated in p.u. values with the laboratory setup. The results are very similar to the predicted ones.

- As the basis for all stability analyses, the 2.2 MVA control design and step response simulations can be reproduced in laboratory. The step responses resemble the designed ones, clearly compared with p.u. values.

- A general influence of a grid resonance introduced to the designed controls cannot be found. In two cases, the critical PI gain is increased, while it is decreased in one case. The result is that the control being deteriorated or not is dependant on the grid resonance. This counts for the laboratory system, as here the critical PI gain was introduced, but is assumed to count also for the 2.2 MVA system.

- The designed active and passive damping methods increase or keep the critical PI gain at least in the same range. An exception is the strong grid trap system, where the critical PI gain is slightly decreased for the parallel C-R damped system, compared to the undamped system. Again, similar to the point before, this counts for the laboratory system, as here the critical PI gain was introduced, but is assumed to count also for the 2.2 MVA system.

- The analysed grid resonance with low resonance frequency is not stability critical, similar to the one with higher resonance frequency for the LCL weak grid system. Only the strong grid trap system is deteriorated by the introduced grid resonance. This corresponds to the 2 MVA stability analysis.

# 6  Conclusion

## 6.1  Generality of the Results

In this work 2 MW / 690 V systems are analysed in theory and simulation, while the experimental validation is done on a p.u. transformed low power 20 kVA / 230 V system. The differences between the power levels have been demonstrated. One question arises: are these results also valid for converter systems of other power classes?

The filter and control design is valid for all systems having the same p.u. values. But the X/R ratios of the passive components for lower power classes decrease, so in this case the p.u. values are slightly changed. Therefore a general statement cannot be given here, but it is assumed that also for low power systems a decrease of the current control bandwidth stabilizes the control regarding grid resonances. For the low power laboratory setup, this is demonstrated here.

The developed grid impedance including a resonance is suited for the medium voltage grid. Therefore, here, an adaption of the analysis would be necessary for other grids.

It is obvious, that the generality question cannot be answered totally. Another point is that wind turbine systems differ in several points which also prevent a general statement:

1. Control/Switching frequency: With increasing power (for example 5 MW), lower switching frequencies are sometimes used. In this case a new current control has to be designed, and also the analysis regarding grid resonances has to be redone.

2. Filter Design: Although this work already covers several filter types, for different filter designs or different filter topologies the analysis has to be renewed.

3. Converter Topology (two level, three level, multilevel, ... ): Different converter topologies are applied for full sized wind turbines. A different converter topology most times also involves different filter designs and therefore needs a new analysis.

4. Different Voltage Levels: Also medium voltage converters are more and more applied for high power wind turbines. In this case again the X/R ratio of the passive components is different. It should be assumed that these systems are damped less, therefore they could be more sensitive to grid resonances.

The present analysis covers 2 MW systems. A relatively easy control loop analysis regarding the stability with grid resonances is provided. It is also shown how the results can be validated with a low power setup. This can be applied quickely to other systems, also examining whether a current control bandwidth decrease stabilises the control.

## 6.2 Conclusion and Outlook

This work is a contribution in the field of wind turbine current control stability analysis with grids containing arbitrary grid resonances. The analysis is kept as close as possible to a real 2 MW wind turbine system. All parameters for this power class are investigated. Trap and LCL filter topologies are developed, one for a weak and one for a strong grid. They are validated experimentally. The dq current control is designed in a standard way. For weak grids it is important to include three-phase simulations and the PLL bandwidth in the design process.

For experimental validation, it is important, that the high power systems (2 MW) have higher X/R ratios than the p.u. transformed laboratory equivalents. This leads to different stability analysis results in the laboratory. Additionally, it is found that the grid voltage measurement for synchronization has to be low pass filtered. If this is not done, the maximal control bandwidth is reduced. The analysis is done for the positive sequence control, while it is also valid for negative sequence control as here exactly the same controllers are utilised.

An important result of the thesis is that with the shown simple transfer function control loop description, valid stability analyses can be performed. No complex integration of the PLL in the analysis is necessary.

Only grids with resonances near the frequency where the phase of the open loop crosses -180 ° are stability critical.

Nevertheless, the overall conclusion of the thesis is that with a good control design all possible grids with resonances can be handled. No additional control parts have to be introduced for stability. Hereby, the dynamic of the current control remains in grid code conforming range: setpoint changes can be followed in time ranges below 20 ms.

During the work several topics could not be considered in more detail. They are listed below to provide stimulation for further research.

The present work analyses a wind turbine connected to a particular medium voltage grid. Often, wind turbines are connected in wind parks to a high voltage grid. The next step on the way to a complete wind park stability analysis would be to apply methods which include several grid connected wind turbines. To do so, the converter systems and controls designed in this work could be used. One way would be to use impedance models for the different turbines.

In this work, only symmetrical grid impedances have been considered. An analysis concerning unsymetrical grid impedances, also including resonances, would be of interest.

Additionally, harmonic distortion resulting from an overlayed grid has only partly been considered. The influence of distorted grids with harmonics on the turbine converters for example of this thesis would be of interest, too.

For all analysis (the filter design and the control design and stability analysis), most of the time fundamental frequency models for the passive elements have been applied. For the filter design, the experimental validation showed, that despite this simplification the spectrum results are as predicted. A theoretical proof that all higher frequency effects like skin and proximity do not play a big role in this frequency range, would be of interest. This also counts for the turbine transformer.

For the present analysis, it has been assumed, that the DC link capacitance is high enough to exclude the DC link voltage control from the analysis. Also for wind turbine converters, it is desirable to reduce the DC link capacitance as much as possible due to cost. For low DC link capacitances the dc link control should be included in the analysis.

Scientific work, this work also, underlies a learning process. For future stability analyses, it is recommended that not only the location of the closed loop poles is analysed, but rather the

critical PI gain. This can be automated using the root locus.

Although the stability analysis for weak grids without PLL corresponds to the experimental results, during the current controller design process the PLL had to be taken into account. In this work, this is carried out by comparing the simulative results. This is at huge time cost. Here, a transfer function control loop model including the PLL would help to directly analyse the PLL influence. Also the influence of the grid voltage low pass filter could be analysed theoretically.

The topic of measurement signal filtering is often neglected in publications. This stands in contrast to the fact, that for all control loop designs and analysis it is essential to know how the current or voltage is measured. The signal filter is a significant part in the main control loop. This counts also for higher harmonics control.

The present analysis is done for an asymetrical regular sampled PWM. Standard wind turbine converters could also run with symmetrical regular sampled PWM. For the present case this would lead to a Nyquist frequency of 1.425 kHz. An analysis for this system could also be of interest.

In this work, the unfiltered, carrier-synchronised sampled converter current is used for the control. Other methods such as an oversampling mean value filter which leads to a delay would be of interest for the same stability analysis.

For the filter design only inductive grids have been considered. A filter design being valid for grids containing resonances would also be of interest.

The control loop analysis in this work does not include the PWM. Switching effects exciting the resonance of a grid could deteriorate the control. This effect should also be considered.

In this work, only passive or active damping methods have been investigated. The inclusion of active damping for an already passively damped system is no increase in cost and could improve the system performance.

The solution to provide stable current controllers despite a grid containing grid resonances was to decrease the bandwidth of the control. In this context, it would be interesting to analyse the influence on a standard harmonic (5th, 7th, ...) controller.

In previous publications grid voltage feedforward (GVFF) was found to be a stabilizing element for the grid current control. In literature, there is argument regarding its advantages and drawbacks. [37] showed a simple way to include it in the transfer function model. Therefore, a deeper analysis concerning the usefulness of GVFF would be of interest.

More complex grid resonances could also be analysed.

The stability criterion presented in [96] experiences wide interest in power engineering. It would be interesting to prove the equivalence of this stability criterion with the simple control loop analysis utilised in this thesis.

As a high percentage of the wind turbines being installed are DFIG turbines, corresponding stability analyses for DFIG turbines should be performed. Here, the directly grid connected generator has to be included in the analysis.

The model which has been developed in this work could be used as reference model for further research, advanced control methods, other PLL structures etc.. All steps and all data is described so it is straightforward to reproduce the results. The author can be contacted via mail@felix-fuchs.de.

# 7 Appendix

## 7.1 Data of Commercial Wind Turbine Transformers

For wind applications, for example the GEAFOL transformers are applied [15]. For some transformers mentioned in [111] X/R ratios and $u_x$ are calculated here. $u_k$, $P_0$ and of course $S_{trsf,r}$ are given in the data sheet. X/R, $u_x$ and $u_r$ ratio are calculated according to Eq. 7.1, 7.2 and 7.3. All data is shown in Tab. 7.1. It can be seen that the X/R ratio varies between 26 and 52. An X/R ratio of 40 is decided to be a good approximation for the present 2 MW system. Some power ratings appear twice. In this case the transformer is also available in a low loss/ low noise version. The $u_x$ value is near $u_k$ and validates the approximation $u_x \approx u_k = 6\%$. The $u_r$ value respectively $R_{trsf}$ varies between 0.116 % and 0.232 %. A value of 0.15 % seems to be a good compromise.

$$\frac{X_{trsf}}{R_{trsf}} = \frac{u_x}{u_r} = \frac{\sqrt{u_k^2 + u_r^2}}{u_r} = \frac{\sqrt{u_k^2 + (\frac{P_0}{S_{trsf,r}})^2}}{\frac{P_0}{S_{trsf,r}}} \tag{7.1}$$

$$u_x = \sqrt{u_k^2 - (\frac{P_0}{S_{trsf,r}})^2} \tag{7.2}$$

$$u_r = \frac{P_0}{S_{trsf,r}} \tag{7.3}$$

## 7.2 X/R Ratio/Parasitic Resistance of Commercial Filter Inductances

In this work, a series resistance and inductance is utilised to model a filter inductance. For inductances, it is possible to distinguish between winding and core losses. They can be influenced by the inductance design. For this work, commercially applied inductances are of interest. Therefore, a data sheet review is performed. Although in practice even higher dampings/resistances are found than in literature/data sheets [51], these values give a starting point. In some data sheets (for example [112]), winding and core losses are listed separately. For the

**Table 7.1:** X/R, $u_x$ and $u_r$ of transformers mentioned in [111]

| $S_{trsf,r}$ /MVA | $u_k$ /% | $U_{r,lv}$ /V | $U_{r,hv}$ /kV | $P_0$ /W | $X/R^{50\ Hz}$ | $u_x$/% | $u_r$/% |
|---|---|---|---|---|---|---|---|
| 2 | 6 | 400 | 10 | 3500 | 34 | 5.997 | 0.175 |
| 2 | 6 | 400 | 10 | 2600 | 46 | 5.98 | 0.13 |
| 2 | 6 | 400 | 20 | 4000 | 30 | 6 | 0.2 |
| 2 | 6 | 400 | 20 | 2900 | 41 | 5.945 | 0.145 |
| 2.5 | 6 | 400 | 10 | 4300 | 35 | 6 | 0.172 |
| 2.5 | 6 | 400 | 10 | 3000 | 50 | 6 | 0.12 |
| 2.5 | 6 | 400 | 20 | 4000 | 38 | 6 | 0.16 |
| 2.5 | 6 | 400 | 20 | 2900 | 52 | 5.9972 | 0.116 |
| 2.5 | 6 | 400 | 20 | 5000 | 30 | 6 | 0.2 |
| 2.5 | 6 | 400 | 30 | 5800 | 26 | 5.9856 | 0.232 |
| 3.15 | 6 | 400 | 10 | 5400 | 35 | 6 | 0.1714 |
| 3.15 | 6 | 690 | 10 | 5400 | 35 | 6 | 0.1714 |
| 3.15 | 6 | 400 | 20 | 6000 | 32 | 6 | 0.19 |
| 3.15 | 6 | 690 | 20 | 6200 | 31 | 6.00317 | 0.197 |
| 3.15 | 6 | 3300 | 20 | 7300 | 26 | 6.002 | 0.232 |

18 $A$ inductance, the distribution is 85% winding and 15 % core losses, for 800 $A$ it is 66% against 33 % core losses. In other data sheets ([113] and [114]) this ratio is taken to divide the total losses into core and winding losses. Only winding losses are considered to compute the series (parasitic) resistance. In Tab. 7.2, the characteristics of different air cooled, commercially available inductances are listed (in bold values taken from the data sheet). It can be seen that the percentage losses (total losses related to their apparent power) are generally higher for the low current inductances than for the high current ones. The X/R ratio is between 43.8 and 59.8 for the high current inductances. Therefore, an X/R ratio of 50 for the inductances of the present 2.22 MVA system is decided to be a good choice. This is in line with [21]. The shunt inductances used in the trap filters and damping circuits are designed to smaller currents because the fundamental current mainly flows into the grid. Here, an X/R ratio of 20 is decided to be a good approximation.

The low current inductances (also those used in the laboratory in this work) have much smaller X/R ratios leading to higher damping. Considering the control analysis, this must be considered (as done in this work). A direct transformation from high to low power is obviously keeping the same X/R ratio which is not possible with low current rated inductances. One solution is to utilise higher current inductances in the laboratory. If it is not exactly the system behaviour, but the control principle that needs to be validated, an inclusion of the higher resistances within simulation and theory is also a solution.

**Table 7.2:** Characteristic parameters of different high and low current inductances (bold values are from data sheet, X/R at 50 Hz)

| | $I_r$ /A | $U_r^{l-l}$ /V | $L$ /µH, /% | $R$ /mΩ, /% | $P_{loss}^{winding} + P_{loss}^{core}$ /W | /% | $X/R$ |
|---|---|---|---|---|---|---|---|
| Siem.[115] | **800** | **690** | **27.9** ‖ 1.76 | 0.02 ‖ 0.004 | **384+190** | 0.06 | 43.8 |
| EPA[113] | **1100** | **400** | **30** ‖ 4.49 | 0.19 ‖ 0.09 | **1000**·(0.$\overline{6}$+0.$\overline{3}$) | 0.13 | 49.5 |
| TDK[114] | **418** | **520** | **120** ‖ 5.2 | 0.63 ‖ 0.09 | **495**·(0.$\overline{6}$+0.$\overline{3}$) | 0.13 | 59.8 |
| Siem.[112] | **18** | **400** | **1120** ‖ 2.7 | 40 ‖ 0.3 | **39+7** | 0.37 | 8.8 |
| EPA[113] | **21** | **400** | **1400** ‖ 4 | 42 ‖ 0.4 | **60**·(0.85+0.15) | 0.41 | 10.6 |
| TDK[114] | **22** | **520** | **1130** ‖ 2.6 | 21 ‖ 0.2 | **35**·(0.85+0.15) | 0.18 | 17.3 |

## 7.3 Parasitic Resistance of Commercial Capacitances

The parasitic inductance of the capacitance is neglected. For the present case, the parasitic series resistance of the capacitances is found to be significantly higher than the parasitic resistance of inductances. Resistance values between $1.7 - 8$ $m\Omega$ for capacitances in the range of $10 - 250$ $\mu F$ are found [116]. The trap filter capacitances are in this range. No dependency of the resistance on the capacitance can be observed. Therefore, 4 $m\Omega$ is decided to be a good approximation. The LCL filter capacitance is higher, and ranges between $1000 - 2300 \mu F$. With the parallel connection of four and nine 250 $\mu F\|2.3$ $m\Omega$, the series parasitic resistance can be approximated to 2.3 $m\Omega/4 = 0.56$ $m\Omega$ and 2.3 $m\Omega/9 = 0.26$ $m\Omega$. These values are decided to be a good approximation.

## 7.4 Minimal DC Link Voltage Computation for Filter Design

The minimal DC link voltage utilised for the filter design in Chap. 2.8 and 2.9.1 is computed according to a single-phase 50 Hz AC phasor calculation. At the medium voltage side of the transformer, a voltage increase of 10 %, rated apparent power (2/0.9 MVA) at a $cos(\varphi) = 0.9$ overexcited is assumed (Fig. 7.1). The grid voltage is assumed to be real valued. With the data of the filter and Eq. 7.4, the corresponding converter voltage is computed. This converter voltage can be adjusted with different DC link voltages and corresponding modulation indices. In this work, the minimal DC link voltage is defined for SVM modulation. Here, the maximum modulation index is $2/\sqrt{3}$ and the voltage is computed with Eq. 7.5.

$$\underline{U}_{\text{shunt}} = \underline{Z}_{\text{trsf}}^{50Hz} \underline{I}_{\text{grid}} + U_{\text{grid}}$$
$$\underline{I}_{\text{shunt}} = \underline{U}_{\text{shunt}}/\underline{Z}_{\text{shunt}}^{50Hz}$$
$$\underline{U}_{\text{conv}} = \underline{Z}_{\text{conv}}^{50Hz}(\underline{I}_{\text{shunt}} + \underline{I}_{\text{grid}}) + \underline{U}_{\text{shunt}} \qquad (7.4)$$
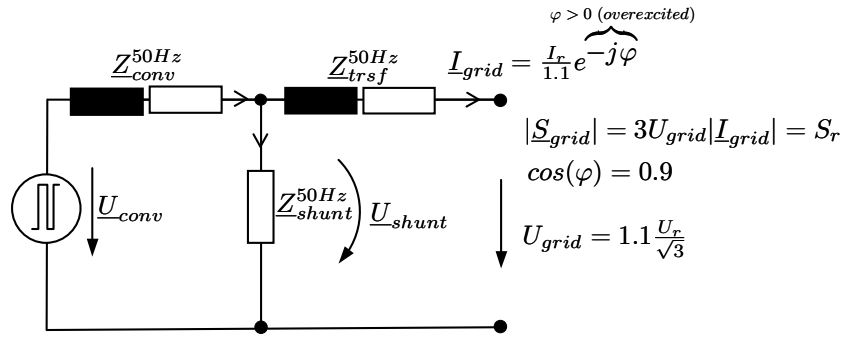
$\varphi > 0$ *(overexcited)*

$\underline{Z}^{50Hz}_{conv}$ $\underline{Z}^{50Hz}_{trsf}$ $\underline{I}_{grid} = \frac{I_r}{1.1}e^{-j\varphi}$

$\underline{U}_{conv}$ $\underline{Z}^{50Hz}_{shunt}$ $\underline{U}_{shunt}$

$|\underline{S}_{grid}| = 3U_{grid}|\underline{I}_{grid}| = S_r$

$cos(\varphi) = 0.9$

$U_{grid} = 1.1\frac{U_r}{\sqrt{3}}$

**Figure 7.1:** Visualisation of minimal DC link voltage calculation

$$\frac{U_{\text{DC,min}}}{2}\frac{2}{\sqrt{3}} = \sqrt{2}|\underline{U}_{\text{conv}}| \rightarrow U_{\text{DC,min}} = \sqrt{6}|\underline{U}_{\text{conv}}| \qquad (7.5)$$

## 7.5 Computation of Total (Fundamental and Harmonic) Losses in Damping Resistances for Filter Design Validation

A rough loss calculation is performed to see any trend between the several damping methods. Therefore, the active power in the ohmic resistances *only of the passive damping circuits* is computed. It is kind of a worst case calculation, since the worst case converter voltage spectrum is utilised. Aspects such as magnetic core losses or skin and proximity effect are neglected.

**Harmonic losses.** The worst case converter voltage spectrum, shown for example in Fig. 2.9 a), is used. For all *shunt* elements of the filter, the admittances from the converter voltage to the current through their ohmic resistances (parasitic and damping) are set up. In this way, their worst case harmonic current spectrum is computed. Their rms values are squared, multiplied by the corresponding ohmic resistance and summed up over a frequency range up to $5 \cdot f_{\text{car}}$. This is related to the rated apparent power $S_r = 2.22\ MVA$.

**Fundamental losses.** The 50 Hz rms rated star voltage $U_r^\star = 690/\sqrt{3}\ V$ is taken as input voltage. Again, the calculated rms current is squared and multiplied by the corresponding resistance.

Both values are summed up, related to 10000 and put in Tab. 2.7. The per ten thousand notation is taken to fit the values in the table.

This loss calculation is a very rough method. Generally, higher frequency models of all involved components improve the accuracy. Nevertheless, the obtained values give indicative values.

## 7.6  Validation of the Precondition for the Simple Nyquist Criterion

Validation is needed as to whether all poles of the open loop transfer function are in the left s-half plane and none, one or two at s=0 [54]. The open loop transfer function corresponds to Eq. 7.6.

$$\underline{G}_0(\underline{s}) = \underline{G}_{\mathrm{PI}}\underline{G}_{\mathrm{PWM}}\frac{\underline{I}_{\mathrm{conv}}}{\underline{U}_{\mathrm{conv}}} \tag{7.6}$$

. Each element can be analysed separately.

1. The PI controller has a pole at s=0 which is OK.

2. For $G_{\mathrm{PWM}}$, using the Tustin approximation according to Eq. 4.4, both complex conjugate pole pairs have a negative real value.

3. $\frac{\underline{I}_{\mathrm{conv}}}{\underline{U}_{\mathrm{conv}}}$ differs depending on the filter and the grid. An analytical computation for the LCL filter with ohmic resistances cannot be interpreted due to complexity. If all ohmic resistances are neglected, $\frac{\underline{I}_{\mathrm{conv}}}{\underline{U}_{\mathrm{conv}}}$ has two poles on the imaginary axis according to Eq. 7.7.

$$\underline{s}_{\infty 1,2} = \pm j\frac{\sqrt{CL_{\mathrm{conv}}L_{\mathrm{grid}}(L_{\mathrm{conv}}+L_{\mathrm{grid}})}}{CL_{\mathrm{conv}}L_{\mathrm{grid}}} \tag{7.7}$$

An inclusion of the ohmic resistances pulls the poles into the left s-half plane. The corresponding proof is out of the scope of this thesis. Nevertheless, for all analysed systems (LCL, Trap, SCR=10,50; no damping and parallel C-R damped), the poles of $\frac{\underline{I}_{\mathrm{conv}}}{\underline{U}_{\mathrm{conv}}}$ are computed numerically. All poles are in the left s half plane.

## 7.7  Validation of Grid Voltage Measurement with Bessel Signal Filter

As discussed in Chap. 3.6 and shown in Fig. 5.1, the measured grid voltage is low pass filtered. In laboratory, a 'switched capacitor' type IC is utilised [63]. The necessary supply and circuit are implemented on a breadboard. All filters exhibit constant DC offsets. These offsets are compensated by subtracting the specific offset in the control in Simulink. This chapter validates whether the sampling problems seen in simulation (Fig. 3.18) are also present in the laboratory. In Fig. 7.2, it can be seen that a direct sampling of the unfiltered grid voltage leads to aliasing. For better visibility, the Bessel filtered voltage is plotted with a slight offset in addition to the mentioned hardware offset. In the filtered voltage, the switching components of the signals are minimised. As mentioned before, the fundamental phase delay has to be compensated in the control.
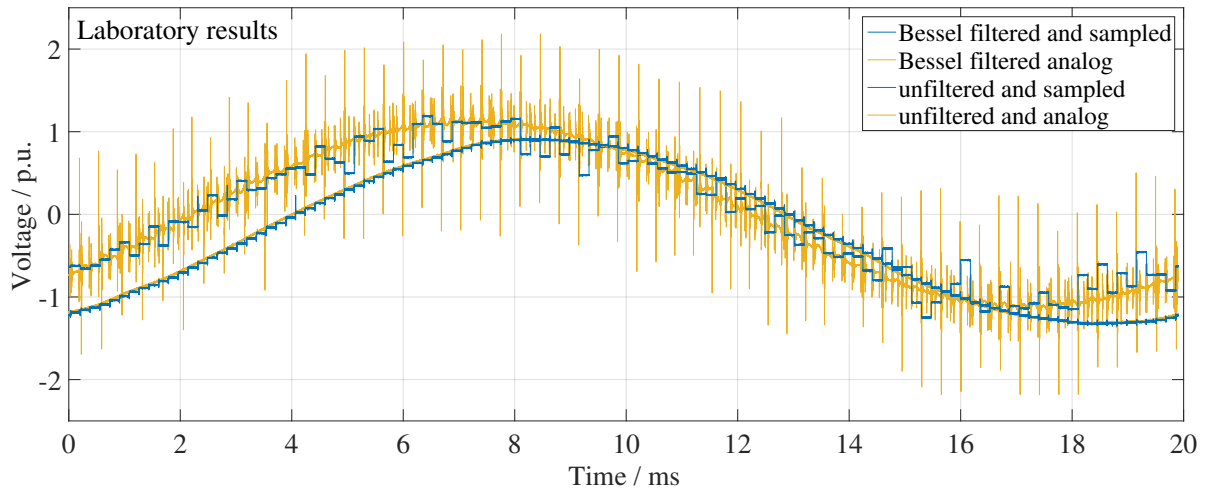
**Figure 7.2:** Laboratory: Comparison of grid voltage measurement during rated operation (strong grid trap filter with parallel C-R damping, related to $\hat{U}_{r,lab}^{\star} = 188\ V$)

## 7.8 Detailed Analysis of the Four Laboratory Filters Including Parasitic Resistances at Several Frequencies

In this chapter, all implemented filter setups are described in detail. As already mentioned, the filters for parallel C-R damping, no (passive or active) damping and active damping are analysed in the laboratory. The hardware system is not changed for all three damping methods and is intended for the parallel C-R damping. For active damping and no damping, this leads to two parameter deviations compared to the originally designed system. For more information, see the caption of Tab. 5.1.

A set of three-phase inductances and single-phase capacitances is available. As capacitance values, 1, 2, 5, 10 and 20 $\mu$F are available. Most of the inductances are three-phase inductances on a single core. Only two three-phase 5-10-15-20 *m*H inductances consist of three single-phase inductances. The aim is now to emulate all four designed filters with the available components. Hereby, the rated current is utilised to match the available capacitances and inductances. This is done using an Excel sheet which calculates all significant parameters. In this way the grid inductance and a possible resonance is also emulated.

For the stability analysis, the damping of the system is important. The higher the ohmic resistances, the higher the damping. In the simulation, the (parasitic) ohmic resistances are used according to App. 7.2 and 7.3. To get a rough estimation of the resistances in the laboratory setup, these are measured using an LCR meter [117]. With the LCR meter, LCR equivalents using four wires can be measured. The frequency can be set with 0.1-1 Hz accuracy. All filter components are measured. Values for 50 Hz and 1 kHz (near the grid resonance frequency) are documented here. Only the resistances are analysed. The frequency dependency of the inductances is not analysed. In the simulation, the inductances given on their name plates are taken. For the sake of completeness, a single inductance measurement is provided here. Three single-phase 5 mH inductances are used as converter inductances for all four filters. All other inductances are three-phase inductances on a single core. The measurement results in a 50 Hz inductance of 4.72 mH and a 1 kHz inductance of 4.44 mH. This deviation from the plate values could be analysed with the slope of the converter current ripple, as shown for example in Fig. 5.3.

Below, the realized setups of the four filters are shown in equivalent single-phase schematics. The corresponding resistance measurement for each inductance is added for 50 Hz and 1 kHz. The 50 Hz value is depicted in orange, the 1 kHz value in green. Regarding the stability analysis concerning resonances which are near 1 kHz, the 1 kHz resistance is considered to be most relevant. The name plate values are given in black, the p.u. transformed from the 2 MW system in light blue and the assumed ones in red. For the first filter system, the strong grid LCL system, the schematics are explained in detail. For the three following schematics, these explanations will not be repeated.

## 7.8.1 Strong Grid LCL Filter

The strong grid LCL system is shown in Fig. 7.3. For all filters, also for the strong grid LCL filter, the converter-side inductance is a 5 mH inductance. Its p.u. transformed resistance is 32 m$\Omega$ (blue). To model the 2 MW inductance in the laboratory with the correct X/R ratio, its parasitic resistance has to be in the same range. This is not the case: The measured 50 Hz resistance is approximately 4 times higher (130 m$\Omega$). This is in line with the X/R inductance analysis in App. 7.2. A higher damping (than intended) is the result. The LCL capacitance is met relatively well (15 $\mu$F compared to 15.2 $\mu$F). As mentioned in the schematic, it is emulated by a parallel connection of a 5 $\mu$F and a 10 $\mu$F capacitance for each phase in star connection. For most of the capacitances, their connection mode is mentioned in their schematics. The parallel C-R damping branch is optional, depending on whether the passively damped or the undamped resp. actively damped system shall be analysed. Its resistance is emulated by a slide resistance.
The grid impedance is modeled with an inductance. According to Fig. 5.1, the converter is connected with an 1:1 galvanically isolated transformer to the grid. As already mentioned, the impedance of the 230 V laboratory grid connection can be neglected, as it is low compared to the other impedances. The 1:1 transformer inductance is calculated using Eq. 5.1. Its (stray) impedance is also included in Fig. 7.3 and all other schematics. Two grid options are available.

1. The top grid schematic in Fig. 7.3 shows the *ohmic inductive grid*. It is designed for SCR=50. The blue values on top of the bracket show the ones from the 2 MW p.u. transformation. These values are the aim of the adaption. The black values on their right are the sum of all component values. It can be seen that the total inductance value is met relatively well (2.514 mH compared to 2.52 mH). Again, the resistance is far too high to model the 2 MW X/R ratio (363 *m*$\Omega$ compared to 22 *m*$\Omega$). Each resistance measurement with the highest available frequency is taken for the summed values.

2. The bottom grid schematic in Fig. 7.3 shows the *grid with resonance*, as developed in Chap. 4.3.2. The specific grid resonance chosen is explained in Chap. 5.7.

## 7.8.2 Strong Grid Trap Filter

Again, the filter design is adapted to the available capacitances and inductances. In Fig. 7.4, the intended values from the p.u. transformation (blue) and the values implemented in the setup
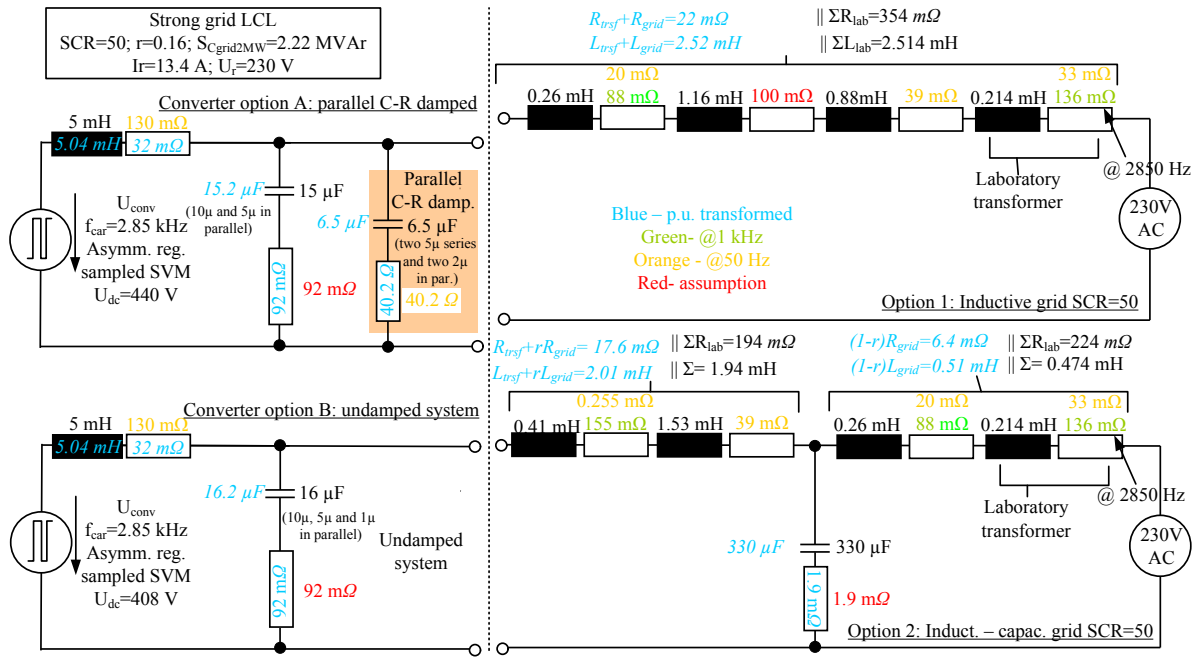
**Figure 7.3:** Laboratory setup to validate the strong grid LCL system $I_r = 13.4\ A$; when summing the resistances, always the resistance for the highest available frequency is taken.
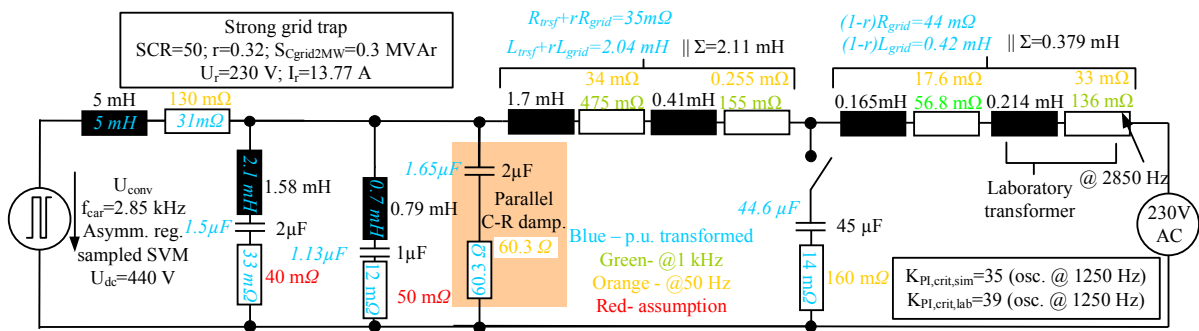


**Figure 7.4:** Schematic of the strong grid trap filter system with parallel C-R damping, as implemented in the laboratory (letters in white on black depict the intended values from p.u. transformation) $I_r = 13.77\ A$

(black) are shown. The capacitance of the first trap filter is increased from the intended 1.5 to 2 $\mu$F. As a result, its inductance has to be decreased to keep the same trap frequency near to 2.85 kHz. For both trap filters, coreless inductances (air coils) are utilised. Their inductance can be adjusted precisely by varying the number of windings. The second trap filter capacitance is slightly decreased. As grid impedance, SCR=50 is analysed.

In Chap. 4.4.4, a specific analysis for the strong grid trap filter system with instable control is done (Fig. 4.12). Here, the same grid resonance is analysed (SCR=50, X/R=30, r=0.32 and $S_{Cgrid} = 0.3\ MVAr$). The intended parameters are met relatively well. The turbine-side inductance is intended to be 2.04 mH, while it is 2.11 mH. The grid-side inductance consists of the earlier mentioned isolated transformer and a 0.165 mH inductance. The sum of 0.379 mH is slightly smaller than the intended 0.42 mH. The grid capacitance matches fairly well.
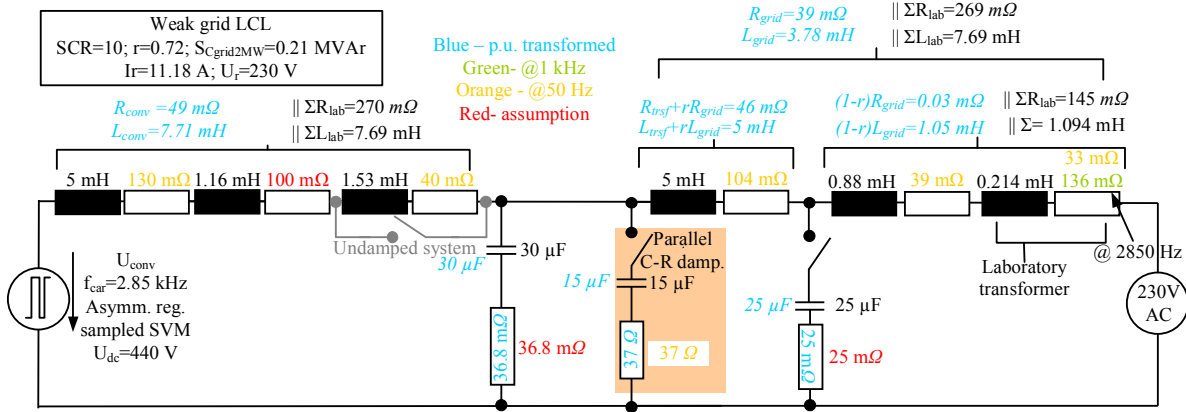
**Figure 7.5:** Laboratory setup to validate the weak grid LCL system $I_r = 11.18\,A$
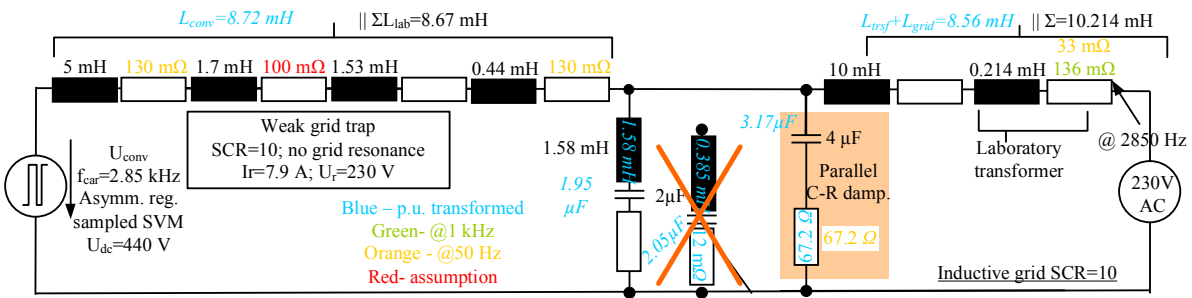


**Figure 7.6:** Laboratory setup to validate the weak grid trap system $I_r = 7.9\,A$

## 7.8.3 Weak Grid LCL Filter

The weak grid LCL system is shown in Fig. 7.5. The 5 mH inductance is again taken as converter inductance. Two inductances are added in series, while the second is omitted for the no damping and active damping analysis. As mentioned in the caption of Tab. 5.1 and seen in Tab. 2.7, for the undamped (and actively damped) 2 MW system, a lower converter-side inductance is needed. The same series inductances are taken for the grid with and without resonance. The implemented inductances and capacitances are very close to the intended values. It can be seen that the grid inductance is significantly higher compared to the strong grid systems.

## 7.8.4 Weak Grid Trap Filter

The implemented trap filter weak grid system is shown in Fig. 7.6. The same trap filter as for the strong grid trap system is implemented. The second would need a significantly lower inductance (0.385 mH) than the strong grid equivalent. For our analysis it is omitted (due to availability). In this way the effect of the (lacking) second trap filter can be evaluated in the current spectra. The rated current has to be decreased to 7.9 A.
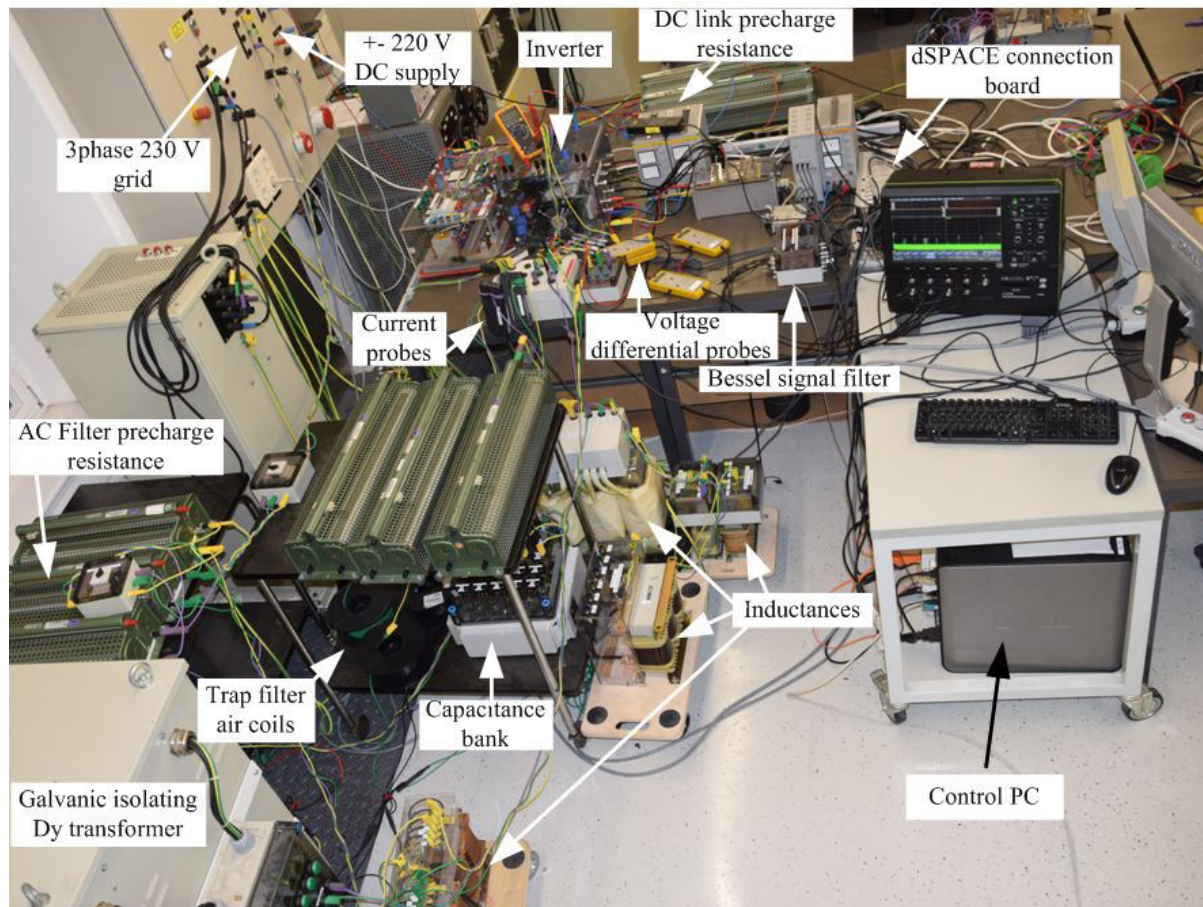
## 7.9  Laboratory Setup Photos



**Figure 7.7:** Laboratory setup (View 1)

## 7.10  List of Student Theses

The following student theses have been supervised during the work.

- 2011: Investigation of the Thermal Load of Power Semiconductors Used in Wind Turbines with Doubly Fed Induction Generator; Master Thesis, Mohammad Jamarani

- 2011: Analyse von Netzfehlern bei Windenergieanlagen mit permanenterregter Synchron-maschine und Mittelspannungsumrichter in der Simulation; Masterarbeit, Michael Koch

- 2012: Regelung eines Netzpulsstromrichters mit MATLAB/Simulink/dSpace; Studienar-beit, Lena Haberjan

- 2012: Vergleich von Netzsynchronisationsverfahren in dreiphasigen Systemen Studienar-beit, Sebastian Roppes
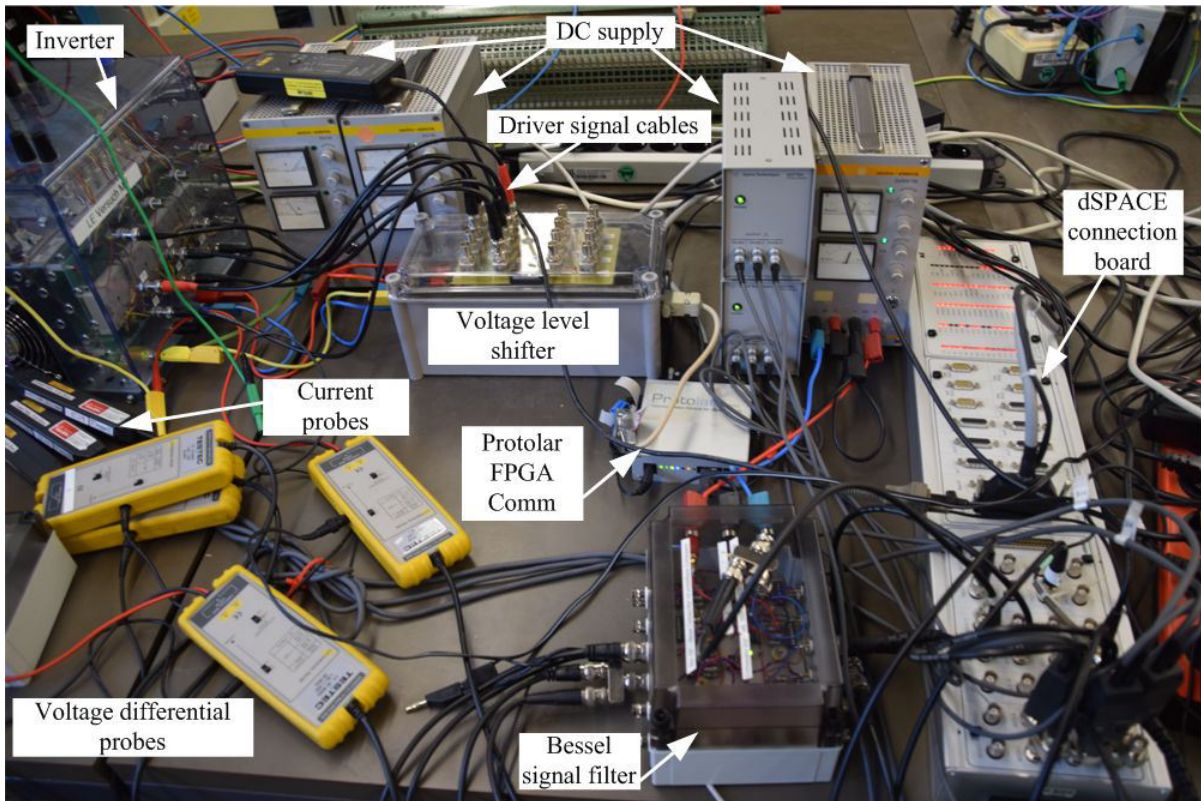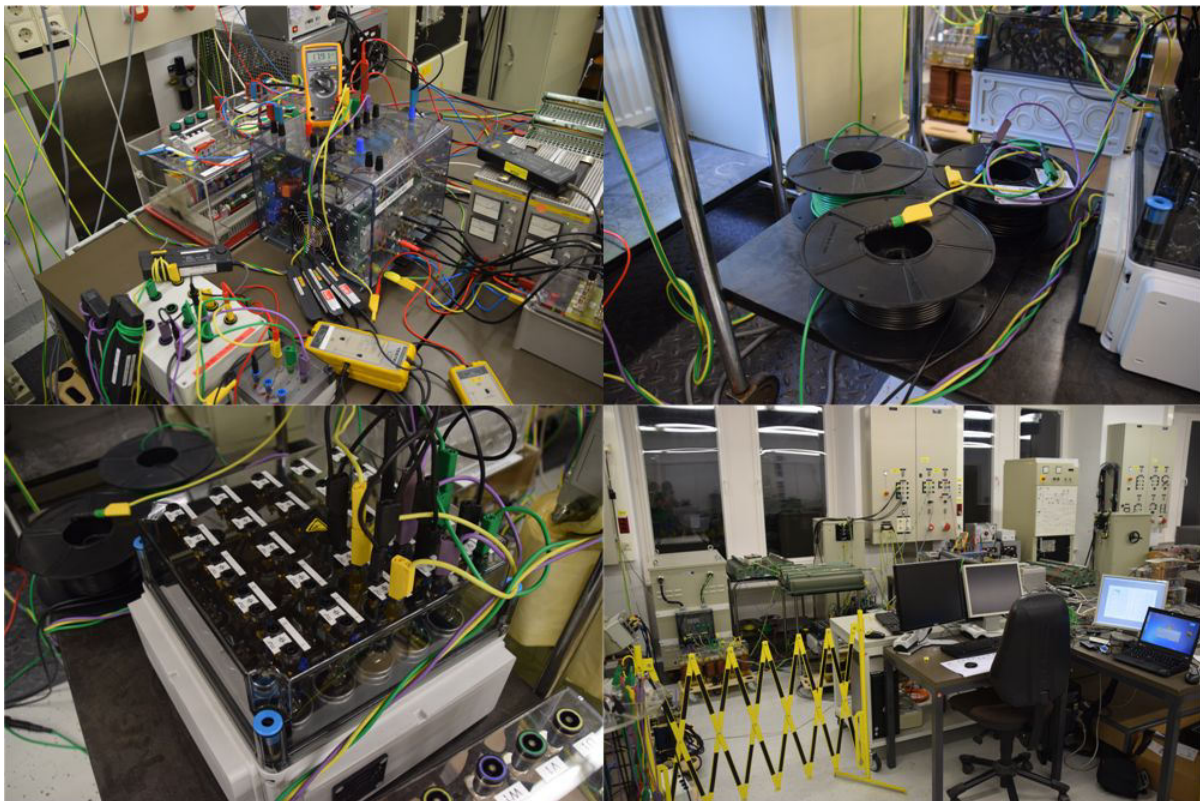
**Figure 7.8:** Laboratory setup (View 2)



**Figure 7.9:** Laboratory setup (View 3) clock-wise: converter, air coils, capacitor bank and total setup

- 2012: Control of the positive and negative sequence of the grid current with NPC Converter and LCL filter; Master thesis, Roberto Rosso

- 2013: Modellierung, Regelung und Simulation eines HGÜ-angebundenen Offshore Windparknetzes; Masterarbeit, Johannes Heseding

- 2013: Stromharmonischenregelung eines netzseitigen dreiphasigen Wechselrichters mit dSPACE; Masterarbeit, Karsten Kusserow

- 2013: Stabilitätsanalyse dreiphasiger Wechselrichter im Netzverbund mit Hilfe des Nyquistkriteriums; Studienarbeit, Duc Viet Pham

- 2013: Inbetriebnahme eines NPC-Wechselrichters mit dSpace inkl. Schaltsignalgenerierung auf FPGA; Bachelorarbeit, Duc Viet Pham

- 2014: Stromharmonischen-Regelung eines dreiphasigen, netzseitigen Wechselrichters mit dSPACE zur Verbesserung der Netzqualität; Masterarbeit, Miodrag Miljanovic

- 2014: Modellierung und experimentelle Validierung des Einflusses paralleler, dezentraler Erzeuger auf die Stromregelung eines netzseitigen, dreiphasigen Wechselrichters; Masterarbeit, Jan Hartke

# Bibliography

[1] Siemens AG, "Environmental product declaration - onshore wind power plant employing SWT-2.3-108," *Product Brochure*, 2014, [Online] Available: http://www.energy.siemens.com/hq/pool/hq/power-generation/renewables/wind-power/pictures/epd/epd-swt-2-3-012015.pdf Retrieved on: 2016-02-11.

[2] F. Blaabjerg, M. Liserre, and K. Ma, "Power Electronics Converters for Wind Turbine Systems," *IEEE Transactions on Industry Applications*, vol. 48, no. 2, pp. 708–719, Mar. 2012, 00270.

[3] B. der Energie-und Wasserwirtschaft e.V. (BDEW), "Generating plants connected to the medium-voltage network," Technical Guideline, 2008, [Online] Available: https://www.bdew.de/internet.nsf/id/A2A0475F2FAE8F44C12578300047C92F/$file/BDEW_RL_EA-am-MS-Netz_engl.pdf Retrieved on: 2016-02-11.

[4] IEEE Industry Applications Society, Static Power Converter Committee, IEEE Power Engineering Society, and Transmission and Distribution Committee, *IEEE recommended practices and requirements for harmonic control in electric power systems*. New York, N.Y.: Institute of Electrical and Electronics Engineers, 1993, 00000 OCLC: 28052013.

[5] "IEEE Standard for Interconnecting Distributed Resources with Electric Power Systems," *IEEE Std 1547-2003*, pp. 1–28, Jul. 2003, Reaffirmed 26-9-2008.

[6] R. Burkart and J. W. Kolar, "Overview and Comparison of Grid Harmonics and Conducted EMI Standards for LV Converters Connected to the MV Distribution System," *Proc. of PCIM 2012*, pp. 11–13, 2012, [Online] Available: http://www.pes.ee.ethz.ch/uploads/tx_ethpublications/Overview_Comparison_PCIM2012_01.pdf Retrieved on: 2016-11-06.

[7] IEC, "61000-4-7: Electromagnetic compatibility (emc)-part 4-7: Testing and measurement techniques–general guide on harmonics and interharmonics measurements and instrumentation, for power supply systems and equipment connected thereto," *Switzerland, Geneva: IEC press*, 2002.

[8] J. Birk and B. Andresen, "Parallel-connected converters for optimizing efficiency, reliability and grid harmonics in a wind turbine," in *Proc. of 12<sup>th</sup> European Conference on Power Electronics and Applications*, 2007, pp. 1–7.

[9] Infineon Technologies AG, "Technical Information ModStackTM HD 6ms30017e43w34404," *Product Brochure*, 2012, [Online] Available: http:

//www.infineon.com/dgdl/Infineon-6MS30017E43W34404-DS-v02_01-en.pdf?
fileId=db3a3043382e83730138958b66eb1660 Retrieved on: 2016-02-11.

[10] Siemens AG, "Technical Information on wind turbine converter LOHER Dynavert XL,"
*Product Brochure*, 2012, [Online] Available: http://w3app.siemens.com/mcms/infocenter/
dokumentencenter/ld/Documentsu20Brochures/lv-umrichter/ws-dynavert-xl-wind-de.
pdf Retrieved on: 2016-02-11.

[11] Woodward, Inc., "Water-cooled frequency converters for wind turbines concycle: CW
1000ld CW 2000lf," *Product Brochure*, [Online] Available: http://www.woodward.com/
WorkArea/DownloadAsset.aspx?id=2147491185 Retrieved on: 2016-02-11.

[12] R. Meyer and A. Mertens, "Design of LCL filters in consideration of parameter variations
for grid-connected converters," in *Proc. of IEEE Energy Conversion Congress and
Exposition (ECCE)*, Sep. 2012, pp. 557–564.

[13] N. E. Rueger, *Zur Anwendung eines bandseparierenden Modulationsverfahrens mit
niedrigen Taktzahlen in der Leistungselektronik.* Fortschritt-Berichte VDI : Reihe 21,
Elektrotechnik, VDI-Verl., 2012, no. 402.

[14] D. G. Holmes and T. A. Lipo, *Pulse Width Modulation for Power Converters: Principles
and Practice*, 1st ed. John Wiley & Sons, 2003.

[15] Siemens AG, "Efficient transformers for the grid integration of wind power - Brochure
(in german)," 2011, [Online] Available: http://www.energy.siemens.com/hq/de/
stromuebertragung/transformatoren/assets/pdf/siemens-transformatoren-windkraft.pdf
Retrieved on: 2016-02-11.

[16] Siemens AG, "The GEAFOL Basic: the optimum foundation for power distri-
bution," 2015, [Online] Available: http://www.energy.siemens.com/hq/pool/hq/
power-transmission/Transformers/Distribution%20Transformers/GEAFOL/GEAFOL_
Basic_EN.pdf Retrieved on: 2016-02-11.

[17] J. Schlabbach, D. Blume, and T. Stephanblome, *Voltage quality in electrical power
systems*. IET, 2001, no. 36.

[18] J. C. Das, *Power System Analysis: Short-Circuit Load Flow and Harmonics, Second
Edition*, 2nd ed. CRC Press, Jul. 2011.

[19] H. Renner, *Spannungsqualitaet und Versorgungssicherheit- Folien zur Vorlesung (in
German).* Technische Universitaet Graz, 2007.

[20] ABB Ltd, "Low voltage wind turbine converter ACS880, 800 kW- 8 MW,"
*Product Brochure*, 2014, [Online] Available: https://library.e.abb.com/public/
9909599816bccbfcc1257c860034fc82/ACS880_brochure_EN_lowres.pdf Retrieved on:
2016-02-11.

[21] J. Bloemink and T. Green, "Reducing passive filter sizes with tuned traps for distribution

level power electronics," in *Proceedings of the 14th European Conference on Power Electronics and Applications (EPE 2011)*, Aug. 2011, pp. 1–9.

[22] P. Brogan, "Current controller device and vector control method for controlling power conversion," Patent, Dec., 2014, [Online] Available: http://google.com/patents/US8907509 Retrieved on: 2016-02-11.

[23] M. Liserre, F. Blaabjerg, and S. Hansen, "Design and control of an LCL-filter-based three-phase active rectifier," *IEEE Transactions on Industry Applications*, vol. 41, no. 5, pp. 1281–1291, Sep. 2005.

[24] S. Araujo, A. Engler, B. Sahan, and F. Antunes, "LCL filter design for grid-connected NPC inverters in offshore wind turbines," in *Proc. of 7th Internatonal Conference on Power Electronics (ICPE)*, Oct. 2007, pp. 1133–1138.

[25] Y. Patel, D. Pixler, and A. Nasiri, "Analysis and design of TRAP and LCL filters for active switching converters," in *Proc. of IEEE International Symposium on Industrial Electronics (ISIE)*, Jul. 2010, pp. 638–643.

[26] A. Rockhill, M. Liserre, R. Teodorescu, and P. Rodriguez, "Grid-Filter Design for a Multimegawatt Medium-Voltage Voltage-Source Inverter," *IEEE Transactions on Industrial Electronics*, vol. 58, no. 4, pp. 1205–1217, Apr. 2011.

[27] U. Raedel, *Beitrag zur Entwicklung leistungselektronischer Komponenten fuer Windkraftanlagen*. Dissertation, University Ilmenau, 2008, [Online] Available: http://www.db-thueringen.de/servlets/DerivateServlet/Derivate-16657/ilm1-2008000222.pdf Retrieved on: 2016-02-11.

[28] T. Wang, Z. Ye, G. Sinha, and X. Yuan, "Output filter design for a grid-interconnected three-phase inverter," in *Proc. of IEEE 34th Annual Power Electronics Specialist Conference, PESC*, Jun. 2003, pp. 779–784 vol.2.

[29] M. Winkelnkemper, *Reduzierung von Zwischenkreiskapazitaeten in Frequenzumrichtern fuer Niederspannungsantriebe*. Dissertation, Technical University Berlin, 2005, [Online] Available: https://depositonce.tu-berlin.de/bitstream/11303/1549/1/Dokument_9.pdf Retrieved on: 2016-02-11.

[30] P. Channegowda and V. John, "Filter Optimization for Grid Interactive Voltage Source Inverters," *IEEE Transactions on Industrial Electronics*, vol. 57, no. 12, pp. 4106–4114, Dec. 2010.

[31] G. Gohil, L. Bede, R. Teodorescu, T. Kerekes, and F. Blaabjerg, "Line Filter Design of Parallel Interleaved VSCs for High Power Wind Energy Conversion System," *IEEE Transactions on Power Electronics*, vol. PP, no. 99, pp. 1–1, 2015.

[32] K. Jalili and S. Bernet, "Design of Filters of Active-Front-End Two-Level Voltage-Source Converters," *IEEE Transactions on Industrial Electronics*, vol. 56, no. 5, pp. 1674–1689, May 2009.

[33] K. R. Meyer, *Fault-Ride-Through-Regelung von Windenergieanlagen mit Vollumrichter und LCL-Netzfilter*. Dissertation, Leibniz Universitaet Hannover, 2014, [Online] Available: http://edok01.tib.uni-hannover.de/edoks/e01dh14/812759397.pdf Retrieved on: 2016-02-11.

[34] J. Muhlethaler, M. Schweizer, R. Blattmann, J. Kolar, and A. Ecklebe, "Optimal Design of LCL Harmonic Filters for Three-Phase PFC Rectifiers," *IEEE Transactions on Power Electronics*, vol. 28, no. 7, pp. 3114–3125, Jul. 2013.

[35] R. W. Erickson and D. Maksimovic, *Fundamentals of Power Electronics*, 2nd ed. Norwell, Mass: Springer, Jan. 2001.

[36] R. Pena-Alzola, M. Liserre, F. Blaabjerg, R. Sebastian, J. Dannehl, and F. W. Fuchs, "Analysis of the passive damping losses in lcl-filter-based grid converters," *IEEE Transactions on Power Electronics*, vol. 28, no. 6, pp. 2642–2646, Jun. 2013.

[37] P. Brogan, "The stability of multiple, high power, active front end voltage sourced converters when connected to wind farm collector systems," in *Proc. of the 3$^{rd}$ European Power Electronics Wind Energy Chapter Symposium*, 2010, pp. 1–6.

[38] L. H. Kocewiak, "Harmonics in large offshore wind farms." Department of Energy Technology, Aalborg University, Ph.D. Thesis, [Online] Available: http://vbn.aau.dk/files/62660098/lukasz_kocewiak.pdf Retrieved on: 2016-02-11.

[39] G. Gohil, L. Bede, R. Teodorescu, T. Kerekes, and F. Blaabjerg, "Design of the trap filter for the high power converters with parallel interleaved VSCs," in *Proc. of IECON 2014 - 40th Annual Conference of the IEEE Industrial Electronics Society*, Oct. 2014, pp. 2030–2036.

[40] J. Xu, J. Yang, J. Ye, Z. Zhang, and A. Shen, "An LTCL Filter for Three-Phase Grid-Connected Converters," *IEEE Transactions on Power Electronics*, vol. 29, no. 8, pp. 4322–4338, Aug. 2014.

[41] F. C. De La Rosa, *Harmonics and Power Systems*. CRC/Taylor & Francis, 2006.

[42] E. Twining and D. Holmes, "Grid current regulation of a three-phase voltage source inverter with an LCL input filter," *IEEE Transactions on Power Electronics*, vol. 18, no. 3, pp. 888–895, May 2003.

[43] R. Beres, X. Wang, F. Blaabjerg, M. Liserre, and C. Bak, "Optimal Design of High-Order Passive-Damped Filters for Grid-Connected Applications," *IEEE Transactions on Power Electronics*, vol. PP, no. 99, pp. 1–1, 2015.

[44] V. Blasko and V. Kaura, "A new mathematical model and control of a three-phase AC-DC voltage source converter," *IEEE Transactions on Power Electronics*, vol. 12, no. 1, pp. 116–123, Jan. 1997.

[45] S. Buso and P. Mattavelli, "Digital control in power electronics," *Synthesis Lec-*

*tures on Power Electronics*, vol. 1, no. 1, pp. 1–158, [Online] Available: http://www. morganclaypool.com/doi/abs/10.2200/S00047ED1V01Y200609PEL002 Retrieved on: 2016-02-11.

[46] R. Teodorescu, M. Liserre, and P. Rodriguez, *Grid converters for photovoltaic and wind power systems.* John Wiley & Sons, 2011, vol. 29.

[47] V. Kaura and V. Blasko, "Operation of a voltage source converter at increased utility voltage," *Power Electronics, IEEE Transactions on*, vol. 12, no. 1, pp. 132–137.

[48] S.-K. Chung, "A phase tracking system for three phase utility interface inverters," *IEEE Transactions on Power Electronics*, vol. 15, no. 3, pp. 431–438, May 2000.

[49] F. Liu, X. Zhang, C. Yu, Z. Shao, W. Zhao, and H. Ni, "LCL-filter design for grid-connected three-phase PWM converter based on maximum current ripple," in *Proc. of IEEE ECCE Asia Downunder (ECCE Asia)*, Jun. 2013, pp. 631–635.

[50] D. Schroeder, *Elektrische Antriebe - Regelung von Antriebssystemen.* Springer Berlin Heidelberg, 2009.

[51] D. Kampen, *Optimierte Filterauslegung fuer dreiphasige Netzpulsstromrichter.* Dissertation, Shaker, Aug. 2013.

[52] V. Blasko and V. Kaura, "A novel control to actively damp resonance in input LC filter of a three-phase voltage source converter," *IEEE Transactions on Industry Applications*, vol. 33, no. 2, pp. 542–550.

[53] J. Dannehl, F. W. Fuchs, S. Hansen, and P. Thogersen, "Investigation of Active Damping Approaches for PI-Based Current Control of Grid-Connected Pulse Width Modulation Converters With LCL Filters," *IEEE Transactions on Industry Applications*, vol. 46, no. 4, pp. 1509–1517, Jul. 2010.

[54] H. Unbehauen, *Control Theory 1: klassische Verfahren zur Analyse und Synthese linearer kontinuierlicher Regelsysteme, Fuzzy-Regelsysteme.* Vieweg+Teubner Verlag / GWV Fachverlage, Wiesbaden, 2008.

[55] C. H. Houpis, S. J. Rasmussen, and M. Garcia-Sanz, *Quantitative Feedback Theory: Fundamentals and Applications.* CRC Press Inc, Nov. 2005.

[56] R. Schoenfeld, *Digital Control of Electrical Drives (in German)*, 1st ed. Berlin: Verlag Technik, 1987.

[57] J. Agorreta, M. Borrega, J. Lopez, and L. Marroyo, "Modeling and control of n-paralleled grid-connected inverters with LCL filter coupled due to grid impedance in PV plants," *IEEE Transactions on Power Electronics*, vol. 26, no. 3, pp. 770–785, Mar. 2011.

[58] J. Lunze, *Control Theory 1–Systemtheoretische Grundlagen, Analyse und Entwurf einschleifiger Regelungen.* Springer, 2010, vol. 39.

[59] G. Schulz, *Control Theory: Grundlagen, Analyse und Entwurf von Regelkreisen, rechn-ergestuetzte Methoden.*    Springer, 1995.

[60] M. Cespedes and J. Sun, "Impedance modeling and analysis of grid-connected voltage-source converters," *IEEE Transactions on Power Electronics*, vol. 29, no. 3, pp. 1254–1261, 2014.

[61] S. Parker, B. McGrath, and D. Holmes, "Regions of Active Damping Control for LCL Filters," *IEEE Transactions on Industry Applications*, vol. 50, no. 1, pp. 424–432, Jan. 2014.

[62] N. Hoffmann, *Netzadaptive Regelung und Aktiv-Filter Funktionalitaet von Net-zpulsstromrichtern in der regenerativen Energieerzeugung*, 2015, [Online] Available:    http://macau.uni-kiel.de/servlets/MCRFileNodeServlet/dissertation_derivate_00005925/dissertation_nils_hoffmann.pdf Retrieved on: 2016-02-11.

[63] Mouser Electronics, "Data Sheet: MAX292cpa+ Maxim Integrated | Mouser," [Online] Available: http://www.mouser.com/Search/ProductDetail.aspx?R=MAX292CPA%2bvirtualkey66880000virtualkey700-MAX292CPA Retrieved on: 2016-02-11.

[64] F. Ballandt, *Beitrag zur Regelung dreiphasiger gepulster Netzstromrichter mit Gleichspan-nungszwischenkreis in der Anwendung für die Energiekonditionierung.*    Dissertation, Shaker, 2000.

[65] J. Dannehl, *Regelung von Netzpulsstromrichtern mit LCL-Filter fuer Antriebe mit kleiner Kapazitaet im Zwischenkreis.*    Dissertation, University of Kiel, Germany, [Online] Available: http://macau.uni-kiel.de/servlets/MCRFileNodeServlet/dissertation_derivate_00004427/diss_dannehl.pdf Retrieved on: 2016-02-11.

[66] C. Schauder and H. Mehta, "Vector analysis and control of advanced static VAr com-pensators," *IEE Proceedings of Generation, Transmission and Distribution of Energy Conference*, vol. 140, no. 4, pp. 299–306, Jul. 1993.

[67] B. Bahrani, S. Kenzelmann, and A. Rufer, "Multivariable-PI-based dq current control of voltage source converters with superior axis decoupling capability," *IEEE Transactions on Industrial Electronics*, vol. 58, no. 7, pp. 3016–3026, Jul 2011.

[68] H. Kim, M. Degner, J. Guerrero, F. Briz, and R. Lorenz, "Discrete-Time Current Regulator Design for AC Machine Drives," *IEEE Transactions on Industry Applications*, vol. 46, no. 4, pp. 1425–1435, Jul. 2010.

[69] J. Holtz, "The representation of AC machine dynamics by complex signal flow graphs," *IEEE Transactions on Industrial Electronics*, vol. 42, no. 3, pp. 263–271, Jun. 1995.

[70] K. Kuepfmueller, W. Mathis, and A. Reibiger, *Theoretische Elektrotechnik: Eine Ein-fuehrung.*    Springer, 2005.

[71] P. C. Magnusson, G. C. Alexander, and V. K. Tripathi, *Transmission Lines and Wave Propagation, Fourth Edition.*   Crc Press Inc, 2000.

[72] J. Arrillaga and N. R. Watson, *Power system harmonics*, 2nd ed.   J. Wiley & Sons, 2003.

[73] Nexans, "Underground Power Cables Catalogue," Mar. 2010, [Online] Available: http://www.nexans.co.uk/UK/files/Underground%20Power%20Cables%20Catalogue% 2003-2010.pdf Retrieved on: 2016-02-11.

[74] H. Haase and H. Garbe, *Elektrotechnik: Theorie und Grundlagen.*   Berlin; New York: Springer, 1998.

[75] IEEE Industry Applications Society, Power Systems Engineering Committee, IEEE Standards Board, and American National Standards Institute, *IEEE recommended practice for industrial and commercial power systems analysis.*   New York: Institute of Electrical and Electronics Engineers, 1998.

[76] D. Patel, R. Varma, R. Seethapathy, and M. Dang, "Impact of wind turbine generators on network resonance and harmonic distortion," in *Proc. of 23rd Canadian Conference on Electrical and Computer Engineering (CCECE)*, pp. 1–6.

[77] S. Papathanassiou and M. Papadopoulos, "Harmonic analysis in a power system with wind generation," *IEEE Transactions on Power Delivery*, vol. 21, no. 4, pp. 2006–2016.

[78] M. Bradt, B. Badrzadeh, E. Camm, D. Mueller, J. Schoene, T. Siebert, T. Smith, M. Starke, and R. Walling, "Harmonics and resonance issues in wind power plants," in *Proc. of IEEE Power and Energy Society General Meeting*, 2011, pp. 1–8.

[79] A. Robert and T. Deflandre, "Guide for assessing the network harmonic impedance," *Electra*, no. 167, pp. 96–131, 1996.

[80] J. Plotkin, R. Hanitsch, and U. Schaefer, "Power conditioning of a 132 MW wind farm," in *Proc. of 12$^{th}$ European Conference on Power Electronics and Applications*, 2007, pp. 1–9.

[81] K. Hasan, K. Rauma, A. Luna, J. Candela, and P. Rodriguez, "Harmonic resonance damping in wind power plant," in *Proc. of IEEE Energy Conversion Congress and Exposition (ECCE)*, 2012, pp. 2067–2074.

[82] F. H. Venter, "Harmonic impedance estimation of power system implementing frequency domain measurement techniques (master thesis)."   Rand Afrikaans University, 2001, [Online] Available: https://ujdigispace.uj.ac.za/bitstream/handle/10210/5585/F.H. %20VENTER_2001_MA.pdf?sequence=3&isAllowed=y Retrieved on: 2016-02-11.

[83] R. Zheng and M. Bollen, "Harmonic resonances associated with wind farms."   Lule a University of Technology, technical report, 2010, [Online] Available: https://pure.ltu.se/ portal/files/4988277/Harmonic_resonances_associated_with_wind_farms.pdf Retrieved on: 2016-02-11.

[84] R. C. Dugan, M. F. McGranaghan, and H. W. Beaty, *Electrical power systems quality*. New York, NY: McGraw-Hill,| c1996, vol. 1.

[85] D. Schulz, *Netzrueckwirkungen-Theorie, Simulation, Messung und Bewertung*. VDE-Schriftenreihe-Normen verstaendlich, 2004, vol. 115.

[86] H. Dorner and M. Fender, *Wissenswertes ueber Netzrueckwirkungen*. Berlin; Offenbach: Vde-Verlag, Jan. 2013.

[87] M. Cespedes and J. Sun, "Mitigation of inverter-grid harmonic resonance by narrow-band damping," *IEEE Journal of Emerging and Selected Topics in Power Electronics*, vol. 2, no. 4, pp. 1024–1031, Dec. 2014.

[88] C. Zhang, T. Dragicevic, J. Vasquez, and J. Guerrero, "Resonance damping techniques for grid-connected voltage source converters with LCL filters; A review," in *Proc. of IEEE International Energy Conference (ENERGYCON)*, May 2014, pp. 169–176.

[89] X. Wang, F. Blaabjerg, M. Liserre, Z. Chen, J. He, and Y. Li, "An active damper for stabilizing power-electronics-based AC systems," *IEEE Transactions on Power Electronics*, vol. 29, no. 7, pp. 3318–3329.

[90] E. Muljadi, C. Butterfield, A. Ellis, J. Mechenbier, J. Hochheimer, R. Young, N. Miller, R. Delmerico, R. Zavadil, and J. Smith, "Equivalencing the collector system of a large wind power plant," in *Proc. of IEEE Power Engineering Society General Meeting*, 2006, pp. 9 pp.–.

[91] J. H. R. Enslin and P. J. M. Heskes, "Harmonic interaction between a large number of distributed power inverters and the distribution network," *IEEE Transactions on Power Electronics*, vol. 19, no. 6, pp. 1586–1593, 2004.

[92] E. Mollerstedt and B. Bernhardsson, "Out of control because of harmonics-an analysis of the harmonic response of an inverter locomotive," *IEEE Control Systems*, vol. 20, no. 4, pp. 70–81, 2000.

[93] M. Lörtscher, *Elektrische Zugförderung im Lötschberg-Basistunnel: Vom Pflichtenheft zur Betriebswilligung für Fahren mit 250 km/h durch die erste europäische Alpentransversale*, 2nd ed. Muenchen: Oldenbourg Industrieverlag, 2010.

[94] Regelwerk SBB, "R-i-20005: Anforderungen an die Eingangs-Admittanz von Umrichter-triebfahrzeugen," Schweiz, 2013.

[95] R. D. Middlebrook, "Input filter considerations in design and application of switching regulators," *IAS Record*, 1976.

[96] J. Sun, "Impedance-based stability criterion for grid-connected inverters," *IEEE Transactions on Power Electronics*, vol. 26, no. 11, pp. 3075–3078.

[97] M. Cespedes and J. Sun, "Modeling and mitigation of harmonic resonance between wind

turbines and the grid," in *Proc. of IEEE Energy Conversion Congress and Exposition (ECCE)*, 2011, pp. 2109–2116.

[98] B. Wen, D. Boroyevich, P. Mattavelli, R. Burgos, and Z. Shen, "Modeling the output impedance negative incremental resistance behavior of grid-tied inverters," in *Proc. of $29^{th}$ IEEE Applied Power Electronics Conference and Exposition (APEC)*.  IEEE, 2014, pp. 1799–1806.

[99] T. Bagnall, C. Ritter, B. Ronner, P. Maibach, N. Butcher, and T. Thurnherr, "PCS6000 STATCOM ancillary functions: Wind park resonance damping."  Proc. of European Wind Energy Conference (EWEC), 2009, [Online] Available: http://proceedings.ewea. org/ewec2009/allfiles2/155_EWEC2009presentation.pdf Retrieved on: 2016-02-11.

[100] F. Fuchs and A. Mertens, "Prediction and avoidance of grid-connected converter's instability caused by wind park typical, load-varying grid resonance," in *Proc. of IEEE Energy Conversion Congress and Exposition (ECCE)*, Sep. 2014, pp. 2633–2640.

[101] F. Fuchs, D. Pham, and A. Mertens, "Analysis of grid current control in consideration of voltage feedforward and cable capacitance demonstrated on a fully sized wind turbine installed in a wind park," in *Proc. of IEEE Energy Conversion Congress and Exposition (ECCE)*, Sep. 2013, pp. 3325–3332.

[102] J. Hartke, *Modellierung und experimentelle Validierung des Einflusses paralleler dezentraler Erzeuger auf die Stromregelung eines netzseitigen dreiphasigen Wechselrichters*. Master Thesis, Institute for Drive Systems and Power Electronics, University Hanover, 2015.

[103] Plexim homepage. [Online] Available: http://www.plexim.com/de Retrieved on: 2016-02-11.

[104] Semikron, "Data sheet of semistack - igbt semitrans stack - semiteach - skm 50 gb 123d skd 51 p3/250f," *Product Brochure*, [Online] Available: https://www.semikron.com Retrieved on: 2016-02-11.

[105] Protolar GmbH, *FPGA Comm: FPGA Extension to DSPACE systems*, [Online] Available: www.protolar.de/en/products/fpgacomm/ Retrieved on: 2016-02-11.

[106] Agilent Technologies, "Data sheet: N2782a 50 mhz/30arms ac/dc current probe," [Online] Available: http://www.keysight.com/en/pd-1062790-pn-N2782A/ 50-mhz-30arms-ac-dc-current-probe?cc=DE&lc=ger Retrieved on: 2016-02-11.

[107] ——, "Data sheet: N2781a 10 mhz/150 arms ac/dc current probe," [Online] Available: http://www.keysight.com/en/pd-1062764-pn-N2781A/ 10-mhz-150-arms-ac-dc-current-probe?cc=DE&lc=ger Retrieved on: 2016-02-11.

[108] Testec, "Instruction manual: Testec differential-probe 25 mhz 20:1, 200:1 1400 v tt-si 9002," [Online] Available: http://www.testec.de/assets/pdf/TT-SI/TT-SI-9002_Manual_ DE.pdf Retrieved on: 2016-02-11.

[109] Tektronix, "Instruction manual: P5200 high voltage differential probe."

[110] Teledyne Lecroy, "Hdo8000 high definition oscilloscopes 1 ghz," [Online] Available: http://cdn.teledynelecroy.com/files/pdf/hdo8000_oscilloscope_datasheet.pdf Retrieved on: 2016-02-11.

[111] Siemens AG, "GEAFOL Cast-Resin Transformers 100 to 16000 kVA," *Product Brochure*, 2007, [Online] Available: http://www.automation.siemens.com/tip-static/dlc/en/Distribution-Transformers/Catalog_TV1_GEAFOL_Cast-resin_Transformers.pdf Retrieved on: 2016-02-11.

[112] ——, "Datasheet- filter inductance, three-phase, 50hz, 18a (4EP3601-5DS00)," *Product Brochure*, 2015, [Online] Available: https://mall.industry.siemens.com/mall/de/WW/Catalog/Product/4EP3601-5DS00 Retrieved on: 2016-02-11.

[113] EPA GmbH, "Line Reactors 2a -1100 A," *Product Brochure*, 2015, [Online] Available: http://epa-filter.de/uploads/downloads/EPA3N/Netzdrosseln_EPA3N.pdf Retrieved on: 2015-04-16.

[114] TDK / EPCOS AG, "EMV-Filter 3-Phasen Netzdrossel fuer rueckspeisefaehige Umrichter (in german)," *Product Brochure*, 2105, [Online] Available: http://de.tdk.eu/inf/30/db/emc_2014_d/B86306A.pdf Retrieved on: 2016-02-11.

[115] Siemens AG, "Datasheet- grid filter inductance, three-phase, 50hz, 819A," *Product Brochure*, 2015, [Online] Available: https://mall.industry.siemens.com/tedservices/DatasheetService Retrieved on: 2016-02-11.

[116] TDK-EPCOS, "Data sheet- film capacitors - power electronic capacitors," *Product Brochure*, Aug. 2013, [Online] Available: http://de.tdk.eu Retrieved on: 2016-02-11.

[117] Hioki E.E.Corporation, "Data sheet: Lcr meter hioki 3522-50," *Product Brochure*, [Online] Available: http://www.asm-sensor.com/asm/pdf/pro/3522_de.pdf Retrieved on: 2016-02-11.

# Wissenschaftlicher Werdegang

Name:                     Felix Fuchs
Geburtsdatum:             20.06.1983
Geburtsort:               Aachen
Staatsangehörigkeit:      deutsch

## Akademische Ausbildung

| | |
|---|---|
| 2002 | Abitur, Gymnasium Elmschenhagen, Kiel |
| 10/2003 - 09/2009 | Studium Elektrotechnik und Informationstechnik an der Christian-Albrechts-Universität zu Kiel, Abschluss: Diplom |
| 4/2010 –9/2015 | Promotionsstudium am Institut für Antriebssysteme und Leistungselektronik, Universität Hannover |

## Beruf

| | |
|---|---|
| 6/2008 - 8/2008 | Praktikum bei Schneider Toshiba Inverter Europe (Pacy-sur-Eure, Frankreich) |
| 4/2010 –9/2015 | wissenschaftlicher Mitarbeiter am Institut für Antriebssysteme und Leistungselektronik, Universität Hannover |
| Seit 10/2015 | Entwicklungsingenieur bei Ingenieurbüro Hoffmann GmbH, Halle a.d. Saale, Bearbeitung von Projekten im Bereich von Windenergieanlagen |

## Veröffentlichungen

2014   Fuchs, F.; Mertens, A, "Prediction and Avoidance of Grid-Connected Converter's Instability caused by Wind Park Typical, Load-Varying Grid Resonance," *Energy Conversion Congress and Exposition (ECCE), 2014 IEEE, 14-18 Sept. 2014, Pittsburgh, USA*

2014   Fuchs, F.; Dietz, R.; Garske, S.; Breithaupt, T.; Mertens, A; Hofmann, L., "Challenges of Grid Integration of Distributed Generation in the interdisciplinary Research Project Smart Nord," *Power Electronics for Distributed Generation Systems (PEDG), 2014 IEEE 5th International Symposium on , pp.1,7, 24-27 June 2014*

2014   Blank, M.; Calabria, M.; Dietz, R.; Fuchs, F.; Klingenberg, T.; Lehnhoff, S.; Mertens, A.; Schumacher, W.: Agentenbasierte Vorhaltung und Erbringung von Primärregelleistung, Automatisierungstechnik 2014, vol. 62, no. 5, pp. 347-363

2013   Fuchs, F; Pham, D.V.; Mertens, A. (2013): Analysis of Grid Current Control in Consideration of Voltage Feedforward and Cable Capacitance Demonstrated on a Fully Sized Wind Turbine Installed in a Wind Park, *IEEE Energy Conversion Congress & Expo, Denver, Colorado, USA*

2013   Fuchs, F.; Pham, D.V.; Mertens, A. : Einfluss der Netzimpedanz auf die Dynamik der netzseitigen Stromregelung am Beispiel einer Windenergieanlage, ETG Kongress 2013, Berlin

2012  Fuchs, F.; Mertens, A. (2012): Dynamic Modeling of a 2 MW Wind Turbine for Converter Issues : part 1, *Power Electronics and Motion Control (EPE PEMC 2011 ECCE Europe), Proceedings of the 2012-15th International Conference and Expositon on, Novi Sad, Serbia*

2012  Mertens, A.; Fuchs, F.; Baruschka, L. : Wandler im Meerespuls, *Erneuerbare Energien, SunMedia Verlag,* 07/2012

2011  Fuchs, F.; Mertens, A. (2011): Steady State Lifetime Estimation of the Power Semiconductors in the Rotor Side Converter of a 2 MW DFIG Wind Turbine via Power Cycling Capability Analysis, *14th European Conference on Power Electronics and Applications 2011, EPE 2011, September 2011, Birmingham, United Kingdom*

2010  Fuchs, F., Dannehl, J., Fuchs, F.W. : Discrete Sliding Mode Current Control of Grid-Connected Three-Phase PWM Converters with LCL Filter; *ISIE 2010 IEEE International Symposium on Industrial Electronics, Bari, Italy*